Intermittencies in transitional and turbulent channel flow

Thesis submitted in accordance with the requirements of
the University of Liverpool for the degree of Doctor in Philosophy
by

Rishav Agrawal

June 2020

Declaration

I hereby declare that no portion of the work referred to in this PhD thesis titled "*Intermittencies in transitional and turbulent channel flow*" has been submitted elsewhere in support of an application for another degree or qualification.

June, 2020 Rishav Agrawal

Abstract

In recent years, events of intermittent low- and high-drag have been observed in turbulent channel flows near transition. During the low-drag events, the wall shear stress, on average, temporarily reduces to about 40% below its time-averaged value and the velocity profile approaches Virk's maximum drag reduction (MDR) asymptote. There are still open questions regarding this phenomenon, for example the characteristics of Reynolds shear stress (RSS) during the events and whether they continue to exist at higher Reynolds numbers (i.e. in the so-called "fully-turbulent" flow regime). Investigating intermittencies in turbulent flow close to transition requires knowledge of intermittencies during the laminar-turbulent transition process. However, there is currently no time-resolved experimental wall shear stress data available in the transitional flow regime for channel flow.

To study the laminar-turbulent intermittency, instantaneous wall shear stress (using hot-film anemometry, HFA) is probed at the transitional Reynolds numbers. Higher order statistics show that with increasing Reynolds numbers (from the laminar flow regime), the laminar-turbulent intermittency firstly grows, then diminishes, and eventually disappears by $Re_\tau \approx 72$, where $Re_\tau = u_\tau h/\nu$ and u_τ, h and ν indicate the friction velocity, channel half-height and kinematic viscosity, respectively. Using multiple hot-film probes, information about the large-scale turbulent structures during transition is inferred. Additionally, a flow visualization has been conducted to observe the large-scale structures, which qualitatively supports the wall shear stress results.

Beyond transition, simultaneous measurements of wall shear stress and velocity (us-

ing laser Doppler velocimetry, LDV) have been conducted to detect and characterize the low- and high-drag intermittencies for $Re_\tau = 70$ - 250. The fraction of time spent in these intermittent events is observed to be independent of Reynolds number when the criteria for minimum time duration is kept constant in "inner" units. The previously observed spike in the ensemble-averaged wall shear stress before and after the low-drag events is found to be an artefact of the conditional sampling and ensemble-averaging process and is not a physical phenomenon. Conditionally-averaged streamwise velocity profiles get closer to Virk's MDR asymptote, near the wall, for all the Reynolds numbers studied. Simultaneous wall shear stress and RSS measurements are carried out for $Re_\tau = 70$ and 85. An increase in the conditionally-averaged RSS is observed during the low-drag events for all the wall-normal locations measured, but is particularly apparent for $y^+ \approx 20$ - 40, where $y^+ = yu_\tau/\nu$ and y is the wall-normal distance.

When using HFA for long-time wall shear stress measurements, minimizing the non-thermal calibration drift is a significant challenge. A new method to minimize recalibration in thermal anemometry using a non-linear regression technique is proposed and investigated. This new method was utilized in the current work and finds potential applications in cases of correcting for non-thermal calibration drifts in long time measurements and also in scenarios where the direct calibration of hot-films is not possible or suffers significant uncertainties.

Publications

Journal Papers

1. **Agrawal R**, Whalley RD, Ng HCH, Dennis DJC and Poole RJ Minimizing recalibration using a non-linear regression technique for thermal anemometry. *Experiments in Fluids* 60:116, 2019

2. **Agrawal R**, Ng HCH, Dennis DJC and Poole RJ Investigating channel flow using wall shear stress signals at transitional Reynolds numbers. *International Journal of Heat and Fluid Flow* 81C:108525, 2020

Peer reviewed conference proceeding

1. **Agrawal R**, Ng HCH, Whalley RD, Dennis DJC and Poole RJ In search of low drag events in Newtonian turbulent channel flow at low Reynolds number. *11^{th} International Symposium on Turbulence and Shear Flow Phenomena*, UK, August, 2019

Conferences (presenter underlined)

1. **Agrawal R**, Ng HCH, Whalley RD, Dennis DJC and Poole RJ In search of low drag events in Newtonian turbulent channel flow at low Reynolds number. *11^{th} International Symposium on Turbulence and Shear Flow Phenomena*, UK, August, 2019

2. **Agrawal R**, Ng HCH, Dennis DJC and Poole RJ Probing transition to turbulence and low-drag turbulent states in channel flow using wall shear stress signals. *90^{th} Annual Meeting of the International Association of Applied Mathematics and Mechanics*, Austria, February, 2019

3. **Agrawal R**, Ng HCH, Whalley RD, Dennis DJC and Poole RJ Instantaneous velocity and wall shear stress measurements during low-drag events in turbulent channel

flow. *UK Fluids Conference*, UK, September, 2018.

Acknowledgements

I am very grateful to Prof. Robert J. Poole for giving me an opportunity to work on such an interesting project. I will be indebted to him for his guidance and support throughout the course of my PhD study. I would like to sincerely thank Dr. David J. C. Dennis for providing an excellent guidance and insightful observation on my work. I am also thankful to Dr. Henry Ng for providing valuable inputs to this research. I would also like thank Dr. Richard D. Whalley and Prof. Michael D. Graham for helpful discussions.

I thank all my office mates, Dr. Bayode Owolabi, Mr. Allysson Domingues, Dr. Mahdi Davoodi, Hesam Maleki, Oguzhan Der, Dr. Osama Maklad, Dr. Simeng Chen, Victor Ibezim for various interesting discussions. I would particularly like to thank Dr. Zografos Konstantinos for helping me with the Linux towards the end of my PhD.

I would like to thank the technical support provided by Mr. Derek Neary and Mr. John Curran during my research. I also acknowledge the excellent administrative support given by Mr. Jack Carter-Hallam.

I would like to thank Dr Jing Guan for being a great companion and keeping me sane during my difficult times of stay in Liverpool. Finally, I would like to thank my parents and my brother and sister for always being with me during various ups and downs which I experienced while my stay in Liverpool.

Contents

List of Figures

List of Tables

Nomenclature

A_t	Arrival time of the seeding particle (s)
a, b, c, d	Hot-film calibration coefficients
B	log-law constant
d_f	Fringe spacing (m)
E	Error function
e_1, e_2	Output voltages from the Wheatstone bridge circuit (Volts)
F	Flatness
f	Fanning skin-friction factor coefficient
f_D	Doppler frequency (Hz)
f_s	Shift frequency of one of the laser beam (Hz)
h	Channel half-height (m)
h_b	Blade height (m)
L_x, L_y, L_z	Dimensions of a computational domain in x, y and z directions (m)
L_s	Slip length
l	Length over which pressure drop is measured (m)
L_{ds}, L_{us}	Distance of the downstream and upstream pressure tappings from the channel inlet, respectively (m)
N	Number of samples
N_x, N_y, N_z	Number of grid cells in the x, y and z directions
O_{HR}	Overheat ratio
P	Pressure (Pa)

Re_h	Reynolds number based on channel half-height and bulk velocity
Re_τ	Reynolds number based on channel half-height and friction velocity
$R_{u_{\tau_1} u_{\tau_2}}$	Correlation between friction velocities u_{τ_i} and u_{τ_j}, where i and j can take values 1, 2 or 3 for hot-film 1, hot-film 2 or hot-film 3, respectively
R_0	Resistance of the hot-film sensor at the ambient temperature (Ohm)
R_W	Resistance of the hot-film sensor at the working temperature (Ohm)
S	Skewness
s	Blade spacing
T_{OSC}	Time period of oscillation (s)
U_b	Bulk velocity (m/s)
U, V	Streamwise and wall-normal velocities (m/s)
U_1, U_2	Velocity components measured using the blue and green pairs of laser beams (m/s)
U_c	Convective velocity (m/s)
U_{cl}	Centreline velocity (m/s)
$U_{cl,lam}$	Laminar centerline velocity (m/s)
U_{rs}	Resampled velocity (m/s)
u, v	Streamwise, wall-normal velocity fluctuations (m/s)
u_τ	Friction velocity (m/s)
V_{px}	Velocity component of the seeding particle crossing the measurement volume perpendicular to the interference pattern (m/s)
V_L	Output voltage from the anemometer (Volts)
T_t	Transit time of the seeding particle (s)
T_w	Working temperature of hot-film sensor (^{o}C)
T_0	Ambient temperature (^{o}C)
w	Channel width (m)
x, y, z	Streamwise, wall-normal and spanwise co-ordinates (m)

α	Beam half-angle (degrees)
α_{r_0}	Coefficient of resistance of hot-film sensor ($1/^{o}$C)
χ	Normalized total stress
δ_ν	Viscous length scale (m)
δt	Time duration for a low-drag or a high-drag event (s)
Δt	Time-lag (s)
ΔP	Pressure drop (Pa)
$\dot{\gamma}$	Shear rate (s^{-1})
κ	von Kármán constant
λ	Wavelength of light (m)
μ	Dynamic viscosity (Pa.s)
ν	Kinematic viscosity (m^2/s)
ϕ	Angle of rotation of the laser head about the spanwise axis (degrees)
ρ	Density (kg/m^3)
σ	root mean square
τ	Total stress (Pa)
τ_w	Wall shear stress (Pa)
ζ	Indicator function

Acronyms

ADC	Analog-to-digital
AR	Aspect ratio
BNC	Bayonet Neill–Concelman
BSA	Burst spectrum analyzer
BR	Bridge Ratio
CCA	Constant current anemometry
CFD	Computational fluid dynamics
CTA	Constant temperature anemometry
DNS	Direct numerical simulation
DP	Directed percolation
DR	Drag reduction
DSLR	Digital single-lens reflex
ECS	Exact coherent states
FR	Frame rate
HDR	High drag reduction
HF	Hot-film
HFA	Hot-film anemometry
ISPR	Intermediate single point recalibration
LDV	Laser Doppler velocimetry

LDR	Low drag reduction
MDR	Maximum drag reduction
MFU	Minimal flow unit
MTV	Molecular tagging velocimetry
PDF	Probability density function
PIV	Particle image velocimetry
PMT	Photomultiplier tube
PPF	Plane Poiseuille flow
PRT	Platinum resisteance thermometer
rms	root mean square
RSS	Reynolds shear stress
SHS	Superhydrophobic surface
TW	Travelling-wave

Chapter 1

Introduction

1.1 Background

Turbulence is everywhere; it is frequently encountered in our daily lives for example in the form of water coming out of a tap or the airflow over an automobile. This familiarity with turbulence has not necessarily brought a clear understanding of this ubiquitous phenomenon. The problem of turbulence has been studied by some of the greatest physicists, mathematicians and engineers of the 19^{th} and the 20^{th} centuries [for review, see books by, McComb, 1990, Frisch, 1995]. Yet, there is no complete understanding of how turbulence occurs and no accurate prediction (to a sufficient level of reliability) of the turbulent flow can be made, even for simple flow geometries [Worth and Nickels, 2011], and the "turbulence problem" is largely considered to be the most important unsolved problem of the classical physics [Feynman et al., 1965].

The history of understanding turbulence goes back to the early sketches of fluid flow drawn by Leonardo da Vinci about 500 years ago. His sketches of the flow of water, along with his in-depth insights, provided the first scientific description of turbulence [Richter et al., 1970]. As centuries passed many great mathematicians such as Newton, Bernoulli and d'Alembert contributed to the theory of fluid mechanics but were challenged by the complexity of turbulent flow. One of the major landmarks in the history of the field of mechanics was made by Navier, a French Engineer in 1822. He provided the first governing equations for hydrodynamics also called Navier-Stokes equations

(in association with Stokes) [for review on the historical development of Navier-Stokes equations, see, Bistafa, 2018]. This set of equations contain all the information about any fluid flow, including turbulent flow. Apart from these theoretical developments, experimental studies were also making progress. One of the earliest developments in experimental fluid mechanics was the invention of the Pitot tube by Henri Pitot (a French engineer) in 1732 [Pitot, 1732]. After about 130 years, in the 1850s, Henry Darcy (another French engineer) modified the previously developed Pitot tube, which greatly improved the accuracy of the measurement of fluid velocity [Darcy, 1858]. Later, Darcy also contributed to the understanding of the calculation of head loss through a pipe that is still used today in the form of Darcy friction factor [Moody, 1944]. In 1839, Hagen (a German engineer) conducted an experiment in laminar pipe flow and obtained a parabolic velocity profile and, a few years later, a French physician Poiseuille (who was unaware of Hagen's work) obtained similar results for laminar pipe flow [Sutera and Skalak, 1993]. This velocity profile was later confirmed using the analytical solution in 1858 and is now commonly called a Hagen-Poiseuille flow profile. Another breakthrough in experimental fluid mechanics was achieved by Osborne Reynolds while working on understanding pipe flow at Manchester [Reynolds, 1883]. He discovered the importance of a non-dimensional number, now called the Reynolds number, in determining when the flow will leave the laminar state to enter transition to turbulence.

Pipe flow, which had been a major area of research to understand turbulence and fluid flow in general, comes under the category of "wall-bounded" flow, which deals with the interaction between fluid flow and a solid boundary. Two other major examples of these types of wall-bounded flows are channel flow and boundary-layer flow. Over the years, researchers have paid significant attention to these flows because of their importance in practical applications such as flow in pipelines, nuclear reactor channels, mixing and cooling devices, and heating, ventilation, and air conditioning (HVAC) systems. Since the experimental work of Reynolds [1883] in pipe flows, various researchers carried out experimental investigations of channel flows, for example, Nikuradse [1933] and Reichardt [1938] in the first half of the 20^{th} century, but near that time, the most

significant experimental contribution to the study of the turbulent channel flows was provided by Laufer [1951]. Since then, there have been numerous experimental and numerical works to further understand channel flows [see, for example, Dean, 1978, Kim et al., 1987, Jiménez and Moin, 1991, Monty, 2005, Ng et al., 2011]. Apart from fully-turbulent flows, transition to turbulence has also been an active area of research for channel flows and the early studies include the work by [Davies and White, 1928] and Patel and Head [1969]. Carlson et al. [1982] observed the presence of large localized coherent structures during the laminar-turbulent transition process in channel flows called "turbulent spots". These localized patches received much attention among researchers over the decades since their discovery, see for example Alavyoon et al. [1986], Li and Widnall [1989], Lemoult et al. [2013], Sano and Tamai [2016]. In the last few decades, various new discoveries, for example existence of sparse "turbulent bands" and the relationship with the directed percolation (DP) near the onset of transition have also been made [see, for example, Xiong et al., 2015, Xiao and Song, 2019, Sano and Tamai, 2016].

The presence of turbulence in wall-bounded flows is a major contributor to the skin-friction drag and there are many situations where it is desirable for the flow to remain in a laminar state to reduce the skin-friction drag, for example in pipelines and aircraft wings. For a conventional aircraft, the skin friction drag contributes almost 50% of the total drag experienced [Ge et al., 2017]. Thus, in addition to its fundamental significance, a better understanding of wall-bounded turbulent flow can hugely help in energy savings, thus benefiting the global economy and climate. In wall-bounded turbulent flows, one of the well-investigated phenomena is the presence of near-wall cycle which consists of the so-called "ejection" and "sweep" events. Ejection is associated with the out-rush of low-speed fluid away from the wall and sweep event is associated with the inrush of high-speed fluid towards the wall. These events in the wall-bounded flows are thought to be responsible for the higher skin-friction drag [Kim et al., 1987] and many control strategies have been developed to reduce the skin-friction drag by suppressing these events. Among these strategies, the addition of polymers in turbulent flows has remained an effective technique to reduce the skin-friction drag [Toms, 1948]. The

maximum drag reduction possible due to polymer additives in turbulent flows is given by the Virk's maximum drag reduction (MDR) asymptote [Virk, 1975]. Many of the other drag reduction techniques rely on the (local) relaminariztion of the turbulent flow and in order to understand the relaminarization, it is also important to have a better understanding of the laminar-turbulent transition process.

The discovery of traveling-wave (TW) solutions for the Navier-Stokes equations has greatly advanced our understanding of wall-bounded flows. These traveling-wave solutions, first discovered by Nagata [1990] for planar Couette flows, are three-dimensional and non-linear and are also sometimes called Exact Coherent States (ECS). Later, Waleffe [2001] found the TW solutions for planar channel flows. These TW solutions have a similar structure to near-wall turbulence, i.e. mean flow with alternating low- and high-speed streaks and counter-rotating vortices. They are found to occur in pairs with two branches: the upper branch and the lower branch. The upper branch has a higher fluctuation amplitude and thus higher drag than the lower branch.

Another major avenue of research in the computational fluid dynamics (CFD) simulations of planar channel flow are the so-called minimal flow units (MFUs) [Jiménez and Moin, 1991]. These MFUs represent the smallest computational domain which can sustain turbulence. The use of MFU has advanced the numerical techniques to study channel flow by reducing computational time. Park and Graham [2015] used DNS in an MFU and found five families of ECS solutions, which they denote as the "P1-P5" solutions. Of these five families of solutions "P4" was the most intriguing. The velocity profile of the upper branch of this solution approaches the classic Prandtl-von Kármán log-law, while the velocity profile of the lower branch approaches the Virk's MDR asymptote [Virk, 1975]. This MDR asymptote is generally associated with viscoelastic turbulent flows. The existence of such solutions for Newtonian flows opens a window of opportunity with potentially significant practical implications. These intermittent moments of higher drag and lower drag in turbulent flows were given the nomenclature of "active" and "hibernating" turbulence by Xi and Graham [2012]. Such intermittent

states will be the focus of a part of this thesis.

Kushwaha et al. [2017] extended the work of Park and Graham [2015] by conducting spatial and temporal analyses of the intermittencies associated with low- and high-drag for extended domains. Whalley et al. [2019] provided the first experimental verification of this so-called hibernating turbulence for channel flows and it was found that the conditional mean velocity during low-drag events is in good agreement with the P4 ECS solution obtained for a minimal domain by Park and Graham [2015]. Park et al. [2018] related the strong turbulent bursts to the hibernating turbulence in the minimal channel flow where they showed that many hibernating events are followed by strong turbulent bursts. Reynolds shear stress (RSS) characteristics during hibernation are studied in a minimal channel flow using DNS by Xi and Graham [2012] and Park and Graham [2015], where it is observed that RSS drops to a low value during hibernation much as observed in MDR [Warholic et al., 1999].

1.2 Motivation

Although there has been significant progress in the understanding of turbulence, a number of questions have remained unanswered. One of the major unresolved issues is transition to turbulence in wall-bounded flows. Ever since the first notable study by Reynolds [1883] for laminar-turbulent transition in pipe flows, there have been numerous investigations studying the transition process. Transition in planar channel flows is subcritical which means that the laminar flow can undergo transition before the critical Reynolds number determined from linear stability [Orszag, 1971]. One major difference in channel flow is the presence of highly inhomogeneous localized coherent structures called "turbulent spots", unlike pipe flows where the transitional structures, for example puffs and slugs, fill the entire cross-section of the pipe. This makes the investigation of the transition process in channel flows a challenge due to the complex spatial inhomogeneity. The transition to turbulence process includes the highly intermittent laminar-turbulent regime when the flow rapidly switches between the laminar and the turbulent events [Patel and Head, 1969]. The characteristics of this intermit-

tency have not been investigated near the wall in channel flow whereas a potential connection between the instantaneous wall shear stress and coherent motions of the flow above the wall in wall-bounded flows has been observed [Marusic et al., 2010, Orlu and Schlatter, 2011]. Therefore, it has become important to have a better understanding of the instantaneous wall shear stress in order to understand the complex nature of transition to turbulence in shear flows and the concomitant intermittent structures. For channel flows, experimental wall shear stress measurements are rather limited, especially, near transition and the lowest Reynolds number at which the higher order statistics of wall shear stress has been studied is by Keirsbulck et al. [2012] for $Re_\tau = 74$. This is generally attributed to the practical challenges in conducting spatially and temporally well-resolved measurements of wall shear stress [Alfredsson et al., 1988b]. Thus, understanding the wall shear stress characteristics for the transitional channel flow forms an important motivation for the current study.

Next to the laminar-turbulent intermittency, the intermittencies in turbulent channel flow have also been observed which give rise to the so-called low- and high-drag events [Xi and Graham, 2010, Park and Graham, 2015, Whalley et al., 2017, Kushwaha et al., 2017]. Until now, the existence of such events has been observed for the flow close to transition [Kushwaha et al., 2017, Whalley et al., 2019] (Re_τ between 70 and 100). To study the temporal intermittency, they employed the following criteria to detect a low-drag (hibernating) or high-drag (hyperactive) events: the instantaneous wall shear stress (τ_w) should remain below 90% or above 110% for a time duration of $t^* = tu_\tau/h = 3$ for low- or high-drag events, respectively where u_τ and h indicate the friction velocity and channel half-height. Whalley et al. [2019], using physical experiment and the aforementioned criteria, observed that the fraction of time spent in the low- and high-drag intermittent regimes decreases significantly while increasing Re_τ between 70 and 100. It is necessary to investigate the effect of changing the criteria, especially exploring different scalings for the time-duration criteria, on the fraction of time spent in these conditional events. It is also necessary to investigate these intermittencies for higher Reynolds number and especially when the flow is commonly regarded

to be "fully-turbulent", i.e. $Re_\tau \geq 180$ [Kim et al., 1987]. It was shown by Park and Graham [2015] and Xi and Graham [2012], using DNS carried out for MFUs, that the Reynolds shear stress (RSS) goes to a very low value during the low-drag events. The characteristics of the RSS during these intermittent events for extended domains (using either physical experiment or numerical techniques) are unknown. Therefore, this is also an important research gap in the understanding of these low- and high-drag intermittencies and is an important motivation for the current study. While carrying out the investigations in the extended domains, Kushwaha et al. [2017] and Whalley et al. [2019] conducted ensemble averaging of all the instantaneous wall shear stresses which meet the requirement for low-drag and high-drag events to obtain ensemble-averaged wall shear stress during the conditional events. They observed that near the start and end of low-drag events the ensemble-averaged wall shear stress spikes to a higher value than the time-averaged wall shear stress, and similarly near the start and end of high-drag events the ensemble-averaged wall shear stress dips to a lower value than the time-averaged wall shear stress. The physical explanation for this phenomenon is still unknown and forms a further motivation for the present study.

1.3 Aim and objectives

The primary aim of this thesis is to undertake an experimental investigation into the intermittencies associated with transitional and turbulent channel flows. Studying intermittencies can provide a better understanding of the flow and can also potentially help in better design of control strategies for drag reduction in wall-bounded flows.

The specific objectives of this thesis are as follows:

- to minimize issues related to the thermal and non-thermal drifts in the wall shear stress signals while studying intermittencies using HFA in order to obtain very long time series.
- to investigate the intermittencies associated with the transition process in channel flow by probing higher order statistics of wall shear stress signals at transitional

Reynolds numbers.

- to carry out an investigation into the large-scale turbulent structures during transition using simultaneous wall shear stress measurements at multiple spatial locations.
- to investigate other possible scalings for the time-duration criteria for the low- and high-drag intermittencies in turbulent channel flow to better understand what quantities are physically important.
- to probe the existence of these low- and high-drag intermittencies at higher Reynolds numbers than has been done before, i.e. $Re_\tau > 100$.
- to find the physical explanation for the spike (dip) in ensemble-averaged wall shear stress near the start and end of low-drag (high-drag) events.
- to investigate the Reynolds shear stress characteristics during the low- and high-drag intermittencies in a channel flow and compare them with the results obtained in minimal channel geometry using DNS.

1.4 Outline of thesis

The content of this thesis is divided into seven chapters. The first (current) chapter provides a brief introduction to this thesis by first discussing the historical background and motivation for the present study. Later it explains the aim and objectives of this thesis.

Chapter 2 discusses the detailed literature review related to the investigations carried out previously in channel flows. The primary focus of this chapter is on the studies related to transition to turbulence, fully-turbulent flows, turbulent drag reduction and the recently observed "low-drag" events in Newtonian turbulence. Relevant background information related to wall-bounded turbulence e.g. the law of the wall, near-wall cycle and exact coherent states (ECS) are also provided in this chapter.

Chapter 3 provides a description of the experimental arrangement used in this study.

The chapter starts with an explanation of the description of the flow rig employed and discusses the various measurement techniques (pressure-drop measurements, laser Doppler velocimetry, hot-film anemometry, and flow visualization) used in this study. Later, an uncertainty analysis is conducted to quantify the error associated with every measured parameter. Finally, the flow conditions inside the channel flow rig are checked to make sure the flow at the measurement location is free of any side-wall or development-length effects.

Chapter 4 is the first results chapter where a novel technique to minimize recalibrations in thermal anemometry is investigated. This method employs non-linear regression to estimate the calibration coefficients for hot-film and hot-wire data using *a priori* knowledge of the first three or four moments for the same flow conditions. The robustness of technique is checked for two different calibration relationship forms, number of samples and available moments, and different flow conditions (using hot-film and hot-wire data). This chapter also discusses the various potential practical scenarios where this technique can be applied.

Chapter 5 investigates the intermittencies associated with transitional channel flow using wall shear stress signals. Wall shear stress measurements at multiple wall locations have been carried out to give insight regarding the size and orientation of large-scale structures. Flow visualization has also been conducted, which provides information about the large-scale coherent structures during the transition process in the employed channel flow facility.

Chapter 6 discusses the intermittencies associated with turbulent channel flow using wall shear stress and velocity data. These intermittencies are called either low-drag or high-drag depending on the magnitude and duration of the intermittency in the wall shear stress signal. The effects of time-duration and threshold criteria on the conditional quantities are discussed. The velocity characteristics during these intermittent events are investigated by carrying out simultaneous measurements of velocity and wall

shear stress data.

Chapter 7 discusses the major conclusions obtained from the present work. It also provides some recommendations for future investigations.

Chapter 2

Channel flow

This chapter aims to provide a detailed literature review of channel flow, a class of canonical wall-bounded flow. The other two canonical wall-bounded flows are pipe flow and zero pressure gradient boundary layer flow. Over the years, researchers have found many similarities between these three types of flows [for more details, please see: Monty et al., 2009, Ng et al., 2011, Chin et al., 2014]. A relevant theoretical background of channel flow (or wall-bounded flow, in general) will also be discussed, wherever necessary.

The chapter begins with a description of the channel flow geometry and the analytical solution for the laminar flow case. Next, the literature related to the laminar-turbulent transition in channel flow is discussed. A section on the theoretical description of turbulent channel flow and some of the seminal works in channel flow are provided. Next, the fundamentals of turbulent drag reduction (with respect to near-wall structures) and some of the major drag reduction techniques for wall-bounded flows are discussed. Finally, the last section discusses the so-called low- and high-drag events, for channel flow near transition, which have been observed and investigated over the last decade, and which will be investigated in this project.

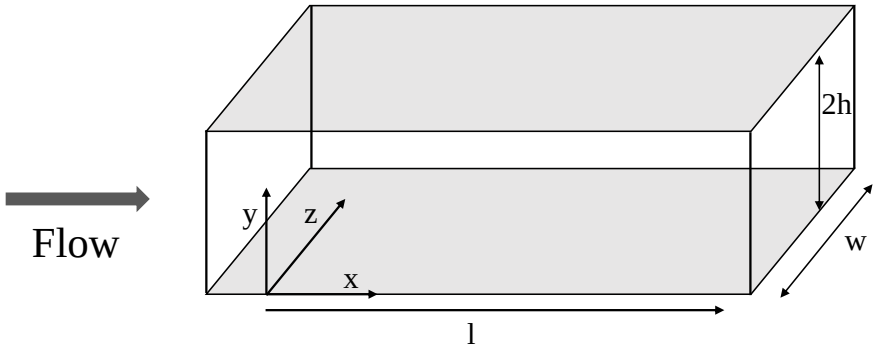

Figure 2.1: Schematic of a channel flow.

2.1 Channel flow description

Channel flow represents the flow through a rectangular duct which is driven by an external pressure gradient. A schematic of a typical channel flow is shown in figure 2.1. The mean flow is in the streamwise (x) direction. The spanwise extent (w) of the channel is usually very large compared to its half-height (h), providing a very large aspect ratio (AR $= w/2h >> 1$). This makes the velocity statistics independent of the spanwise direction when sufficiently away from the side-wall, as side-wall effects are minimized. The streamwise (axial) length of the channel is also usually very long ($l/h >> 1$), therefore inlet effects can be ignored and the flow can be considered to be "fully-developed" [Durst et al., 2005]. In this fully-developed region, the velocity statistics are independent of the streamwise (x) direction. Therefore, a wide, fully-developed channel flow is statistically one-dimensional with the velocity statistics varying only in the wall-normal (y) direction. It has also been shown using various experiments and computational studies that the flow is statistically symmetric about the channel centerline ($y = h$).

The channel flow is generally very attractive among experimentalists as well as computational fluid dynamicists. Channel flow has a relatively simple geometry, especially fully-developed channel flow between two parallel plates. An additional advantage is that this geometry uses a Cartesian coordinate system, unlike pipe flow. This makes this geometry more favourable to be simulated by numerical researchers.

A fully-developed channel flow maintains a balance between the pressure drop (dP) acting on a streamwise separation (dx) and the wall shear stress acting on the lateral surface of the channel. Here, the pressure drop is induced by an external source. For the case of AR $>>$ 1, such that the flow can be assumed to be spanwise invariant, the wall shear stress has contribution only from the top and bottom walls. A force balance can be applied to obtain a relation between the wall shear stress and the pressure drop for a fully-developed channel flow and is given by the following equation:

$$\tau_w = h \left| \frac{dP}{dx} \right|. \tag{2.1}$$

In practical experiments, the aspect ratio is always finite, however large. Therefore, there will be an effect of the side walls on the contribution to the total wall shear stress. Considering the effect of the side walls, the force balance provides the following relation between the wall shear stress and the pressure-drop in a fully developed region of a channel flow:

$$\tau_w = \frac{wh}{(w+2h)} \left| \frac{dP}{dx} \right|. \tag{2.2}$$

The wall shear stress shown in equation 2.2 is perimeter-averaged as opposed to the wall shear stress shown in equation 2.1 which assumes that there is no side-wall effects. In this study, the wall shear stress as calculated in equation 2.2 will be used. This wall shear stress is used to calculate the skin friction factor. Fanning friction factor, which is named after John Thomas Fanning, is a non-dimensional number which is commonly used to represent skin friction coefficient and is given as follows:

$$f = \frac{2\tau_w}{\rho {U_b}^2}. \tag{2.3}$$

Here, ρ is the density of the fluid and U_b is the bulk velocity of the flow. Combining equation 2.2 and equation 2.3 gives a relation between the skin friction coefficient and

the pressure drop for a fully-developed channel flow of finite aspect ratio:

$$f = \frac{2wh}{(w+2h)\rho {U_b}^2} \left| \frac{dP}{dx} \right|. \tag{2.4}$$

When the flow is in a laminar state, a channel flow is also known as a plane Poiseuille flow (PPF). PPF is defined as a flow between two infinitely long parallel plates driven by a constant pressure gradient, applied in the direction of the mean flow. There exists an analytical solution for the mean streamwise velocity, $U(y)$ for a plane Poiseuille flow and it is given by equation 2.5 where μ represents the fluid dynamic viscosity,

$$U(y) = \frac{-1}{2\mu} \frac{dP}{dx} \big(y(2h-y) \big). \tag{2.5}$$

The bulk velocity (U_b) can be calculated by integrating equation 2.5 with respect to y. Using equation 2.5 it can be shown that U_b in a channel is two-thirds of the centerline velocity (U_{cl}), $U_b = 2U_{cl}/3$. For laminar channel flow, f can also be obtained analytically as a function of Reynolds number (Re_h) where $Re_h = U_b h\rho/\mu$ and is given by:

$$f = \frac{6}{Re_h}, \tag{2.6}$$

Dean [1978]

2.2 Transition to turbulence in channel flows

The transition to turbulence in shear flows has remained an active topic of investigation in fluid mechanics since the classical experimental work of Osborne Reynolds in the 19$^{\text{th}}$ century [Reynolds, 1883]. Figure 2.2 shows a sketch of the apparatus used by Osborne Reynolds for his classic dye experiment to study transition in a pipe flow. Since the work of Reynolds, there has been an extensive amount of work in the field of instability and transition in shear flows and numerous papers are available describing the advancement made in understanding this phenomena [for reviews, see, for example: Eckhardt et al., 1998, Manneville, 2016]. Understanding the transition phenomenon

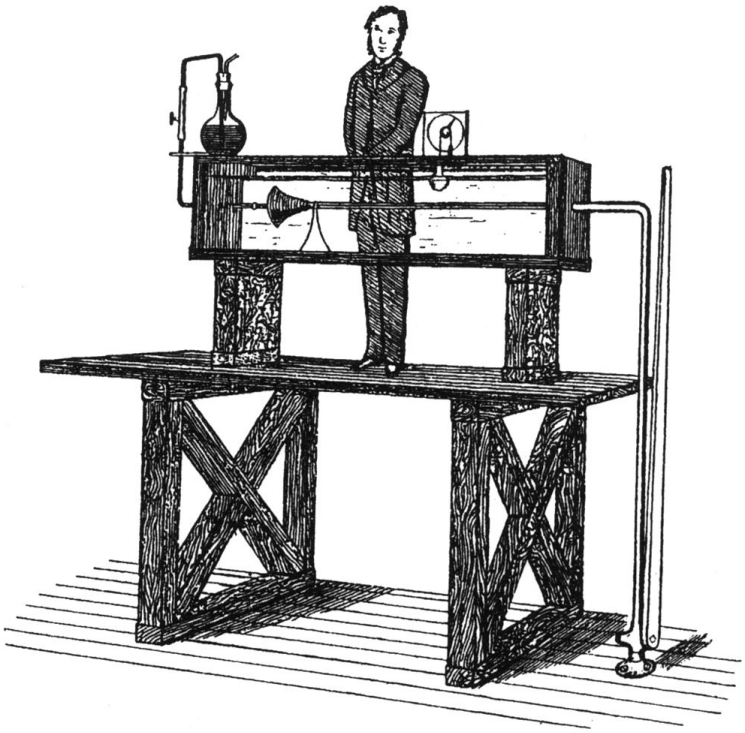

Figure 2.2: Sketch of the apparatus used by Reynolds [1883] for his classic dye experiment in a pipe. Source: Reynolds [1883].

is useful for fundamental research as well as practical applications. For example, turbulent flow provides better mixing and heat transfer than laminar flow and therefore understanding the transition phenomenon may help in more efficient designs for mixing and heat transfer applications. There are also many situations where the flow can be manipulated to remain in a laminar state to reduce the skin friction drag. In this section, the focus will be on the transition studies for smooth channel flows.

The transition to turbulence in channel flow is called "subcritical" which means that the laminar flow can enter into the turbulent state well below the critical Reynolds number of linear stability if finite-amplitude disturbances are present [Orszag, 1971]. Since the seminal work of Reynolds [1883] for pipe flows, the first well-known experimental study of this subcritical transition to turbulence in channel flow was carried out by Davies and White [1928]. They conducted pressure drop measurements to study transition in a channel of aspect ratio varying between 38 and 165. The next major study investigating the transition phenomena in channel flow was conducted by Patel and Head [1969].

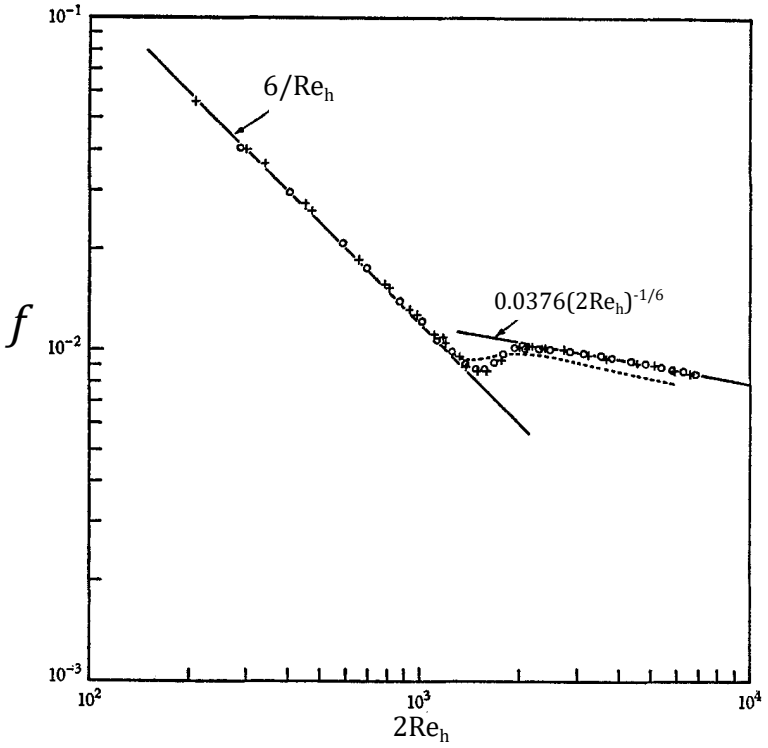

Figure 2.3: Skin friction dependence on the Reynolds number for channel flow. Here, y-axis is the Fanning skin friction coefficient ($f = \tau_w/0.5\rho U_b^2$) and x-axis is the Reynolds number ($2Re_h = 2U_b\rho h/\mu$). Circle (o) and plus (+) symbols indicate the results obtained for the case of clear entry and 1/3 inch diameter wire at entry, respectively. The dashed line shows the result by Davies and White [1928]. Source: Patel and Head [1969]

They obtained skin friction, using pressure-drop measurements, for varying Reynolds number from laminar to turbulent flow regimes in a channel flow facility with aspect ratio of 48. Figure 2.3 shows the skin friction dependence on Reynolds number as obtained by Patel and Head [1969]. The skin friction plot is a convenient way to understand the laminar-turbulent transition phenomenon from the perspective of changes in skin friction factor with changing Reynolds number. As shown in figure 2.3, the flow was found to be in a laminar state until $2Re_h \approx 1350$ as f is approximately equal to $6/Re_h$, see equation 2.6. The transitional state was found to be until $2Re_h \approx 2500 - 3000$. The turbulent state was found to start after $2Re_h \approx 2500 - 3000$ with the friction factor varying with Reynolds number approximately as $f = 0.0376(2Re_h)^{-1/6}$. They also compared their results with skin friction results obtained by Davies and White [1928]. The skin friction results were found to be different between the two works, especially after the flow left the laminar state, as is evident in figure 2.3. They attributed this

variation to an issue with the Davies and White [1928] experiments, as their pressure drop measurements were carried out close to the entry of the channel where the flow was still "developing". Patel and Head [1969] also observed apparently random "turbulent bursts" in the velocity signals, obtained using a hot-wire, near the onset of transition in channel flows. Kao and Park [1970] carried out an investigation of transition in a channel flow of lower aspect ratio (AR = 8) with and without providing artificial excitation to the flow. A hot-film anemometer was employed to measure the instantaneous flow velocity. The critical Reynolds number with or without artificial excitation was found to be in good agreement, a result which was also previously shown by Patel and Head [1969]. Orszag [1971] carried out linear stability analysis for plane Poiseuille flow and obtained a critical Reynolds number of $1.5Re_h = 5773$ ($Re_h = 3850$). Linear stability analysis was carried out by solving the Orr-Sommerfield equation numerically using expansions in Chebyshev polynomials. Nishioka et al. [1975] investigated transition in channel flow of AR = 27.4 by minimizing the background turbulence to a level of 0.05%. They employed hot-wire anemometry to investigate the linear and nonlinear instability, and breakdown to transition in channel flow. They could maintain laminar flow until $Re_h = 5333$ which is above the critical Reynolds number for linear stability ($Re_h = 3850$) as calculated by Orszag [1971]. This difference is also attributed to the finite aspect ratio of the channel where the side-walls are shown to have a stabilizing effect on the flow.

2.2.1 Coherent structures in transition

The most well-observed coherent structures associated with transitional channel flow are the so-called turbulent spots. These turbulent spots are localized coherent structures and were first observed during the investigation of the transition process in a boundary-layer flow by Emmons [1951]. In later years, the characteristics of these turbulent spots were extensively studied for boundary-layer flows, [see, for example: Cantwell et al., 1978, Wygnanski et al., 1979]. In early experiments, using flow visualization in a channel flow, Carlson et al. [1982] and Alavyoon et al. [1986] observed the presence of turbulent spots during laminar-turbulent transition. They found that these

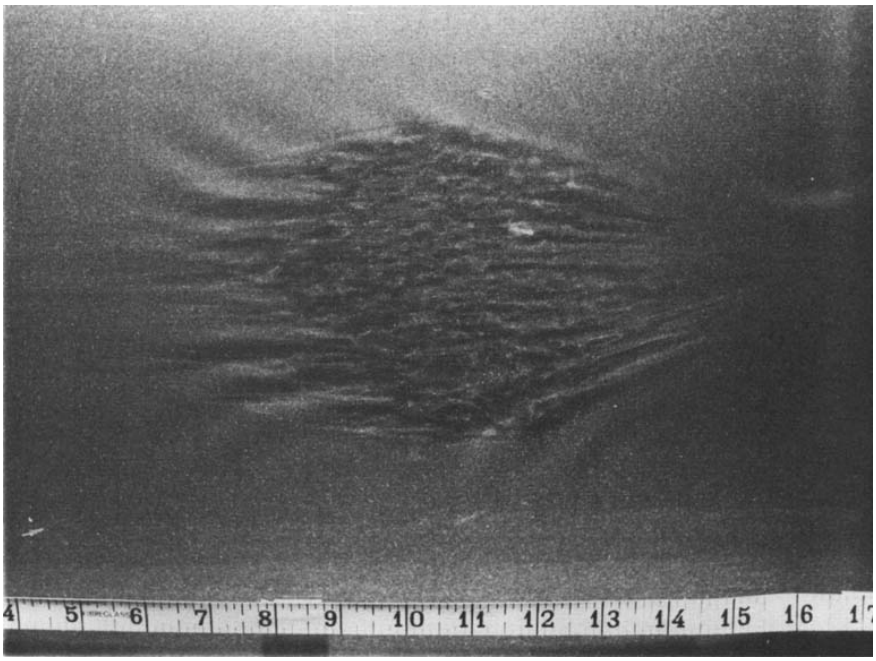

Figure 2.4: Turbulent spot as observed by Carlson et al. [1982] at $128h$ away from the inlet for $Re_h = 1000$. The mean flow direction is from left to right. Scale indicates the distance from the generator in inches. Source: Carlson et al. [1982]

turbulent spots grow as they flow downstream with their leading-edge propagating at a higher speed than the trailing edge. A typical spot, as observed by Carlson et al. [1982], is shown in figure 2.4. The presence of oblique waves surrounding the arrowhead-shaped coherent structure can be seen from figure 2.4. The angles these oblique waves make with the mean flow direction were also investigated. Li and Widnall [1989], using numerical techniques, further investigated the behaviour of the oblique waves which are associated with the turbulent spots in plane Poiseuille flow. More recently, Lemoult et al. [2013] used particle image velocimetry (PIV) to investigate the formation and growth of a turbulent spot in a plane Poiseuille flow (PPF). They used a channel flow facility of aspect ratio AR = 7.5 and showed that the flow region around the spot can be divided into two scales: large-scale (>5h) and small-scale (<5h). Sano and Tamai [2016] studied the characteristics of turbulent spots while investigating the transition in channel flow using flow visualization. Further discussion on the results obtained by Sano and Tamai [2016] will be discussed in subsection 2.2.2.

Numerical investigation of transitional channel flow remained challenging for a long

time due to the extended size of the near-wall streaky structures observed during transition, thus requiring very large computational boxes. Most of the efforts to use large computational domains were made to study high Reynolds number flows to investigate the large scale motions in the outer region of such wall-bounded flows [Liu et al., 2001, Jiménez, 1998]. Tsukahara et al. [2005] carried out direct numerical simulations (DNS) for channel flow at low Reynolds number 790 (60) $< Re_h(Re_\tau) <$ 2865 (180) by using different computational domain sizes. The largest computational domain, which they called an extra-large (XL) box, had a dimension of $L_x \times L_z \approx 51.2h \times 22.5h$, for Re_τ = 80. They applied a periodic boundary condition in the streamwise and spanwise directions and a no-slip condition on the top and bottom walls. They investigated the transition process by decreasing the Reynolds number from a fully-turbulent state to the onset of flow laminarization. They observed the presence of a periodic weak-turbulence region for $Re_h = 1160$ which looked similar to puff-like structures observed in transitional pipe flows [Wygnanski and Champagne, 1973, Wygnanski et al., 1975]. These periodic weak-turbulence structures were found to be inclined with the streamwise direction at an angle of about 24°. They were found to consist of two distinct regions: low-turbulence region and high-turbulence region. Figure 2.5 shows this puff-like structure for $Re_h = 1145$ where region A and region B indicate the region of "laminar-like" flow and highly disordered turbulent flow, respectively, as obtained by Tsukahara et al. [2005]. Both regions can be seen to be inclined with the streamwise direction. The propagation velocities of these puff-like structures were found to be almost equal to the bulk velocity.

Aida et al. [2010] carried out DNS in a plane Poiseuille flow and increased the Reynolds number starting with the onset of transition, which was opposed to Tsukahara et al. [2005], where the Reynolds number was decreased from the fully-turbulent state to study transition. They observed that the turbulent spots, which originate at the onset of transition, develop into stripes with increasing Reynolds numbers. Using flow visualization in a channel, Tsukahara et al. [2014] found turbulent stripes for $Re_h = hU_b/\nu$ between 850 and 1000. These stripy structures were observed to consist of laminar and

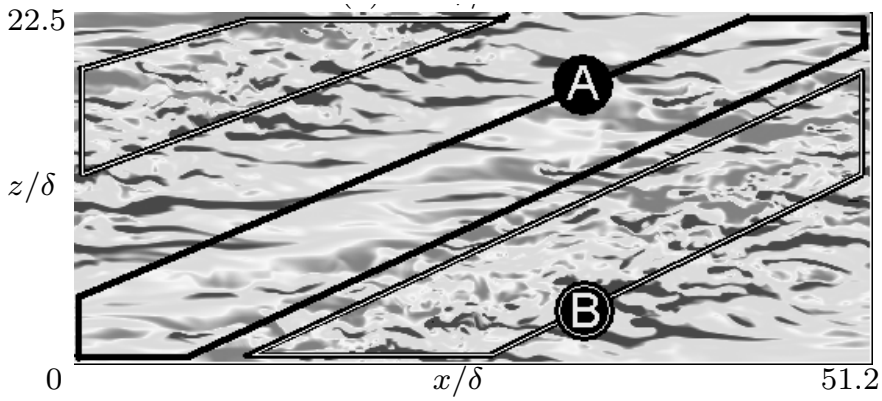

Figure 2.5: Contours of streamwise velocity fluctuation for one snapshot at $y/h \approx 0.5$ for $Re_h = 1145$. δ indicates the channel half-height (h). The mean flow direction is from left to right. Source: Tsukahara et al. [2005]

turbulent regions, and inclined at an angle of 20°-30° with the streamwise direction. Using DNS, Aida et al. [2014] investigated the growth of a single turbulent spot and observed the presence of "stripy" structures inside the spots which contain so-called quasi-laminar and turbulent regions.

Xiong et al. [2015] carried out DNS in a channel flow at transitional Reynolds numbers using periodic boundary conditions in the streamwise and spanwise directions, and no-slip boundary conditions on the wall. The computational domain had a size of $L_x \times L_z = 160h \times 120h$. They observed another significant type of coherent structure during the initial phase of transition in channel flow called "turbulent bands". It was seen that localized perturbations evolve into oblique turbulent bands beyond $Re_h = 660$. But, these bands break and decay due to interaction with other turbulent bands and localized perturbations for lower Reynolds numbers. Only for $Re_h \geq 1000$, these turbulent bands can give rise to sustained turbulence. Tao et al. [2018] conducted DNS of channel flow using similar boundary conditions as used by Xiong et al. [2015], and observed the presence of sparse oblique turbulent bands near the onset of transition. They employed different sizes of the computational domains to investigate the dependency of the band growth and breaking on the size of the computational domain. They also found that these sparse bands can lead to very small values of turbulence fraction in an arbitrarily large flow domain. Xiao and Song [2019] studied the characteristics of these oblique

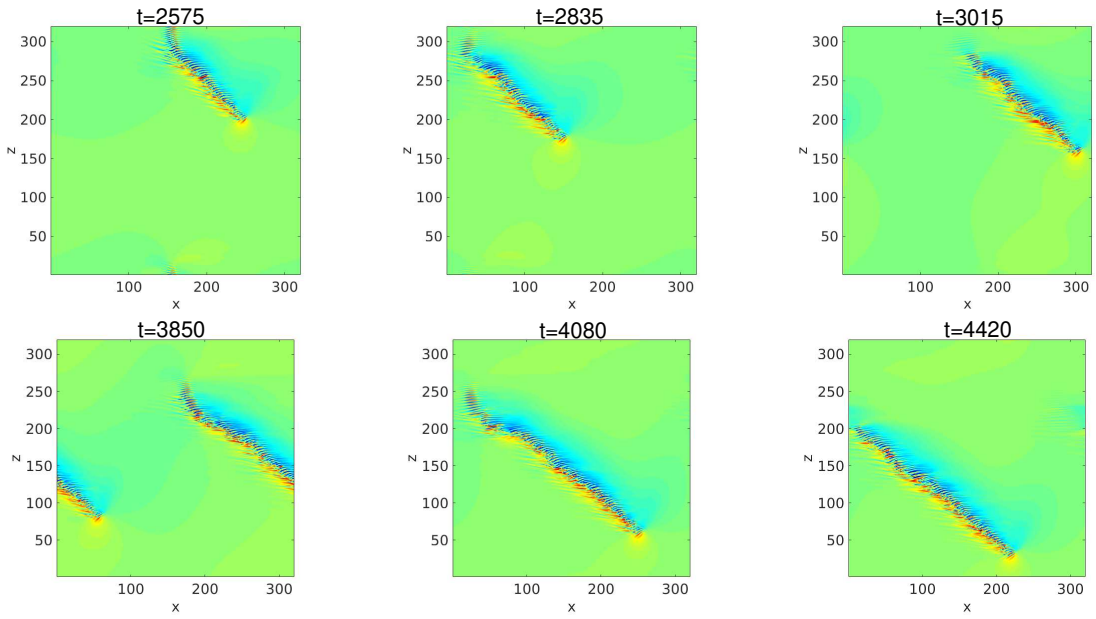

Figure 2.6: The turbulent bands observed for $Re_h = 750$. The mean flow direction is from left to right. Source: Xiao and Song [2019]

turbulent bands in a large channel flow domain (up to $L_x \times L_z = 320h \times 320h$) using DNS. They employed similar boundary conditions as used by Tao et al. [2018], Xiong et al. [2015]. They studied in detail the kinematics and dynamics of these localized turbulent bands for $Re_h = 750$ and provided a possible self-sustaining mechanism for these bands. Figure 2.6 shows the time evolution of turbulent bands in a large domain, as obtained by Xiao and Song [2019]. Each turbulent band is associated with a 'head' and a 'tail' which are simply the downstream and the upstream ends of the turbulent band, respectively. The head of the band is observed to be more active than the tail, which are rather diffusive. The large computational domain in this work minimized the head-tail interaction which were previously seen because of the periodic boundary condition.

2.2.2 Directed percolation (DP)

In recent years, there has been some investigation of the transition to turbulence in canonical shear flows using the directed percolation (DP) model. DP is a class of non-equilibrium phase transitions that can be used to explain different stochastic spreading processes [Hinrichsen, 2000]. The DP universality class has a characteristic set of

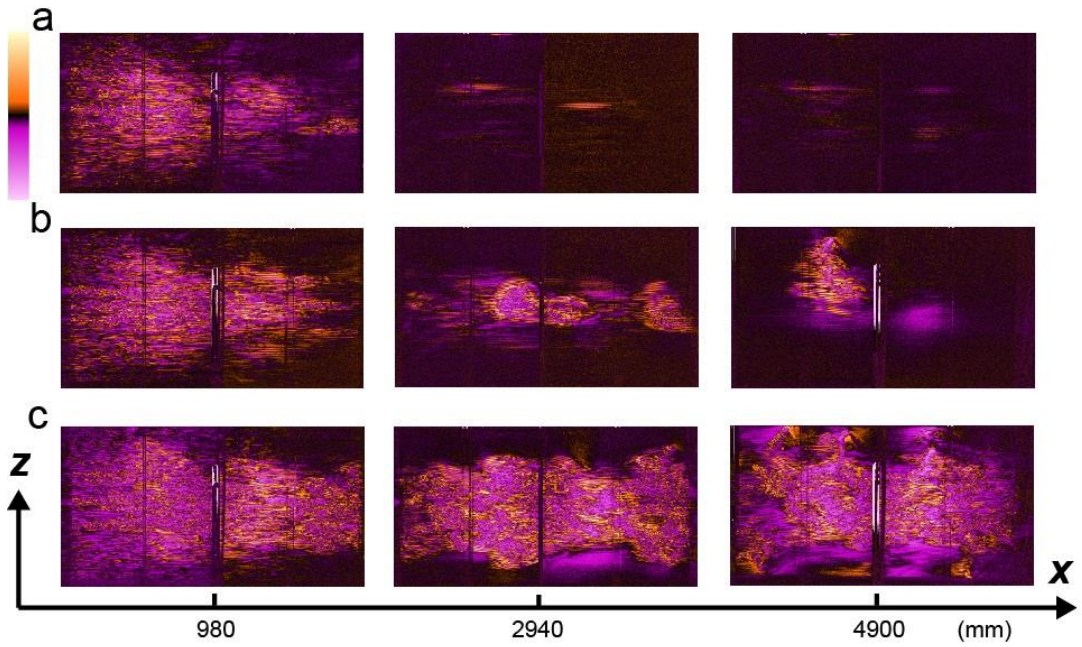

Figure 2.7: Spatial variation of the flow for three Reynolds number (a) $Re_h = 532$ (b) $Re_h = 561$, and (c) $Re_h = 670$. Color indicates the normalized image intensity and the black color indicates the laminar region. The mean flow direction is from left to right. Source: Sano and Tamai [2016]

critical exponents which usually depend on the spatial dimension (D) of the physical process. Many physical processes such as spreading of wildfires, epidemics and flow through a porous media are found to be possibly related to this class. Further literature on relevance of DP universality class on different physical processes can be found in Hinrichsen [2000], Takeuchi et al. [2007], Henkel et al. [2008]. In 1986, Pomeau [1986] conjectured that the transition to turbulence is potentially related to the DP university class. This conjecture was based on the idea that the intermittent nature of transition in wall-bounded flows can be modeled using DP theory. Recently, Sano and Tamai [2016] attempted to observe the analogy between the transition to turbulence in channel flows and the DP universality class. They carried out an experimental investigation of transition in a channel flow facility using a flow visualization technique. They injected perturbations at the inlet which either decayed or spread depending on the Reynolds number. Snapshots of the flow, as obtained by Sano and Tamai [2016], is shown in figure 2.7. For $Re_h = 532$, the perturbations given at the inlet decays as it flows downstream. For $Re_h = 561$, the flow can be seen to sustain turbulence intermittently.

For $Re_h = 670$, the flow has become turbulent everywhere in the domain. Close to the onset of transition, the critical exponents were found to be similar to the (2+1)D DP universality class. This observation led to the conclusion that the spatiotemporal intermittency, which is generally observed in the laminar-turbulent transition in wall-bounded flows, belongs to the DP universality class. The relationship between DP and laminar-turbulent transition is also shown in the same journal issue for Taylor-Couette flow by Lemoult et al. [2016]. Although the similarity between the DP universality class and transition to turbulence in channel flow is shown by Sano and Tamai [2016], Pomeau [2016] debated this and stated that this similarity may not be true by suggesting that the existence of turbulent-nonturbulent state in turbulent spots (arising from subcritical transition) cannot be explained based on the DP model.

2.2.3 Critical Reynolds number

Table 2.1 summarizes some of the major experimental works conducted in the field of laminar-turbulent transition in channel flows. The table shows the aspect ratio of the channel, transition mechanism, techniques used to characterize the transition and the critical Reynolds number. The Reynolds number is also shown in the form of critical friction Reynolds number ($Re_\tau = u_\tau h/\nu$, where u_τ represents the friction velocity), which is given by $Re_\tau = \sqrt{3Re_h}$ for laminar flow. Further description and physical significance of the friction Reynolds number will be discussed in section 2.3. It can be seen that channels of different aspect ratios, varying from 8 [Kao and Park, 1970] to 277 [Alavyoon et al., 1986], have been used in these previous experiments. Different transition mechanisms, for example, natural transition, artificial excitation, turbulence grid, are employed to study transition. A natural question arises about how the critical Reynolds number depends on the aspect ratio and the transition mechanism. Tatsumi and Yoshimura [1990] showed that the side-walls have a stabilizing effect on channel flow during transition which means that channels of lower aspect ratio should be more stable than the larger aspect ratio channels, for the same mode of transition mechanism. But, it has also been well shown that the stability of these flows depends not only on the aspect ratio but also on the mode of perturbation or the transition mechanism. In

Table 2.1: Summary of major experimental works conducted in the field of laminar-turbulent transition in channel flows. Re_τ in the last column is calculated using the formula $Re_\tau = \sqrt{3Re_h}$, which is valid for laminar flows.

Authors	**Aspect Ratio**	**Transition mechanism**	**Transition characterisation technique**	**Critical** Re_h	**Critical** Re_τ
Patel and Head [1969]	48	Natural	Pressure drop and velocity	650	44
Kao and Park [1970]	8	Natural/artifical excitation	Velocity	731	47
Carlson et al. [1982]	133	Artificial excitation	Flow visualization	667	45
Alavyoon et al. [1986]	166; 277	Artificial excitation	Flow visualization	733	47
Tsukahara et al. [2014]	40	Turbulence grid	Flow visualization	650	44
Sano and Tamai [2016]	180	Artificial excitation	Flow visualization	553	41

physical experiments which must have finite size perturbations [unless specifically controlled, for example, Nishioka et al., 1975], the mode of disturbance plays an important role in determining the critical Reynolds number. For example, Sano and Tamai [2016] used a channel flow facility of AR = 180 and by minimizing the perturbations they could maintain laminar flow until a much higher Reynolds number than $Re_h = 553$. However, this critical Reynolds number was obtained because of the artificial perturbation given to the flow at the inlet. Takeishi et al. [2015] studied the effect of aspect ratio on transition in rectangular duct flows using DNS. They showed that the lowest Reynolds number of sustained localized turbulence decreases monotonically with increasing aspect ratio of AR = 1 (square duct) until it reaches an almost minimum value for AR = 5. The localized structure was found to look similar to "puffs" (akin to those found in pipe flow) for AR = 1-3 and "spots" for AR = 5-9.

Deciding on when the flow has left a "transitional" state and entered a "fully-turbulent" state in a channel flow has remained an open question. Patel and Head [1969] discusses the different definitions for fully-turbulent channel flow: the disappearance of intermittency, the emergence of $-1/6$ power law scaling for skin friction and Reynolds number, and log-law relationship with "universal" constants for the mean velocity profile. From their experiments on channel flows they obtained different values of Reynolds number for the first sight of disappearance of intermittency ($Re_h \sim 1800$), skin friction agreement with $-1/6$ power law ($Re_h = 2500$-3000) and log-law relation with universal constants ($Re_h \sim 3000$). The "correct" values of log-law constants for fully-turbulent channel flows has remained a topic of research for several decades [for example, see Nagib and Chauhan, 2008, Smits et al., 2011]. Seki and Matsubara [2012] carried out hot-wire measurements in channel flow at transitional Reynolds numbers. They defined the term "marginal" Reynolds number based on sustainment of turbulent flows and observed that for the channel flow the upper value of marginal Reynolds number (Re_h) is 1300. Kushwaha et al. [2017] used DNS in channel flow and observed that by $Re_h = 993$, the flow was significantly three-dimensional and consisted of fluctuations throughout the computational domain. Tsukahara et al. [2014] carried out flow

visualization to study the "stripy" structures in a channel flow. For $Re_h = 1200$, the flow appeared to be similar to a high-Reynolds number turbulent flow i.e. no apparent large-scale structure typically associated with transitional channel flow. On decreasing the Reynolds number the laminar-turbulent bands or turbulent stripes started to appear below $Re_h = 1000$.

2.3 Turbulent channel flow

Now, the fully-turbulent case will be discussed, where the transitional effects have disappeared from the flow (subject to the difficulty of deciding this as previously discussed). In this section, first, a brief description of wall-bounded turbulent flows in general and turbulent channel flow, in particular, is provided. Later, a discussion of some of the seminal works carried out in the turbulent channel flow is given. As the literature is vast, only the most significant and relevant literature will be discussed here.

2.3.1 Mean flow

To discuss the mean flow, the flow is supposed to be fully-developed and free of any side-wall effects. Therefore, statistically, the flow velocity and stresses depend only on the wall-normal direction (y). In such one-dimensional channel flow, the total stress $\tau(y)$ is, therefore, the sum of viscous stress $\mu d\overline{U}/dy$ and the Reynolds shear stress $-\rho\overline{uv}$. Here, u_i and v_i indicate streamwise and wall-normal velocity fluctuations ($u_i = U_i - \overline{U}$ and $v_i = V_i - \overline{V}$) and the overbar indicates the time-averaged quantity (for example, $\overline{U} = \sum_{i=1}^{i=N} U_i$, where i and N indicate the i^{th} value and total number, respectively). Zero streamwise and wall-normal velocity fluctuations, due to no-slip and no-penetration boundary conditions, respectively makes the Reynolds shear stress at the wall identically zero. Therefore, the stress acting on the fluid at the wall is solely due to the viscous contribution. This stress acting at the wall is also generally referred to as the wall shear stress (τ_w). A profile of the total stress and Reynolds stress is provided in figure 2.8. The profile shown here is for the entire height of the channel (i.e. $2h$). It can be seen that in the near-wall region the Reynolds stress is negligible, and the major contribution to the total stress is from the viscous stress. The Reynolds

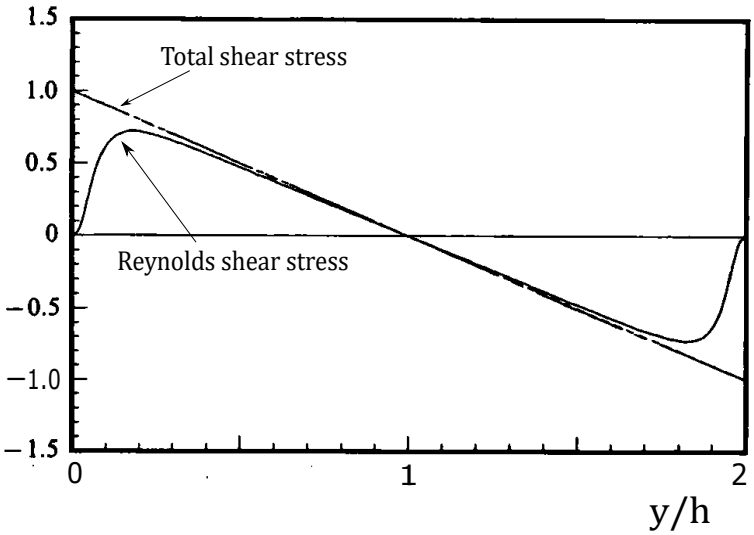

Figure 2.8: Profile of the normalized Reynolds shear stress ($-\rho\overline{uv}/\tau_w$) and normalized total stress (τ/τ_w) for $Re_\tau = 180$ in a channel flow. Source: Kim et al. [1987]

.

shear stress reaches a maximum with the increasing wall-normal distance and then decreases until it reaches zero at the centerline. The viscous stress is maximum at the wall and then decreases with increasing wall-normal distance. The wall shear stress ($\overline{\tau_w}$) is given by:

$$\overline{\tau_w} = \mu\left(\frac{d\overline{U}}{dy}\right)_{y=0}. \tag{2.7}$$

Based on the above discussion and figure 2.8, it can be seen that very close to the wall the viscous forces are more dominant than the Reynolds shear stress. Therefore, dimensional analysis suggests that there is a need to scale the physical quantities appropriately near the wall which should be based on this viscous force. Such reasoning leads to the introduction of a new scale for the length and velocity near the wall. This scale is also called as the "viscous" scale and is based on the wall shear stress (τ_w), and the density (ρ) and viscosity (μ) of the fluid. The velocity based on the viscous scaling is called the friction velocity (u_τ) and is given by:

$$u_\tau = \sqrt{\frac{\overline{\tau_w}}{\rho}}. \tag{2.8}$$

The viscous length scale is given by:

$$\delta_\nu = \nu\sqrt{\frac{\rho}{\overline{\tau_w}}} = \frac{\nu}{u_\tau}, \tag{2.9}$$

where ν is the kinematic viscosity. The Reynolds number, based on viscous scaling, is unity. Therefore, a new Reynolds number, called the friction Reynolds number (Re_τ), is defined. Re_τ is given by:

$$Re_\tau = \frac{u_\tau h}{\nu}. \tag{2.10}$$

The wall-normal distance (y) in channel flow can be scaled using the viscous length scale:

$$y^+ = \frac{y u_\tau}{\nu}, \tag{2.11}$$

note that the y^+ is the representative of the local Re_τ and Re_τ is nothing but the centerline ($y = h$) y^+ value.

Based on the above discussion, it can be said that the wall-bounded flow can be divided into two regions: the one where the viscous forces dominate, and one where the viscous effects are negligible and turbulence dominates. In the former region, the important parameters influencing the streamwise velocity (U) are: ν, u_τ and y. Based on dimensional analysis for fully-turbulent channel flow, the streamwise velocity can be expressed in the following form:

$$\frac{\overline{U}}{u_\tau} = f\big(y^+\big). \tag{2.12}$$

Equation 2.12 was first proposed by Prandtl [1953] and therefore is also known as *Prandtl's law of the wall* [Monty, 2005]. From now on $\overline{U}/u_\tau$ will be indicated as $\overline{U}^+$. Using equation 2.7 and integrating equation 2.12, the following linear relation can be

obtained:

$$f(y^+) = \overline{U}^+ = y^+. \tag{2.13}$$

Note that this relation is valid very close to the wall ($y^+ \leq 5$), also known as the viscous sublayer [Pope, 2000]. For $y^+ > 5$, the departure from this relation becomes significant. For example, for $Re_\tau = 180$ using DNS, Kim et al. [1987] observed the departure of $\overline{U}^+$ from this linear relation to be greater than 25% for $y^+ > 12$.

It has been discussed previously that the viscous effects are negligible at sufficiently large y^+. From dimensional analysis based on this assumption, the following relation for the mean velocity gradient can be obtained:

$$\frac{d\overline{U}^+}{dy^+} = \frac{1}{\kappa y^+}, \tag{2.14}$$

where κ is a constant (the so-called "von Kármán" constant). This equation can be integrated to obtain the relation for the streamwise velocity:

$$\overline{U}^+ = \frac{1}{\kappa} \ln y^+ + B, \tag{2.15}$$

where B is also a constant. Equation 2.15 is known as the von Kármán log-law or simply the log-law. In the literature, various values for κ and B have been reported [George, 2007]. Typical values for κ and B are 0.4 and 5.5, respectively, and the variation of these values from most other values as reported in the literature are generally within a few percent. The universality of the streamwise velocity profile in turbulent channel flows can be observed when plotted in a semi-log plot. To explain the law of the wall and different flow regions (viscous dominated and turbulent dominated), a velocity profile plot is shown in figure 2.9. This profile was obtained by Eckelmann [1974] using hot-film measurements in an oil channel flow for Reynolds numbers $Re_\tau = 150$ and 210. From this figure, three almost distinct flow regions based on y^+ can be observed. First is the viscous sublayer, where the viscous forces are dominant, for $y^+ \leq 5$. In this flow region the velocity profile for both Reynolds number collapse quite well to the *law of*

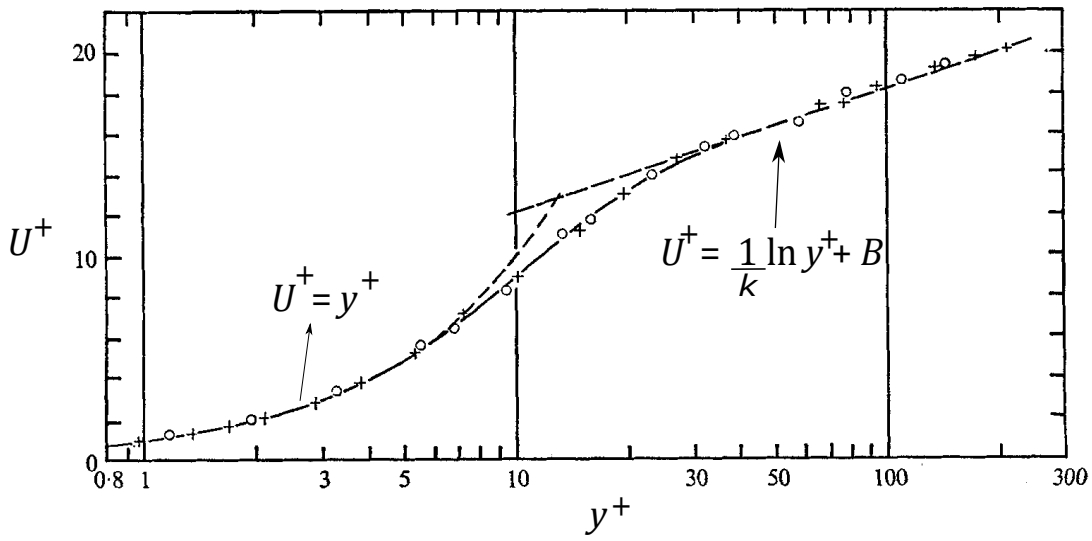

Figure 2.9: Profile of the streamwise velocity normalized by the viscous scaling for Re_τ = 150 (o) and 210 (+) in a channel flow obtained using hot-film anemometry. Source: Eckelmann [1974].

the wall, $\overline{U}^+ = y^+$. Second flow region is the von Kármán log-law which appears to start after $y^+ \geq 30$ in figure 2.9. The measured profile matches well with the log-law slope in this region. The third flow region is between $5 < y^+ < 30$, also called the *buffer layer*, where the flow is transitioning from the viscosity dominated region to the turbulence dominated region. For the sake of completeness, a different division of the flow regions should also be discussed. These flow regions are called as: inner layer, located at $y/h < 0.1$, and outer layer, located at $y^+ > 50$. This division of the flow is specifically useful when the Reynolds number is very high ($Re_\tau \gtrsim 10^4$) [Pope, 2000]. In the present study, the highest Reynolds number studied is $Re_\tau \approx 250$. Therefore, further discussion on this classification of flow regions is not relevant to this work.

2.3.2 Seminal works in turbulent channel flow

Nikuradse [1933] and Reichardt [1938] were among the first to investigate turbulent channel flows. Nikuradse [1933] employed hot-wire anemometry and measured the mean flow. Reichardt [1938] measured velocity fluctuations in the streamwise and wall-normal directions, but the measurements couldn't be done close to the wall. Later, an exhaustive study of turbulent channel flow was conducted by Laufer [1951]. Experiments were conducted for three Reynolds numbers of 12300, 30800 and 61000, based

on the channel half-height and centerline velocity (U_{cl}). Velocity fluctuations in all three directions and the correlation coefficient between streamwise and wall-normal velocities were reported. Comte-Bellot [1963] reported extensive data for channel flows for Reynolds number range 57000-230000 (based on h and U_{cl}). Higher order statistics such as two-point correlations, energy spectra, skewness and flatness factors were calculated. Patel and Head [1969] measured mean-velocity profiles and skin friction for channel flows for the Reynolds number range 1000-10000 (based on h and U_b) and it has been discussed earlier in subsection 2.2.3. Until then, most of the experiments were conducted for high Reynolds numbers (except the work by Patel and Head [1969]) using air as the working fluid. Eckelmann [1972, 1974] used hot-film anemometry for low Reynolds number ($Re_\tau = 156$ and 210) to carry out measurements using oil as the working fluid in a channel flow. Two-component velocity measurements were carried out close to the wall. Figure 2.9 shows the streamwise velocity profile obtained by Eckelmann [1974]. Dean [1978] carried out an extensive literature review of all the major works in the field of channel flows up to 1978. A classification of all these works was made based on the aspect ratio and the length of the channel. Skin friction results obtained from the previous works were compiled in a single plot which helped in estimating the skin-friction coefficient for the channel flow, which is widely used today by many researchers [for example, Kim et al., 1987, Jiménez and Moin, 1991, Owolabi et al., 2017, Rastegari and Akhavan, 2018, Whalley et al., 2019, Jha et al., 2019].

The first detailed fully-resolved numerical analysis of the turbulent channel was conducted by Kim et al. [1987]. They carried out DNS in a channel flow for $Re_\tau = 180$ and provided detailed information on the statistics and structures of the turbulent flow. After this, there have been various efforts to study channel flow using DNS for higher Reynolds numbers [for example, see: Del Alamo et al., 2004, Hoyas and Jiménez, 2006, Abe et al., 2004, Moser et al., 1999]. With the increasing power of the supercomputers, DNS has shown to be very effective in providing various information about the flow which is very difficult to obtain using experiments (for example, asymptotic behaviour of the near-wall region). Study of channel flow for $Re_\tau < 180$ has also been an active

area of study for its significance in transition and relaminarization process. Tsukahara et al. [2005] carried out the first DNS study for the very low Reynolds number using, for that time, a very large computational domain. Sandham and Kleiser [1992], using DNS data, studied the late stages of transition in a channel flow. Hu et al. [2006] carried out DNS in channel flow for Re_τ as low as 90 to study the wall shear stress and pressure fluctuations.

One of the major advancements made in the study of channel flow in this century is the discovery of exact coherent states (ECS) by Waleffe [2001, 2003] for channel flows. The ECS will be discussed in detail in a later section of this chapter. An important motivation to study channel flow is related to drag reduction in turbulent flows. In the next section, the basics of turbulent drag reduction phenomena and various drag reduction techniques will be discussed.

2.4 Turbulent drag reduction

Turbulent drag contributes a significant proportion of the total drag experienced by vehicles moving in air or water. For conventional aircraft or ships, at cruising speed, the skin friction drag contributes almost 50% of the total drag experienced [Ge et al., 2017]. From an economics perspective, a 30% reduction in the skin friction drag can lead up to the saving of almost $38 billion per year only from the shipping industry [Kim, 2011]. Other than financial benefits, reduction in fuel will also result in environmental benefits by reducing the emission of greenhouse gases. This makes reducing skin friction drag in wall-bounded flows an active area of research. The skin friction drag or viscous drag is found to be closely related to the near-wall coherent structures in wall-bounded flows. Therefore, before discussing the details of drag reduction techniques investigated in the past, a brief introduction to the description of near-wall coherent structures in wall-bounded flows is provided here.

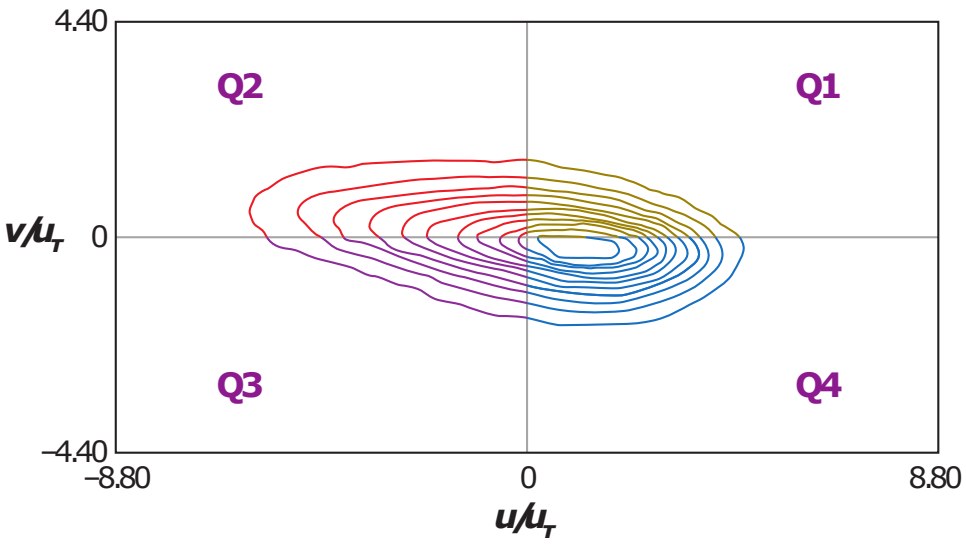

Figure 2.10: Joint probability distribution of streamwise and wall-normal velocity fluctuations, $P(u, v)$ at $y^+ = 45$ for turbulent channel flow at $Re_\tau = 194$. Here, u and v are normalized by the friction velocity (u_τ). Source: Wallace [2016].

2.4.1 Near-wall structures

It is well known that near-wall coherent structures in shear flows consists of quasi-streamwise vortices, and low- and high-speed streaks alternating in the spanwise direction [Kim et al., 1971]. These streaks have a streamwise length of $x^+ \approx 1000$ and spanwise width of $z^+ \approx 100$ [Smith and Metzler, 1983]. The quasi-streamwise vortices are slightly angled away from the wall and they normally stay in the near-wall region for $x^+ \approx 400$ [Jeong et al., 1997]. The near-wall streaks are found to be created by these quasi-streamwise vortices by the advection of the mean velocity gradient [Kim et al., 1987]. Kline et al. [1967] and Corino and Brodkey [1969], using flow visualization, observed that the lift-up and ejection of low-speed streaks from the near-wall to the outer layer. Kim et al. [1987] observed that the sweep event (inrush of high-speed fluid towards the wall) which is caused by the quasi-streamwise vortices, creates local regions of high wall shear stress. Ejections and sweeps are found to be associated with the production of turbulent kinetic energy. One way to understand these events is through the quadrant analysis of the Reynolds shear stress [Willmarth and Lu, 1972, Wallace et al., 1972]. In quadrant analysis, the Reynolds shear stress can be divided into four components: Q1 ($+u$,$+v$), Q2 ($-u$,$+v$), Q3 ($-u$,$-v$) and Q4 ($+u$,$-v$). Out of

these four quadrants, Q2 and Q4 can be related to the ejection and sweep phenomena, respectively. As discussed above, ejection involves a lift-up of low-speed fluid ($u < 0$) away from the wall ($v > 0$), hence indicates Q2 motion. Similarly, a sweep event is the inrush of high-speed fluid ($u > 0$) towards the wall ($v < 0$), which indicates a Q4 motion. Figure 2.10 shows the probability density functions of the streamwise and wall-normal velocity fluctuations. It can be seen that the probability for the motion is skewed in the Q2 and Q4 quadrants which suggest that on an average the flow has a higher probability for the Q2 and Q4 motions. Q2 and Q4 motions contribute the Reynolds shear stress (RSS) positively ($\overline{-uv} > 0$), which is consistent with the positive sign of the RSS above the wall [Kim et al., 1987], and thus suggesting that these motions (Q2 and Q4) are more probable than Q1 and Q3 motions (which contribute to the negative value of the RSS).

The majority of the approaches to reduce drag rely on the suppression of the Q2 and Q4 events. Different approaches for skin friction reduction are investigated in the past and can be broadly classified into two categories: active control and passive control. Active control strategies require continuous addition of mass, momentum or energy to the flow, and passive control strategies do not require them but generally involve surface modification. In this section, four major drag reduction strategies are discussed where two of them are passive control methods: riblets and hydrophobic surfaces, and the other two are active control methods: spanwise oscillation and additive based drag reduction. A brief detail of these drag-reduction techniques is provided in this section.

2.4.2 Superhydrophobic surfaces (SHS)

In normal cases, when fluid flows over a solid surface the velocity of the fluid at the wall is equal to the velocity of the wall. This is known as the 'no-slip' boundary condition [Lauga et al., 2007, Rothstein, 2010]. But, when the wall is made of a superhydrophobic material, there is an entrapment of air in solid-fluid interface [also called as the Cassie state, see Cassie and Baxter, 1944]. The fluid can 'slip' in the region where the air is entrapped in the solid-fluid interface and the 'no-slip' boundary

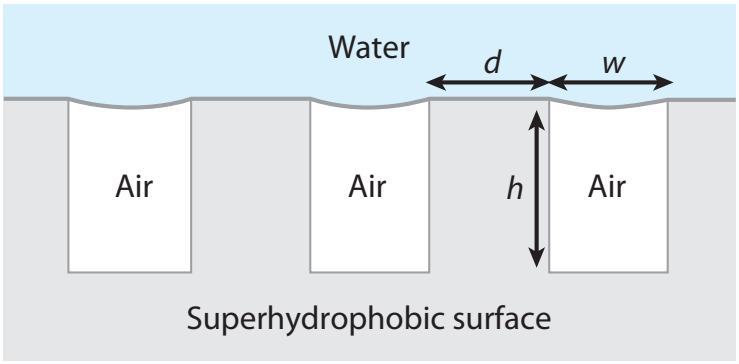

Figure 2.11: Scheamtic diagram to show the liquid-solid interface for a fluid flowing over a superhydrophobic solid surface in Cassie state. Source: Rothstein [2010].

condition is then not easily applicable. A schematic of the flow over a superhydrophobic surface is shown in figure 2.11. This slip velocity in the streamwise direction indicates the lowering of skin friction drag because of the lower dissipation of the energy. Min and Kim [2004] carried out a detailed investigation of the effect of hydrophobic surfaces on skin friction drag in turbulent channel flow using DNS. They observed that the turbulent intensities and turbulent structures weaken when a streamwise slip velocity is employed in the boundary condition. Streamwise vortices and skin friction were also significantly weakened. Whereas, when a spanwise velocity slip is included in the boundary condition, there is an increase in skin friction drag. This behaviour is attributed to the different modifications of the turbulent structures with respect to different directions of slip velocities. Figure 2.12 shows the mean streamwise velocity profiles for $Re_\tau = 180$ (for the case of no-slip) with different levels of streamwise slip. In this study, the drag reduction (DR) is defined based on the percentage change in the skin friction drag for the constant mass flow rate. The investigation was made for slip lengths (L_s) varying from $L_s = 0.0002$ ($L_s^+ = 0.036$) to $L_s = 0.02$ ($L_s^+ = 3.566$) and the maximum DR was found to be 29% for the case of $L_s = 0.02$. This behaviour can also be seen from figure 2.12. Over the last two decades, significant investigations to study the effects of SHS on the skin friction drag have been carried out [for example, see: Park et al., 2014, Gogte et al., 2005, Zhao et al., 2007, Gose et al., 2018]. Different levels of drag reduction have been observed in the past which generally depend on the geometry of the SHS (for example, ridges, posts, etc.), length of the tested surface, contact angle and the Reynolds number studied.

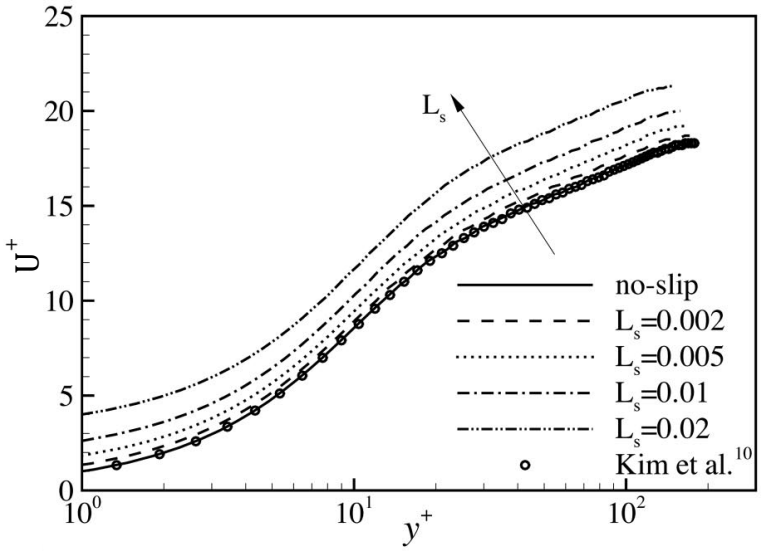

Figure 2.12: Mean streamwise velocity profiles for different levels of streamwise slip length (L_s) in turbulent channel flow for $Re_\tau = 180$ (for the case of no-slip). In this figure, Kim et al.[10] indicates Kim et al. [1987]. Source: Min and Kim [2004].

2.4.3 Riblets

Riblets are surfaces with longitudinal small surface protrusions and are an important way to reduce skin friction drag by manipulating the near-wall coherent structures. The first use of riblets as a mechanism to reduce skin friction drag was carried out by Walsh and co-workers [Walsh and Weinstein, 1978, Walsh, 1982, Walsh and Lindemann, 1984]. Walsh and Lindemann [1984] carried out a parametric study of different types of riblets (for example, triangular, sinusoidal, U-shaped) and observed that in order to obtain a net reduction of skin friction drag, the size of the riblets should be about 15 wall units. They obtained a maximum of approximately 8% drag reduction by using triangular riblets of appropriate dimensions. Benschop and Breugem [2017] carried out an investigation of drag reduction due to riblets in a channel flow using DNS. Figure 2.13 shows a schematic of the parallel blade riblet texture for drag reduction used by Benschop and Breugem [2017]. The blade height (h_b) to blade spacing (s) is kept at a constant ratio, $h_b/s = 0.5$. For $Re_\tau = 180$ ($Re_h = 2750$), using parallel blade riblet texture, a maximum drag reduction of approximately $6 - 8\%$ was observed for a riblet spacing of $s^+ \approx 16 - 18$. The use of riblets is one of the few drag reduction techniques which have also been successful in a practical setting. For example, riblets have led

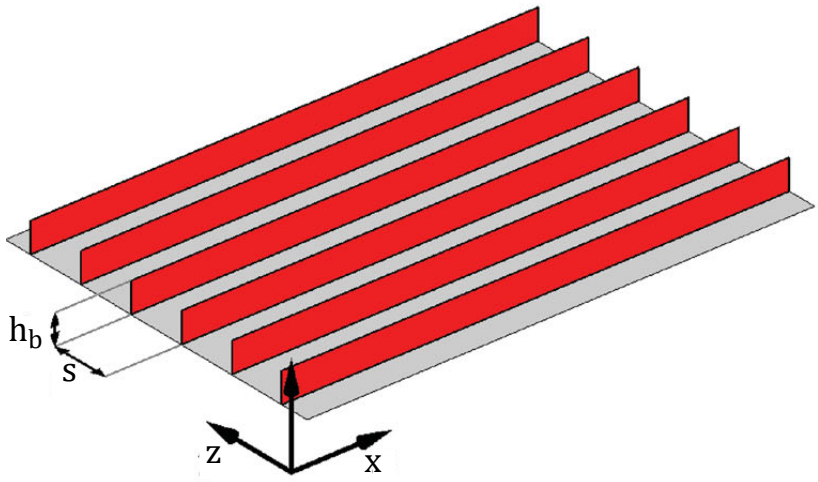

Figure 2.13: Schematic of the parallel blade riblet texture in which the blades are aligned with the mean flow direction. Here, h_b and s represent blade height and spacing, respectively. Source: Benschop and Breugem [2017].

to a successful reduction in viscous drag in aerofoils by keeping the riblet separation distance in the order of $30 - 70\mu m$ [Lee and Jang, 2005]. Report on the flight tests conducted on Airbus 32, with riblets on 70% of its surface, provided a net drag reduction of 2%, based on fuel consumption [Szodruch, 1991]. To explain the mechanism of drag reduction using riblets, various theories over the years have been proposed. Bacher and Smith [1985] suggested that there is a presence of small eddies near the riblets, which weakens the streamwise vortices and retains the low-speed fluid. Choi [1987] suggested that there is a restriction in the spanwise movement of these streamwise vortices which leads to the skin friction drag reduction. Further information on the use of riblets for drag reduction can be found in Choi [1989] and García-Mayoral and Jiménez [2011].

2.4.4 Spanwise oscillation

Skin friction drag can be reduced by applying a spanwise oscillation (of appropriate frequency and amplitude) to the wall. The drag reduction using high-frequency spanwise oscillation of the channel wall was first studied numerically by Jung et al. [1992]. They applied spanwise oscillation with a period of $25 \leq T_{osc}^{+} \leq 500$, where $T_{osc}^{+} = T_{osc}u_{\tau}^{2}/\nu$ and observed a sustained reduction in the turbulent drag (between $10\% - 40\%$) and all components of the Reynolds shear stresses. Here, T_{osc} indicates the time period of the wall oscillation. A schematic of this technique is shown in figure 2.14. The frequency

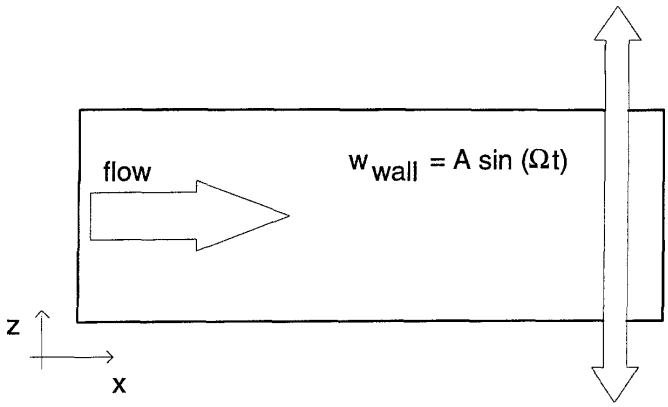

Figure 2.14: Schematic of the spanwise wall oscillation. A and ω indicate the amplitude and frequency of oscillation, respectively. Source: Baron and Quadrio [1995].

and amplitude of the oscillation is observed to play a major role in the level of drag reduction. This technique requires an external power supply for the oscillation which makes it an active drag reduction technique. No feedback system is required for this technique therefore, it is practically less complex to operate. Laadhari et al. [1994] provided the experimental verification for this phenomenon in turbulent boundary layers. They also provided a basic mechanism for the drag reduction using spanwise oscillation. In simple terms, the spanwise oscillations weaken the production process (e.g. sweeping and bursting events) of turbulence near the wall leading to lower drag. Ricco [2004] used a water channel and a flow visualization technique (using hydrogen bubbles) to study drag reduction due to an oscillating wall. The Reynolds number (Re_θ, based on momentum thickness and free-stream velocity) was kept at 1400 for the stationary wall. They observed that the spanwise oscillation of the wall could lead to a net drag reduction of the order of $\approx 10 - 40\%$, based on different oscillatory conditions (wall velocity and oscillation period). Here, net drag reduction represents the drag reduction at the expense of energy provided for the wall oscillation. Use of spanwise oscillating Lorentz force is also employed by various researchers to reduce the skin friction drag [for more information, see: Pang and Choi, 2004, Huang et al., 2010].

2.4.5 Additives

Another major approach for skin friction reduction is the addition of long-chain polymers to the turbulent flow, first discovered by Toms [1948]. These long-chain polymer

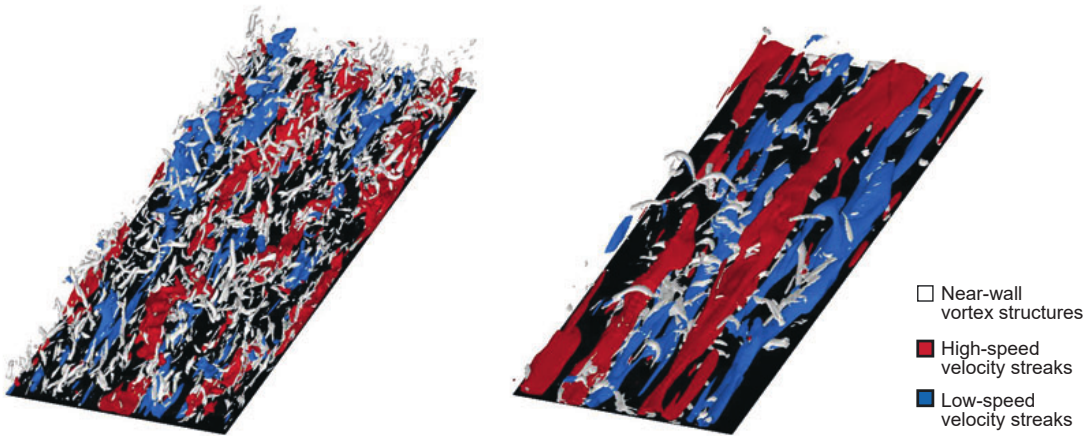

Figure 2.15: (a) Newtonian flow (b) drag reduced flow due to polymer additive (DR = 60%). Flow is from bottom left to top right. Source: White and Mungal [2008].

additives, even in small quantities (few ppm), can cause significant skin friction reduction (up to about 80%) in turbulent flows [Virk, 1975, White and Mungal, 2008]. Figure 2.15 illustrates the differences in the flow structures because of the phenomenon of drag reduction due to polymer addition. It can be observed that the near-wall vortical structures are significantly weakened due to polymer addition. The coupling between the skin friction drag and the near-wall vortices leads to a significant lowering of the skin friction drag. The exact mechanism for this reduction of skin friction drag due to polymer addition has remained an active area of research since its first observation by Toms [1948]. This drag-reduction technique has been employed in the Alaska pipeline where a significant increase in pumping capacity is obtained by adding polymers [Burger et al., 1982] and in fracking where polymers are mixed with fracking fluids to increase the hydrocarbons extracted [King et al., 2012]. In addition to polymers, some micelle-forming surfactants are also shown to have drag-reducing behaviour [Zakin et al., 1998, Drappier et al., 2006]. The drag-reducing property of long-chain polymers gives rise to a phenomenon called the maximum drag reduction (MDR) asymptote which was first noted by Virk [1975]. MDR suggests that the value of drag reduction increases with increasing polymer concentration in the flow, but saturates after a certain value. Virk [1975] collected data from different past experiments and observed that the mean velocity profile collapses, to a reasonable approximation, to a curve similar to von Kármán curve but with different constants than for Newtonian flows. This curve is

the maximum drag reduction (MDR) asymptote as it represents the maximum level of drag reduction possible due to polymer addition. This drag reduction due to polymer additives is found to be characterized by a significant reduction in the Reynolds shear stress and weakening of streamwise vortices and three-dimensionality [Kim et al., 2007, White and Mungal, 2008, Graham, 2014], as can also be seen in figure 2.15. The reduction in the turbulent energy dissipation has also been observed due to polymer addition [Bonn et al., 2005].

Polymer drag reduction and related MDR phenomena can be understood from figure 2.16. It can be observed that for the Newtonian flow the velocity profile lies on the von Kármán log-law. With increasing polymer concentration, the profile shifts upwards from the von Kármán log-law until it reaches close to the Virk's MDR asymptote. The velocity profile for the Virk's MDR asymptote is given by: $U^+ = 11.7 \ln y^+ - 17.0$. In this figure, for the highest drag reduction (DR = 72%), the profile seems to be not perfectly collapsing on the Virk's MDR asymptote, but they are within its 95% confidence interval [Graham, 2014]. Investigation of drag reduction using shear-thinning polymers was carried out in the same channel facility as used in the present study by Escudier et al. [2009]. Like MDR, there is found to be the presence of two other regions of drag reduction (DR), which are namely low-drag reduction (LDR) and high drag reduction (HDR). The critical drag reduction value between these regions is roughly around DR $\approx$ 40% [White and Mungal, 2008]. Detailed experimental investigation on LDR-HDR regimes for polymeric drag reduction has been carried out by Warholic et al. [1999]. The major characteristic of LDR is that the velocity profile follows the Virk's MDR asymptote until the certain wall-normal location and after that, the velocity profile essentially becomes parallel to the Newtonian log-law. The distance between the Newtonian log-law and the velocity profile generally depends on the level of drag reduction. The Reynolds shear stress decreases to a lower value than its Newtonian counterpart, and the resulting stress deficit is managed by the polymeric stress. As opposed to LDR, the velocity profile for HDR is not parallel to the Newtonian log-law, rather is tilted towards the Virk's MDR asymptote. The Reynolds shear stress is significantly lower

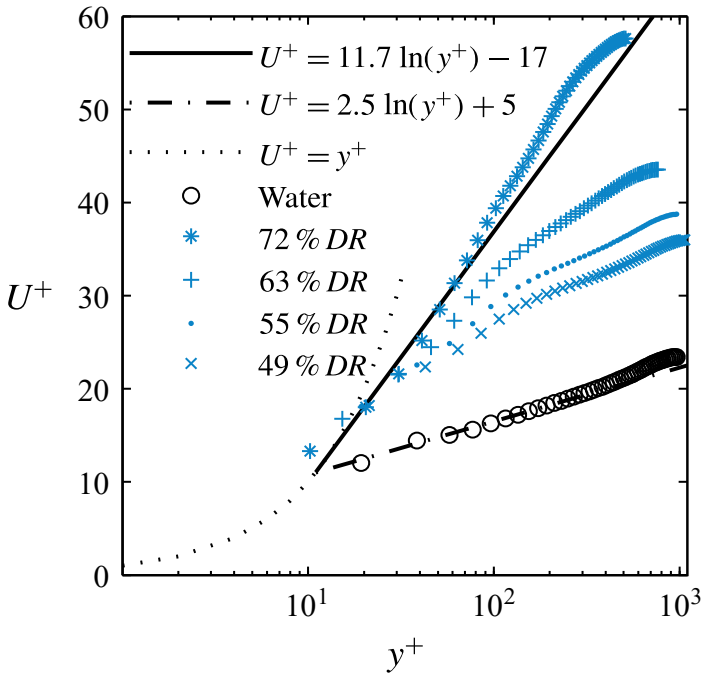

Figure 2.16: Streamwise velocity profiles for different levels of drag reduction. Source: Owolabi et al. [2017].

than the Newtonian counterpart in the HDR regime, and also significantly lower than the LDR regime.

2.5 Low-drag events in Newtonian turbulence

All the drag reduction techniques, which have just been discussed, rely on either surface modification or oscillation or adding drag-reducing additives to the flow. During the last decade, there has been a detailed study of so-called low-drag events even in Newtonian flows. Before discussing this newly observed phenomenon, a brief introduction to the fundamentals of exact coherent states (ECS) is provided. This discussion is important because the majority of the recent numerical works in channel flows employ this technique to investigate these low-drag states [Xi and Graham, 2010, 2012, Park et al., 2014, 2018].

2.5.1 Exact coherent states

In the past few decades, the understanding of near-wall coherent structures has greatly improved by the discovery of traveling-wave (TW) solutions. These TW solutions

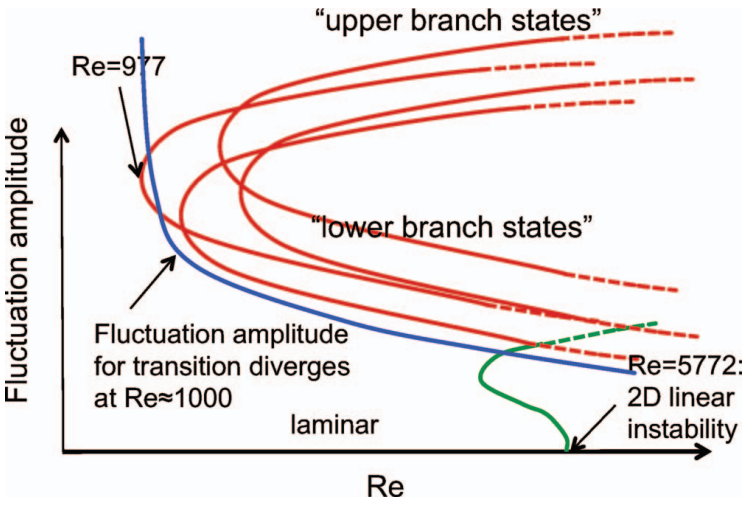

Figure 2.17: Bifurcation diagram for simple plane channel flow. Red lines indicate different families of solutions. Here, Re is the Reynolds number based on laminar centreline velocity and is equal to $1.5Re_h$. Source: Graham [2014]

were first obtained by Nagata [1990] for plane Couette flow. They are non-trivial invariant solutions to the Navier-Stokes equation and are also sometimes called "exact coherent states (ECS)". Later, Waleffe [2001, 2003] found these nonlinear steady TW solutions for plane channel flow. The spatial structure of these solutions is similar to the commonly observed structure of near-wall turbulence: mean flow with counter-rotating streamwise vortices and alternating low- and high-speed streaks. Most of these ECS solutions are observed to occur in pairs at a saddle-node bifurcation point, arising at a finite value of Reynolds number. The difference between the solutions keeps growing with increasing Reynolds number. The upper branch solution is found to have higher fluctuation amplitude than the lower branch solution [Nagata, 1990, Waleffe, 2001, 2003, Nagata and Deguchi, 2013]. Higher and lower fluctuation amplitudes correspond to higher and lower drag, respectively. A schematic of this bifurcation diagram for channel flow is shown by Graham [2014] and is also reproduced in figure 2.17. Here, the y-axis indicates the solution fluctuation amplitude and the x-axis indicates the Reynolds number. Different families of solutions can be seen where each solution family has two branches of solutions: upper and lower. It can be also observed that the bifurcation happens at a slightly lower Reynolds number than the transition. This phenomenon was shown by Waleffe [2003], where for plane channel flow bifurcation this occurs at

$Re \approx 977$ and the finite-amplitude transition begins after $Re \approx 1000$. Although the TW solutions are useful in predicting turbulent dynamics in canonical shear flows, they cannot provide exactly the same structure as observed in a real turbulent flow. This is because of the steady or periodic nature of the TW solutions which generally depends on the frame of reference [Xi and Graham, 2012].

2.5.2 Minimal flow unit (MFU) results

One way to investigate the complex turbulent dynamics using TW solutions is to employ "minimal flow units". The minimal flow units or MFU denotes the smallest computational domain where turbulence can persist [Jiménez and Moin, 1991] at a given Reynolds number. Jiménez and Moin [1991] observed a cyclic and intermittent behaviour of the fluctuations of all important quantities while employing MFU to study plane channel flow. They also observed a rapid increase in the fluctuations and wall shear stress during the 'active' part of the cycle. Later, Hamilton et al. [1995] and Jiménez and Pinelli [1999] further studied this cycle and observed that during the time when the wall shear stress is near its lowest values the streamwise variation of the flow is also reduced and the streamwise streak becomes straight and finally breaks into three-dimensional turbulence. The flow again becomes dominated by a straight streamwise streak and the process is repeated. The presence of intermittency in Newtonian turbulent flow is not a new result and has been already discussed earlier by McComb [1990]. Xi and Graham [2010] carried out DNS in an MFU for low Reynolds number, $Re_\tau = 85$ for both Newtonian and viscoelastic flows. They observed that even in the limit of Newtonian flows, there are the moments of 'low-drag' or 'hibernating' turbulence which display many similar features as MDR (a phenomenon generally associated with the polymeric turbulent flow, as already discussed in subsection 2.4.5). They provided the nomenclature of 'hibernating' state when the flow was drag-reducing and resembles MDR and 'active' state for the rest of the flow. The major flow characteristics observed during hibernation were the significantly weak streamwise vorticity and three-dimensionality, and lower than average wall shear stress. The frequency of these events increases with increasing viscoelasticity, although the events remain unchanged,

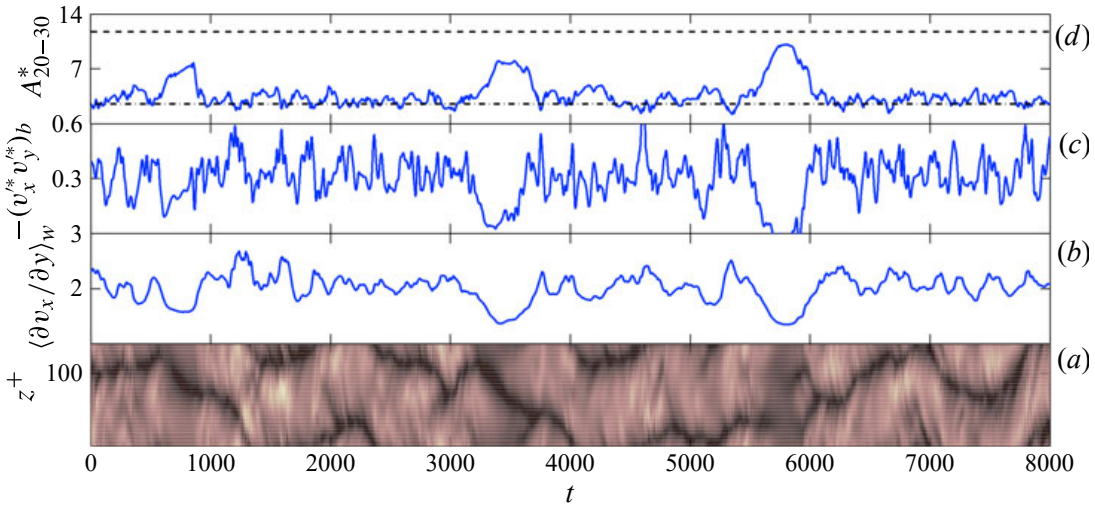

Figure 2.18: Time evolution of a typical Newtonian trajectory. (a) pattern on spatio-temporal wall shear rate, where dark indicate low wall shear rate and vice-versa; (b) area-averaged wall shear rate on the bottom wall; (c) volume averaged Reynolds shear stress for the bottom half of the channel; (d) instantaneous log-law slope for $20 \leq y^+ \leq 30$. Here, dashed and dotted lines indicate the Virk's MDR slope and the von Kármán log-law slope. Source: Xi and Graham [2012].

i.e. they display similar flow properties as to MDR. The connection between the polymeric drag reduction in turbulent flows and transition to turbulence in Newtonian flows has also been discussed earlier by Dubief et al. [2011]. They showed that MDR is a transitional state between laminar and turbulent states, and is present even in the limit of Newtonian flows, and therefore is not unique to the polymeric drag reducing flows.

Xi and Graham [2012] further investigated this phenomenon to provide detailed characteristics of active and hibernating turbulence in Newtonian and viscoelastic flows. They defined hibernation when the area-averaged wall shear stress was below 90% of the mean for a time duration of $t^* = tu_\tau/h \approx 3.5$. Figure 2.18 shows the hibernation phenomenon for Newtonian flow at $Re_\tau = 85$, as obtained by Xi and Graham [2012]. There are a few intervals when the area-averaged wall shear rate goes below its mean value for a relatively extended period of time $t \approx$ 700-900, 3300-3700 and 5700-6000. During these intervals, the volume-averaged Reynolds shear stress decreases to a very low value and the slope of the log-law (between $y^+ = 20$ - 30) approaches the Virk's MDR slope value (11.7). These are similar to the features of weak-turbulent activity in a drag-reduced flow due to polymer addition. Park and Graham [2015] carried out

DNS for MFU in a channel flow geometry, close to transition. They obtained five families of ECS solutions, which they denote as the "P1, P2, P3, P4 and P5" solutions. Out of these five families of solutions, "P5" solution shows an interesting behaviour. For the upper branch solutions, the velocity profile approaches the classic von Kármán log-law, while for the lower branch solutions the velocity profile approaches the Virk's MDR asymptote. This result provided a further verification of the 'hibernating' intervals previously observed by Xi and Graham [2010], Xi and Graham [2012] and Graham [2014]. Park and Graham [2015] suggested that most of the time the turbulent trajectories remain at the upper-branch state (or the 'active' state) with few excursions to the lower-branch state (or the 'hibernating' state). These observations of hibernating events provide a potential connection between the transition to turbulence, ECS and additive based drag reduction in turbulent flows. The existence of such solutions for Newtonian flows has a potential application in drag reduction, which makes it an interesting as well as practically significant field of research.

One major characteristic of wall-bounded turbulent flows is the so-called bursting process, which is an abrupt breaking of a low-speed streak as it moves away from the wall [Kline et al., 1967]. Itano and Toh [2001] investigated the bursting process for channel flow at $Re_\tau = 130$ by computing TW solutions in a MFU using a shooting method. They observed that the bursting process is linked to the instability of the TW solution. Recently, Park et al. [2018] studied the connection between the bursting process and the ECS solutions in minimal channel flow for $75 < Re_\tau < 115$. They focussed on the "P4" family of ECS solutions, as identified earlier by Park and Graham [2015]. To detect a hibernating event they used the criteria that the area-averaged wall shear stress should go below 90% of the mean wall shear stress and stays there for a duration of $tU_{cl,lam}/h > 65$, where $U_{cl,lam}$ is the laminar centerline velocity. They defined bursting events based on the increase in the volume-averaged energy dissipation rate by 50% of its standard deviation for a duration of $tU_{cl,lam}/h > 15$. They observed that many of the low-drag or "hibernating" events are followed by strong turbulent bursts. Based on this observation, they divided the turbulent bursts into two categories: weak

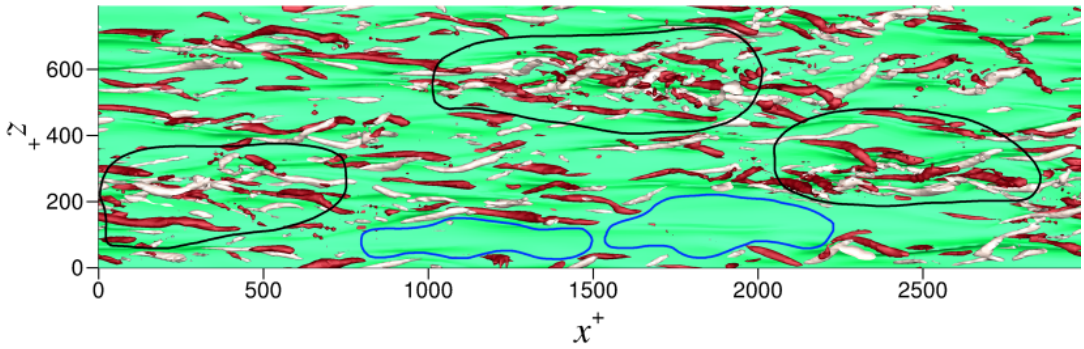

Figure 2.19: Flow structure of a typical snapshot obtained using DNS for $Re_\tau = 85$. The mean flow direction is from left to right. The green sheet is the isosurface of streamwise velocity. Source: Kushwaha et al. [2017].

and strong bursts and suggested that the strong bursts are the ones which are always preceded by a hibernating event. They also investigated the possible link between the turbulent bursts and the instability of the P4-lower branch solution. Very similar trajectories were observed for the strong bursts and the lower branch of the P4 solution, which provides further evidence that the turbulent bursts are directly related to the instability of the ECS.

2.5.3 Investigations in extended domains

Initially, the investigation of these low-drag events was conducted in minimal channels and therefore, the need was to study this phenomenon for fully turbulent flow in extended domains. The relation between the minimal channels and flow in large domains was studied by Jiménez et al. [2005] and Flores and Jiménez [2010]. They suggested that the flow dynamics in minimal channels are only a part of fully turbulent flows. Kushwaha et al. [2017] carried out an investigation in an extended computational domain for transitional channel flow at three Reynolds numbers, $Re_\tau = 70$, 85 and 100. The computational domain, in wall (or inner) units, was $L_x^+ \approx 3000$ and $L_z^+ \approx 800$ long in the streamwise and spanwise directions, respectively. Figure 2.19 shows the flow structure of a typical snapshot obtained using DNS for $Re_\tau = 85$ by Kushwaha et al. [2017]. The regions of high turbulence activity (corresponding to high-drag) and weak turbulence activity (corresponding to low-drag) can be observed. They carried out a temporal and spatial analysis for extended domains and compared the results

between the two. Regions or events of both low- and high-drag events are investigated in large domains, unlike previous MFU studies where the focus was primarily on low-drag events. To study the temporal intermittency, they employed the following criteria to detect low-drag (hibernating) or high-drag (hyperactive) events: the instantaneous wall shear stress (τ_w) should remain below 90% or above 110% of time-averaged value for a time duration of $t^* = tu_\tau/h = 3$ for low or high drag events, respectively. For studying the velocity characteristics during these low- and high-drag intervals in the flow, a conditional sampling technique was employed. They observed that, although the temporal and spatial analyses are independent of each other, the characteristics of low- and high-drag events obtained using these two methods were very similar. They found that for $Re_\tau = u_\tau h/\nu$ between 70 and 100, the regions of low-drag in an extended domain show similar conditional mean velocity profiles as obtained from temporal interval of low-drag in minimal channels for $y^+ = yu_\tau/\nu < 30$. This showed that the spatiotemporal intermittency in extended channel flow is related to the temporal intermittency in a minimal channel. Figure 2.20 shows the comparison of the velocity profiles for $Re_\tau = 85$ obtained using spatial and temporal analysis in the extended domain and using a minimal channel. A good agreement can be observed between the velocity profiles obtained using three different techniques.

Whalley et al. [2017, 2019] carried out an experimental investigation of the low- and high-drag events in a plane channel flow for transitional Reynolds numbers, $70 < Re_\tau < 100$. A channel flow facility, of aspect ratio of 11.92, was employed to characterize these events. (The same channel flow facility will also be used in this study). Instantaneous velocity, wall shear stress, and flow structure measurements were conducted using laser Doppler velocimetry (LDV), hot-film anemometry (HFA) and stereoscopic particle image velocimetry (SPIV), respectively. They employed the same criteria as Kushwaha et al. [2017] to detect the low-drag events but for the high-drag events, the criteria were slightly relaxed in order to obtain more events, as the high-drag events were found to occur at a lower frequency than the low-drag events. Instantaneous velocity and wall shear stress measurements were made at the same streamwise and spanwise location.

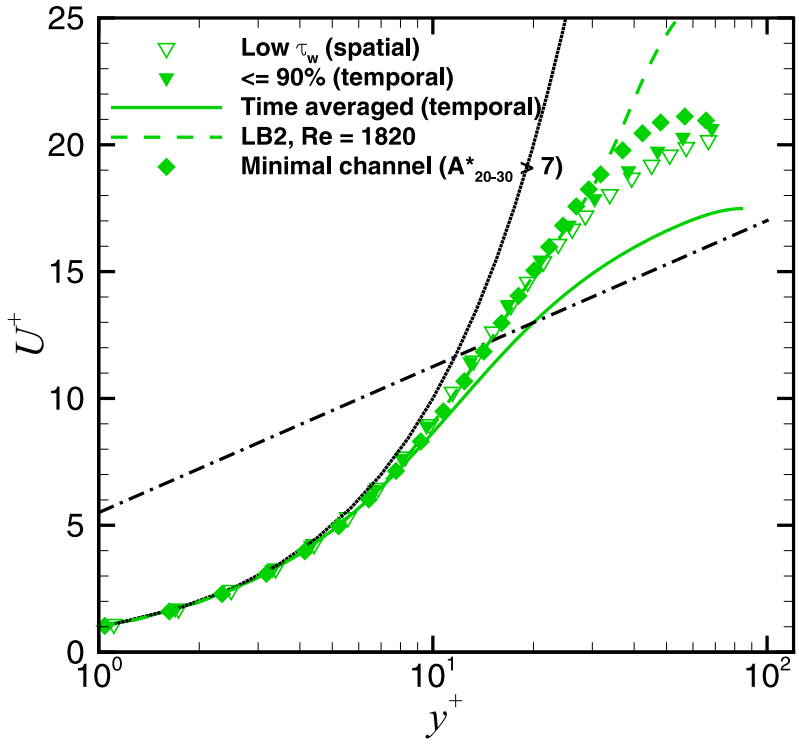

Figure 2.20: Conditionally averaged streamwise velocity profiles using space and time criteria for the extended domain and velocity profile obtained in MFU during low-drag events for $Re_\tau = 85$. Source: Kushwaha et al. [2017].

Using the criteria discussed above for the wall-shear stress, the instantaneous velocity was conditionally sampled and averaged. The conditionally averaged streamwise velocity and wall shear stress were found to be highly correlated until $y^+ \approx 40$. A resemblance was observed between the conditionally sampled mean velocity profiles for $y^+ \lesssim 40$ and the lower branch of the "P4" ECS solution as observed earlier in minimal channels [Park and Graham, 2015]. They also observed that the fraction of time spent in hibernation (low-drag), based on the used criteria, decreases with increasing Reynolds number for $70 < Re_\tau < 100$.

Recently, Pereira et al. [2019] carried out DNS in channel flow of domain size, $L_x \times L_y \times L_z = 8\pi \times 2 \times 1.5\pi$ (normalized by h). The flow was identified as hibernating if the spatially-averaged wall shear stress was lower than 95% of its time-averaged value and no time criteria were used [unlike previous studies where a minimum time duration was also used to detect a hibernating event, for example, Park et al., 2018, Kushwaha

et al., 2017, Whalley et al., 2019]. They demonstrated that the transition to turbulence in Newtonian flows shares various common features to the polymer induced drag reduction in turbulent flows. They showed that near the boundary of laminar-turbulent transition the velocity profile during hibernation approaches the Virk's MDR asymptote. They also provided a general explanation regarding the transition and hibernation processes. For the low Reynolds number, below the transition regime, the laminar solution is the only stable solution. During the transition, there are two solutions which are marked by upper branch solution and lower branch solution (this is also discussed earlier, see, § 2.5.1). The solutions intermittently visit the upper and lower branch solutions, where the attraction for the upper branch solution increases with increasing Reynolds number. As the Reynolds number is further increased, the distance between the two branches increases significantly such that the upper branch solution becomes a powerful attractor and the incursion to the lower branch solution becomes rarer. With increasing Reynolds number, inside the transitional regime, the velocity profile during hibernation was observed to undergo a similar transition as the HDR-LDR transition generally associated with polymer drag reduction [Warholic et al., 1999].

2.6 Summary

Based on the literature review provided in § 2.2, it is observed that there has been a significant amount of work to understand the laminar-turbulent transition in wall-bounded flows. However, there are still unanswered question in this field which needs to be addressed. There is a scarcity of instantaneous wall shear stress data during the transition process. Wall shear stress is associated with the skin-friction drag in shear flows, and therefore their characteristics during the transition process needs to be investigated. Wall footprint of the large-scale turbulent structures, which are generally associated with the transition process, has not been well-studied in the literature. Literature review for the so-called low- and high-drag intermittent events (discussed in § 2.5) suggest that more research is needed to improve their understanding. Until now, these events are investigated for the flow close to transition. Therefore, the characteristics of these events in the so-called fully-turbulent flow regime needs to investigated.

The characteristics of Reynolds shear stress during these events is studied using the DNS in MFUs, and there is no data available (experimental or numerical) for their characteristics in extended domains. Therefore, the behaviour of RSS during these intermittent events needs to be studied in an extended domain.

In this thesis, firstly, an experimental investigation of instantaneous wall shear stress in a channel flow is conducted. Using single-point statistics of wall shear stress fluctuations, the "start" and the "end" of the laminar-turbulent intermittency is studied. The large-scale turbulent structures are probed by carrying out correlations of the wall shear stress for different spatial locations, and also using flow visualization. Next, the low- and high-drag intermittencies are investigated in a channel flow facility using wall shear stress and velocity measurements. Study is made for Reynolds number up to $Re_\tau = 250$, to study the characteristics of these events for fully-turbulent channel flow. Reynolds shear stress characteristics during these conditional events is also investigated for $Re_\tau = 70$ and 85.

Chapter 3

Experimental arrangement

The present work aims to investigate intermittencies in transitional and turbulent channel-flow. Based on this aim, there is a need for a channel-flow facility and measurement techniques which can provide well-resolved information of the flow behavior. In this chapter, a detailed description of the employed channel-flow facility and different measurement techniques are provided. Every measurement technique is prone to uncertainty, and therefore an estimate of uncertainties has been carried out for the various measurement techniques. The present study aims to study "simple" channel-flow which means that the measurement location should be devoid of any development length effects or side-wall effects. Inclusion of the effect of these parameters can complicate the obtained results which makes them harder to interpret. Therefore, attempts are made to make sure that the measurement location in the channel-flow facility is devoid of any of these unwanted parameters and, therefore can be considered fully-developed and two-dimensional.

3.1 Channel-flow facility

In this study, a channel flow facility, at the Fluid Engineering Laboratory, in the University of Liverpool has been used. This channel-flow facility, with slight modifications, has been used earlier by Escudier et al. [2009], Whalley et al. [2017], Owolabi et al. [2017] and Whalley et al. [2019]. A schematic and photograph of the channel-flow facility are shown in figure 3.1(a) and 3.1(b), respectively. The channel-flow facility

is a rectangular duct consisting of 6 stainless steel modules and a test section (see § 3.2 for details). The test section is connected at the downstream of five stainless steel modules. Each module is of length 1.2 m and the test section has a length of 0.25 m. The width (w) and half-height (h) of the duct are 0.298 m and 0.0125 m, giving an aspect ratio ($AR = w/2h$) of 11.92. The modules are connected using angle irons and threaded bars. Four threaded bars are used (two on the top side of the channel and two on the bottom) to attach each pair of modules. An O-ring is used to ensure that there is no leakage of the fluid and a hydraulically smooth transition between the modules. The modules are then aligned carefully using a laser targeting device. The

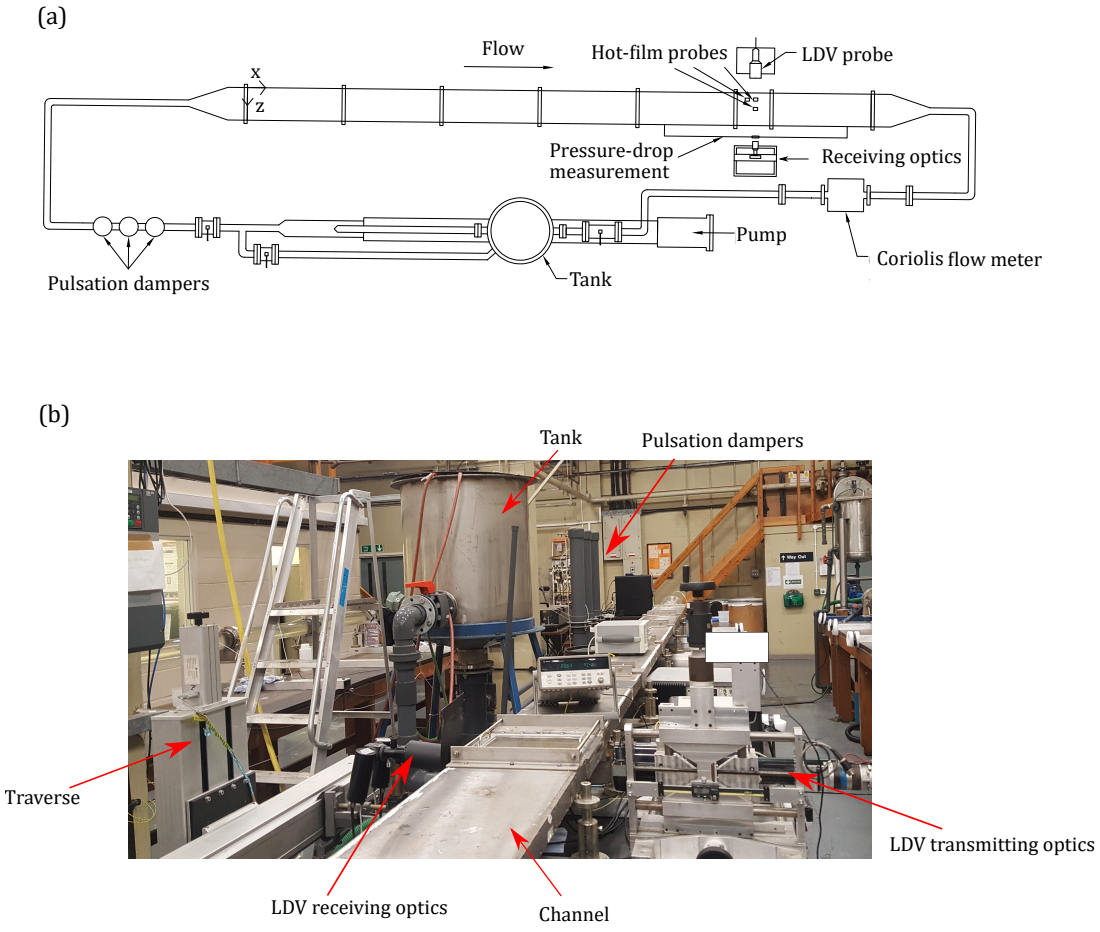

Figure 3.1: (a) Schematic of channel-flow flow facility (not to scale). (b) Photograph of the channel-flow facility.

working fluid is stored in a stainless steel header tank of capacity about 500 litres. The tank is positioned higher than the channel to provide enough gravity head to fill the channel. A Mono type E101 progressive cavity pump is used to circulate the fluid via

the tank in a closed loop. The flow loop also consists of an additional mixing loop which provides an opportunity for having lower flow rates. Three pulsation dampers are situated just after the pump, which helps in damping any pulsations in the flow before entering the channel. A Promass Coriolis flow meter is installed in the return loop to measure the mass flow rate ($\dot{m}$) of the fluid. This enables to obtain information about the bulk velocity (U_b) by the relation: $U_b = \dot{m}/(\rho A)$, where A is the cross-section area of the channel and ρ is the density of the working fluid. A platinum resistance thermometer (PRT) is present in the last module of the channel. The PRT is powered by an Agilent 34970A switch unit, which provides temperature readings with a resolution of 0.01 ^{o}C. Throughout this study, only Newtonian fluids are used as working fluids (a small study is also made using polymer additives, but it does not form a major part of thesis and is only discussed in Appendix A). These are water-glycerol mixtures of different concentrations where glycerol is used to increase the viscosity to get to lower Reynolds number. For example, while studying the flow for $Re_\tau > 180$, water is used as the working fluid and while studying low Reynolds number flow ($Re_\tau < 70$), a $65\% - 35\%$ by weight glycerol-water mixture is used as the working fluid. The density of the working fluid is measured using an Anton Paar DMA 35N density meter. The shear viscosity of the working fluid is measured using an Anton Paar MCR 302 rheometer. A cone and plate geometry is employed to measure shear viscosity for shear rate ($\dot{\gamma}, s^{-1}$) ranging from 10^{-2} to 10^{2}. During the viscosity measurement, the temperature is controlled to a precision of ± 0.1 ^{o}C using a Peltier system incorporated into the plate.

For pressure-drop measurements, pressure tappings are provided on the various locations of the channel: x/h = 120, 216, 312, 408 and 574, where x is the streamwise distance from the inlet of the channel. These tappings are provided on both the top and bottom walls of the channel for each streamwise location. The details of the pressure-drop measurements will be discussed in § 3.3. Instantaneous wall shear stress and velocity measurements are carried out using a hot-film anemometry (HFA) system and a laser Doppler velocimetry (LDV) system, respectively. Flow visualization is also carried out using a planar laser sheet and a camera. These three experimental techniques

are conducted in the test section of the channel and will be discussed in detail in the following sections. Note that not all these three experimental techniques are employed for every part of this study. Chapter 4 employs HFA, chapter 5 employs HFA and flow visualization, and chapter 6 employs HFA and LDV.

Over the last few decades, another major technique to measure turbulent flow which is well developed and highly used is the particle image velocimetry (PIV) [Adrian and Westerweel, 2011]. For the present study, where long time intermittencies ($\sim$ few hours) are investigated with high temporal resolution, using this technique is challenging due to accumulation of a very large amount of data in a short period of time. For example, while acquiring data at a rate of few 100 Hz, the maximum time for which the images could be stored in the cameras available within our laboratory remains in the order of a few seconds. Therefore, practically, it becomes enormously time consuming to collect the images, transfer them to a PC - which takes $\sim$15-20 minutes during which time no more data can be collected - and then repeat this process until sufficient events have been captured. In addition the probability of capturing a low- or high-drag event (discussed in chapter 6) during this data capture is low and means most of this data collected in this way could not be used. This makes the use of PIV - beyond obtaining some representative snapshots as was done by Whalley et al. [2019] - essentially remains impractical for this study and is therefore not utilized.

3.2 Measurement test section

The test section, as shown in figure 3.2(a), is the part of the channel-flow where velocity and wall shear stress measurements are conducted. The side- and top-walls of the test section are made of borosilicate glass to provide optical access for the LDV measurements and flow visualization. The transmitting optics (also called the laser "head") of the LDV can be traversed across the entire height of the channel for the streamwise velocity measurements. Wall-normal velocity measurements cannot be made close to the bottom wall because of the cut-off of the laser beams and therefore some modifications to the transmitting optics of the LDV set-up are made (discussed in § 3.4.3). For the

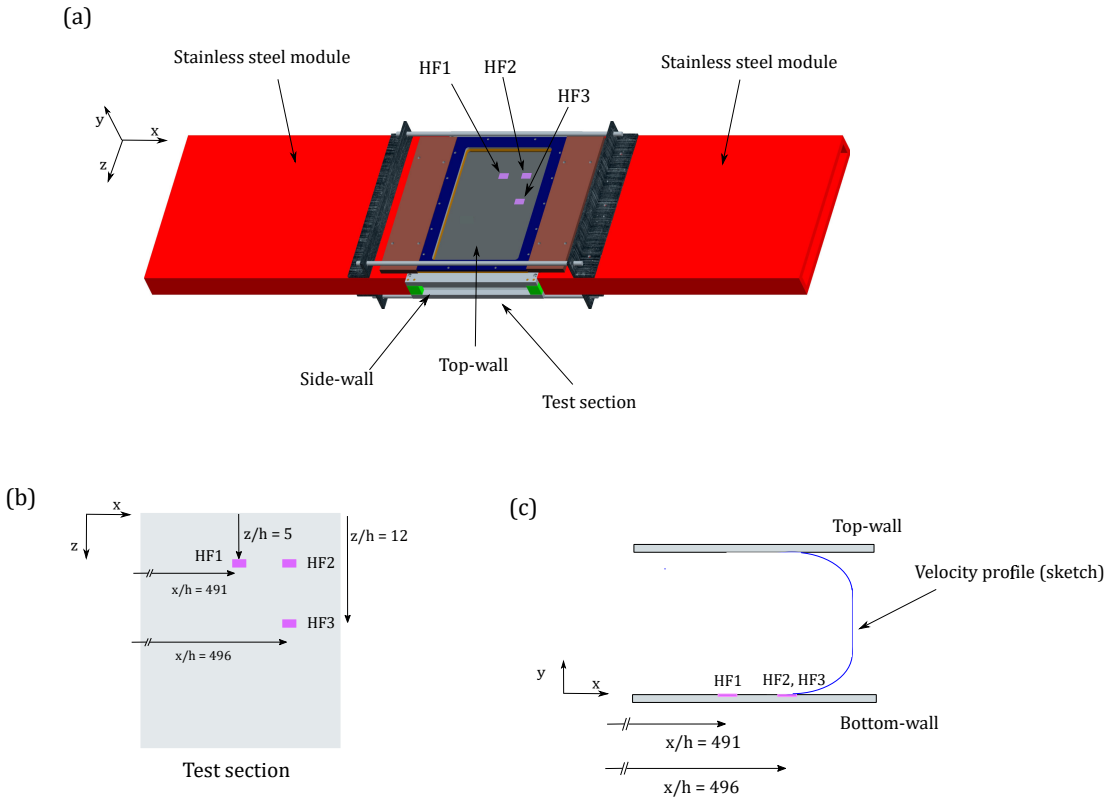

Figure 3.2: (a) Schematic of the test section. The test section is attached on both sides by the stainless steel modules. HF1, HF2 and HF3 indicate the locations on the bottom plate where the wall shear stress measurements are conducted. (b) Schematic showing the top-down view of bottom plate of the test section and the locations of the hot-films. (c) Schematic showing the side view of the test section and the locations of the hot-films. A sketch of the velocity profile is shown for reference. In all the three figures, x axis shows the mean flow direction.

flow visualization, the planar laser sheet enters through the side-wall, parallel to the x-z plane, while the image is captured using a camera from the top-wall (discussed in § 3.6). For wall shear stress measurements, removable Delrin plugs are designed and fabricated inhouse and the hot-film probes are glued on these plugs. These plugs are then inserted into the bottom wall of the test-section. It is ensured that the hot-films are flushed with the bottom wall of the test section. In this work, the wall shear stress measurements are conducted at three spatial locations and are given the nomenclature of HF1, HF2, and HF3. HF1 and HF2 are located at the same spanwise location of z/h = 5 but different streamwise locations of x/h = 491 and 496, respectively. Here, $z = 0$ and $x = 0$ indicate the side-wall and inlet of the channel, respectively. HF3 is located at a spanwise location of $z/h = 12$ and streamwise location of $x/h = 496$. For clarity, the locations of the hot-films are also shown in figure 3.2(b, c). The $5h$ streamwise gap between HF1 and HF2 is taken because that is the minimum distance such that the lower cartridge of the two hot-film plugs (shown in figure 3.14) does not physically touch each other. Further description of the mounting process of hot-film probes is discussed later in § 3.5.3.

3.3 Pressure-drop measurements

Obtaining accurate pressure-drop measurements is critical as they provide mean wall shear stress for the fully-developed section of the channel. This mean wall shear stress is used for calibrating the hot-film signal and also providing the friction velocity ($\overline{u_\tau} = \sqrt{\overline{\tau_w}/\rho}$, where $\overline{\tau_w}$ is the time-averaged wall shear stress) data for the channel. Pressure-drop measurements were conducted using a Druck LPX-9381 low-differential pressure transducer which has a working range of 5 kPa with an accuracy of ±5 Pa. It is a diaphragm-type transducer, with an Inconel X750 diaphragm material, and the sensor body is made of 316L stainless steel. This kind of differential transducer needs to be calibrated *in situ* against a reference pressure [Tropea and Yarin, 2007]. Therefore, a Baratron differential pressure transducer made by MKS is used to calibrate the Druck pressure transducer. This calibration is conducted using air as the working fluid. An example of this calibration is shown in figure 3.3. It can be seen that there is a linear

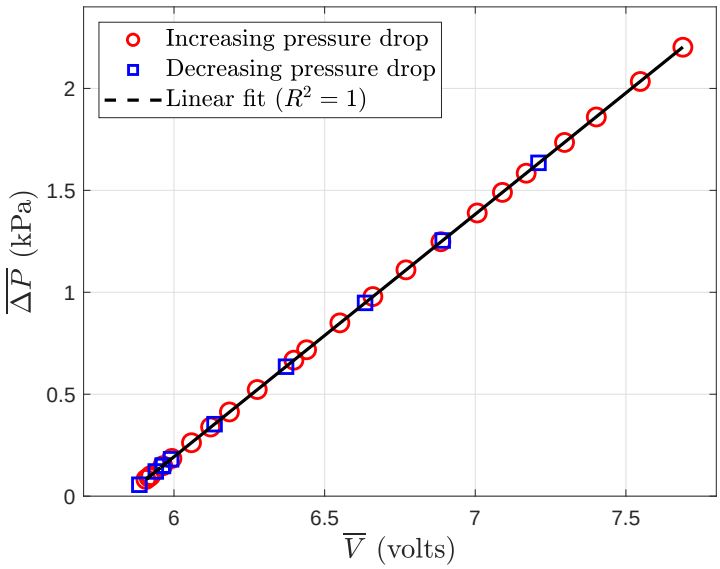

Figure 3.3: An example of a typical calibration curve for the pressure transducer.

relationship between the pressure differential obtained from the MKS pressure transducer and the voltage data obtained from the Druck pressure transducer. No noticeable hysteresis is observed while measuring with increasing pressure and decreasing pressure.

To make the pressure-drop measurements in the channel, two long vinyl tubes of equal length are taken and one end of each tubing is attached to the inlet and outlet of the transducer, respectively. The other ends of the tubes are connected to the pressure tappings between which the pressure-drop is to be measured. In this study, pressure tappings at the bottom wall of the channel are used for the pressure-drop measurements. The working fluid enters the tubes and inside of the transducer from both pressure tappings. Great care is taken to remove all the air bubbles from the tubes and the transducer as the presence of air bubbles can significantly affect the measurement. The bleed valves, provided in the transducer, are used to remove all the air bubbles before the start of a measurement. The voltage output from the pressure transducer is sampled using an analog-to-digital (ADC) inbuilt into the burst spectrum analyzer of the LDV system. The mean voltage data obtained from the transducer is then converted to the mean pressure-drop using the calibration data obtained from the MKS Baratron, as shown in figure 3.3.

3.4 Laser Doppler velocimetry (LDV)

3.4.1 Introduction and working principle

Laser Doppler velocimetry (LDV) is employed for instantaneous velocity measurements in the channel-flow facility. The LDV works on the principle of Doppler shift, which states that there is a shift in frequency of light when it is reflected from a moving object. The major characteristics of LDV as a flow measurement technique are as follows:

a) Non-intrusive technique: LDV is a non-intrusive flow measurement technique which means it does not disturb the flow in the measuring volume, unlike thermal anemometry measurements, for example, hot-wire or hot-film anemometry.

b) No calibration required: There is no requirement of any *in situ apriori* calibration of the LDV as there is an almost absolute linear relation between the output voltage from the LDV and the flow velocity.

c) High spatial and temporal resolution: The measurement volume in LDV has a very small size which can provide a very high spatial resolution and the associated fast signal processing tools help in providing well time-resolved instantaneous velocity data (just to note here that the suitability of the size of the measurement volume is also a function of Reynolds number in turbulent flows i.e. the higher the Reynolds number is, the smaller should be the size of the measurement volume to resolve all scales of motion).

The first successful flow measurement using LDV was conducted by Yeh and Cummins [1964]. Since then there has been a multitude of investigations made to further improve this novel technique by enhancing its opto-electronic performance, and hardware and software related performances [Zhang, 2010]. The general working principle of the LDV is described here. For simplicity, the working principle of LDV for only one component velocity measurement is shown. In LDV, two monochromatic beams of the same wavelength (λ) are emitted from the transmitting optics at the same angle (α) and are made to cross each other in a specified region of fluid flow where the measurement needs to be carried out. This crossing region of the two beams is called the measurement volume. A schematic of the crossing of the laser beams and the formation of measurement volume is shown in figure 3.4(a). This crossing of two beams gives rise

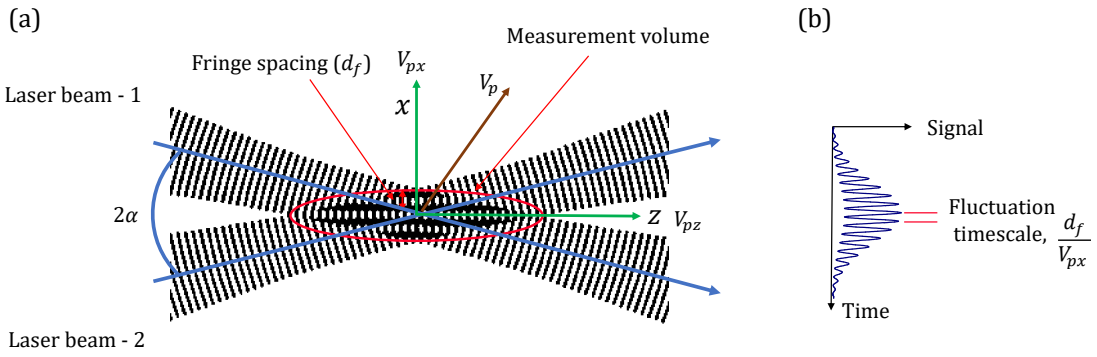

Figure 3.4: (a) Schematic of the fringe model explaining the working principle of LDV for one component velocity measurement. α represents the beam half-angle and V_p is the velocity of the seeding particle crossing the measurement volume. (b) Schematic of the burst signal varying with time as one seeding particle crosses the measurement volume.

to an interference fringe pattern. This interference fringe pattern contains alternating bright and dark zones and can be seen from figure 3.4(a). The fringe spacing (d_f) can be calculated based on the wavelength of the incident light (λ) and the beam half-angle (α) and is given by:

$$d_f = \frac{\lambda}{2\sin\alpha}. \tag{3.1}$$

The flow is seeded with particles which scatter the laser light in all directions. As these seeding particles pass through the pattern, the intensity of the scattered light fluctuates with the intensity of fringes. A schematic of this phenomenon is shown in figure 3.4(b). Therefore, the amplitude of the signal burst varies based on the timescale which is given by d_f/V_{px}, where V_{px} is the velocity component of the seeding particle crossing the measurement volume perpendicular to the interference pattern. The Doppler frequency is the reciprocal of this time scale and is given by $f_D = V_{px}/d_f$. Therefore, V_{px} can be calculated from:

$$V_{px} = f_D \frac{\lambda}{2\sin\alpha}. \tag{3.2}$$

Note that the LDV frequency doesn't depend on the direction of the motion of the seeding particle crossing the measurement volume, but depends only on its magnitude. It means that the V_{px} or $-V_{px}$ will give the same value of the Doppler frequency.

Therefore, based on the above discussion the direction of the seeding particle crossing the measurement volume cannot be resolved by the LDV. To obtain the information regarding the flow direction, the frequency of one of the incoming laser beam is shifted by a known frequency f_s. This shifting of frequency of one of the incoming beam causes the fringe pattern to move towards the unshifted beam with a speed of $f_s d_f$. Therefore, the Doppler frequency changes to:

$$f_D = |f_s + \frac{2V_{px} \sin \alpha}{\lambda}| \tag{3.3}$$

Now, the direction of velocity is reflected in f_D based on whether the seeding particle is moving in the same direction as the moving fringes or opposite. This technique works provided that $f_s > |2V_{px} sin\alpha/\lambda|$. The scattered light from the seeding particle is detected by the photomultiplier tube (PMT), which converts the fluctuations in scattered light intensity to voltage signal fluctuations. The frequency of these voltage signal fluctuations is then converted to flow velocity using signal processing. Further details on the working principle of LDV can be found in the books by Durst et al. [1981], Albrecht et al. [2013] and Zhang [2010].

3.4.2 Measurement chain

A detailed description of the measurement chain of the employed LDV system is now discussed. A schematic of the entire measurement chain is shown in figure 3.5. A

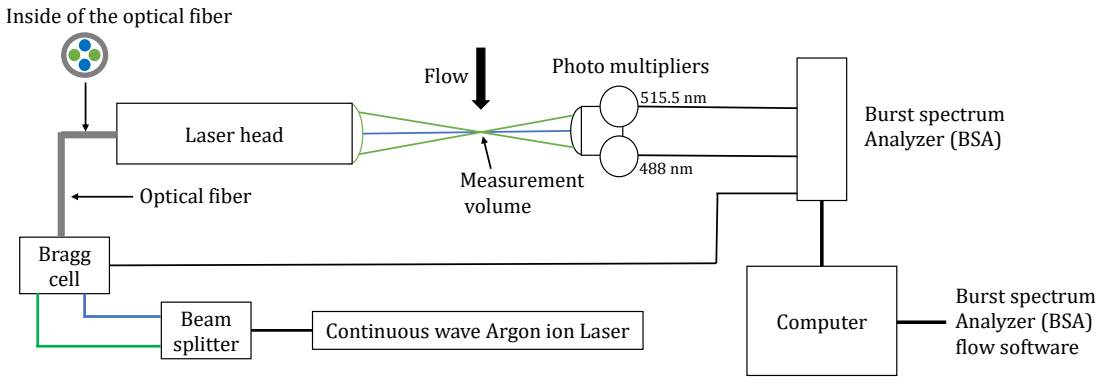

Figure 3.5: Schematic of the measurement chain for the two component velocity measurements using LDV in forward scatter mode.

Dantec FiberFlow laser system is employed which uses a 300 mW argon-ion continuous

wave laser. Up to two component velocity measurements have been carried out thus requiring two pairs of laser beams of different wavelengths. The laser beam passes through a beam splitter which consists of an arrangement of prisms and allows the beams to be split into wavelengths of two different colours: blue (488 nm) and green (515.5 nm). The two laser beams of different frequencies then enter the Bragg cell. The Bragg cell has a vibrating piezoelectric crystal which provides a frequency shift to the beam without changing its intensity. As discussed earlier, this frequency shift is important to resolve the directional ambiguity of the velocity of seeding particles, as measured by LDV. In this study, the frequency shift given to the laser beams is 40 MHz. The output from the Bragg cell is four laser beams: two green beams and two blue beams where one of each colour beams have a frequency shift. The four parallel beams enter the transmitting optics via an optical fiber. The transmitting optics focus the four parallel laser beams to a measurement volume where the focal distance depends on the internal optics of the transmitter. The transmitting optics provide a focal length of 160 mm and a beam separation of 51.5 mm and therefore the crossing of beams of the same colour creates a measurement volume of $24\mu m$ diameter and $150\mu m$ length in air. The LDV is operated in the forward-scatter mode which means that the receiving optics are positioned opposite to the transmitting optics. The transmitting optics (laser head) is placed on a traverse which allows movement of the measurement volume in all three directions. The transmitting and receiving optics need to be aligned with each other to obtain a good data rate. Therefore, the receiving optics are also placed on a traverse and the alignment can be conducted by moving the traverse. For the seeding particles, generally, natural particles present in the working fluid (for example, supply water) are found to be sufficient to obtain a good data rate. In cases where the natural seeding particles are found to be low, for example when the working fluid has a high concentration of glycerol, Timiron Supersilk MP-1005, having an average size of $5\mu m$, are added to the working fluid. The laser head emits the two pairs of beams (green and blue) in perpendicular to each other to resolve streamwise and wall-normal velocities. The typical data rate is around 100-500 Hz which for this study depends mainly on three parameters: distance from the wall, bulk flow speed, and signal gain. A higher

data rate is observed while measuring away from the wall which is generally because of lower seeding particle density near the wall. Higher velocity gives higher data rate typically because more seeding particles can pass through the measurement volume. Higher signal gain increases the data rate but may also increase the noise level in the data. The scattered light from the seeding particle enters the photodetector and is split based on the wavelength of the laser beam and is then passed to the photomultiplier tubes (PMTs). The Doppler frequencies obtained from the PMTs are sampled using a flow processor, burst spectrum analyzer (BSA)-F50, made by Dantec Dynamics. Here, the signals are converted to the corresponding velocity signals using the inbuilt signal processors in the flow processor. BSA flow software, installed in the computer, is used to control the LDV parameters and acquisition of the data.

3.4.3 Near-wall two component velocity measurements

Reynolds shear stress (RSS) is given by $-\overline{uv}$, where u and v are the streamwise and wall-normal velocity fluctuations. Therefore, the calculation of RSS requires simultaneous measurements of streamwise and wall-normal velocities. As discussed above, two pairs of laser beams are required to resolve the two velocity components in LDV. Figure 3.6(a) shows a schematic of a laser beam arrangement for the measurement of streamwise and wall-normal velocity components using LDV. The green pair of beams are used for the measurement of streamwise velocity component and a blue pair of beams are used for the wall-normal velocity component. It can be seen that the near-wall measurements of the wall-normal velocity component cannot be obtained with the current set-up of LDV due to the cut-off of blue beams near the wall. This is because the bottom wall of the test-section is made of stainless steel thus providing no optical access for the laser beams. Getting near-wall data for the wall-normal velocity components using LDV is a common challenge to study RSS behaviour. Various techniques have been employed in the past to get closer to the wall for the wall-normal velocity component measurement in channel-flows. Melling and Whitelaw [1976], Walker and Tiederman [1990] and Günther et al. [1998] rotated the laser head by 45^{o} along the spanwise axis to obtain the wall-normal velocity component near the wall. Niederschulte et al. [1990]

tilted the transmitting optics by 0.7° towards the surface allowing them to measure as close as 0.12 mm from the surface. In this work, the following modifications are made to the transmitting optics (or laser head) for measuring closer to the bottom wall.

(a) Rotation of laser head along spanwise direction

The first modification is to rotate the laser head by 45° about the spanwise axis to get closer to the bottom wall. Figure 3.6 shows the effect of the rotation of laser head by 45° about the spanwise axis. It can be seen from figure 3.6 that the minimum vertical height where the measurement of the wall-normal velocity component can be made reduces by a factor of $1/\sqrt{2}$. Figure 3.7 shows the velocity components measured by

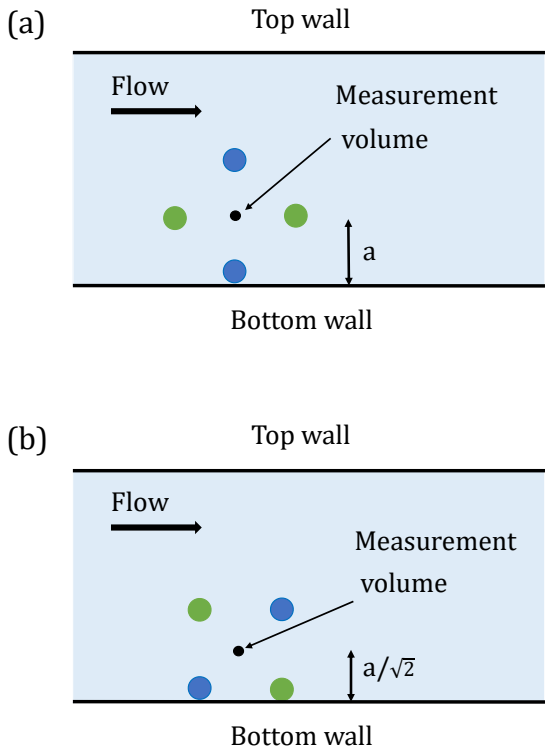

Figure 3.6: (a) Schematic showing the orientation of laser beams in orthogonal rotation where green and blue pairs of laser beams are used to measure streamwise and wall-normal velocity components, respectively. a indicates the nearest vertical distance where the wall-normal velocity measurement can be made in this orthogonal orientation. (b) Schematic showing the orientation of laser beams by rotating the laser head (transmitting optics) by 45° along the spanwise axis. It can be seen that the nearest vertical distance where the wall-normal velocity measurement can be made is $a/\sqrt{2}$ in this orientation. In both figures the laser beams are exaggerated for clarity; not to scale.

blue and green beams which are represented by U_1 and U_2 respectively. ϕ denotes the angle of rotation of laser head along the spanwise axis which is 45°. Streamwise and

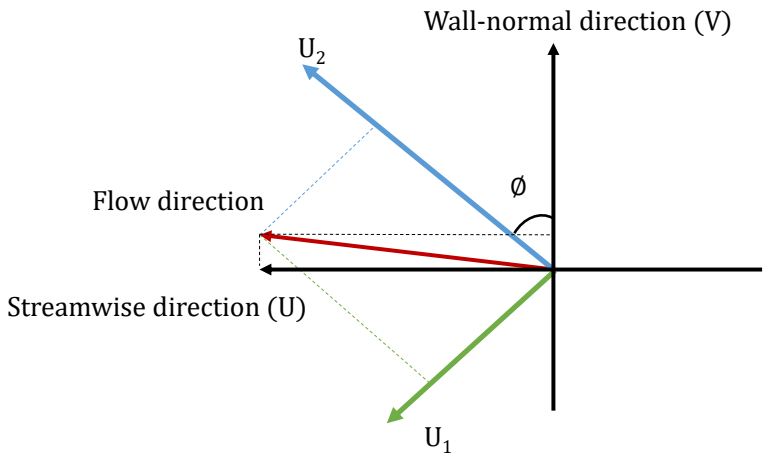

Figure 3.7: Schematic showing the orientation of velocity components measured by each pair of beams.

wall-normal velocity components are recovered based on the coordinate transformation equation, as shown below:

$$\begin{bmatrix} U \\ V \end{bmatrix} = \begin{bmatrix} cos\phi & sin\phi \\ -sin\phi & cos\phi \end{bmatrix} \begin{bmatrix} U_1 \\ U_2 \end{bmatrix}. \tag{3.4}$$

From equation 3.4, the streamwise and wall-normal velocity components can be calculated as:

$$U = U_1 \cos\phi + U_2 \sin\phi, \tag{3.5}$$

$$V = -U_1 \sin\phi + U_2 \cos\phi. \tag{3.6}$$

(b) Addition of an external lens to laser head

As mentioned before, the laser head used in this study provides a focal length of 160 mm in air for both green and blue pairs of laser beams. Next step to measure closer to the bottom wall is by increasing the focal length of the laser beams. This is carried out by placing an external bi-concave lens in front of the laser head. Effect of adding an

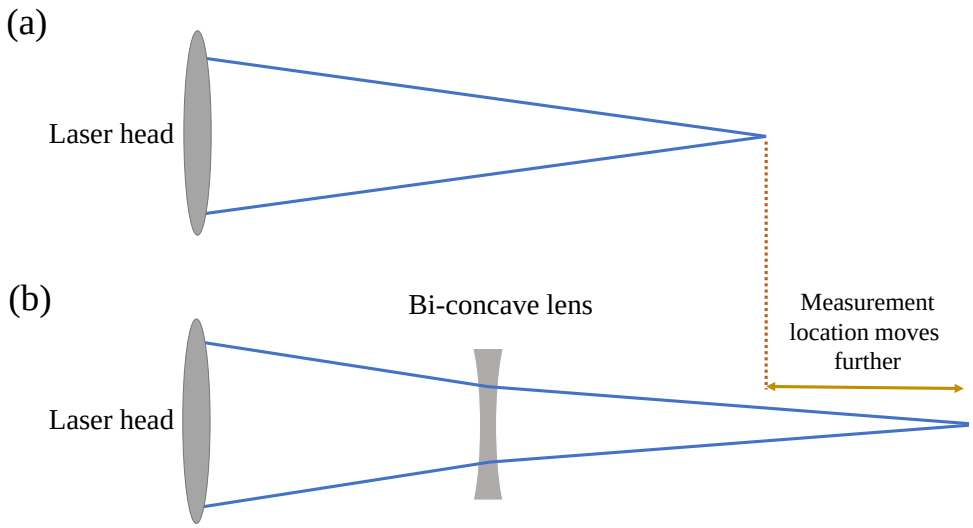

Figure 3.8: Schematic showing the effect of addition of a bi-concave lens on a pair of laser beams in air (a) without external lens and (b) with external bi-concave lens.

external lens to the laser beams in air is shown in figure 3.8. For ease of understanding, the effect of adding lens is shown only for air as the medium, and the effect of side-wall glass of the test section and the working fluid are ignored. It can be seen that increasing the focal length enables the measurement volume to go further into the test section from the side-wall. Therefore, if the aim is to measure at the same spanwise location in the test section, the laser head needs to be moved further back from the side-wall. This modification makes the laser beams to be closer to each other while they enter the side-wall, and this phenomenon is shown in figure 3.9. It can also be clearly seen that the measurement volume gets closer to the bottom wall as the laser beams get closer to each other. Thus, RSS measurements can be carried out closer to the bottom-wall after the addition of a bi-concave lens in front of the LDV head. Although, the longer the focal point of the laser beams are, the better it is to measure closer to the bottom wall as the laser head can be moved further from the side-wall. However, the intensity of the laser beams is found to reduce as the data rate starts to decrease by extending the distance of the measurement volume from the laser head. Another potential issue can arise from the velocity gradient broadening of the streamwise velocity because it can lead to unwanted extension of the measurement volume in the spanwise direction.

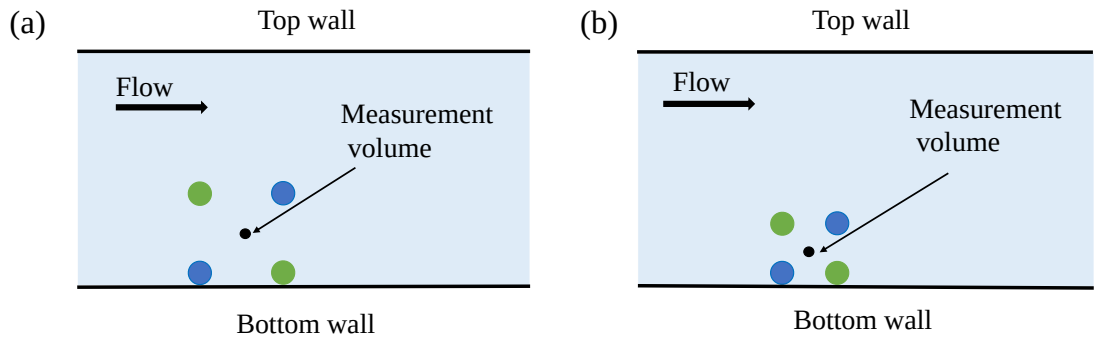

Figure 3.9: Schematic showing the effect of addition of a external lens laser beams while measuring at the spanwise location in the test section (a) without external lens and (b) with external bi-concave lens. The laser beams are exaggerated for clarity; not to scale.

An LD1613-N-BK7 bi-concave lens made by THORLABS is employed. This lens has a diameter of 25.4 mm and a focal length of 100 mm. The lens is connected on a lens mount which is attached to an optical post. The optical post is then attached to the traverse of the transmitting optics. Therefore, the entire lens system can be traversed with the transmitting optics. It is important that both pairs of laser beams are aligned properly to the external lens. This alignment is checked based on the high data rate of the LDV signal in co-incident mode and validating the time-averaged RSS profile against the available DNS data at the same Reynolds number (later shown in figure 6.20).

By making these two modifications, the two-component velocity measurements can be conducted for $y/h \geq 0.3$ at a spanwise location of $z/h = 5$ in the channel-flow facility. The results for the Reynolds shear stress measurements are presented in § 6.7.3.

3.4.4 Post-processing of LDV data

The output obtained from the BSA flow software is the time history of the velocity at the measurement location. Since the LDV acquires data at random intervals the time history contains information about the arrival time (A_t), transit time (T_t) and velocity (U) of the seeding particle crossing the measurement volume. In the present thesis, both single component and two-component velocity measurements have been carried

out. In the case of two-component velocity measurements, the data are acquired in co-incident mode. This mode samples both velocity components of the same seeding particle simultaneously in the measurement volume. Once the time history of the velocity is recorded, the data is exported for the post-processing. A few important points about the post-processing of LDV data are discussed below

(a) Velocity bias in LDV data

Turbulence is a stochastic process and therefore one way to investigate it is by using statistical techniques. One of the most common statistical investigations is the calculation of moments of the obtained time histories. In LDV, there is found to be velocity bias because of the fluctuating speeds of the tracer particles crossing the measurement volume [Zhang, 2010], as can be seen from the varying transit times (T_t) of the tracer particles [Benedict et al., 2000]. Therefore, a transit-time weighting is generally carried out for the calculation of moments of the LDV data [Durst et al., 1981]. In this study mean, root mean square (RMS) and Reynolds shear stress (RSS) of the velocity data are generally calculated and are given by the following equations:

$$\text{Mean}, \overline{U} = \sum_{i=1}^{N} \eta_i U_i, \tag{3.7}$$

$$\text{RMS}, \sigma(u') = \sqrt{\sum_{i=1}^{N} \eta_i (U_i - \bar{U})^2}, \tag{3.8}$$

$$\text{Reynolds shear stress (RSS)}, -\overline{u'v'} = \sum_{i=1}^{N} -\eta_i (U_i - \bar{U})(V_i - \bar{V}), \tag{3.9}$$

where N is the number of velocity samples and η_i indicate the two different types of weighting: uniform weighting and transit-time weighting. The formula for these two weightings are given by:

$$\eta_i = \frac{1}{N} (\text{Uniform weighting}) \tag{3.10}$$

$$\eta_i = \frac{T_{t_i}}{\sum_{j=1}^{N-1} t_j} (\text{Transit-time weighting}) \tag{3.11}$$

In equation 3.11, T_{t_i} indicates the transit time of tracer particle i crossing the measurement volume. Further explanation about the transit time weighting for the velocity-bias correction for LDV data can be found in Buchhave et al. [1979].

(b) Interpolation of LDV data on to a constant time interval

For many other time-series analyses conducted in the present work, e.g. spectral analysis and conditional averaging, it is necessary for the time series data to be acquired at a constant time interval. But, as discussed above, the LDV acquires data at random intervals due to random arrival times of particles in the measurement volume and thus time series obtained are distributed at uneven time points. Therefore, it is necessary to interpolate the time series data on a constant time interval. In this study, the sample-and-hold interpolation method is used for the resampling of unevenly distributed LDV data. In this method, sampled velocity is assumed to be constant until a new sample indicates that the velocity has changed:

$$U_{rs}(t) = U(t_i)|(t_i \leq t \leq t_{i+1}). \tag{3.12}$$

From equation 3.12, it can be seen that the resampled velocity $U_{rs}(t)$ takes the value of $U(t_i)$ until $U_{t_{i+1}}$ appears. Further analysis of sample-and-hold interpolation as a way to resample unevenly spaced LDV can be found in Adrian and Yao [1986] and Edwards and Jensen [1983]. Figure 3.10 shows a schematic of the sample-and-hold interpolation resampling technique on a streamwise velocity time series. It is observed that for the resampling rate of twice the average data rate the first four moments of the time-series obtained using the transit-time weighting of the acquired data and equal-weighting of the resampled data are in good agreement (within 1%). Therefore, a resampling rate of twice the average data rate is chosen in this work wherever the sample-and-hold interpolation technique is employed for the resampling data obtained in an uneven time interval.

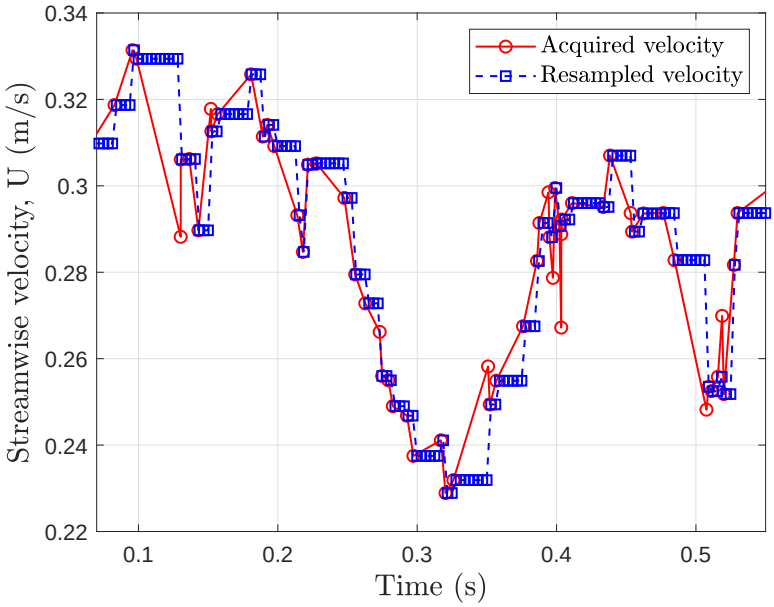

Figure 3.10: Schematic showing random sampling and sample and hold resampling. Resampling rate of 2 times the average sampling rate by LDV is used here.

3.5 Hot-film anemometry (HFA)

3.5.1 Introduction and working principle

Hot-film anemometry is a part of thermal anemometry [also called as "hot-wire anemometry" because of the historical reasons as this technique started with the use of fine wires as the sensors see; Fingerson, 1994]. As stated by Comte-Bellot [1976], it is difficult to know the exact origin of thermal anemometry, but this method arguably started in the beginning of the 20^{th} century. Among the earliest studies, the study of heat transfer from a heated wire by Boussinesq [1905] is considered to have paved the way for the development of hot-wire anemometry. Later, King [1914] extended this work by carrying out an investigation of heat convection from a cylinder immersed in a stream of fluid and thus providing the first design for hot-wire anemometry. Early research using this technique focused on the measurement of mean velocities [Boussinesq, 1905, King, 1914]. The first measurement of velocity fluctuations was conducted by Dryden and Kuethe [1929], where they employed constant-current (CC) anemometry to measure the fluctuations in airflow. First constant-temperature (CT) anemometry measurement was carried out by Ziegler [1934] who maintained a constant wire resistance using a feedback amplifier. The hot-wire sensors, which are commonly used for airflow

measurements suffer issues because of their fragile nature while measuring water flows [Bruun, 1996]. Also, it is necessary to insulate the sensor for measuring in liquid flows, for example, water, as it is a conducting medium. It is difficult to insulate and maintain the insulation on such thin wires ($\approx 5\mu m$ diameter). Therefore, hot-film sensors were developed which are sturdier in design and can be insulated relatively easily as they are deposited on a substrate [Bruun, 1996]. The first hot-film anemometry was developed by Ling and Hubbard [1956] for liquid turbulence measurements. Extensive hot-film measurements were conducted by Eckelmann and co-workers to investigate turbulent channel-flow using oil as a working fluid [Eckelmann, 1972, 1974, Kreplin and Eckelmann, 1979]. Many review articles and books are available which discuss in length about the historical development and working principle of thermal anemometry [see, for example: Comte-Bellot, 1976, Laufer, 1975, Perry, 1982, Lomas, 2011, Bruun, 1995].

In this study, constant temperature anemometry (CTA) is employed for measuring the instantaneous wall shear stress using hot-film sensors. CTA works on the principle of convective heat transfer where the cooling of the heated hot-film sensor by the flow is a measure of the local instantaneous wall shear stress. The hot-film is essentially a part of the Wheatstone bridge where one of the resistors is replaced by a hot-film probe with resistance, R_w. A schematic describing the working principle of constant-temperature anemometry is shown in figure 3.11. The sensor temperature (T_w) is kept at a higher temperature than the ambient temperature (T_0) of the working fluid. The difference between these two temperatures is called the over temperature, and is given by $T_w - T_0$. Overheat ratio (O_{HR}) is the term generally used in the CTA which is given by:

$$O_{HR} = \frac{R_w - R_0}{R_0}, \tag{3.13}$$

where R_w and R_0 are the resistances of the sensor at the working temperature and at the temperature of the working fluid, respectively. The over temperature and overheat ratio are connected by the following relation:

$$T_w - T_0 = \frac{O_{HR}}{\alpha_{r_0}}, \tag{3.14}$$

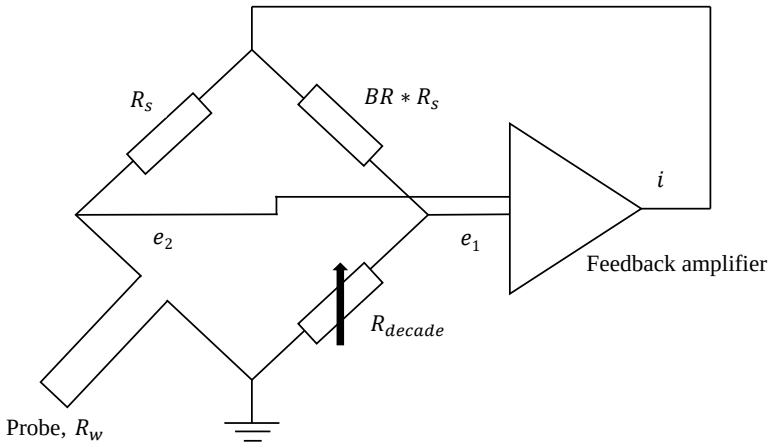

Figure 3.11: An schematic of the Wheatstone bridge and the feedback amplifier used in a typical CT anemometer. BR indicates the bridge ratio of the Wheatstone bridge and usually has a value between 5 and 20 [Bruun, 1995].

where α_{r_0} is the coefficient of resistance of the sensor at T_0. Compared to the turbulence measurements in air using hot-wires, the overheat ratio for the currently used glue-on probes are recommended to be much lower. The recommended highest working temperature of the glue-on probe in water flow measurement is 60 ^{o}C, as provided by Dantec Dynamics. This is mainly since the high temperature of the sensor can cause the formation of bubbles because of the local boiling of the working fluid. The decade resistance (R_{decade}) can be calculated based on the principle of Wheatstone bridge. This bridge is incorporated with a feedback amplifier to compensate for the instantaneous changes in the wall shear stress by rapidly varying the heating current. The difference between the voltage outputs e_1 and e_2 is a measure of the change in resistance of the hot-film probe. This error in voltage forms the input for the feedback amplifier and it gives output current i. This current i is inversely proportional to the change in resistance of the hot film probe and is provided at the top of the bridge thus helping in restoring the resistance of the probe. Therefore, the output of the anemometer is a direct measure of the change in instantaneous wall shear stress at the measurement location.

The operation of the hot-film anemometer can be checked by observing the frequency response of the bridge and the feedback amplifier used in the anemometer. Typically, the frequency response of a hot film probe is measured by applying a square wave to

the top of the bridge. The time it takes for the bridge to balance itself is representative of the frequency response of the anemometer [Bruun, 1995].

3.5.2 Measurement chain

As explained above, the measurement test-section allows to hold three hot-film probes for measuring wall shear stress at different spatial locations. Therefore, three 91C10 CTA modules, made by Dantec Dynamics, are used for hot-film measurements. These three modules are attached to the Streamline Pro frame, made by Dantec Dynamics. For the sake of simplicity, the measurement chain is discussed considering only one hot-film in operation, with CTA module 1 as the anemometer. The working principle of the other two hot-films with the corresponding CTA modules (CTA module 2 and CTA module 3) remains the same. A schematic of the measurement chain is shown in figure 3.12. The chain starts with the measuring probe which detects the wall shear

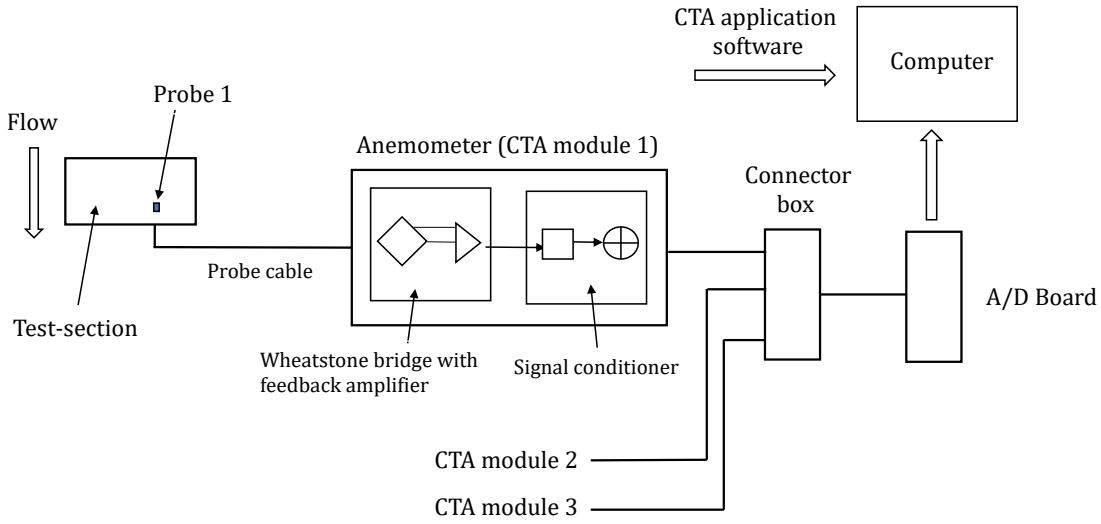

Figure 3.12: An schematic of the measurement chain used in this study for wall shear stress measurements using constant thermal anemometry (CTA).

stress fluctuations and sends the signal to the anemometer through the probe cable. The probe is powered by a StreamLine Pro velocimetry system and is operated under constant temperature (CT) mode. In this anemometer, the bridge ratio (BR) and the overheat ratio (O_{HR}) are set to be at 10 and 1.1, respectively. The present anemometer has an inbuilt square-wave generator which is used to check the frequency response of this amplifier. The typical frequency response of the anemometer is found to be around

10-30 kHz, which is generally considered sufficient for turbulence measurements [Bruun, 1995]. The output voltage signal then passes to the signal conditioner. The signal conditioning is used to filter (low-pass and high-pass) and amplify the signal before digitizing it by the A/D converter. Low-pass filter frequency is representative of the highest frequency of fluctuations present in the flow. It allows to pass all the frequencies below the selected cut-off frequency and attenuate all the frequencies above it [Bendat and Piersol, 2011]. The output voltage signal from the anemometer needs to be low-pass filtered to avoid the higher frequencies from aliasing. For this study, the voltage signal from the anemometer is low-pass filtered at 1 kHz. A high-pass filter is used if the signal contains frequency lower than the sampling period. A high-pass filter is found to be irrelevant in this study as the data are acquired mainly for long time periods and are found to be statistically stationary. In the case of non-thermal drift observed in the hot-film output voltage, a linear filter is used to remove the unwanted linear trend during post-processing. The output voltage signal then goes to an amplifier where the voltage signal is amplified to utilize the full resolution of the A/D converter board. A gain of 32 is found to be adequate to utilize the full resolution of the A/D converter employed. The signal passes to a connector box, which is particularly useful when more than one hot-film is used simultaneously. The connector box is used to connect different output voltages from the anemometer in case two or more probes are used simultaneously, as can be seen from figure 3.12. The voltage signal is then digitized in the A/D converter. A 14-Bit USB6009 Multifunction I/O device made by National Instruments is employed as the A/D converter. After A/D converter, the signal is acquired using the CTA application software, StreamWare Pro, installed on the computer. In the case of simultaneous measurements of velocity and wall shear stress, the voltage from the A/D converter is sampled by the BSA flow processor. This helps in the acquisition of time-synchronized velocity and wall shear stress data.

3.5.3 Hot-film probe

Commercially available 55R48 glue-on hot-films probes, made by Dantec Dynamics, are utilized for the instantaneous wall shear stress measurements. A schematic of the

glue-on probe is shown in figure 3.13. The sensing element is made of nickel and is deposited on a 50 μm Kapton foil having a dimension of 8×16 mm. The sensing element has a dimension of 0.9×0.1 mm and is connected to gold-plated lead areas. The probe is coated with a quartz coating to provide electrical insulation and protection against abrasive particles while used for liquid flows [Bruun, 1996]. This probe can be glued

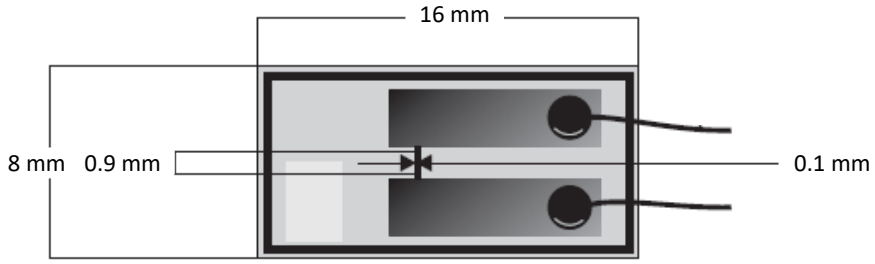

Figure 3.13: An schematic of glue-on probe used for the measurement of instantaneous wall shear stress. Source: Dantec Dynamics. For the shown hot-film probe orientation, the mean flow direction is from left to right.

onto the wall with the sensor direction generally oriented perpendicular to the mean flow direction.

To measure wall shear stress the probe needs to be mounted on the wall of the test section of the channel-flow facility. There are a few challenges associated with the mounting of these wall shear stress probes. The first challenge is that these probes should be precisely flush with the wall so that there is no apparent step change in the surface of the wall due to the finite thickness of the probe. The second challenge is that these probes are not very robust over long time periods and are prone to get destroyed, primarily due to the presence of abrasive particles in the working fluid. Thus, the mounting of these probes is not a one-time process rather these probes need to be replaced often with a frequency of about 2-3 months of measurement. Therefore, rather than directly mounting the probes onto the wall of the test section a plug, made of Delrin, is used to mount the probe and then the plug is attached to the wall of the test section. Figure 3.14 shows a detailed description of the Delrin plug used for mounting the hot-film probes. The test section has holes drilled on the bottom to mount these plugs so that the exposed surface of the plug is flush with the bottom wall of the test section. The leads from the probes enter through the two small holes made on the

upper cartridge of the Delrin plug, as shown in figure 3.14. The two holes are then soldered from the bottom side of the upper cartridge to fill them completely to avoid any leakage of the working fluid through the holes. Avoiding this leakage is critical because working fluid entering the plug can cause shorting of the two leads. The leads are then soldered to a BNC cable (probe cable as mentioned before) which passes the signal to the anemometer. A strain relief is added to the lower cartridge to protect the soldering of the leads and the probe cable.

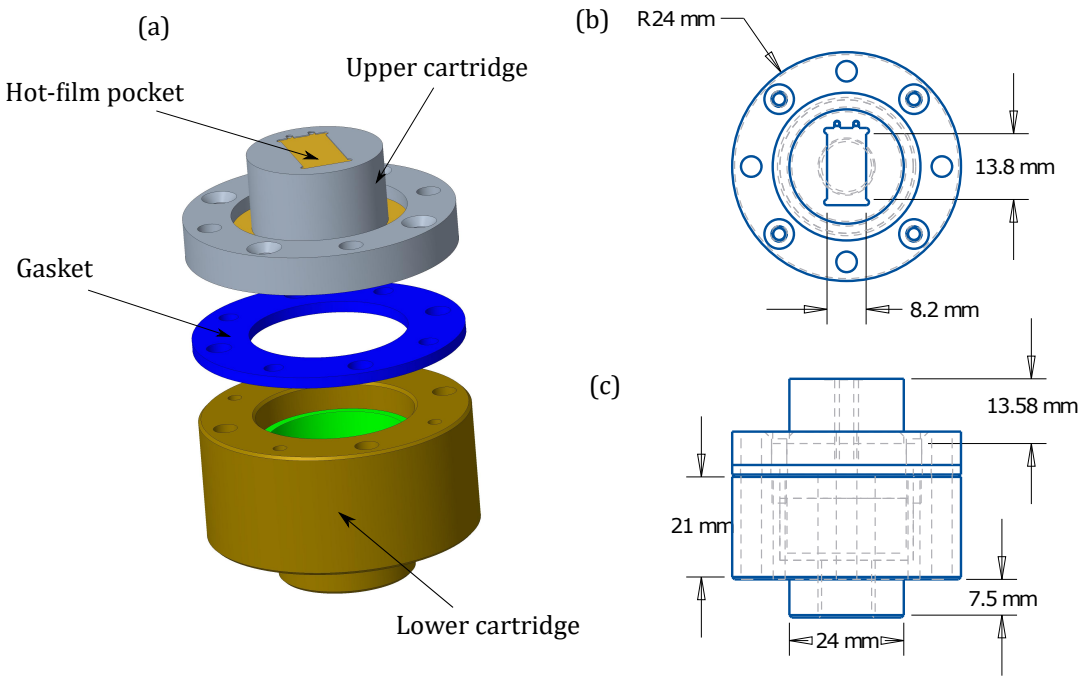

Figure 3.14: (a) Exploded view of the hot-film plug. It primarily consists of three parts: upper cartridge with the hot-film pocket, a gasket and a lower cartridge. (b) and (c) show the top and the side view of the assembled hot-film plug, respectively.

One important issue in turbulence measurements, especially using thermal anemometry, is the spatial resolution effects of the sensor [Johansson and Alfredsson, 1983]. Ligrani and Bradshaw [1987] showed that some of the important flow physics can be attenuated if the spatial resolution of the sensor is not sufficient. For example, Ng et al. [2011] compared the peak of the streamwise turbulent intensities, $\sigma(u')^+$ for $1000 < Re_\tau < 3000$ in channel- and pipe-flows using hot-wire measurements. They found that for the hot-wire length of $l^+ = 22$, the peak of the $\sigma(u')^+$ increases with

increasing Reynolds number from $Re_\tau = 1000$ to 3000. They also showed that this behaviour can be masked if the sensor length is not kept constant in inner units but rather kept constant in physical units (mm). Various other works have been carried out to address the measurement resolution issues in thermal anemometry [see, for example: Hutchins et al., 2009, Monty, 2005, Chin et al., 2009b]. Ligrani and Bradshaw [1987] considered the sensor length of about $l^+ \lesssim 20 - 25$ to be acceptable to make well-resolved turbulence measurements. In this study, the wall shear stress measurements using hot-film are conducted for Reynolds number between $35 < Re_\tau < 250$. The hot-film sensor has a physical spanwise length of 0.9 mm. In inner units, the range of the sensor lengths are $l^+ = 2.5$ for $Re_\tau = 35$ to $l^+ = 18$ for $Re_\tau = 250$. Therefore, for the present case the effect of measurement resolution issues due to hot-film sensor size are thought to be negligible. For LDV, this issue is even less significant because the measurement volume of the LDV has a spanwise width of 150 μm, corresponding to a length in inner units of 3 for $Re_\tau = 250$.

3.5.4 Temperature control

Thermal anemometry works on the principle of convective heat transfer from the sensing element due to fluid flow over it. Thus, all the changes in the fluctuations in voltage output from the anemometer should be the representative of the fluctuations in the flow [Bruun, 1996]. Therefore, the temperature variation in the flow should be minimized during the experimental run. To account for thermal drift in the voltage various correction schemes have been suggested in the past [see, for example: Collis and Williams, 1959, Hultmark and Smits, 2010, Tropea and Yarin, 2007]. In this set-up, the issue of thermal drift is quite important as the experiment is run in a closed loop with the help of a positive-displacement pump. This causes viscous heating of the working fluid over time. An increase of about 1 °C is observed during one hour of measurement time at moderate pump speed. To make the situation even more challenging, this study requires very long measurement times (up to 6-10 hours) to study long time intermittencies in the flow. It is observed that there is an approximate 5% of mean voltage drift from the glue-on hot film probes for every 0.1 °C change in the working

fluid temperature. Therefore, rather than relying on the correction schemes for thermal drift, an attempt is made to eliminate the drift issue by adding a cooling coil for the working fluid to the channel-flow facility. An open-loop copper cooling coil is added to the overhead tank and the main supply water is used to control the temperature of the working fluid. Using this set-up, the temperature of the working fluid could be controlled to the precision of $\pm$ 0.01 °C for the entire experimental run of the day. This helped in minimizing the thermal drift issue of the hot-film.

3.5.5 Calibration of hot-film

The voltage output signals from the anemometer need to be converted to instantaneous wall shear stress signals. This conversion is enabled by calibration of the hot-film signal against the mean pressure-drop obtained from the pressure transducer. The mean pressure-drop is converted to mean wall shear stress using the equation.

$$\overline{\tau_w} = \frac{\overline{\Delta P} w h}{l(w+2h)}. \tag{3.15}$$

Here, l indicates the distance between the pressure tappings used for pressure-drop measurement and the overbar indicates the time-averaged quantities. This equation is similar to the equation 2.2 in section 2.1, where the $|dP/dx|$ is replaced by $\Delta P/l$ and time-average of τ_w and ΔP has been taken (as can be seen from the overbars in equation 3.15).

To conduct the hot-film calibration, data from the pressure transducer and the anemometer are acquired simultaneously through the BSA flow processor for varying mass flow rates. The data rates are typically around 200 Hz and for each mass flow rate, the data are sampled for about 10,000 convective time units (tU_b/h) to obtain well-converged mean values of hot-film voltage and pressure-drop. In physical units, this time corresponds to a few minutes (2-10 minutes), depending on the flow rates. It is important that during the calibration the range of hot-film voltage should cover a significant part of the fluctuations observed during the actual measurement. Therefore, the calibrations are conducted over a large range of hot-film voltages, which is generally acquired over

10-15 calibration points. An example of a hot-film calibration is shown in figure 3.15. A 3rd order polynomial is used to fit the calibration points and the calibration equation is given by:

$$\overline{V_L} = a\overline{\tau_w}^3 + b\overline{\tau_w}^2 + c\overline{\tau_w} + d. \tag{3.16}$$

Here a, b, c and d are the calibration constants and $\overline{V_L}$ is the time-averaged voltage obtained from the anemometer. In addition to the 3rd order polynomial, an extended power-law equation is also used to fit the calibration data and a good agreement is found in the instantaneous wall shear stress signals using these two different calibration equations. A comparison of these two calibration relationships will be discussed in detail in chapter 4. Further details into different types of calibration equations for hot-film/hot-wire anemometry can found in Wu and Bose [1994] and Bruun [1995].

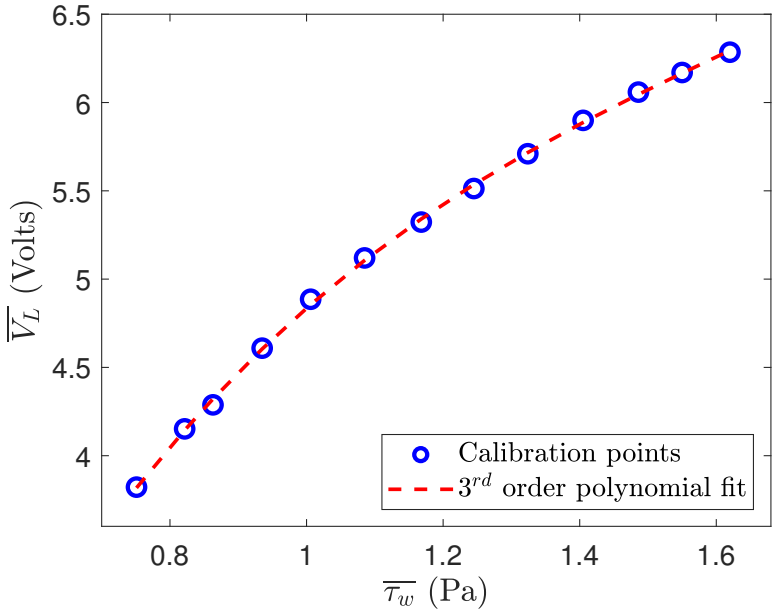

Figure 3.15: Calibration plot of mean hot-film voltage against mean wall-shear stress for $Re_\tau = 61.5$. The calibration curve is fitted with a 3rd order polynomial. The ambient fluid temperature is maintained at $T = 19.10$°C with a precision of ± 0.01°C.

3.5.6 Other challenges in thermal anemometry

The two commonly encountered challenges in CTA are calibration against a known mean value and keeping the calibration drift to a minimum for the entire measure-

ment run. As for the first challenge, many methods have been employed over the past decades for practical and accurate calibration of hot-wire/hot-film probes. For hot-wire measurements in air flows, the hot-wire is calibrated against the mean velocity measured in a known flow. The hot-wire can be calibrated with a purpose-built calibration device or, *in-situ* where, for example, a hot-wire may be calibrated in the free-stream of a wind tunnel against the mean velocity measured by a Pitot-Static tube pair [e.g. Hutchins et al., 2009]. Calibration of hot-film wall shear stress sensors are also commonly conducted against the mean measured pressure-drop along the streamwise direction for fully developed channel [e.g. Whalley et al., 2019] and pipe flows. Although these calibration procedures work well in providing the respective time series of velocities or wall shear stresses, there are still many examples where the calibration of sensors is either inaccurate or quite challenging. For example, in many external flows (e.g. turbulent boundary layer), correlations such as the Clauser chart are required to calibrate hot-films [Hutchins et al., 2011]. As stated before, another commonly encountered challenge in thermal anemometry is to keep the calibration constant for the entire measurement run. The calibration drifts which are commonly observed can be attributed to temperature change [Comte-Bellot, 1976, Perry, 1982], commonly referred to as thermal drift or non-thermal drifts which can be caused by various reasons such as contaminant deposition on the sensing element [see, for example Collis, 1954, who studied the effect of dust on hot-wires]. Correction of thermal drifts has been investigated using various techniques in the past [see, for example: Collis and Williams, 1959, Cimbala and Park, 1990, Bruun, 1995, Tropea and Yarin, 2007, Benjamin and Roberts, 2002, Hultmark and Smits, 2010]. But, only a few works have been done to correct for the non-thermal calibration drifts in thermal anemometry [Durst et al., 1996, Talluru et al., 2014, Nekrasov and Savostenko, 1991]. In this work, an attempt is made to address the issues related to the challenges in calibrations and correcting for the non-thermal calibration drifts by investigating a novel technique which is based on non-linear regression. This investigation will be discussed in detail in chapter 4.

3.6 Flow visualization

Flow visualization is one of the most direct techniques to study the flow structure in wall-bounded flows. The first well-known experimental study in fluid mechanics was carried out by Reynolds [1883] where he employed flow visualization using dye to investigate laminar-turbulent transition in pipe flows. Since then, numerous researchers have employed flow visualization as a tool to investigate the transition process in wall-bounded flows. In planar channel flows, some of the previous studies where flow visualization is used for the study of the transition process in channel flow are Carlson et al. [1982], Alavyoon et al. [1986], Tsukahara et al. [2014], and Sano and Tamai [2016].

Flow visualization is conducted using a planar laser sheet and a DSLR camera to image the flow. The side-wall of the test section is used to send the laser sheet into the channel and the top-wall is used to image the flow. The laser pointer made by MegaLaser (UK) is used in this study. Using a plano-concave lens, a very thin sheet of light ($\approx$ 1mm thickness) is created with a divergence of about 35^{o}. The intensity of the light is 902 mW, as provided by the manufacturer. The laser is powered by rechargeable power supplies. It is a hand-held laser pointer and therefore it was required to make a holder for this laser in order to acquire a stable laser sheet for long-time, high-quality measurements. A holder, made of Delrin, is designed and built for the laser pointer to keep it in the same traverse as the LDV transmitting optics. The laser pointer, positioned in the holder, can then be moved using the traverse. The laser pointer can provide light for up to about 15 seconds at one time due to the limited power of the laser power supply. Timiron Supersilk particles, the same as used for LDV measurements, are added in the fluid as reflecting particles. The green-coloured laser sheet from the laser pointer enters the test section from the side-wall. It is carefully checked that the laser sheet enters the test section horizontally such that it is well-aligned with the streamwise/spanwise plane of the channel.

To capture the flow motion, Nikon Digital SLR Camera D5200 with AFMicro Nikkor 60 mm lens is used. The camera is used in the "movie" mode at the maximum frame

rate of 50 fps where the frames have a dimension of 1920×1080 pixels. The camera is positioned using a tripod such that the flow can be recorded from the top glass of the test section. The camera is also well-aligned such that it is facing vertically down without any unwanted tilts in other directions. To convert the dimensions of the recorded frames into physical units a grid paper of resolution 1 mm $\times$ 1 mm has been utilized. Prior to the measurement, the grid paper is placed on the bottom wall of the test section (in the empty channel) to obtain the conversion factor for the dimensions. Once the conversion factor is obtained, the grid paper is removed, and the channel is refilled with the working fluid for the visualization. The flow visualization has been carried out at a wall-normal location of $y/h = 0.4$. Figure 3.16 shows a schematic of the laser sheet employed and a typical snapshot of the flow using flow visualization. It was observed that the image plane of the camera is larger than the region illuminated by the laser in the flow. Therefore, only the part of the image plane which is well-illuminated using the laser light is shown and are used for the investigation of the flow structure during transition in the channel flow facility.

The videos of the flow recorded are processed in MATLAB using inhouse codes. Images are extracted from each video based on the current frame rate of 50 fps. The images, originally coloured, are converted in greyscale prior to processing. To obtain the flow structures, the frames are stitched together along the streamwise direction. To stitch the frames, only the most illuminated area of the frame is chosen. The approximate frame rate (FR) to stitch the frames is based on the streamwise length of each frame and the convective velocity of the flow. To carry out the stitching of the frames along the streamwise direction, every frame is cropped such that the streamwise length of each frame is $0.7h$. The bulk velocity (U_b) is used as the approximation for the convective velocity. A median filtering has also been carried out to minimize the artifacts related to the stitching of frames to obtain an approximately "continuous flow" structure.

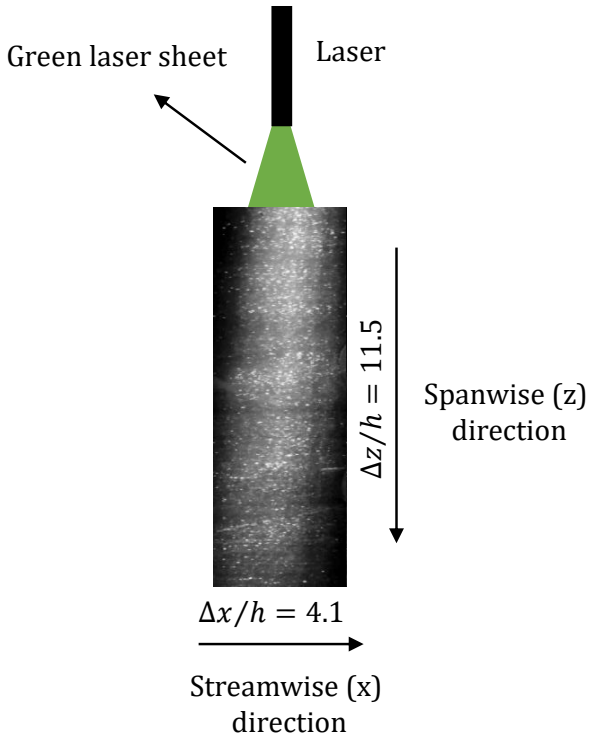

Figure 3.16: Schematic of the laser sheet along with a typical snapshot of the flow. The snapshot is cropped to focus only on the well-illuminated region due to the laser sheet. The image, originally acquired as coloured, has been converted to grey scale.

3.7 Uncertainty analysis of experimental data

Kline and McClintock [1953] provided a method for conducting an uncertainty analysis which states that if the measured quantity ϕ depends on independent variables by the following relation:

$$\phi = X_1^a X_2^b X_3^c X_4^d ... X_M^m \tag{3.17}$$

then the uncertainty in ϕ, i.e. $\Delta\phi$, is given by the following equation

$$\frac{\Delta\phi}{\phi} = \pm\left\{ \left(a\frac{\Delta X_1}{X_1}\right)^2 + \left(b\frac{\Delta X_2}{X_2}\right)^2 + \left(c\frac{\Delta X_3}{X_3}\right)^2 + \cdots + \left(m\frac{\Delta X_M}{X_M}\right)^2 \right\}^{1/2} \tag{3.18}$$

This equation is used for the uncertainty estimation for all the measured quantities obtained using different instruments. These estimates are discussed below.

The Druck LPX-9381 pressure transducer has an accuracy of ±5 Pa, as quoted by

the manufacturer. The measured pressure-drop from the transducer is used to calculate the mean wall shear stress using equation 3.16. The employed channel-flow facility is carefully machined to provide negligible relative uncertainties ($\approx 0.15\%$) in the channel dimensions (w and h) and the length between the pressure tappings, l. Therefore, the relative uncertainty in the mean wall shear stress is $\Delta\tau_w/\overline{\tau_w} = 2-5\%$.

The density (ρ) of the working fluid is measured using an Anton Paar DMA 35N density meter which has a quoted accuracy of ± 1 kg/m^3. This gives the relative uncertainty in the density of the working fluid as $\Delta\rho/\rho = 0.09\%$. The quoted relative error in the Promass flow meter is $\Delta\dot{m}/m = \pm 0.05\%$. This gives the uncertainty in bulk velocity ($U_b = \dot{m}/2\rho wh$) calculation as $\Delta U_b/U_b = 0.2\%$. The relative uncertainty in the viscosity (μ) measurement of the working fluid using Anton Paar MCR 302 rheometer is $\Delta\mu/\mu = 2\%$. Therefore, the relative uncertainty in the Reynolds number ($Re_h = U_b h/\nu$) is $\Delta Re_h/Re_h = 2.02\%$

The relative uncertainty in the friction velocity ($u_\tau = \sqrt{\tau_w/\rho}$) is $\Delta u_\tau/u_\tau$ = 1-2%. This gives an uncertainty in the friction Reynolds number ($Re_\tau = u_\tau h/\nu$) measurement as $\Delta Re_\tau/Re_\tau$ = 3-4 %. Friction factor ($f = \tau_w/0.5\rho U_b^2$) has a relative uncertainty of $\Delta f/f = 2-5\%$

The major sources of error in LDV data are due to velocity gradient broadening, velocity bias effect or fringe distortion [Zhang, 2010]. These combined effects, in general, give the relative uncertainties in the mean velocity of 2-3% and the turbulent intensities of 4-6%. In inner units, the relative uncertainties in the mean velocities and turbulent intensities are $\Delta U^+/U^+$ = 3-5% and $\Delta\sigma(u')^+/\sigma(u')^+$ = 5-8%. The traverse of transmitting optics for LDV has a precision of 0.001 mm, providing the relative uncertainty in the wall-normal position (y) measurement, close to the wall ($y = 0.5$ mm), to be $\Delta y/y = 0.2\%$. In inner units, at this wall-normal location, y^+ has an uncertainty of $\Delta y^+/y^+$ = 3-4 %.

3.8 Flow conditioning

It is important to make sure that the flow conditions inside the channel are optimum to make useful measurements i.e. the measurement location should be free of any side-wall or flow development length effects. An attempt is made here to check for both issues and is discussed below.

3.8.1 Side-wall effects

The presence of secondary flows near the corners of the side-walls in channel-flows is well-known in the literature. These secondary flows are sometimes also referred to as Prandtl's secondary motion of the second kind [Prandtl, 1953]. Although these secondary motions are much weaker than the streamwise component of the flow, they are strong enough to influence the statistics of the flow [Bradshaw, 1987]. Therefore, it is pertinent to check the effect of side-walls on the flow statistics for the used channel-flow facility. To check the effect of side-walls, streamwise velocity profiles for $Re_\tau = 78$ ($Re_h = 1116$) are measured for spanwise locations of z/h of 2 to 8 for a constant streamwise location of $x/h = 496$. It is emphasized here that all the velocity profiles reported in this thesis are measured for the bottom half of the channel unless stated otherwise. It was confirmed that the velocity profiles measured for the bottom-half and the top-half provide similar results, as expected due to symmetry of the flow along the channel centerline. The measurement is carried out using LDV by first traversing the measurement volume to the specified spanwise location. Then the streamwise velocity profile is measured from the bottom wall to the channel centerline by traversing the laser head in the wall-normal direction. Each wall-normal location is sampled for around 300 seconds at an average data rate of about 100 Hz. This provided sufficient data (around 30,000 velocity samples) to obtain a statistically-converged mean of the velocity data. Figure 3.17 shows the variation of streamwise velocity with wall-normal locations for various spanwise distances. Here, the streamwise velocity (U) is normalized by the bulk velocity (U_b) and the wall-normal distance (y) is normalized by the channel half-height (h). From figure 3.17 it can be seen that the velocity profiles approximately collapse after a spanwise distance of $4h$. An additional measurement of velocity profile

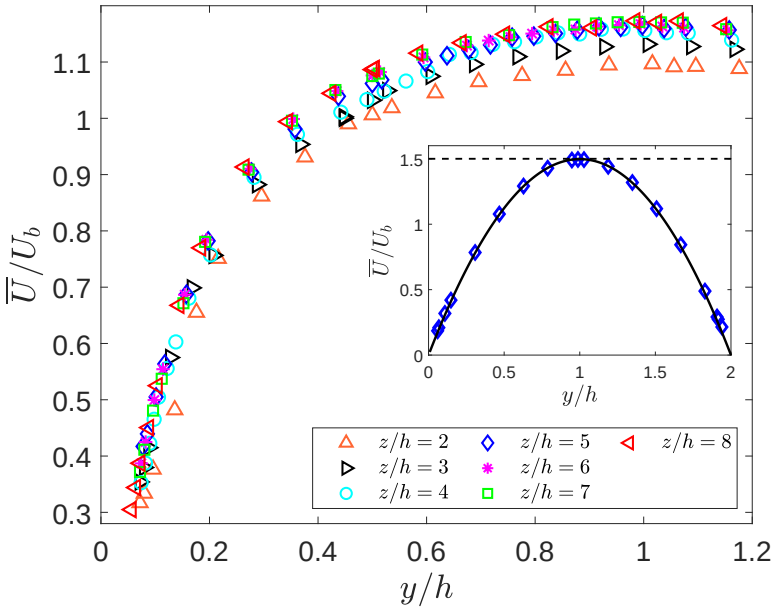

Figure 3.17: Normalized streamwise velocity profiles for $Re_\tau = 78$ ($Re_h = 1116$) for spanwise locations varying from $z/h = 2$ to $z/h = 8$. Inset shows the velocity profiles obtained for an experiment in a laminar flow (blue diamonds) for $Re_\tau = 39$ ($Re_h = 498$). Solid black line and dashed black line indicate laminar theoretical profile and constant value of 1.5, respectively.

is conducted for laminar flow for $Re_\tau = 39$ ($Re_h = 498$) at $z/h = 5$ and is shown in the inset of figure 3.17. This plot shows the velocity profile measured over the entire height ($2h$) of the channel. The inset plot shows that there is a good agreement between the velocity profile with the laminar theoretical profile. A DNS study by Vinuesa et al. [2015] shows the effect of side-walls in channel-flows by calculating the kinetic energy of secondary flows for $Re_\tau = 180$. This kinetic energy is shown to approximately decay to zero after $z/h = 4$. Thus, a spanwise location of more than $5h$ from the side-wall can be considered to have a negligible side-wall effect in the employed flow facility. Measuring at this spanwise location also gives an opportunity to measure the wall-normal velocity using LDV closer to the bottom wall without having any side-wall effects. Therefore, unless stated, in the rest of this thesis velocity measurements have been carried out at a spanwise location of $z/h = 5$.

3.8.2 Development length effects

In this study, the channel-flow should be free of any inlet effects, which means that the measurements should be conducted in the so-called "fully-developed" region of the flow

[Durst et al., 2005]. Investigation of development lengths in laminar and fully-turbulent channel flows has been studied by many researchers in the past. Durst et al. [2005] proposed a correlation for the calculation of development length in laminar channel-flows using a numerical technique. Dean [1978] compiled data from the previous experiments in channel flows and found that the entry length varies from $46h$ to $600h$. Lien et al. [2004] recommended the development length to be $300h$ using velocity profile measurements in turbulent channel flow. The effect of development length on pressure-drop measurements near the transitional channel flows has still not been reported in the literature. This investigation is important because the flow near transition has been shown to be spatially inhomogeneous and therefore the definition of development length during the transition process becomes ambiguous. In this study, pressure drop-measurements are used to calculate the mean wall shear stress, which is then used for the hot-film calibration to obtain instantaneous wall shear stress data. Therefore, an attempt is made here to study the development length effects in the channel flow facility with the focus being on the transitional Reynolds numbers.

Inlet effects in this flow facility are investigated using pressure-drop measurements over different streamwise distances. The Reynolds number (Re_h) is varied between 515 and 1460 for this study. Pressure-drop measurements are conducted for four different upstream pressure taps $L_{us}/h = 120$, 216, 312 and 408 while the downstream pressure tap is kept at a constant location of $L_{ds}/h = 572$, where L_{us} and L_{ds} represent the distance of the upstream and downstream pressure taps from the channel inlet, respectively. Fanning friction factor ($f = \overline{\tau_w}/0.5\rho U_b^2$) is calculated from the mean wall shear stress ($\overline{\tau_w} = \overline{\Delta P} w(2h)/(2l(w+2h))$, where $\overline{\Delta P}$ is the mean pressure-drop over length (l). The laminar theoretical value for the Fanning friction factor, i.e. $f = 6/Re_h$ can be obtained using the assumption that the flow is parabolic for the laminar flow. Figure 3.18(a) shows the variation of f with Re_h for various locations of upstream pressure taps and figure 3.18(b) shows the relative error of f compared to the laminar theoretical values ($(f - 6/Re_h)/(6/Re_h)$) with Re_h for various locations of upstream pressure taps. The empirical correlation obtained by Dean [1978], based on an extensive litera-

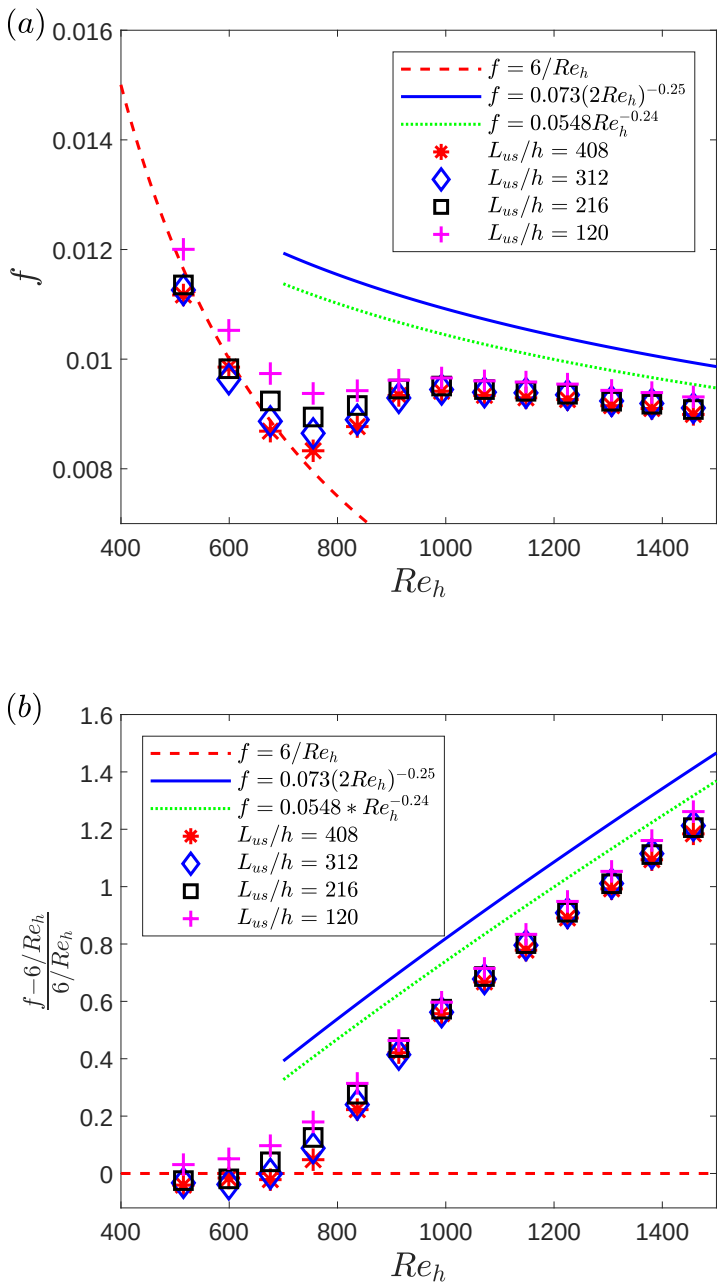

Figure 3.18: (a) Fanning friction factors against Reynolds number for different locations of upstream pressure tap. Red dashed line represents theoretical laminar friction factor. Green dotted line and blue solid line show the correlations obtained from Pope [2000] and Dean [1978], respectively. (b) Variation of the fractional error in the friction factor from the theoretical laminar friction factor with the Reynolds number for different locations of upstream pressure tap. Symbols and lines represent same quantities as in (a).

ture review, for turbulent channel flows is shown for comparison. Pope [2000] obtained an approximate relation between the length scales of mean flow and viscous flow for turbulent channel flow, given by $Re_\tau \approx (2Re_h)^{0.88}$. This relation is converted to obtain a relation between f and Re_h and is shown in figure 3.18. There are two effects which are both playing a role in the variation of the Fanning skin-friction coefficient (f) with L_{us}/h for the same bulk Reynolds number (Re_h) as shown in figures 4(a) and 4(b). First is the flow-development region which is generally associated with the streamwise length required for the flow to become fully-developed [Durst et al., 2005]. It can be seen that for a streamwise distance of the upstream pressure tapping of $L_{us}/h = 120$, f is significantly higher than for $L_{us}/h \geq 216$ for $Re_h \leq 600$. As will be discussed in chapter 5, the flow remains laminar up to $Re_h \approx 610$ in the channel flow facility. This suggests that for the Reynolds numbers when the flow is laminar, for the streamwise distance of $L_{us} = 120h$ the flow is still developing and after $L_{us} = 216h$ the flow can be considered to be fully-developed.

Second is the effect of spatial inhomogeneity of the flow for the transitional Reynolds numbers [Carlson et al., 1982, Sano and Tamai, 2016] which has a significant effect on the friction factor for $600 \leq Re_h \leq 1000$. From figure 4(a,b) it can be seen that after $Re_h \approx 600$, f becomes more sensitive to L_{us}/h as f keeps decreasing with increasing L_{us} and for $Re_h \approx 770$ the difference are most significant. This behaviour can be attributed to the presence of large-scale intermittencies generally associated with spatially inhomogeneous structures near the onset of transition. For example, Carlson et al. [1982] and Sano and Tamai [2016] showed that near the critical Reynolds number artificially-generated finite amplitude perturbations grew or decayed (based on the Reynolds number) as they moved downstream. Therefore, the turbulent structures which are present at the inlet near the critical Reynolds number may decay as they flow downstream and thus reduce the value of f for higher L_{us}, as f is lower for laminar flow compared to turbulent flow for the same Re_h. After $Re_h \approx 770$, the effect of these large-scale intermittencies during transition starts to decrease gradually and after $Re_h \approx 1000$, the friction factor values start to collapse for $L_{us}/h \geq 216$. Thus, it can

be said that it is difficult to define a "development length" (i.e. when the flow becomes independent of x) during transition which by its very nature is spatially inhomogeneous (i.e. the flow necessarily varies in x). Based on the above discussion, the farthest streamwise location of $L_{us}/h = 408$ is chosen for the pressure-drop measurements in this study. It is also observed that the friction factor values do not seem to collapse for the $Re_h \approx 1400$ to the results given by Dean [1978] and Pope [2000]. This is believed to be the consequence of low Reynolds number effects as Dean [1978] also observed a large scatter in the data for similar Reynolds numbers and after $Re_h = 3000$ the empirical correlation worked well in being an accurate description of the skin-friction for channel flows.

Chapter 4

Minimizing recalibration in thermal anemometry

4.1 Introduction

As discussed in § 3.5.6, two of the major challenges in thermal anemometry are the calibration of the sensor against a known value and maintaining the calibration for the entire experimental run. In this chapter, a new method to minimize recalibration in thermal anemometry using a non-linear regression technique is investigated. This method finds potential applications in cases of correcting for non-thermal calibration drifts in long measurements and scenarios where direct calibration of the hot-films or hot-wires is not possible or suffers significant uncertainties. The essential input for this technique is the *a priori* knowledge of the first three or four moments of velocity or wall shear stress for a given Reynolds number. These can be obtained from a separate database (experimental or numerical) in cases where this technique is used as an alternative to direct calibration, or from a previous or simultaneous set of experiments when correcting for non-thermal calibration drifts. Using this input, the coefficients for the assumed calibration functional form can be obtained by an error minimization process. Illustrative results are shown for channel flows where glue-on hot-film probes and hot-wire probes are used for wall shear stress and streamwise velocity measurements, respectively. The hot-film wall shear stress data are obtained from the present

channel flow facility as described in § 3.5. The hot-wire velocity data are taken from Ng et al. [2011]. There is found to be a good agreement between the velocity and wall shear stress obtained using regression and prior calibration, which is confirmed using both time history and probability density function (PDF) plots. Sensitivity to the form of calibration relationship, the number of moments and number of samples required for the regression are conducted. Through examples, it is observed that this method works well in estimating the data when moments obtained from a numerical database are used and also works well in correcting for non-thermal calibration drifts. This technique is also shown to work well for the estimation of data from the voltage signals if moments are available for a Reynolds number "close" to, but not the same as, the measured Reynolds number. One additional potential scenario for application related to the measurement in external flows is then discussed.

The results and discussion presented in this chapter have formed the basis for recently published paper:
"Minimizing recalibration using a non-linear regression technique for thermal anemometry", *Experiments in Fluids* 60:116, 2019
R Agrawal, R D Whalley, H C H Ng, D J C Dennis and R J Poole

4.2 Non-linear regression technique

This technique is based on an error minimization method where the error between the *a priori* known moments and the moments obtained after providing the raw voltage and the initial guess for the calibration coefficients are minimized. The first four moments used in this technique are defined as follows: mean, $\overline{q}$, is the arithmetic average of the quantity q ('U' for velocity and 'τ_w' for wall shear stress), RMS, $\sigma(q')$, is the root mean square of the fluctuation about the mean $q' = q - \overline{q}$, and skewness and flatness are given by $S(q') = \overline{q'^3}/\sigma(q')^3$ and $F(q') = \overline{q'^4}/\sigma(q')^4$, respectively. The function to be minimized is the sum of squares of relative errors in the first four moments, as shown below

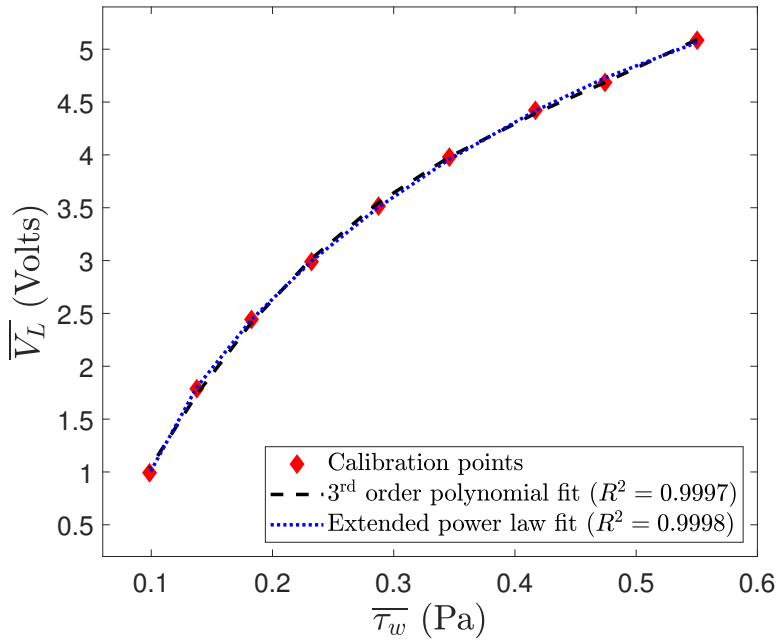

Figure 4.1: Calibration plot of mean hot-film voltage against mean wall-shear stress for $Re_\tau = 180$. The calibration curve is fit with a 3$^{\text{rd}}$ order polynomial and an extended power law. The ambient fluid temperature is maintained at T = 20.80 °C with a precision of ± 0.01 °C.

$$E = \left(1 - \frac{\overline{q_r}}{\overline{q_t}}\right)^2 + \left(1 - \frac{\sigma(q')_r}{\sigma(q')_t}\right)^2 + \left(1 - \frac{S(q')_r}{S(q')_t}\right)^2 + \left(1 - \frac{F(q')_r}{F(q')_t}\right)^2. \tag{4.1}$$

Subscript *'t'* shows the "true" moments which simply denote the known moments. Subscript *'r'* shows the moments calculated using regression. Two different functional forms of calibration, i.e. 3$^{\text{rd}}$ order polynomial ($\overline{V_L} = a_1\overline{q}^3 + b_1\overline{q}^2 + c_1\overline{q} + d_1$) and extended power law ($\overline{V_L}^2 = a_2\overline{q}^{2d_2} + b_2\overline{q}^{d_2} + c_2$) are investigated in this study. Here, $\overline{V_L}$ represents the mean output voltage. A detailed description of the hot-film calibration carried out in the present study is discussed previously in § 3.5.5. Figure 4.1 shows an example of the hot-film calibration where a 3$^{\text{rd}}$ order polynomial and an extended power law are used to fit the calibration points. It is observed that both calibration forms work well in fitting the calibration points.

The inputs for this regression technique are the raw voltage from the anemometer, the "true" moments and the initial guess for the calibration coefficients. To calculate

the moments, the coefficients are input as variables and the time history of velocity or wall shear stress and its first four moments are calculated. Moments are substituted into equation 4.1 and the error function (E) is calculated. First, the error is calculated based on the initial guess for the coefficients given by the user. If the error is more than the tolerance threshold, then a new set of coefficients is calculated using non-linear regression. In this study, MATLAB's fmincon, a nonlinear programming solver, is used to calculate the new values of the calibration coefficients using the default interior point algorithm. This is an iterative algorithm where the non-linear regression keeps iterating until the error is below the tolerance threshold. Further details about this algorithm can be found in Dennis and Schnabel [1996]. Once the error is below the tolerance threshold, the obtained (final) calibration coefficients are used to generate the regressed time history of velocity or wall shear stress. A simple step-by-step flowchart of the method is as shown in figure 4.2. Good initial guesses for the coefficients and a low tolerance threshold for the minimization, as with all other optimization techniques, are important parameters and need to be appropriately considered. The validity of the presented technique is confirmed by using other standard minimization methods such as Solver in Excel, which produced very similar results.

4.3 Sensitivity analysis

To check the robustness of this technique, an exhaustive sensitivity analysis is conducted for the wall shear stress data obtained at $Re_\tau = 180$ in the channel flow facility. This is conducted using a reference hot-film data, acquired at a location of HF2 ($x/h = 496$ and $z/h = 5$), which did not display any significant non-thermal drift. A time history of voltage data was obtained with a length of about $tU_b/h \approx 40000$. This voltage data was converted to instantaneous wall shear stress via calibration against pressure drop data. The "true" or "known" moments were then obtained from this instantaneous wall shear stress. The sensitivity analysis studies the effects of type of calibration relationships, number of moments used for regression and length of time series used are investigated. Later in this section, the effect of Reynolds number on the presented technique is also shown by investigating for two other Reynolds numbers $Re_\tau = 61$ and 84.

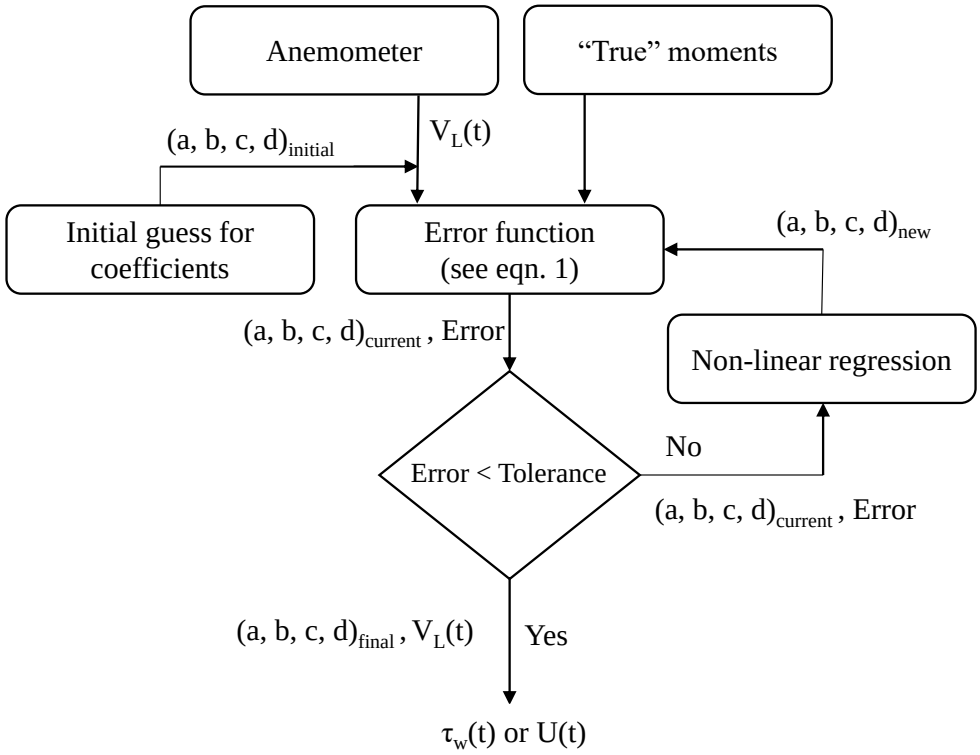

Figure 4.2: A flowchart showing the various steps of this non-linear regression technique. Here, (a, b, c, d) are the calibration coefficients based on the 3rd order polynomial fit.

4.3.1 Calibration relationships

As stated before, the two commonly used calibration equations for thermal anemometry are 3rd polynomial and extended power law Table 4.1 shows the comparison of the moments obtained from the calibration and using the regression for wall shear stress measurements at $Re_\tau = 180$. It can be observed that there is an excellent agreement between the moments obtained from calibration and non-linear regression using the two different functional forms which confirms that this technique performs well in recovering the "true" moments. Fifth and sixth order moments, which are given by $\overline{q'^5}/\sigma(\tau'_w)^5$ and $\overline{q'^6}/\sigma(\tau'_w)^6$, are also calculated and it is observed that there is a good agreement in the moments obtained from regression and calibration till the sixth order. Figure 4.3 shows that there is a good match between the instantaneous normalized wall shear stress fluctuations and their corresponding PDFs obtained using calibration and regression for both calibration relationships where t and U_b represents time and bulk velocity, respectively. The PDF of wall shear stress fluctuations obtained by Sreenivasan and

Table 4.1: Comparison of the first six moments obtained using calibration and regression for $Re_\tau = 180$

Moments	Calibration (3^{rd} order polynomial)	Regression (3^{rd} order polynomial)	Regression (Extended power law)
$\overline{\tau_w}$(Pa)	0.2536	0.2536	0.2536
$\sigma(\tau_w')/\mu(\tau_w)$	0.2677	0.2677	0.2653
$S(\tau_w')$	0.5279	0.5279	0.5279
$F(\tau_w')$	2.8958	2.8956	2.8958
$\overline{q'^5}/\sigma(\tau_w')^5$	4.3040	4.3036	4.3036
$\overline{q'^6}/\sigma(\tau_w')^6$	15.2829	15.2793	15.4870

Antonia [1977] using hot-film in a channel flow facility at $Re_\tau = 289$ is also shown for comparison.

4.3.2 Number of moments used for regression

Sensitivity of the non-linear regression to the number of moments used in equation (4.1) is investigated at $Re_\tau = 180$ for the 3^{rd} order polynomial fit. Regressions are conducted for the cases where errors in the first four, first three and first two moments are minimized. Figures 4.4(a) and 4.4(b) reveal good agreement between the PDFs and time series for the case where the first four and first three moments are employed for the non-linear regression, but if peaks of the PDFs are focussed (shown in the inset plot of figure 4.4(a) it is clear that the first four moments provide more accurate recovery of the PDF. The standard deviation of the error in the predicted time series for the first three moments is found to be $\sim 10^{-4}$ but for the first four moments, it is $\sim 10^{-6}$. Thus, it can be said that both the first three and first four moments work well for the non-linear regression, but for more accurate results, the first four moments should be used.

4.3.3 Number of samples used for regression

In this study, the number of samples is converted to the corresponding non-dimensional convective time units. Before employing the non-linear regression technique, it is neces-

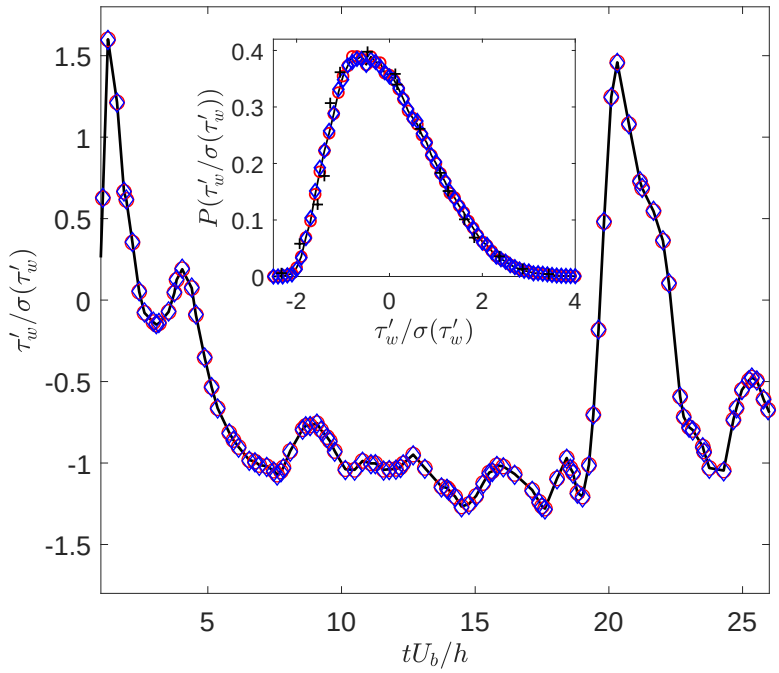

Figure 4.3: Instantaneous normalized wall shear stress fluctuations obtained using a hot-film at $Re_\tau = 180$ where the black line (-), red circles ($\circ$) and blue diamonds ($\Diamond$) show the time history obtained using calibration, non-linear regression for a polynomial fit and non-linear regression for an extended power law fit, respectively. Data shown here are reduced by a factor of 5 for clarity. Inset plot shows PDFs of normalized wall shear stress fluctuations at $Re_\tau = 180$ where the line and symbols are as the main plot. Black plus (+) represent PDF data obtained from Sreenivasan and Antonia [1977] for $Re_\tau = 289$.

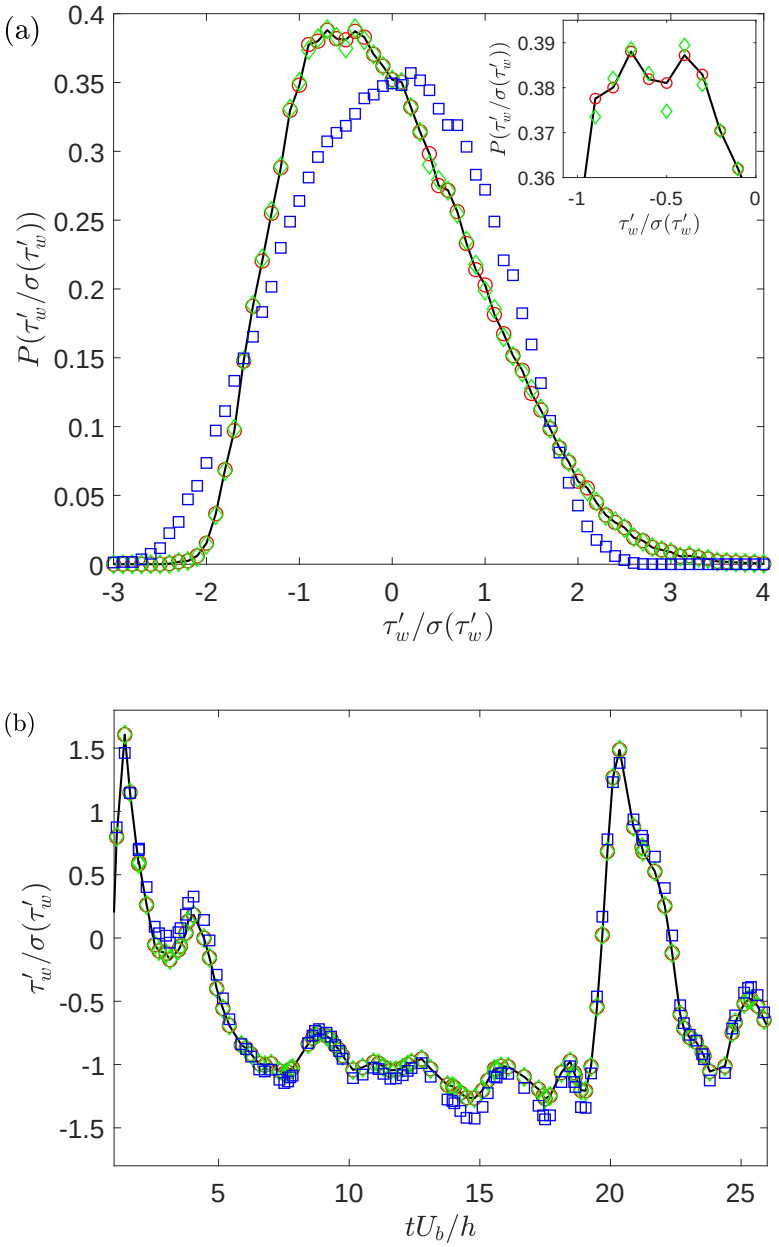

Figure 4.4: (a) PDFs of normalized wall shear stress fluctuations obtained using a hot-film at $Re_\tau = 180$ where non-linear regression is used for a 3^{rd} order polynomial fit. Black line ($-$) shows the PDF obtained using calibration and the red circles ($\circ$), green diamonds ($\diamond$), blue boxes ($\square$) show the PDFs obtained when the first four, first three and first two moments are used for the minimization of equation (4.1), respectively. (b) Instantaneous wall shear stress fluctuations where the line and symbols are as in figure 4.4(a). Data shown here are reduced by a factor of 5 for clarity.

sary to check the statistical convergence of the first four moments which will be used for the regression, as this technique heavily depends on the first four moments. To do this, the entire time series is broken into smaller time segments for various convective times ranging from $tU_b/h = 1$ to 40000, where one convective time unit ($tU_b/h = 1$) comprises only 18 data points. The first four moments are calculated for each time interval along the entire length of the time series and then the absolute percentage error is calculated based on reference moments for $tU_b/h = 40000$, and the absolute percentage errors are then averaged. Figure 4.5(a) shows the variation of average absolute percentage errors of the first four moments obtained using calibration for different length of time series. After 10000 convective time units all the four moments are converged within 5% of the moments obtained from the data comprising 40000 convective time units. Thus, the data presented here can be considered statistically converged for $tU_b/h > 10000$. A related, but distinct question is what is the minimum length of time series required for the regression technique to work? To answer this, the entire time series is again broken into smaller time segments, for various convective times ranging from $tU_b/h = 1$ to 40000. The first four moments are calculated for each of the time intervals along the entire length of the time series and then these moments are used for the regression over the same length of time series. The absolute percentage error is calculated between the calibrated and regressed moments, and the absolute percentage errors are then averaged. Figure 4.5(b) shows the average absolute percentage error in the regressed moments for various length of time series. It is observed that the regression works well in recovering the moments for the length of time series above $tU_b/h = 100$. Therefore, making a decision regarding the length of time series necessary should depend mainly on whether the moments are converged; however, it can be seen that non-linear regression technique is quite robust and capable of recovering the 'input' moments even for as small sample size as $tU_b/h = 100$.

4.3.4 Reynolds number effects

The effect of Reynolds number on the regression for wall shear stress measurements in the channel flow is investigated by following a similar approach for two other Reynolds

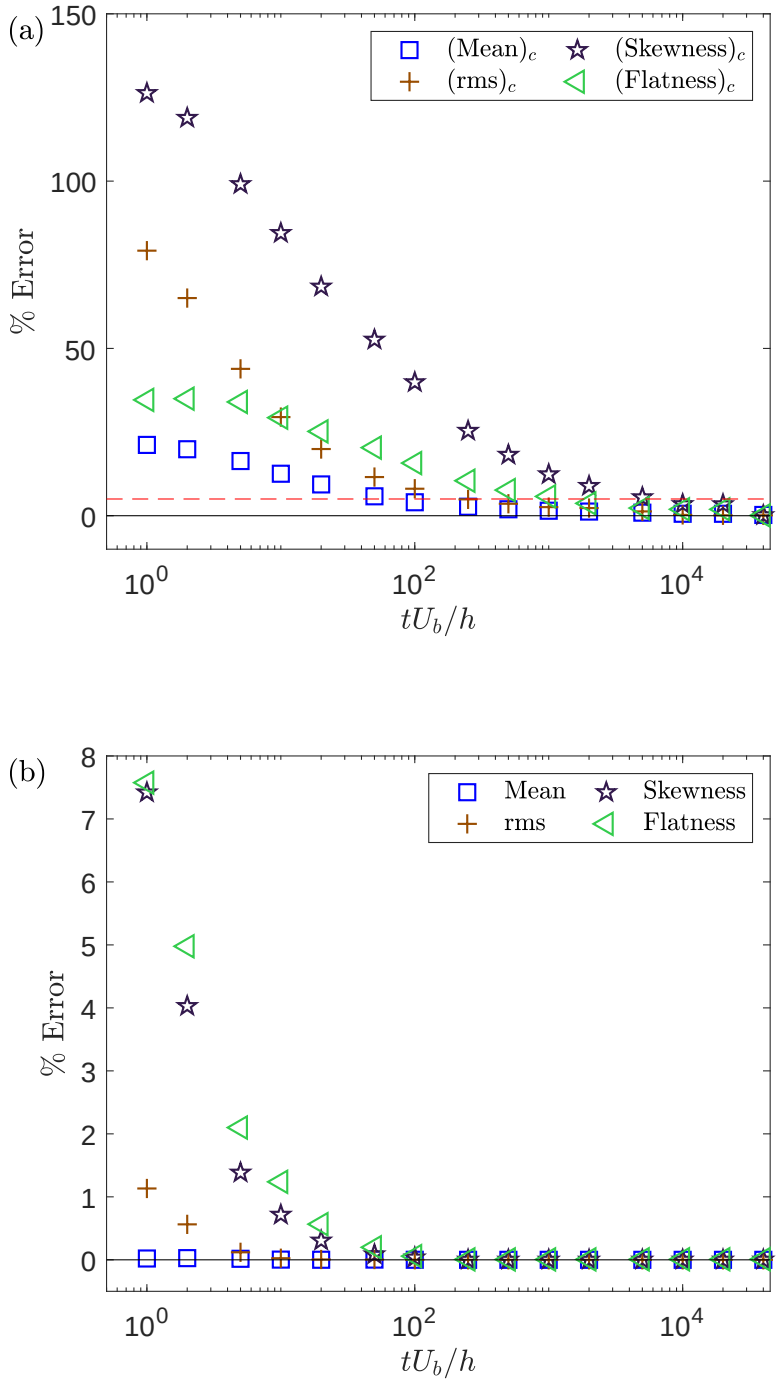

Figure 4.5: (a) Variation of the average absolute % error for the first four moments obtained using calibration for $Re_\tau = 180$ with the convective time over which the measurement is conducted, where the error is calculated using the corresponding moments obtained for highest convective time ($tU_b/h = 40000$). Red dashed line (−−) and black solid line (-) shows the constant values of 5% and 0%, respectively. (b) Variation of the average absolute % error in the first four moments obtained using calibration and regression for various lengths of measurement times. Black solid line (-) shows the constant values of 0%.

numbers $Re_\tau = 61$ and 84. Figure 4.6 shows the instantaneous wall shear stress fluctuations and the corresponding PDFs obtained using calibration and regression for $Re_\tau = 61$ and 84. There is observed to be an excellent agreement for both of these Reynolds numbers which confirms the validity of the presented technique for wall shear stress data obtained in different flow conditions at least over this range of Reynolds number.

4.4 Validation against hot-wire data

An additional study is made to check how well this technique works for an independent test case where a hot-wire is employed for instantaneous velocity measurements at higher Reynolds numbers. Data of streamwise velocity measurements obtained with a hot-wire from a channel flow facility at the University of Melbourne for $Re_\tau = 1053$, reported in Ng et al. [2011] are used. Here, the "true" moments were obtained from the velocity signals measured using a hot-wire probe that was calibrated *in-situ* at the channel centerline against the centerline velocity measured by a Pitot-static probe. The spanwise width of hot-wire probe was $l^+ = 22$ with further details regarding the experimental procedure found in Ng et al. [2011]. Data of velocities for three wall normal locations at $y^+ = 16$, 107 and 1053 for $Re_\tau = 1053$ are investigated.

The procedure used for the regression is briefly explained here. Data were a long time history of raw hot-wire voltage and the corresponding calibrated velocity data for the three wall normal distances at $Re_\tau = 1053$. Firstly, the first four moments are calculated from the calibrated velocity signal and then used for the regression. A 3^{rd} order polynomial calibration relationship was assumed as the fitting function. After running the regression, the predicted calibration coefficients were obtained. These coefficients were then used to reconstruct velocity time series from the hot-wire data. Table 4.2 shows an excellent agreement of moments obtained from calibration and non-linear regression for $Re_\tau = 1053$ at $y^+ = 107$ which further validates this technique in recovering the moments. Segments of the instantaneous normalized streamwise velocity fluctuations and their corresponding PDFs shown in figures 4.7(a) and 4.7(b) respectively, shows that this technique performs well in reconstructing the signal for all three

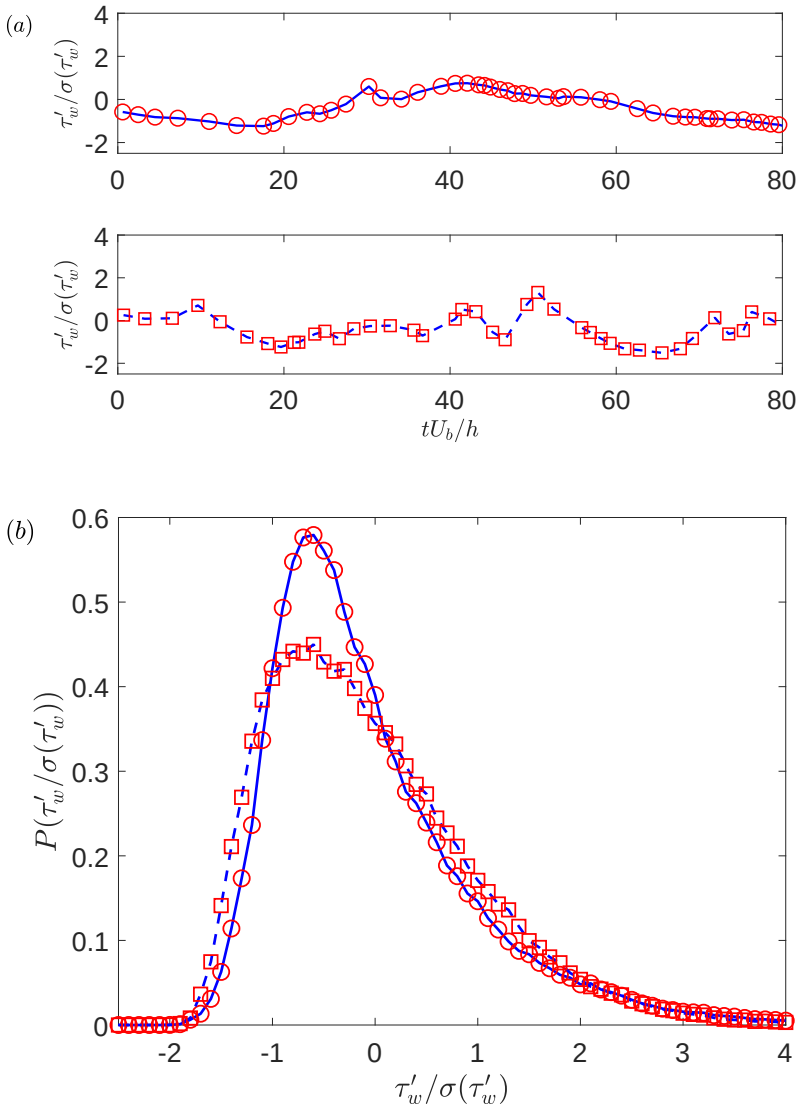

Figure 4.6: (a) (Top to bottom) Instantaneous normalized wall shear stress fluctuations obtained using a hot-film at $Re_\tau = 61$ and 84. Blue solid ($-$) and dashed ($--$) lines show the data obtained from *in-situ* calibration for $Re_\tau = 61$ and 84, respectively. Red circle ($\circ$) and red square ($\square$) indicate the regression data obtained using 3^{rd} order polynomial calibration form for $Re_\tau = 61$ and 84, respectively. Data shown here are reduced by a factor of 12 for clarity. (b) PDF of normalized wall shear stress fluctuations at where various lines symbols represent same quantities as in (a).

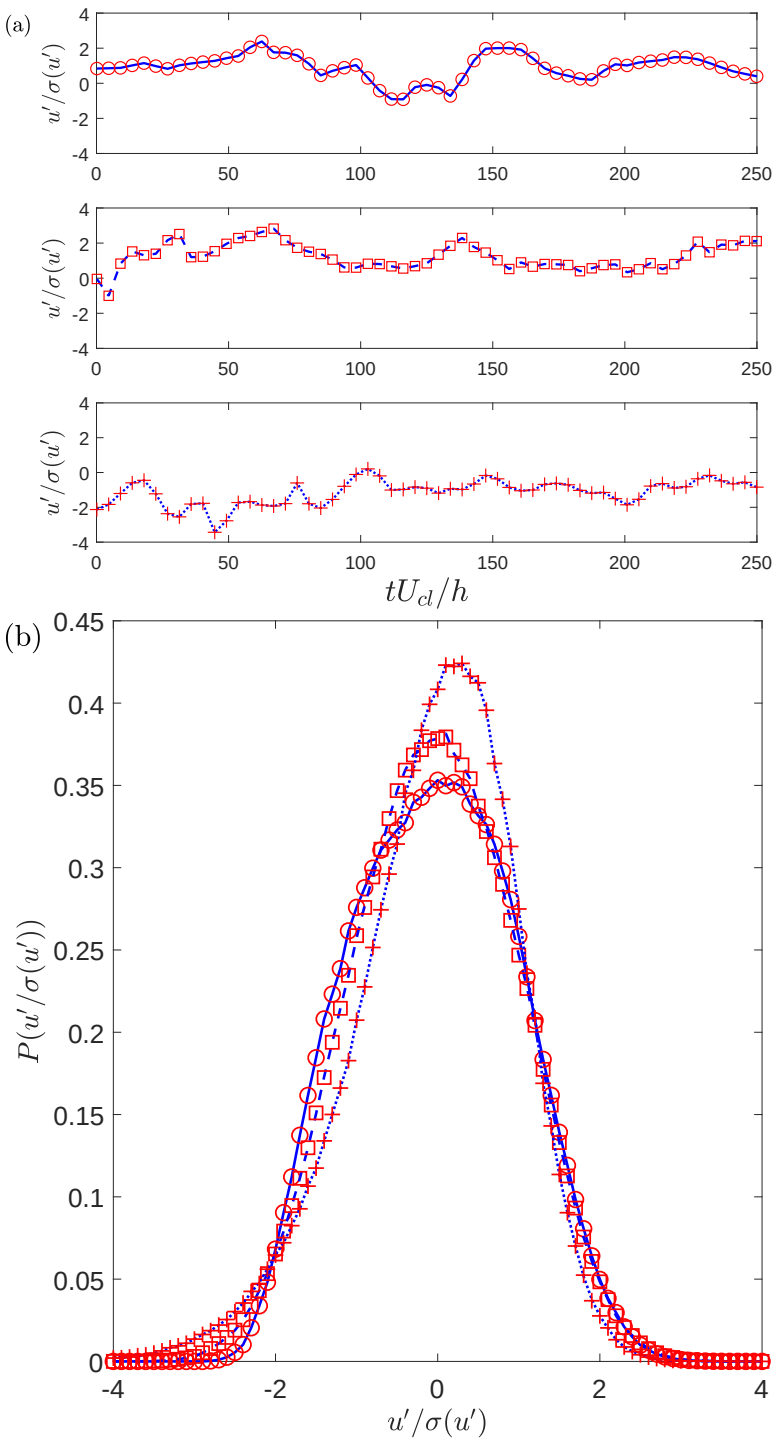

Figure 4.7: (a) (Top to bottom) Instantaneous normalized streamwise velocity fluctuations obtained using a hot-wire at $Re_\tau = 1053$ for $y^+ = 16$, 107 and 1053. Blue solid ($-$), dashed ($--$) and dotted ($\cdot\cdot$) lines show the data obtained from *in-situ* calibration for $y^+ = 16$, 107 and 1053 respectively. Red circle ($\circ$), red square ($\square$) and red plus ($+$) indicates the regression data obtained using 3^{rd} order polynomial calibration form for $Re_\tau = 1053$ at $y^+ = 16$, 107 and 1053, respectively. Data shown here are reduced by a factor of 30 for clarity. (b) PDF of normalized streamwise velocity fluctuations at $Re_\tau = 1053$ where various lines symbols represent same quantities as in (a).

Table 4.2: Comparison of the first four moments obtained using calibration and regression for $Re_\tau = 1053$ at $y^+ = 107$

	Calibration (3^{rd} order polynomial)	Regression (3^{rd} order polynomial)
$\overline{U}$(m/s)	5.3926	5.3926
$\sigma(u')/\mu(U)$	0.1171	0.1171
$S(u')$	-0.0481	-0.0481
$F(u')$	2.6919	2.6933

wall normal locations where U_{cl} represents centerline velocity. Validation against the hot-wire data shows that this technique works for different kinds of flow conditions as the hot-film and hot-wire data shown here have different skewness i.e. $S(\tau_w') > 0$ for hot-film at $Re_\tau = 180$ but $S(u') < 0$ for hot-wire at $Re_\tau = 1053$ at $y^+ = 107$. As it is shown that the non-linear regression technique performs well for hot-film and hot-wire data collected in fully developed channel flow for friction Reynolds numbers between $61 \leq Re_\tau \leq 1053$, it is expected that the non-linear regression technique should continue to perform well at even higher Reynolds numbers as a method for minimizing (re-)calibrations and correcting non-thermal drift. However, it must be noted that this technique is dependent on the quality of the inputs and cannot account for, or correct, measurement resolution issues necessarily encountered at high Reynolds numbers [see, for example, Hutchins et al., 2009].

4.5 Potential scenarios for application

In this section, four potential scenarios for application are discussed where the proposed technique might be useful in practical experiments.

4.5.1 Non-thermal drift in long runs

In this scenario, the use of the presented technique for correcting the data which has suffered non-thermal drifts is investigated. There are two types of cases that are possible in the case of non-thermal drifts: drift from a sensor when simultaneous multi-probe measurements are conducted in the fully-developed region of the flow or drift from the same hot-wire/hot-film sensor during a long measurement. In the former case, since

the measurements are conducted in a fully-developed region, the long-time statistics should be the same for all the sensors. In this section, the (non-thermally) drifted data (most likely due to contaminant deposition) from a hot-film sensor is corrected using the moments acquired from another hot-film, when both sensors were running simultaneously in the fully-developed region of the flow. Long run measurements of wall shear stress were conducted for $Re_\tau = 84$ in the channel flow facility using two glue-on hot-films. Figure 4.8(a) shows the test section with the location of the two hot-films. Both hot-films are located 5 channel half-heights away from the side wall, but hot-film 1 and hot-film 2 are located 496 and 491 channel half-heights away from the inlet, respectively. The long time moments of the wall shear stress should be the same at these two spatial locations. Simultaneous acquisition of data from both hot-films is conducted at a typical data rate of around 250 Hz. Pre and post calibration is conducted with a long run measurement of about $tU_b/h = 10000$. An isothermal condition was maintained for the entire run where the fluid temperature varied only by about ± 0.01 °C. Hot-film 2 is observed to have drifted in the voltage output over time which is an example of non-thermal drift. Figure 4.8(b) shows a pictorial representation of the current scenario. As the drift led to a non-stationary mean voltage value, a first order polynomial was fitted to the data and used to remove the linear trend in the drifted data and then the regression technique was conducted using moments from hot-film 1. Figure 4.8(c) shows the time history of the wall shear stress obtained from the entire run. It can be observed that hot-film 2 has suffered calibration drift prior to the removal of the aforementioned linear trend. From figure 4.8(d) it can be said that the non-linear regression works well in recovering the PDF of wall shear stress from the hot-film which has suffered non-thermal drifts. The standard deviation of the error in the two PDFs is found to be about 0.0048.

Correcting data obtained from a hot-wire/hot-film which has suffered non-thermal drifts are also particularly relevant for the cases where long measurements are required for studying conditional properties of the flow. In the absence of a second probe, this technique can provide an alternative to correct for the non-thermal calibration drifts

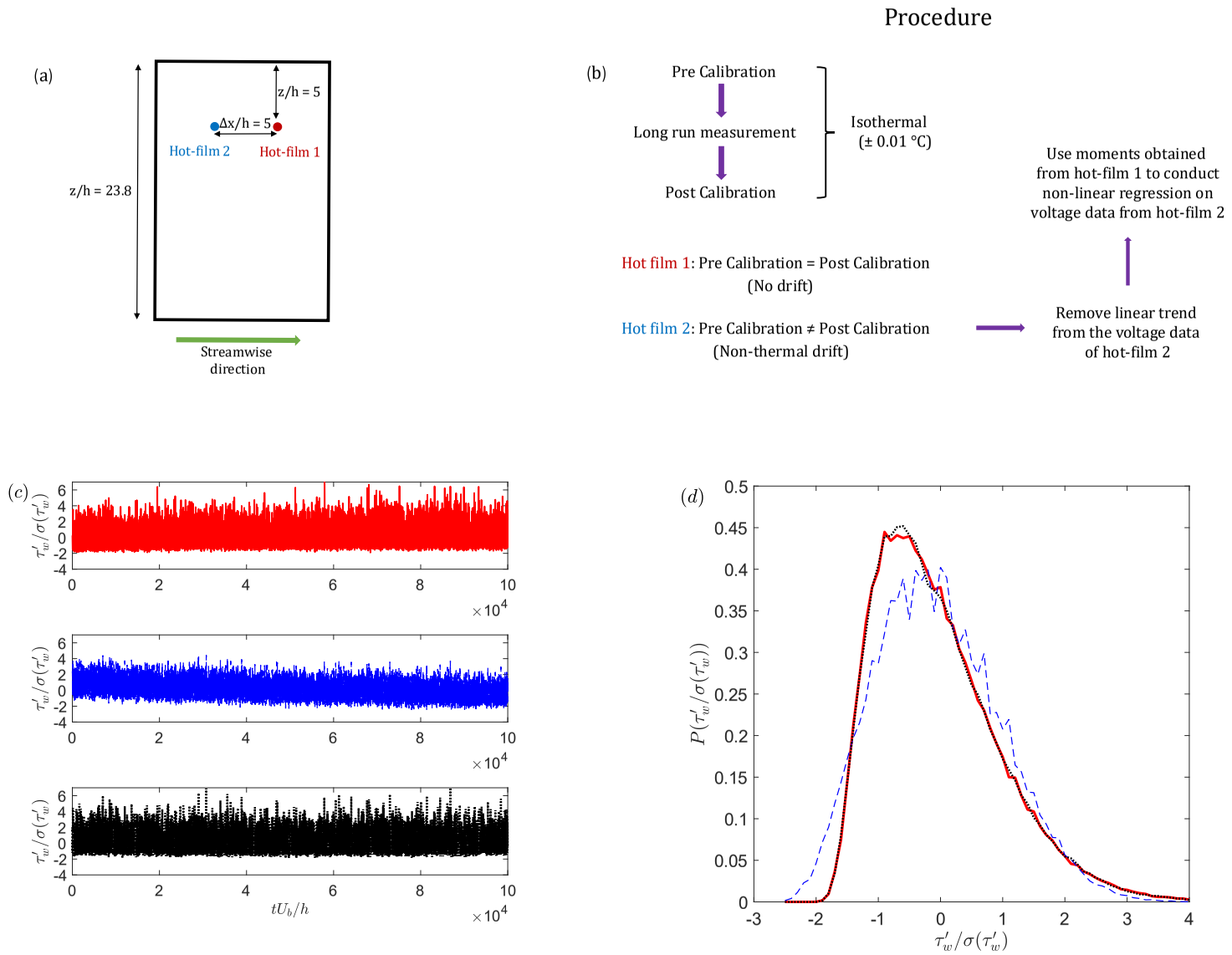

Figure 4.8: (a) Schematic of the test section of the channel flow facility (not to scale); (b) Procedure which is followed in the current scenario; (c) (Top to bottom) Instantaneous wall shear stress fluctuations for $Re_\tau = 84$ obtained using hot-film 1 (–) and hot-film 2 (– –) and the corrected data from hot-film 2 (··). (d) PDF of wall shear stress fluctuations with the lines indicated as in (c).

by taking the moments from the initial long-run measurement, before the non-thermal drift of the sensor becomes significant. Then the obtained moments can be used to correct for the drifted data obtained later for the same flow conditions to reconstruct the velocity or wall shear stress signal. A previous study by Talluru et al. [2014] has discussed a technique to correct for the drift issues in hot-wire anemometry which is applicable for all kinds of drifts (thermal or non-thermal). This technique relies on regular recalibrations of the hot-wire in the free-stream of a boundary layer during the experiment in what they term intermediate single point recalibration (ISPR). Whilst the proposed technique can be useful in minimizing the number of recalibrations performed (in the case of non-thermal drifts), thus saving time, it can also be used on glue-on hot-film probes where the ISPR methodology may not be practical. Correction for humidity effects in air flow (another example of non-thermal drifts) was studied previously by Durst et al. [1996]. Although validity of this correction technique couldn't be checked for humidity effects, because a liquid is used as a working fluid, it is believed that this technique can correct for the humidity effects if the first three or four moments can be acquired *a priori* for similar flow conditions, at lower humidity.

4.5.2 Estimation from numerical database

This non-linear regression technique can be useful in the scenario when a direct calibration is not possible, but the moments for that particular flow can be obtained independently from a numerical database. Using the present technique, an attempt is made here to reconstruct the wall shear stress fluctuations from the hot-film voltage data using the moments obtained from the DNS database of Hu et al. [2006]. The DNS data used is for $Re_\tau = 180$ in a channel flow. Here, the size of the computation box is $L_x \times L_y \times L_z = 24 \times 2 \times 12$ with grid points $N_x \times N_y \times N_z = 256 \times 121 \times 256$ in the x (streamwise), y (wall-normal) and z (spanwise) directions. The streamwise and spanwise grid spacings are $x^+ = 16.88$ and $z^+ = 8.44$, respectively. Further description of the numerical method can be found in Hu et al. [2006]. The moments of wall shear stress obtained from the present experiment and the DNS (and thus the shape of the corresponding PDF) are not equal, even at the same Reynolds number.

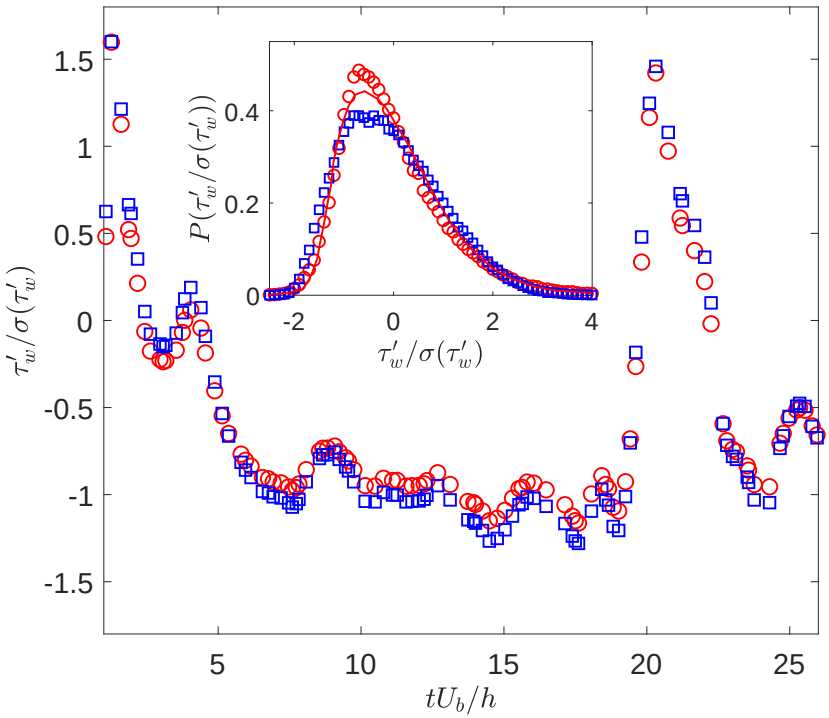

Figure 4.9: Instantaneous normalized wall shear stress fluctuations at $Re_\tau = 180$ obtained using non-linear regression for a 3$^{\text{rd}}$ order polynomial fit where red circle (○) and blue square (□) represent data when the moments were obtained from DNS [Hu et al., 2006] and the present experiment, respectively. Data shown here are reduced by a factor of 5 for clarity. Inset plot shows the PDFs of normalized wall shear stress fluctuations at $Re_\tau = 180$ where symbols represent the same quantities as the main plot. Red line (−) shows the PDF of normalized wall shear stress fluctuations obtained using DNS at $Re_\tau = 180$ [Hu et al., 2006].

This difference in the moments are generally attributed to the spatial and temporal resolution issues of the hot-films and the substrate on which these hot-film are glued [Khoo et al., 2001, Alfredsson et al., 1988b]. Therefore, one should be careful while taking moments from the numerical database and using it for this regression technique to estimate meaningful time history from the raw hot-film voltage data. The method suggested by Chin et al. [2009a] can be a potential way to correct for the differences in the moments through spatial filtering of the DNS data to match the spatial resolution of the sensor. In the current scenario, regression is conducted using a 3$^{\text{rd}}$ order polynomial as the fitting function for the calibration equation where the input to the regression are the moments from the DNS and the measurement. From figure 4.9, it can be seen that the regression technique is able to provide a fairly good estimate of the time histories obtained using two different sets of moments. The inset plot of figure

4.9 shows that the PDF of the wall shear stress fluctuations obtained by DNS is in fairly good agreement with the PDF obtained using DNS except at the peak, which highlights the aforementioned differences between physical experiments and numerical databases. It can be seen that although two different sets of moments are used, this regression technique performs well in providing qualitatively similar wall shear stress signals from the same hot-film voltage data.

4.5.3 Transferability to other Reynolds numbers

Until now, the one condition for this technique to work is the availability of well converged moments for the same Reynolds number. In this scenario, an attempt is made to investigate the robustness of this technique if the moments for Reynolds numbers close to the desired Reynolds number are available. It is tested to see if the wall shear stress signals can be estimated from the hot-film voltage data without conducting an *in-situ* calibration if the moments are available for a different Reynolds number. To make this technique work, the one condition is that for every measurement run there should be one set of measurements done at the same Reynolds number where the moments of wall shear stress are already known. Therefore, using the new hot-film voltage signals and the previously known moments, both at the same Reynolds number, a new set of calibration coefficients can be obtained via regression. And then this set of calibration coefficients can be used for the conversion of voltage to wall shear stress information for another Reynolds number. This hypothesis is based on the assumption that the calibration curve obtained for a particular Reynolds number should also work well for the other Reynolds number.

To validate the accuracy of this hypothesis an illustrative example is discussed here for the wall shear stress measurements conducted in a channel flow facility. Two different sets of measurements are conducted on two different days where on day 1 a long run measurement was conducted for $Re_\tau = 84$ with a pre and post calibration and on day 2 long run measurements were conducted for $Re_\tau = 61$, 73 and 84 again with pre and post calibration, using the same hot-film sensor located at 496 and 5 channel half-

heights away from the inlet and side wall, respectively. An isothermal condition was maintained with a temperature variation of ± 0.01 ^{o}C during the entire experimental run, thus providing negligible differences in the pre and post calibration. Using the moments obtained on day 1 for $Re_\tau = 84$, regression is conducted on the hot-film voltage signal obtained on day 2 for $Re_\tau = 84$ to obtain a new set of calibration coefficients assuming a 3^{rd} order polynomial calibration relationship. Figure 4.10(a) shows the comparison of the calibration curves obtained using regression for $Re_\tau = 84$ and using *in-situ* calibration on day 2. It can be observed that the regression provides a good estimate of the calibration curve except at the lower and higher ends of the curve. The calibration coefficients obtained via regression are used for the estimation of wall shear stress signal for $Re_\tau = 61$ and 73. Figure 4.10(b) and 4.10(c) show the comparison of wall shear stress fluctuations and their corresponding PDFs for $Re_\tau = 61$ and 73. It can be observed that the calibration coefficients obtained using regression for $Re_\tau = 84$ provide a fairly good estimate of the time history of wall shear stress and the corresponding PDFs for $Re_\tau = 73$. Figure 4.10(b) shows a fairly good estimate of the wall shear stress obtained for $Re_\tau = 61$ using the two different aforementioned methods. But figure 4.10(c) shows that for $Re_\tau = 61$, there is less good agreement in the PDFs of wall shear stress obtained using the two different methods. The reason for this less good estimate is clear in the calibration curves of figure 4.10(a). At $Re_\tau = 73$, the data are still within the range where the curves obtained from calibration and regression are very similar, and so the technique works well. At $Re_\tau = 61$, there is a small difference in the curves and hence there is an error in the estimated wall shear stress using the regression technique. Of course, the wall shear stress values indicated for each Re_τ on figure 4.10(a) are the average values and the fluctuations in the flow mean that a range of the calibration curve is being utilized at each Reynolds number. As $Re_\tau = 61$ is at the lower end of this curve, it is evident that high wall shear stress events will likely be recovered well (because they will be in a region of the calibration which is still valid). However, low wall shear stress events will be taking the calibration to the extremity of its validity and therefore produce less accurate results. This interpretation is clearly evident in the PDF for $Re_\tau = 61$ in figure 4.10(c) (and also to some extent in the time

series of figure 4.10b), where at the low wall-shear stress end of the PDF significant differences in the curves from regression and calibration can be seen, whereas at the high wall shear stress end the agreement appears to be much better. It is concluded that this technique works well if the wall shear stress at the new Re_τ is largely within the range of the reference Re_τ. This is to be expected and is true for any calibration technique (i.e. the experiment has to be conducted in the range that the calibration is valid).

4.5.4 Wall shear stress measurements in external flows

The proposed technique can also have applications in external flows where the mean wall shear stress is not a simple function of the mean pressure drop, e.g. zero-pressure gradient turbulent boundary layers. Although there are "direct" measures of mean wall shear stress such as the floating element drag balance and oil film interferometry [see, for example, the review of Fernholz et al., 1996], the Clauser chart probably remains the most commonly used method to calibrate hot-films, which adds uncertainty in the measurement [Hutchins et al., 2009]. In these kinds of flows, or in more complicated external flows (e.g. flow with strong adverse pressure gradient where the Clauser chart and Preston tubes don't work) the presented technique can be of potential use if it is possible to reach the viscous sublayer using an independent measurement technique such as LDV or near-wall hot wire probes at various spatial locations in the flow. Once the moments are known from the velocity gradient data, wall shear stress data can be recovered from the hot-film raw voltage signal using the non-linear regression. In case of investigating the spatial distribution of wall shear stress using simultaneous measurements of multi-sensor probes, the proposed technique can be particularly useful because then a single LDV or other probing devices can be used to measure the moments at various spatial locations and later using multiple hot-film probes, simultaneous measurements can be conducted on those spatial locations.

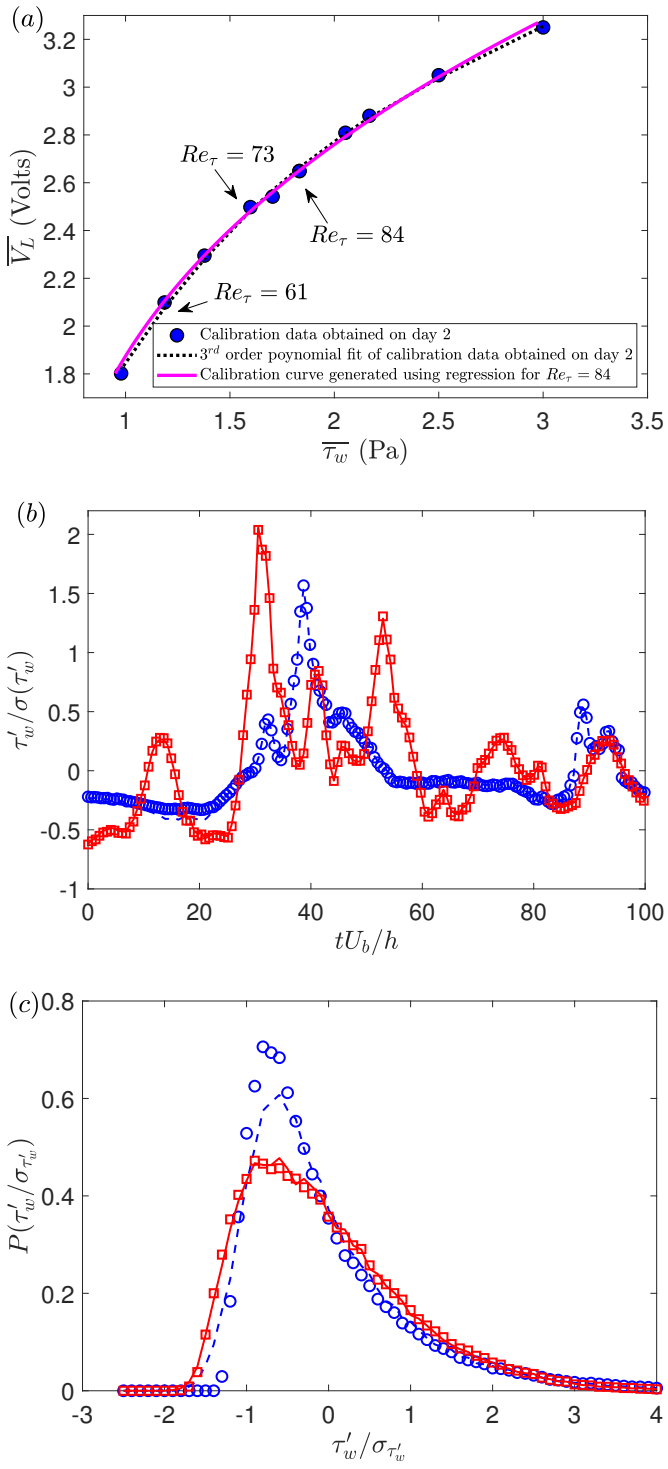

Figure 4.10: (a) Calibration plot of mean hot-film voltage against mean wall shear stress; (b) Instantaneous normalized wall shear stress fluctuations obtained using a hot-film at $Re_\tau = 61$ shown by blue dashed line (−−) and blue circle (○) for calibration equation obtained using calibration and regression based on moments for $Re_\tau = 84$, respectively. Instantaneous normalized wall shear stress fluctuations obtained using a hot-film at $Re_\tau = 73$ shown by red dashed line (−) and red square (□) for calibration equation obtained using calibration and regression based on moments for $Re_\tau = 84$, respectively. Data shown here are reduced by a factor of 5 for clarity. (c) PDFs of normalized wall shear stress fluctuations where the line and symbols are as figure 4.10(b).

4.6 Summary

In this chapter, a new method to minimize the recalibration in thermal anemometry is investigated. This method relies on a non-linear regression technique to predict the calibration coefficients for velocity and wall shear stress data obtained using thermal anemometry measurements. This method is checked against two commonly used calibration equations and for hot-wire and glue-on hot-film datasets. It is seen that using the first three moments for the regression provides a reasonable approximation, but using the first four moments for the regression provides better agreement. This technique can be used to compensate for the non-thermal calibration drifts and thereby reducing the need for continuous *in-situ* post-calibration for long measurements. Moments obtained from a numerical database provide a reasonable estimate of the wall shear stress signal. This technique is also shown to work well if the moments are available at a nearby Reynolds number from a previous measurement. This technique can potentially be used to reconstruct the time series of wall shear stress in situations where direct calibration methods are not readily available, such as in external flows. The present non-linear regression technique is employed in the current study for cases where non-thermal drifts of the hot-film signals were observed during long measurements.

Chapter 5

Intermittencies in transitional channel flows

5.1 Introduction

In this chapter, an experimental investigation of intermittencies associated with the wall shear stress for transitional channel flow using hot-film anemometry has been carried out. Using single-point statistics of wall shear stress fluctuations, an attempt is made to characterize the "start" and "end" of transition related intermittencies in the channel flow facility. This has been implemented by probing the higher order statistics of wall shear stress at the transitional Reynolds numbers. Using spatial correlations of the wall shear stress at different locations, a study into the localized transitional structures is also accomplished. To complement the wall shear stress results, flow visualization has also been conducted. Instantaneous wall shear stress measurements are conducted for Re_τ (Re_h) of 39.8 (510), 40.6 (541), 42.9 (609), 44.5 (642), 45.4 (673), 46.8 (706), 48.7 (738), 51.5 (763), 53.9 (807), 61.5 (887), 67.2 (969), 73.4 (1043), 79.3 (1125) and 84.2 (1213). Simultaneous wall shear stress data are acquired using the three hot-films for time durations of more than 100,000 convective time units ($tU_b/h > 100,000$) for every Reynolds number, where t indicates measurement time in seconds. This gives the opportunity to calculate well-converged higher order statistics of wall shear stress during transition. In a separate set of experiments, flow visualization has been carried out

for Re_τ (Re_h) of 45.4 (673), 48.1 (732), 52.1 (774), 55.4 (824), 60.8 (870) and 67.5 (959).

The results and discussion presented in this chapter have formed the basis for recently published paper:
"Investigating channel flow using wall shear stress signals at transitional Reynolds numbers", *International Journal of Heat and Fluid Flow* 81C:108525, 2020
R Agrawal, H C H Ng, D J C Dennis and R J Poole

5.2 Single point statistics of wall shear stress

In this section, results obtained from a single hot-film measurement, HF2, located at $z/h = 5$ and $x/h = 496$, are discussed. The location of the hot-films in the current channel flow facility is discussed in § 3.2 and shown in figure 3.2. As a first step of investigating the wall shear stress behaviour, for the transitional Reynolds numbers, the time history segments of wall shear stress are studied. Careful study of the time history will also make analysis of statistical properties of wall shear stress fluctuations easier to interpret.

5.2.1 Time histories

Figure 5.1 shows segments of instantaneous normalized wall shear stress for various Reynolds numbers where τ_w' and $\overline{\tau_w}$ represent the instantaneous wall shear stress fluctuations and time-averaged wall shear stress, respectively. This plot also shows the corresponding values of normalized intensity of the wall shear stress fluctuations, indicated by the root mean square of the wall shear stress fluctuations, $\sigma(\tau_w')$. It can be observed that there are no significant fluctuations in wall shear stress for $Re_\tau =$ 40.6 and 42.9, which is also shown by the $\sigma(\tau_w')/\overline{\tau_w}$ values lower than 0.01 for these two Reynolds numbers. So it can be said that the flow is in the laminar state at these Reynolds numbers. For $Re_\tau = 44.5$ the appearance of some small amplitude fluctuations is apparent and at $Re_\tau = 45.4$ and 46.8, large amplitude fluctuations emerge in an otherwise laminar background. It is postulated that these large amplitude fluctuations represent the localized turbulent structures which sustain themselves up to at least a

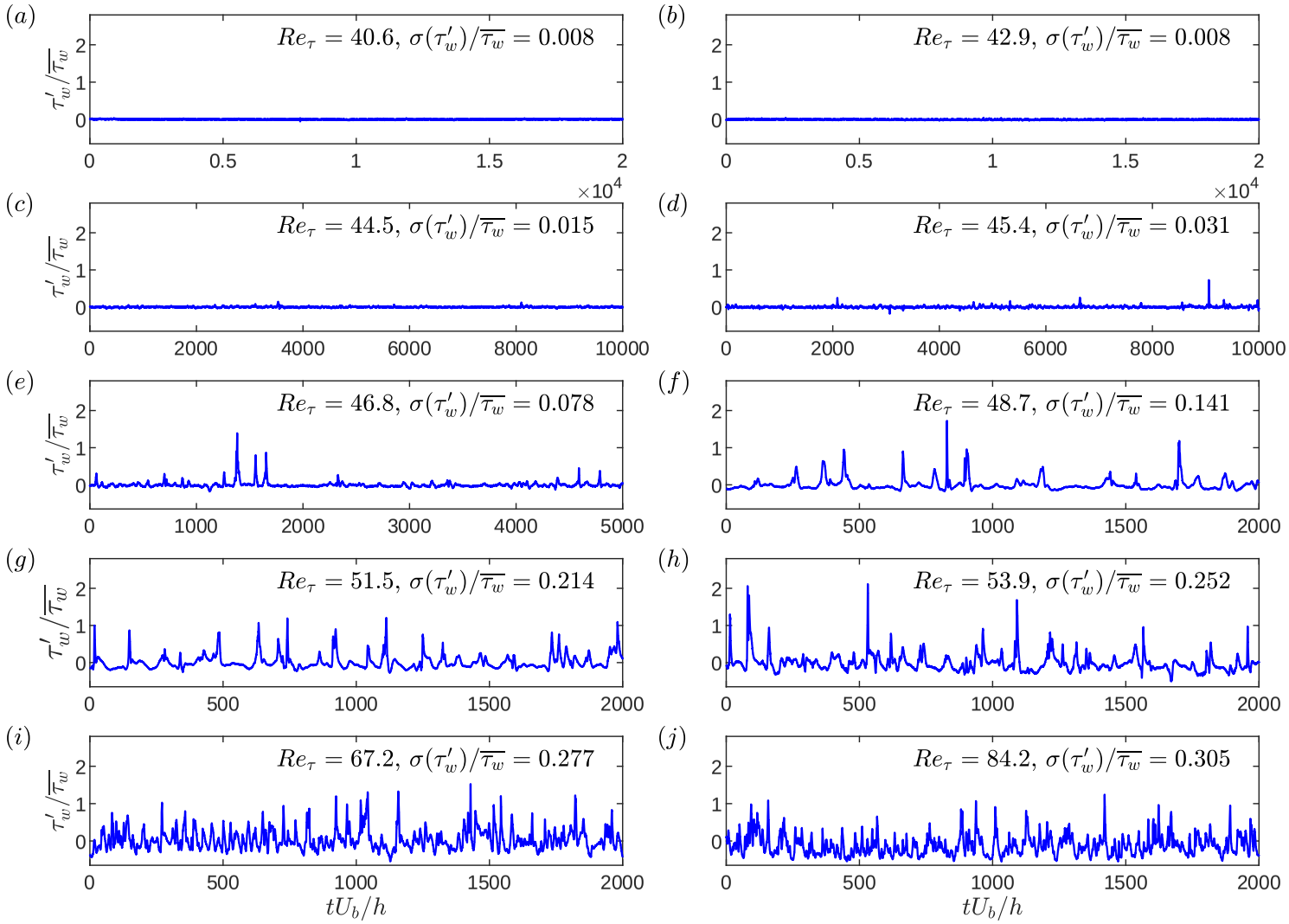

Figure 5.1: Segments of instantaneous normalized wall shear stress fluctuations measured using HF2 located at $z/h = 5$ and $x/h = 496$ for various Reynolds numbers. The plots also show the corresponding values of normalized RMS of wall shear stress fluctuations.

streamwise distance of $x/h = 496$ as they flow downstream from the inlet. Patel and Head [1969] observed a similar phenomena of apparently random appearance of large amplitude fluctuations in their hot-wire data at the onset of transition in channel flows and they called these large amplitude fluctuations "turbulent bursts". The frequency of these localized structures is observed to increase with increasing Reynolds numbers of $Re_\tau = 48.7$, 51.5 and 53.9, as shown in figure 5.1(f,g,h). For these Reynolds numbers the flow can be seen to be highly intermittent, frequently switching between laminar and localized turbulent states. By $Re_\tau = 67.2$ laminar flow is almost entirely absent and the flow can be seen to consist mostly of turbulent events. This indicates the disappearance of laminar-turbulent intermittency at higher Reynolds numbers.

5.2.2 Higher order statistics

To further investigate the characteristics of wall shear stress fluctuations, higher-order statistics and probability density functions (PDFs) of wall shear stress are calculated. The second order statistics, as also discussed earlier, is given by the RMS of wall shear stress fluctuations. As can be seen from figure 5.2, $\sigma(\tau'_w)/\overline{\tau_w}$ values are observed to increase monotonically from $Re_\tau = 44.5$ to $Re_\tau = 84.2$. But a significant decrease in the rate of change is observed at $Re_\tau \approx 53$. This significant difference in the rate of change of the RMS values can be explained based on the time histories of wall shear stress as shown in figure 5. It can be observed that until $Re_\tau \approx 53.9$, the signals are highly intermittent and after this Reynolds number the signal starts to become uniformly turbulent and therefore the rate of change of RMS of wall shear stress fluctuations also starts to decrease. Third and fourth order moments of wall shear stress fluctuations, i.e. the skewness $S(\tau'_w)$ and flatness (or kurtosis) $F(\tau'_w)$, respectively, are given by $S(\tau'_w) = \overline{\tau'^3_w}/\sigma(\tau'_w)^3$ and $F(\tau'_w) = \overline{\tau'^4_w}/\sigma(\tau'_w)^4$. Figure 5.3 shows the skewness and flatness of wall shear stress fluctuations for various Reynolds numbers. From figure 5.3(a) and (b) it can be seen that for $Re_\tau \leq 42.9$, $S(\tau'_w) \simeq 0$ and $F(\tau'_w) \simeq 3$, thus indicating the presence of laminar flow, as for a Gaussian signal the skewness and flatness values are 0 and 3, respectively (i.e. the background noise is likely to be white-noise). There is a sharp increase in the skewness and flatness of wall shear stress for $Re_\tau \geq 44.5$ which can

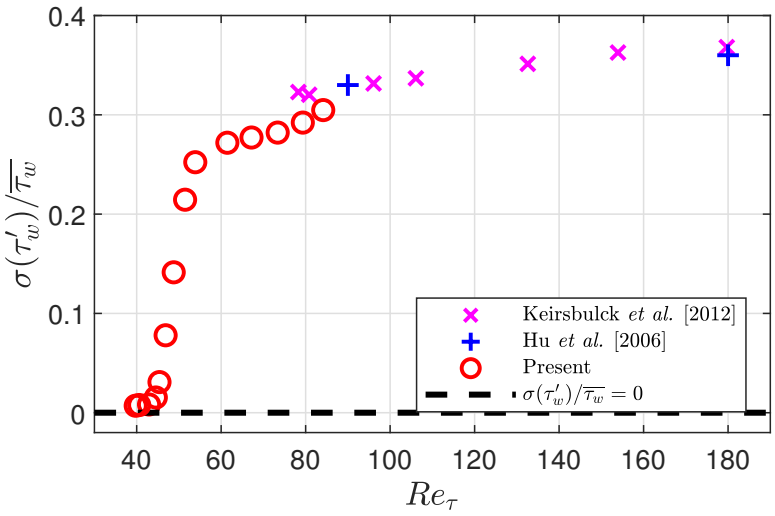

Figure 5.2: Variation of normalized RMS of wall shear stress fluctuations with Reynolds number

be explained from figure 5.1(c, d). As discussed in § 5.2.1, it can be seen that there are few fluctuations at these Reynolds numbers which leads to very high values of skewness and flatness of the signals as shown in figure 5.3. For Re_τ close to 48 the skewness and flatness peak to a very high magnitude. This high magnitude indicates a very high level of laminar-turbulent intermittency in the flow. And for increasing Reynolds numbers the third and fourth order moments start to decrease which indicates the increasing dominance of turbulent events in the flow and thus decreasing intermittency (as can also be seen from figure 5.1).

Jovanović et al. [1993] executed a least-square fit of the skewness and flatness of the streamwise velocity data obtained in previous studies for pipe, channel and boundary layer flows and obtained the relation $F \simeq 2.65 + 1.62S^2$ (note F does not go to a value of three as S tends to zero which is explained as a consequence of the least-square fit). A good agreement is observed with the least square fit (obtained from the streamwise velocity data) and the current experimental data for wall shear stress. One interesting point to note is that the least-square conducted by Jovanović et al. [1993] contained maximum values of S^2 and F data as 4 and 8 respectively but the present result shows that this relation still provides a good approximation for very high magnitudes of skewness and flatness i.e. $S^2 \sim 50$ and $F \sim 10^2$. Figure 5.2 and 5.3 also show the data

obtained by Keirsbulck et al. [2012] and Hu et al. [2006] who employed an electrochemical technique and DNS, respectively to investigate wall shear stress fluctuations in channel flow. For $Re_\tau > 73.4$, the trend of the moments obtained using the current experiment seem to approach the values given by Hu et al. [2006] and Keirsbulck et al. [2012] with a slight discrepancy especially in the second and fourth moments. This discrepancy is speculated to arise because of the limited frequency response, and spatial and temporal resolutions of the hot-film probes [Alfredsson et al., 1988a].

Figure 5.4(a) and 5.4(b) show the probability density functions (PDFs) of normalized wall shear stress ($\tau_w/\overline{\tau_w}$) and normalized wall shear stress fluctuations ($\tau'_w/\sigma(\tau'_w)$), respectively. Figure 5.4(a) shows that for $Re_\tau \lesssim 42.9$, the PDFs of normalized wall shear stress values collapse onto each other with the maximum value of the PDF lying at about $\tau_w/\overline{\tau_w} = 1$, thus indicating the flow to be in a laminar state. This result is consistent with the time history and higher-order moments results discussed earlier. The PDF for $Re_\tau = 44.5$ deviates from the laminar PDF, which shows the presence of finite amplitude fluctuations in the flow. The PDF for $Re_\tau \geq 44.5$ has a longer tail for the values above the mean for all the given Reynolds numbers thus giving rise to positive skewness. Figure 5.4(b) shows that there is a slight Reynolds number dependency between the PDFs for $Re_\tau = 73.4$ and $Re_\tau = 79.3$, which can also be seen from their skewness and flatness values in figure 5.3(a,b). But for $Re_\tau \geq 79.3$ there is no significant Reynolds number dependency on the PDFs of normalized wall shear stress fluctuations. This is consistent with result by Kushwaha et al. [2017] and Tsukahara et al. [2014] where it is shown that the large scale "stripy" structures in the flow seem to disappear as the Reynolds number increases beyond $Re_\tau \sim 70$ and gradually the flow becomes uniformly turbulent. Current result is also compared with the DNS result by Hu et al. [2006]. There seems to be a good agreement between the PDF obtained by Hu et al. [2006] for $Re_\tau = 90$ and present experiment for $Re_\tau = 84.2$, but, as discussed before the slight differences might be caused by the limited frequency response and spatial and temporal resolution issues of hot-film probes. Therefore, from the higher order statistics and PDF of wall shear stress it can be said that any significant Reynolds

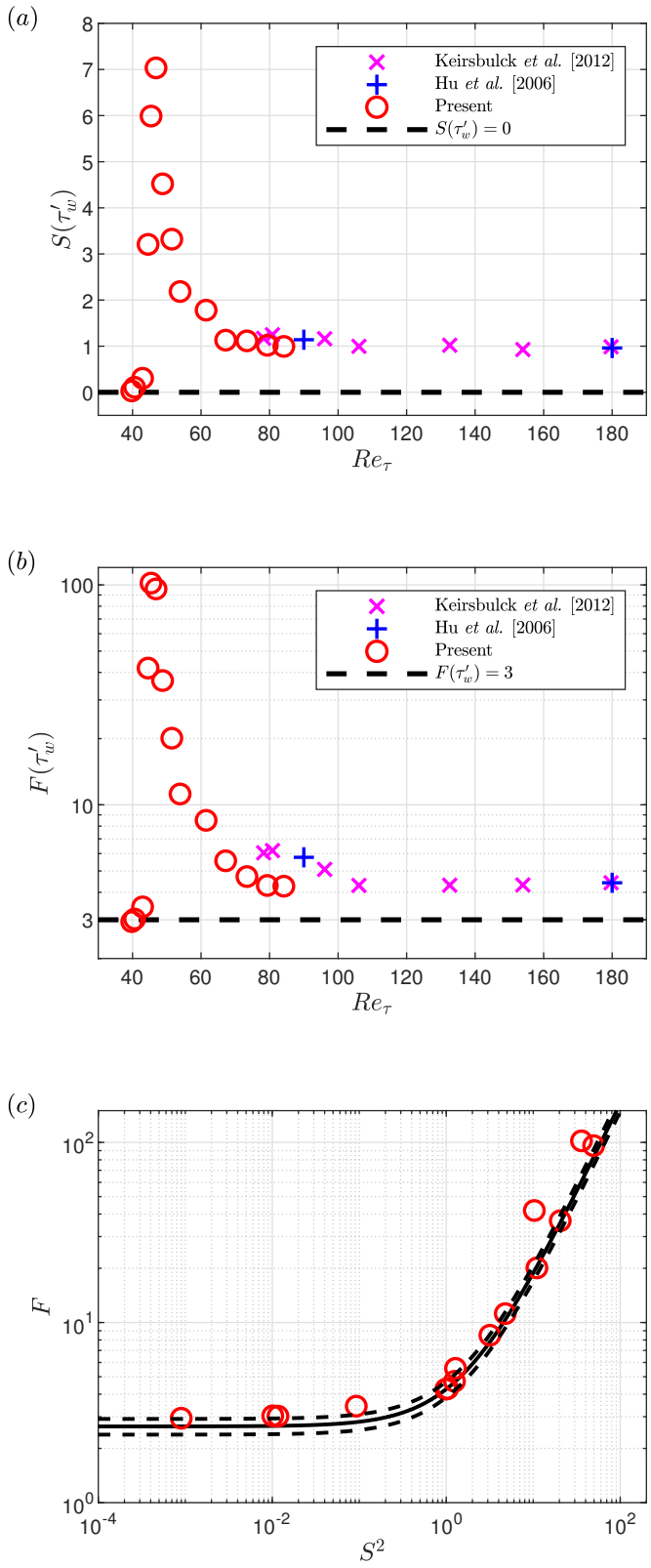

Figure 5.3: (a) Variation of skewness with Reynolds number; (b) Variation of flatness with Reynolds number; (c) Relation between flatness and skewness^2 where the solid line indicates the emperical relation obtained by Jovanović et al. [1993] for streamwise velocity data: $F \simeq 2.65 + 1.62S^2$, the dashed lines indicates $\pm 10\%$ of $F \simeq 2.65 + 1.62S^2$ and red circles represent the moments of wall shear stress data obtained from this study.

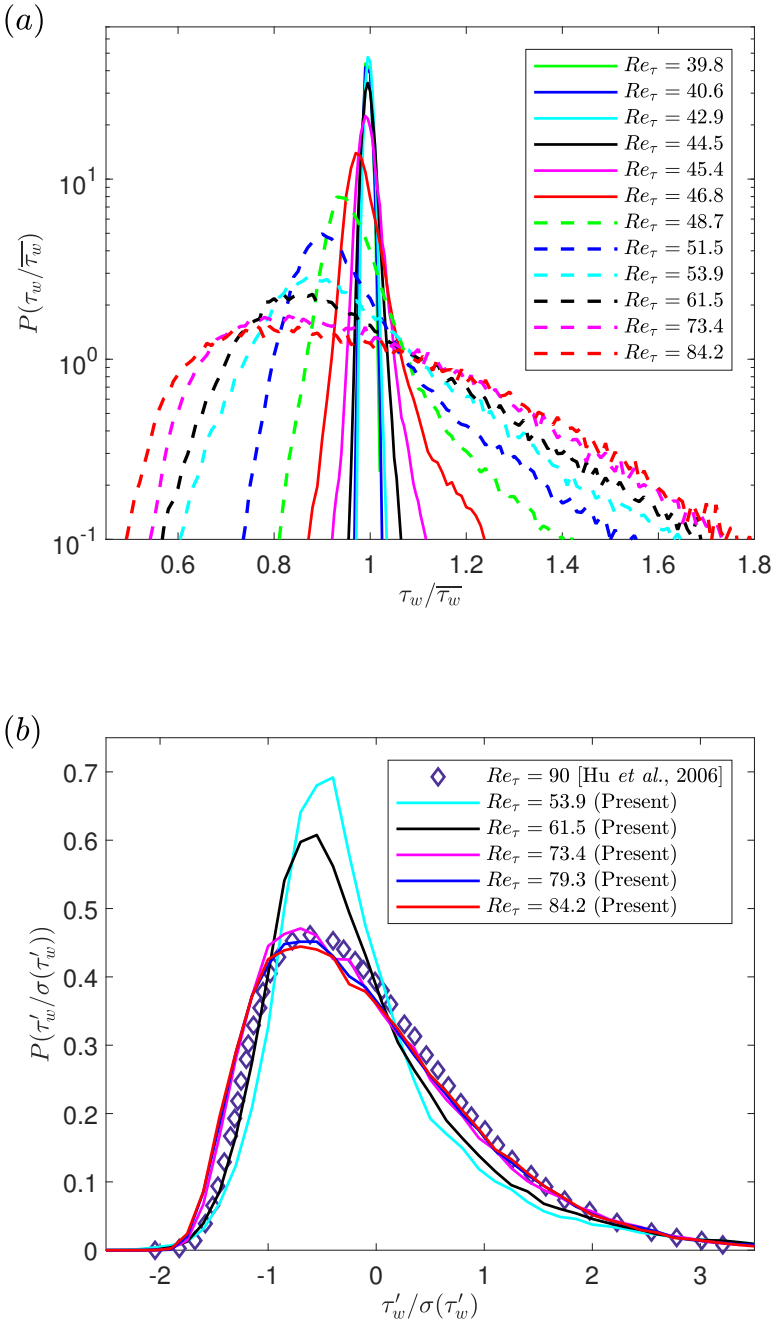

Figure 5.4: PDFs of normalized wall shear stress for varying Reynolds numbers. (b) PDFs of normalized wall shear stress fluctuations for varying Reynolds numbers.

number dependency of the flow fluctuations during transition have started to disappear by friction Reynolds number value somewhere between 73.4 and 79.3.

5.3 Wall footprint of large-scale turbulent structures

5.3.1 Representative segments of time histories

Simultaneous measurements using three different hot-films are conducted to investigate the characteristics of the large-scale turbulent structures in the channel-flow facility for transitional Reynolds numbers. The locations of the three hot-films (HF1, HF2 and HF3) were shown in figure 3.2. Figure 5.5 shows the segments of normalized wall shear stress fluctuations for $Re_\tau = 48.7$, 51.5 and 61.5, which are obtained simultaneously using the three hot-films. It can be seen that for $Re_\tau = 48.7$ some of the large amplitude fluctuations appear to occur almost simultaneously at all the three hot-film locations with some time lags. This suggests the presence of large-scale structures which are at least 7 channel half-heights wide. This seems to be consistent with the previous studies where the presence of large-scale turbulent structures called turbulent spots have been observed near the onset of transition [Carlson et al., 1982, Aida et al., 2010, Sano and Tamai, 2016]. Although the aspect ratio of the channel is $AR \approx 12$, it is believed that this aspect ratio is enough to have sustained localized structures during transition. Takeishi et al. [2015] showed the presence of turbulent spots for $AR \geq 5$ similar to those in channel flows of very large aspect ratio, for example Carlson et al. [1982] and Tsukahara et al. [2014]. In figure 5.5(a), some of the large amplitude fluctuations can be seen to not occur in all three hot-film signals. This is not unexpected because these structures are found to be localized not only in the streamwise direction but also in the spanwise direction [Sano and Tamai, 2016, Patel and Head, 1969]. This phenomena is very different from the transition in pipe flows where the transitional structures called puffs are localized only in the streamwise direction and are found to fill the entire cross-section of the pipe at a given time [Wygnanski and Champagne, 1973]. Therefore, it is possible that for some instances one hot-film (e.g. HF2) cannot detect the presence of a turbulent spot passing by the HF3, which is located at another spanwise location or vice versa. From figure 5.5 (b, c) it can be seen that there is a decreasing number

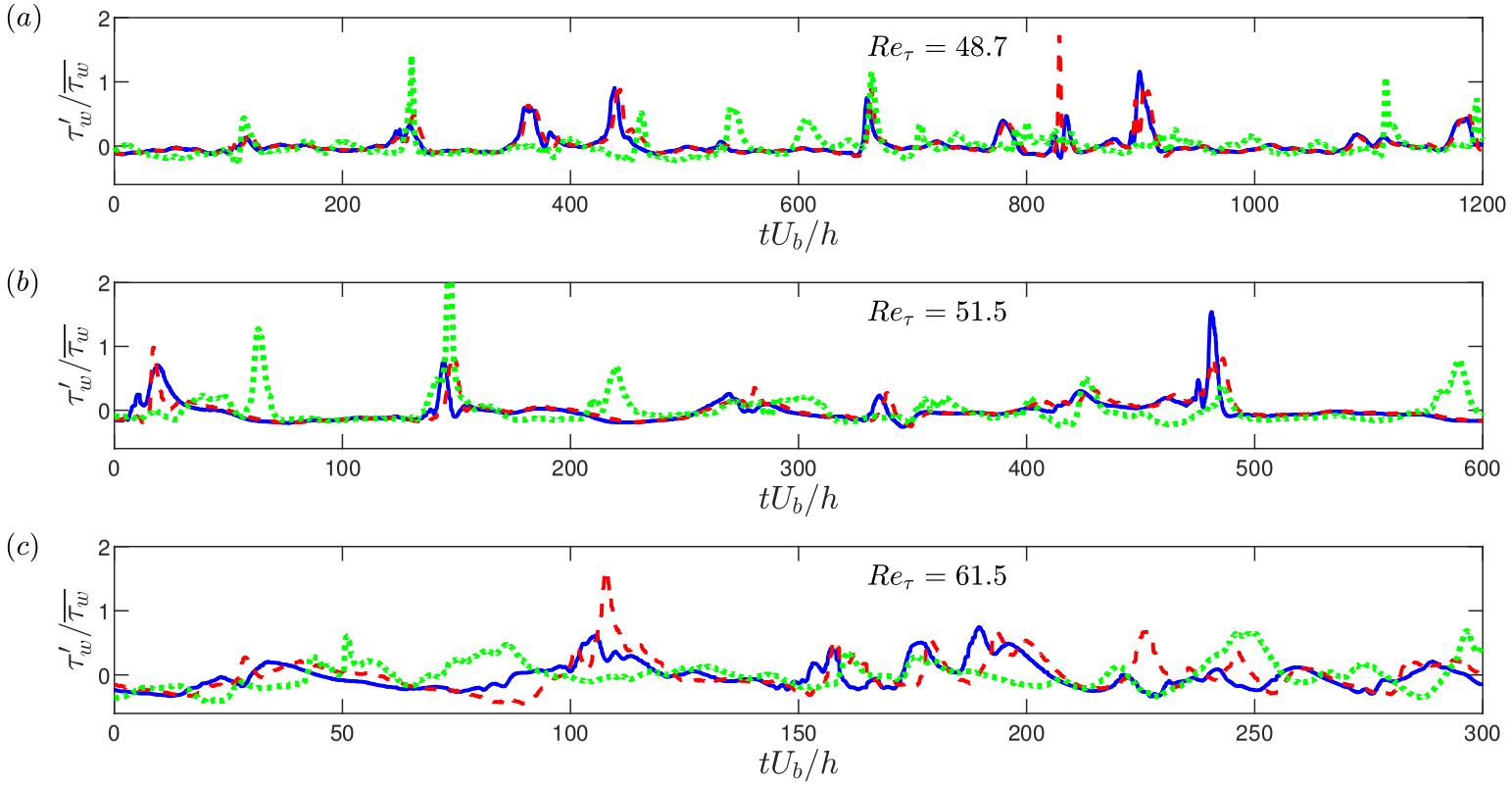

Figure 5.5: Segments of normalized wall shear stress fluctuations for (a) $Re_\tau = 48.7$, (b) $Re_\tau = 51.5$ and (c) $Re_\tau = 61.5$, where blue solid lines, red dashed lines and green dotted lines represent data obtained using HF1, HF2 and HF3, respectively.

of such high amplitude fluctuations occurring simultaneously with increasing Reynolds numbers. Therefore, with increasing Reynolds number the presence of such large-scale structures decreases and then disappears entirely.

5.3.2 Two-point spatial correlations

Cross-correlations of the wall shear stresses for all combinations of spatial location pairs are conducted. To calculate cross-correlations, instantaneous wall shear stress is converted to the corresponding friction velocity using the relation $U_\tau = \sqrt{\tau_w/\rho}$. The fluctuating friction velocities are then calculated by subtracting the time-averaged friction velocity from the instantaneous values, $u_\tau = U_\tau - \overline{U_\tau}$. The cross-correlation is then calculated using equation 5.1.

$$R_{u_{\tau_i} u_{\tau_j}} = \frac{\overline{u_{\tau_i}(t) u_{\tau_j}(t + \Delta t)}}{\overline{u_{\tau_i}(t) u_{\tau_j}(t)}}, \tag{5.1}$$

where u_{τ_i} and u_{τ_j} represent friction velocities calculated using wall shear stress measurements from two of the three hot-films and Δt represents the time-lag. Here the subscript i and j can take values 1, 2 or 3 which represents the hot-films HF1, HF2 and HF3, respectively. Figure 5.6 shows the cross-correlations of friction velocities for the same spanwise location of $z/h = 5$, but two different streamwise locations of $x/h = 491$ and 496, which are obtained using HF1 and HF2. It can be seen that the magnitude of the peak of the correlations decreases with increasing Reynolds numbers, which can be explained based on the increasing fluctuations and thus lower correlations with increasing Reynolds numbers. It is also observed that there is a lag in the peak of correlations for all the Reynolds numbers. The streamwise separation between the probes has been used to estimate the convective (or propagation) velocity of the flow previously by Krogstad et al. [1998]. They observed that the obtained value of convective velocity changes with changing probe separation distance because the convective velocity of the flow depends on the scale of motion. Therefore, the measurement can be biased towards the motion of large scales if a larger probe distance is chosen as they dominate the correlation. In this study the convective velocity calculated from

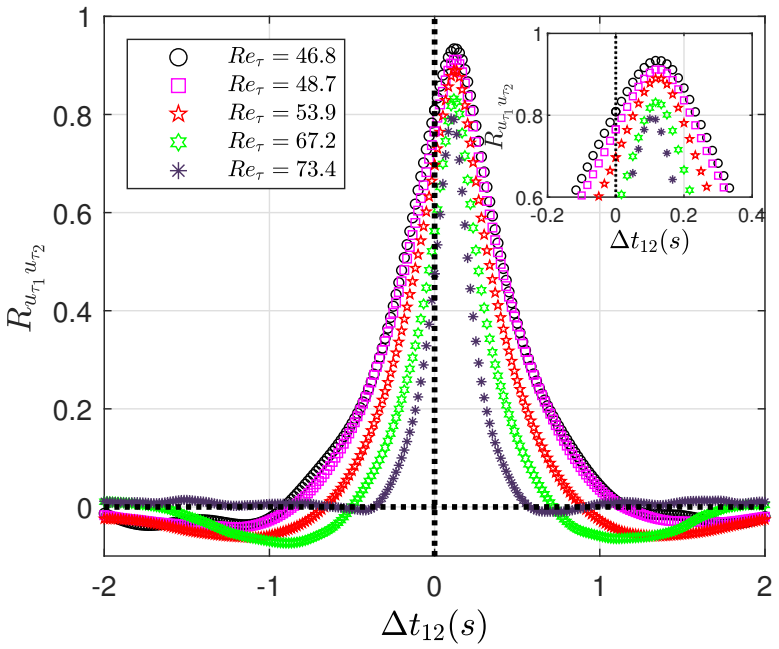

Figure 5.6: Cross-correlations of friction velocities calculated using the wall shear stress from the streamwise-aligned hot-films: HF1($x/h = 491; z/h = 5$) and HF2($x/h = 496; z/h = 5$).

the correlation is used to convert the time lag to a spatial separation using:

$$U_c = 5h/\Delta t_{12,max}, \tag{5.2}$$

where $\Delta t_{12,max}$ is the temporal separation for which the $R_{u_{\tau_1} u_{\tau_2}}$ is maximum.

5.3.3 Calculating average angles of large-scale turbulent structures

Figure 5.5 shows that there occur almost simultaneous large amplitude fluctuations in the wall shear stress time history data obtained from hot-films HF2 and HF3 for $Re_\tau = 48.7$. These two hot-films are separated in the spanwise direction with a gap of $7h$ and are at the same streamwise distance of $496h$ from the inlet. Figure 5.7(a) shows the correlation of wall shear stress obtained at these two spatial locations. It can be seen that there is a significant correlation of the wall shear stresses for Re_τ between 46.8 and 53.9 which indicates the presence of large-scale turbulent structures in this range of Reynolds numbers which are at least $7h$ large. It can also be seen that there is a positive lag in the correlation coefficient which shows that the same structures do not occur directly above both of the hot-films at the same time, but

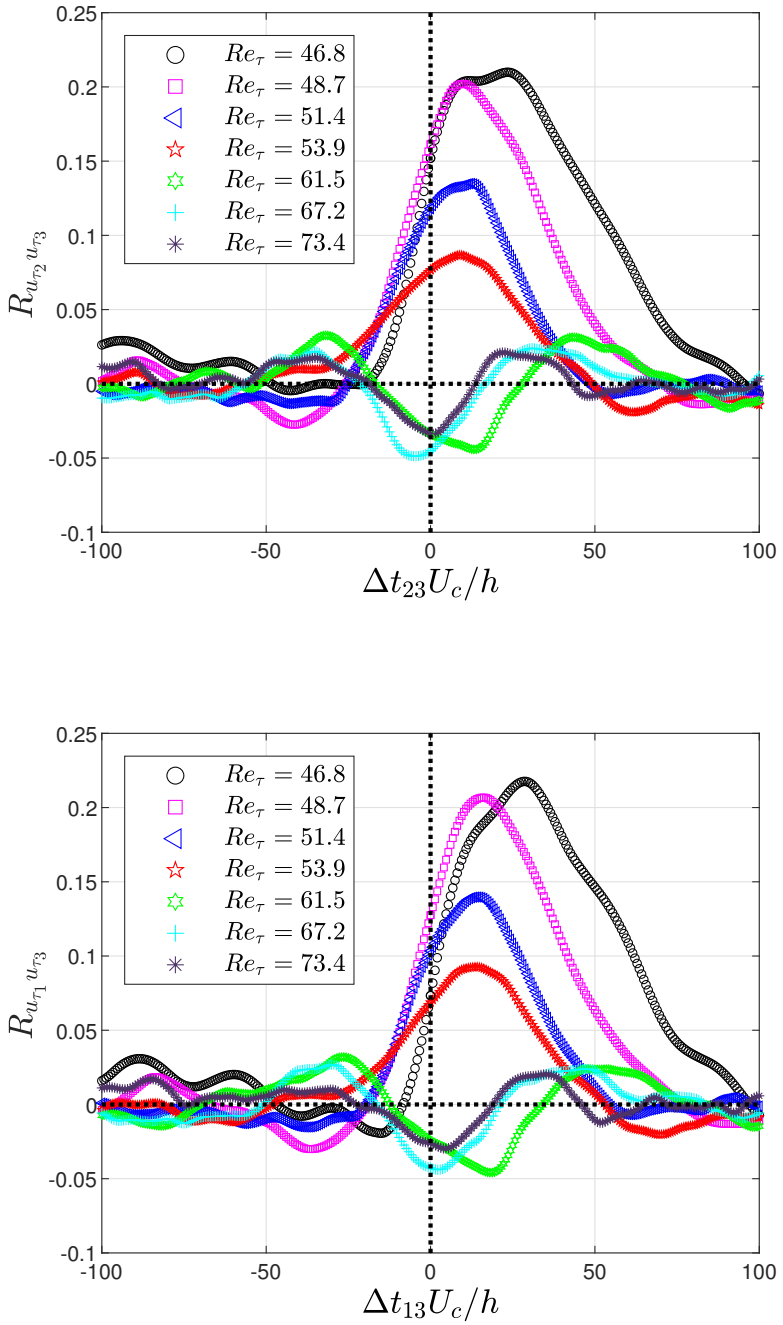

Figure 5.7: Cross-correlations of friction velocities calculated using wall shear stress data for (a) HF2 and HF3, (b) HF1 and HF3.

there is some delay. Since correlation is an integral measure, the lag indicates the structures are, on average, inclined in the x - z plane. For $Re_\tau \geq 61.5$ the correlation peak has a magnitude lower than 0.05, thus indicating no significant correlation. A similar correlation is also conducted for HF1 and HF3 and is shown in figure 5.7(b). This figure shows very similar behaviour as figure 5.7(a), which is expected because HF1 and HF2 lie at the same spanwise location but are separated by a streamwise distance of $5h$. Table 5.1 shows the laminar centerline velocity ($U_{cl,lam} = 1.5U_b$), and the convective velocity (U_c) obtained using equation 5.2 for Re_τ between 46.8 and 73.4. Table 5.1 also shows the time lags (in seconds) between each pair of hot-film locations for Re_τ between 46.8 and 53.9. Time lags $\Delta t_{23,max}$ and $\Delta t_{13,max}$ indicate the temporal separation for which the $R_{u_{\tau_2}u_{\tau_3}}$ and $R_{u_{\tau_1}u_{\tau_3}}$ are maximum, respectively. Note that $\Delta t_{13,max} = \Delta t_{12,max} + \Delta t_{23,max}$ should be true theoretically. Here, the maximum values of the correlations are calculated by carrying out a Gaussian fit near the peak of the correlations for all data. A nice agreement with the theoretical prediction is observed between the time lags and the minor differences with the theoretical prediction can be attributed to the uncertainty associated with the calculation of correlations. The time lag $\Delta t_{12,max}$ is observed to be independent of the Reynolds number for Re_τ between 46.8 and 53.9. This is thought to be the consequence of small steps in the increment of Reynolds number thus leading to the change in the $\Delta t_{12,max}$ being within the measurement uncertainty. The $\Delta t_{12,max}$ value is calculated by fitting a Gaussian function near the peak of the correlations which also adds uncertainty to its value.

An attempt is made to calculate the average structure angles of the structures present during the onset of transition. Figure 5.8 shows the hot-film arrangements with the assumed flow behaviour of the large-scale transitional structures passing through the three hot-films. Structure angles between the two-pairs of hot-films (HF2 - HF3 and HF1 - HF3) are calculated using:

$$\tan\theta_{23} = \frac{7\Delta t_{12,max}}{5\Delta t_{23,max}}, \tag{5.3}$$

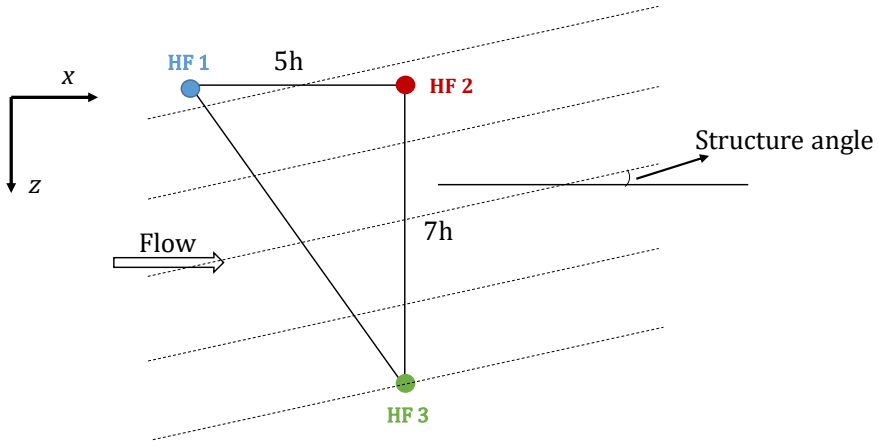

Figure 5.8: Schematic of the hot-film arrangements.

$$\tan\theta_{13} = \frac{7\Delta t_{12,max}}{5(\Delta t_{13,max} - \Delta t_{12,max})}. \tag{5.4}$$

The structure angles obtained are shown in table 5.1. It should again be noted that theoretically $\theta_{23} = \theta_{13}$, i.e. the average structure angle obtained from the correlations between HF2 - HF3 and HF1 - HF3 should be the same.

For $Re_\tau = 46.8$, the average structure angle obtained using both of the hot-films are about 17° and the average structure angles for Re_τ between 48.7 and 53.9 are found to be between 32° and 37°. This big change in angle (from 17° to 32° - 37°) is predicted to be a consequence of the significant change in the flow behaviour between these two Reynolds numbers. It can be seen from the single-point statistics of wall shear stress fluctuations, as shown in table 5.1, that the $\sigma(\tau_w')/\overline{\tau_w}$ values almost doubles for Re_τ between 46.8 and 48.7, and $S(\tau_w')$ peaks for $Re_\tau = 46.8$ and starts to decrease after this Reynolds number. There is also a discrepancy in angles obtained for $Re_\tau = 48.7$ and 51.5 by using two different correlations, as shown in table 5.1. This discrepancy is an artifact of the differences observed in the respective time lag calculations.

Carlson et al. [1982], using flow visualization, observed oblique waves associated with the turbulent spots in channel flows. They obtained the angle of the leading-edge waves between 18° and 25° for lower Reynolds numbers and 37° for higher Reynolds number. The angles obtained in this study are in good agreement with the results obtained by

Table 5.1: Time lags (in seconds) of maximum peak locations between each pair of hot-films and average structure angles (in degrees) along the streamwise direction between each pair of hot-films. Second and third order moments of wall shear stress fluctuations, and the laminar centerline velocity ($U_{cl,lam}$) and the convective velocity (U_c) are also shown.

Re_τ	$U_{cl,lam}$ (m/s)	U_c (m/s)	$\sigma(\tau'_w)/\overline{\tau_w}$	$S(\tau'_w)$	$\Delta t_{12,max}$ (s)	$\Delta t_{23,max}$ (s)	$\Delta t_{13,max}$ (s)	θ_{23} (deg.)	θ_{13} (deg.)
46.8	0.51	0.51	0.078	7.03	0.12	0.57	0.69	17	17
48.7	0.53	0.52	0.141	4.52	0.12	0.26	0.39	33	32
51.5	0.56	0.50	0.214	3.32	0.12	0.26	0.36	34	37
53.9	0.59	0.51	0.252	2.18	0.12	0.23	0.34	36	36
61.5	0.65	0.52	0.272	1.78	-	-	-	-	-
67.2	0.71	0.55	0.277	1.13	-	-	-	-	-
73.4	0.76	0.59	0.282	1.11	-	-	-	-	-

Carlson et al. [1982]. It is predicted that the average structure angles indicate the presence of oblique waves which are generally associated with turbulent spots [Carlson et al., 1982, Alavyoon et al., 1986, Li and Widnall, 1989, Aida et al., 2010]. This also suggests that the turbulent spots observed in previous studies using flow visualization and velocity field measurements possess a significant wall footprint.

5.4 Flow visualization

Flow visualization is conducted for transitional Reynolds numbers ranging from $45.4 \leq Re_\tau \leq 67.5$ at a streamwise distance of about $x/h = 496$ and a wall-normal location of $z/h = 0.4$. The images are acquired at 50 fps for about 20 seconds at every Reynolds number. The images are cropped and stitched together to create a continuous flow structure (as discussed in § 3.6).

Figures 5.9 and 5.10 show the flow structures obtained using the flow visualization for $Re_\tau = 45.4$, 48.1 and 52.1, and for $Re_\tau = 55.4$, 60.8 and 67.5, respectively. Here, the spanwise extent of the plots are at a constant values of $3.8 \leq z/h \leq 16.4$. The streamwise extent of the flow is calculated using U_b as the convective velocity. In figure 5.9, it can be seen that for $Re_\tau = 45.4$, the flow is almost always quiescent with some fluctuations at $tU_b/h \approx 80$. With increasing Reynolds number, the presence of large localized turbulent structures, with intermittent quiescent states, can be observed for $Re_\tau = 48.1$. These large-scale structures are observed to spread over the entire spanwise extent of the flow visualization i.e. z/h between 3.8 and 16.4. This also provides the visual evidence of the large-scale turbulent structures as reported from the wall shear stress measurements. When the Reynolds number is further increased to $Re_\tau = 52.1$, the frequency of these large-scale structures starts to increase with fewer instances of laminar states. Similar behavior can also be seen from the time history of wall shear stress signals in figure 5.1 for $Re_\tau = 48.7$ and 51.5. Therefore, it can be said that for $48.1 \leq Re_\tau \leq 52.1$, the flow is highly intermittent with switching between the laminar and turbulent states. This can also be seen from figure 5.3, where at these Reynolds numbers the skewness and flatness of wall shear stress fluctuations peak to very high

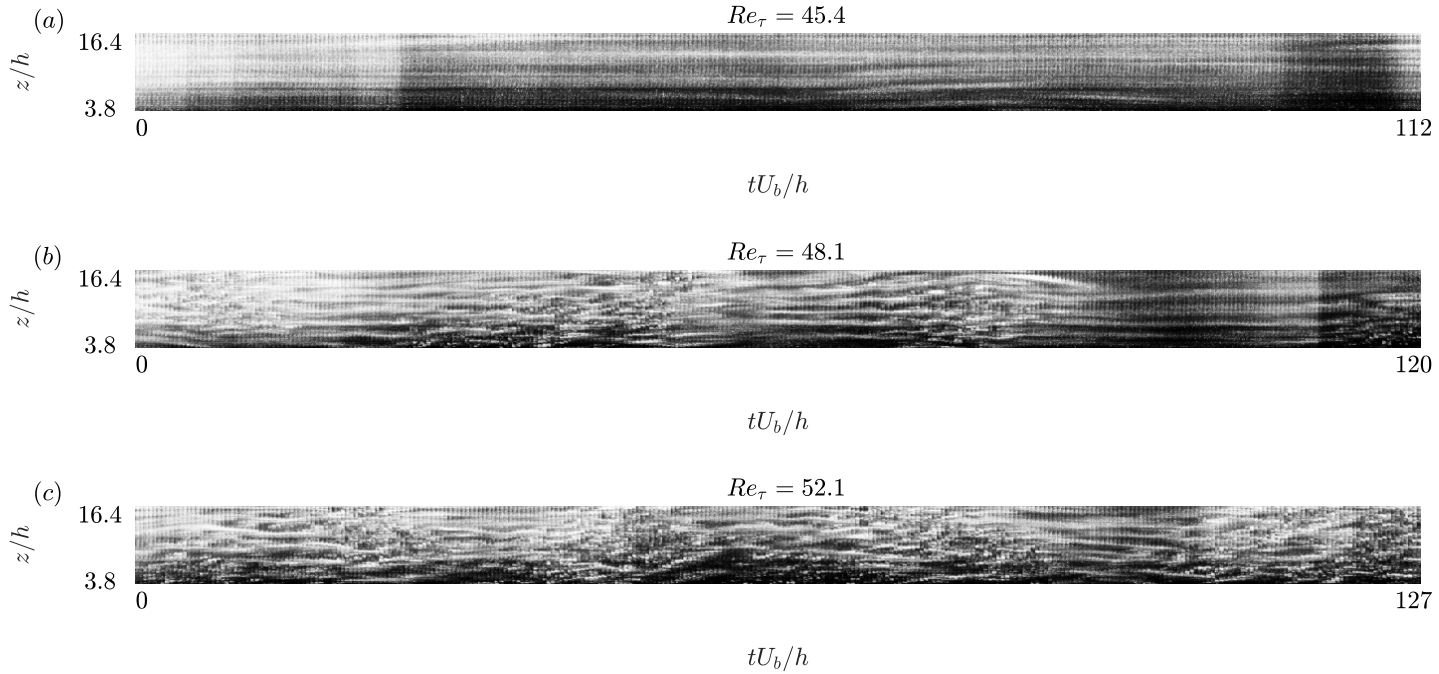

Figure 5.9: Flow structure visualization for (a) $Re_\tau = 45.4$, (b) $Re_\tau = 48.1$ and (c) $Re_\tau = 52.1$.

values, thus indicating very high levels of intermittency in the flow. The presence of some angles associated with these turbulent structures can be seen for $Re_\tau = 48.1$ and 52.1 from figure 5.9. Quantitative measurements of these angles have not been conducted due to the limited duration and quality of these flow visualization results.

Figure 5.10 shows that for $Re_\tau = 55.4$, there is less laminar-turbulent intermittency in the flow. This intermittency starts to disappear with increasing Reynolds numbers and by $Re_\tau = 67.5$, the flow can be seen to have almost no laminar flow regions. Similar results were also obtained using the wall shear stress signals in figure 5.1 where by $Re_\tau \approx 67$, the laminar flow is almost disappears and the flow primarily consists only of turbulent events.

5.5 Summary

An experimental investigation of wall shear stress characteristics for transitional channel flow has been conducted using hot-film anemometry and this investigation is also complemented by flow visualization. Single-point measurements of wall shear stress indicates that the time history is free of any significant perturbations in the flow for $Re_\tau \lesssim 42.9$, suggesting that the flow is in a laminar state. There is an appearance of high amplitude fluctuations beyond $Re_\tau = 42.9$, whose frequency seems to be increasing with increasing Reynolds numbers until the flow is seen to consist only of turbulent events by $Re_\tau = 67.2$. Skewness and flatness of wall shear stress fluctuations jumps at the onset of transition and reaches to a very high magnitude which is an indication of laminar-turbulent intermittency for these Reynolds numbers. After $Re_\tau \approx 48$, these two moments start to slowly decrease with increasing Reynolds number until there is no significant Reynolds number effects for $Re_\tau \simeq 73$ - 79. Simultaneous measurements of wall shear stress at three different locations indicate the presence of large-scale turbulent structures near the onset of transition. The average angles of these large-scale structures near the onset of transition are estimated using two-point correlations and the values obtained are about 17^o for $Re_\tau = 46.8$ and between 32^o and 37^o for $Re_\tau = 48.7$ and 53.9. Based on the angles obtained, these structures are predicted to be waves

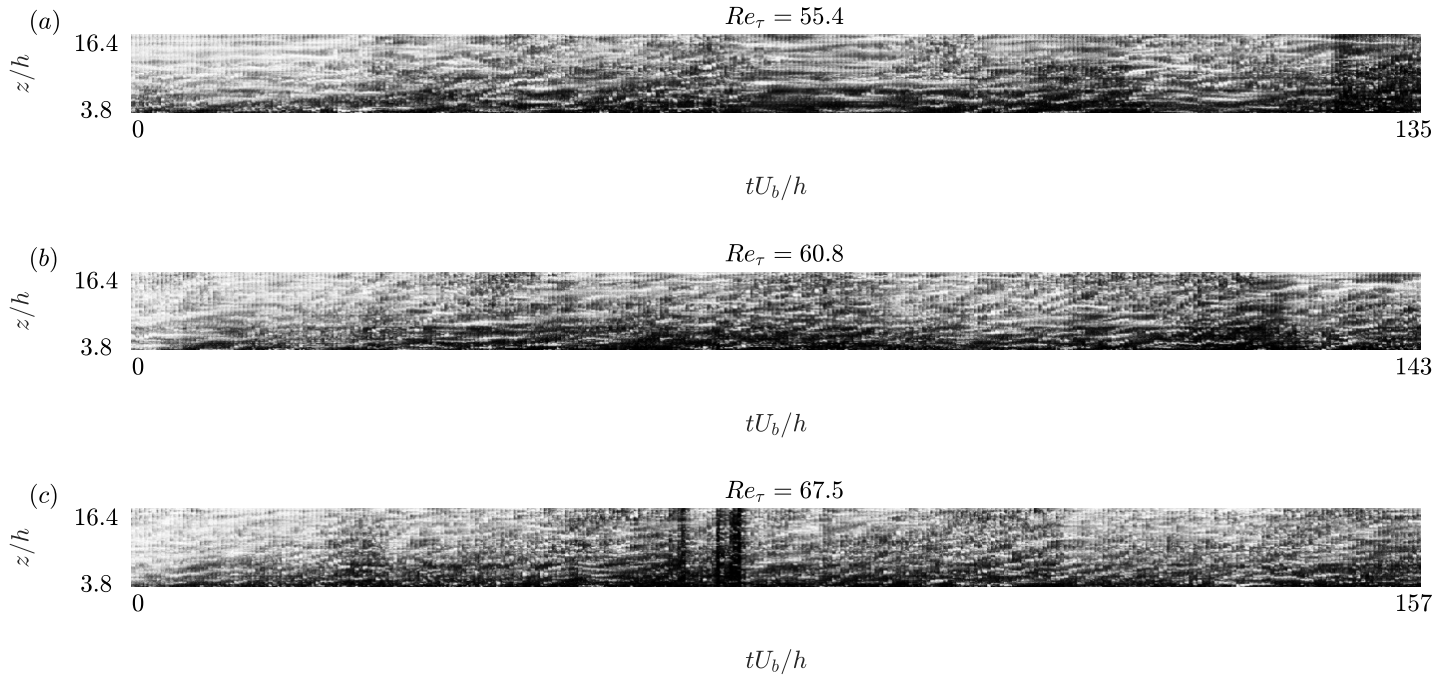

Figure 5.10: Flow structure visualization for (a) $Re_\tau = 55.4$, (b) $Re_\tau = 60.8$ and (c) $Re_\tau = 67.5$.

which are generally associated with turbulent spots during the transition process. Flow visualization results provide a further verification of the results obtained using the wall shear stress signals. The flow is seen to almost laminar for $Re_\tau = 42.9$ and after this Reynolds number the flow is composed of intermittent laminar and turbulent regimes and for $Re_\tau = 48.1$ and 52.1 the flow is highly intermittent. After about $Re_\tau \approx 53$, the laminar-turbulent intermittency starts to diminish and by $Re_\tau = 67.5$ it seems to disappear from the flow.

Based on this study, the transition related intermittency starts at $Re_\tau \approx 43$ in the current channel flow facility. To calculate the Reynolds number where this intermittency ends, an average of values obtained using different techniques (time history and higher order moments of τ_w, and flow visualization) is calculated. This given an approximate value of $Re_\tau \approx 72$. Therefore, it is concluded that the transition related intermittency disappears in the present flow facility by $Re_\tau \approx 72$. Although it should be noted that there is $\pm$ 3-4 % uncertainty in the calculation of Re_τ in the present study, as mentioned earlier in § 3.7.

Chapter 6

Intermittencies in turbulent channel flows

6.1 Introduction

As discussed in § 2.5, recent DNS and experiments in turbulent channel flow have found intermittent low- and high-drag events in Newtonian fluid flows, at friction Reynolds numbers between 70 and 100. These intervals of low-drag and high-drag have been termed "hibernating" and "hyperactive", respectively [Kushwaha et al., 2017], and in this chapter, a further investigation of these intermittent events is conducted. Simultaneous measurements of wall shear stress and velocity are carried out using HFA and LDV, respectively. Experiments are conducted at friction Reynolds number of 70, 85, 120, 180 and 250. The effect of varying the criteria (time-duration and magnitude threshold) to detect these intermittent events is also studied. The use of different scalings for the time-duration criterion for the conditional events is also explored. The explanation for the presence of a spike in the ensemble-averaged wall shear stress data before and after the low-drag events (previously discussed in § 1.2) is investigated. Studying the velocity characteristics during the low-drag events reveals that the conditionally-averaged streamwise velocities get closer to Virk's MDR asymptote close to the wall for all Reynolds numbers studied. Reynolds shear stress characteristics during these conditional events, where it was possible to do so (explained in § 6.2), are

also investigated for $Re_\tau = 70$ and 85. In marked contrast to minimal channel flow DNS [Park and Graham, 2015], Reynolds shear stress is observed to increase during the low-drag events for $y^+ \approx 20$ - 40, whereas during the high-drag events the Reynolds shear stress remains almost unchanged.

6.2 Experimental condition

In the chapter 5, it is observed that the flow in the present channel consists only of turbulent events by $Re_\tau \approx 67$ and the significant Reynolds number dependence on the skewness and flatness of wall shear stress fluctuations starts to disappear by $Re_\tau \simeq 73 - 79$. Based on these results, in this chapter, the intermittencies associated with the turbulent flow is investigated for $Re_\tau \geq 70$. Experiments are conducted for five Reynolds numbers: $Re_\tau = 70$, 85, 120, 180 and 250 in the channel flow facility described in chapter 3. For each Reynolds number, wall shear stress and velocity data are acquired simultaneously in the measurement test section (discussed in § 3.2) using HFA and LDV, respectively at a location of $z/h = 5$ and $x/h = 496$. Velocity acquisition is realized at 10 different wall-normal locations, where each wall-normal location is sampled for 2 hours at a typical data rate of around 300 - 400 Hz. Table 6.1 shows the Reynolds numbers, corresponding wall-normal locations studied and the parameters measured in this part of the thesis. For $Re_\tau = 70$ and 85, both streamwise and wall-normal velocity components are measured simultaneously with the wall shear stress. This has been conducted to study the RSS behaviour during the low- and high-drag events. For other Reynolds numbers, due to experimental limitations (discussed previously in § 3.4.3), only streamwise velocity measurements has been executed with the wall shear stress because the near peak region of the RSS could not be measured for higher Reynolds numbers as this moves physically closer to the wall at higher Reynolds numbers where the LDV beams are blocked.

In this chapter, two different ways of averaging the measured variables are carried out: time-averaging and conditional-averaging. To differentiate between these two averages the following nomenclature are used: an overbar indicates a time-averaged quantity (e.g.

Table 6.1: Reynolds numbers and various wall-normal locations studied. Parameters measured for each Reynolds numbers are also shown.

Re_τ	y^+	Parameters measured
70	21, 24, 28, 32, 35, 40, 46, 51, 60, 68	τ_w, U, V
85	26, 31, 36, 32, 41, 47, 54, 61, 76, 85	τ_w, U, V
120	22, 26, 30, 37, 46, 59, 71, 85, 103, 123	τ_w, U
180	24, 30, 38, 48, 60, 75, 98, 128, 157, 188	τ_w, U
250	35, 45, 58, 74, 94, 118, 143, 171, 202, 242	τ_w, U

$\overline{U}$), and an overbar with an L or H superscripts indicates the conditionally-averaged quantity for low- and high-drag events (e.g. $\overline{U}^L, \overline{U}^H$), respectively. Similarly, friction velocities are calculated using two different wall shear stress: time-averaged wall shear stress ($\overline{u_\tau}$) and conditionally-averaged wall shear stress ($\overline{u_\tau}^L, \overline{u_\tau}^H$). Based on these definitions of the friction velocities, the wall-normal locations are also normalized in three different ways: $y^+ = y\overline{u_\tau}/\nu$, $y^{+L} = y\overline{u_\tau}^L/\nu$ and $y^{+H} = y\overline{u_\tau}^H/\nu$.

6.3 Identifying low- and high-drag events

Figure 6.1 shows the PDF of wall shear stress fluctuations (τ_w') obtained for $Re_\tau = 180$. It can be seen that the PDF of wall shear stress has a longer positive tail which means that the PDF is positively skewed. This shows that some of the positive fluctuations have much larger magnitude than the negative fluctuations. In the present study, the wall shear stress is the representative of the drag (or the skin-friction drag, to be more accurate). Previously, Gomit et al. [2018] used the PDF of wall shear stress to divide low- and high-wall shear stress events in a turbulent boundary layer. They divided the PDF into four quartiles, where each quartile contains one-fourth of the realizations. In this study, to define the low- and high-drag "events", two significant parameters are considered: the magnitude of the wall shear stress fluctuations and the duration of time the fluctuations stay below or above the time-averaged value. The PDF of wall shear stress fluctuations, as shown in figure 6.1, provides statistical information about

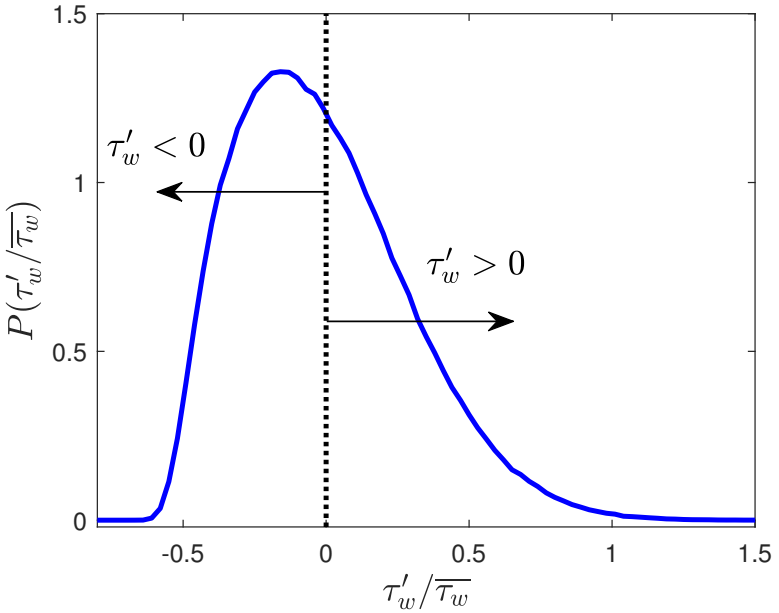

Figure 6.1: PDF of wall shear stress fluctuations for $Re_\tau = 180$ measured at $z/h = 5$ and $x/h = 496$. Skewness and flatness of the wall shear stress flutuations for $Re_\tau = 180$ are $S(\tau'_w) = 0.65$ and $F(\tau'_w) = 3.2$, respectively.

the magnitude of the fluctuations but the information regarding the time-duration of the fluctuations cannot be inferred. Therefore, it is necessary to find a novel way to visualize all the positive and negative fluctuations as a function of the magnitude and time-duration. This is carried out by calculating the distribution of all the fluctuations (τ'_w) about the time-averaged value ($\overline{\tau_w}$) with their corresponding time durations (δt) of staying above or below the time-averaged value. Figure 6.2 shows an example of this distribution of the negative and positive shear stress fluctuations for $Re_\tau = 180$. Here, so-called inner scaling (u_τ^2/ν) is used to scale the time-duration (δt) of the negative and positive wall shear stress fluctuations. The strength of the wall shear stress fluctuations is given by: $\tau'_w/\overline{\tau_w}$. It can be seen that the number of these fluctuations is higher for the lower strengths and lower time-durations.

Figure 6.3 (a) and figure 6.3 (b) show the "top-down" view of the distribution of the low- and high-wall shear stress fluctuations for $Re_\tau = 85$ and 180. Figure 6.3 (c) shows the PDF of wall shear stress fluctuations for these two Reynolds numbers. The distribution of the low- and high-drag events for these two Reynolds numbers is quite similar based on a simple visual inspection. To detect a low-drag or a high-drag event,

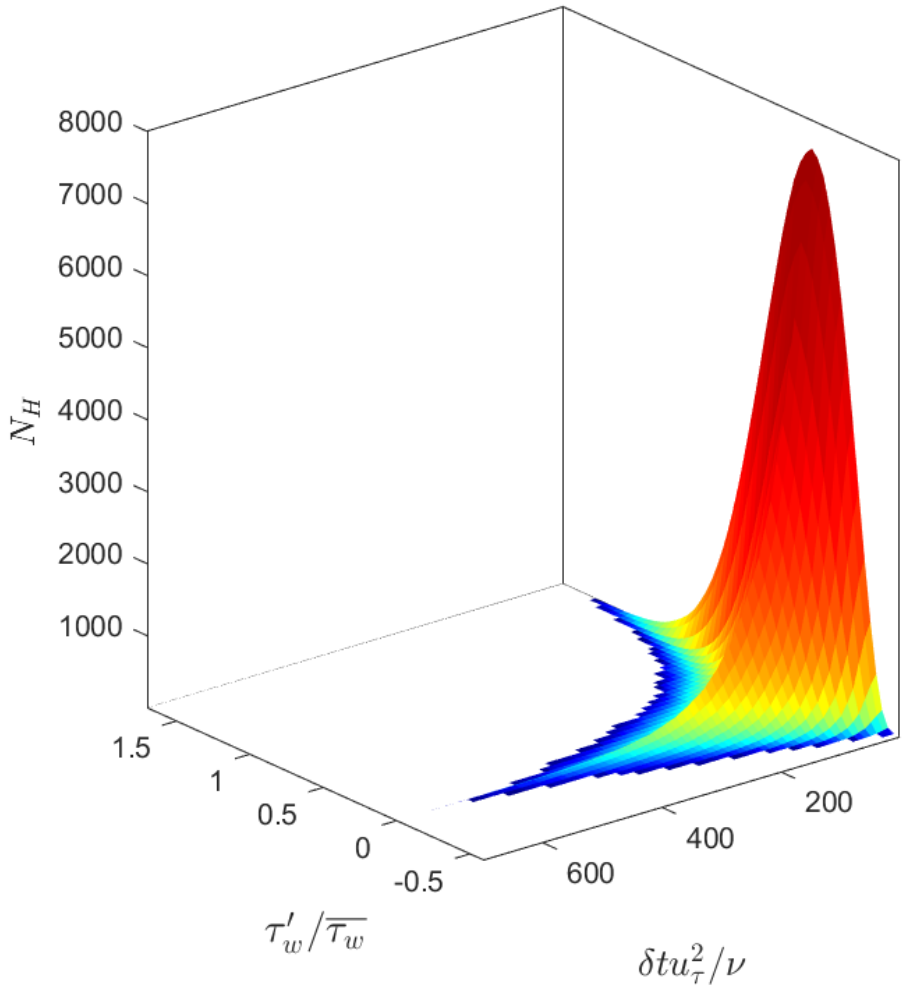

Figure 6.2: Visualization of the distribution of negative and positive wall shear stress fluctuations as a function of their strengths and time-durations for $Re_\tau = 180$. N_H represents the number of occurrences of these fluctuations for every hour of the measurement.

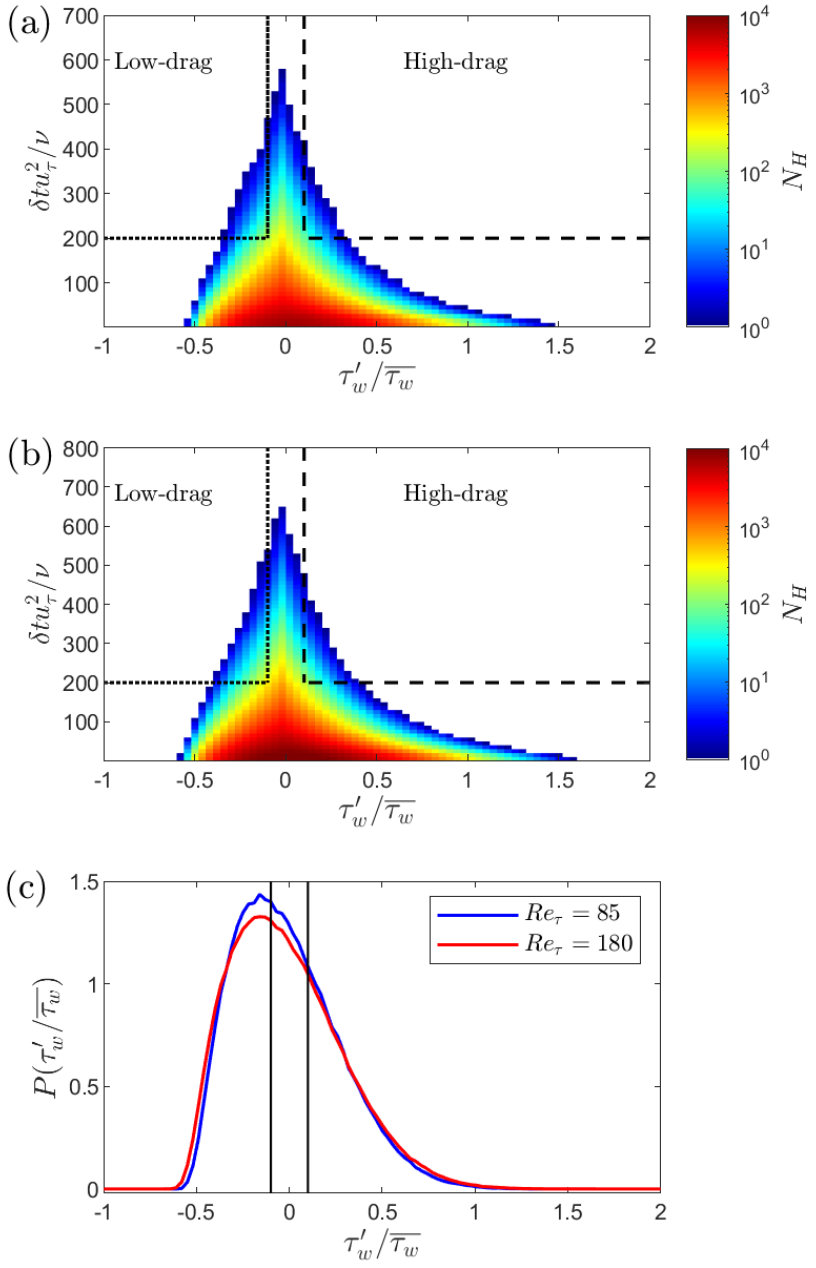

Figure 6.3: Top-down view of the distribution of negative and positive wall shear stress fluctuations per hour for (a) $Re_\tau = 85$ and (b) $Re_\tau = 180$. The black dotted lines cover the region of low-drag events based on the criteria: $\tau_w/\overline{\tau_w} < 0.9$ and $\delta t_{cr}^+ = 200$ and the black dashed lines cover the region of high-drag events based on the criteria: $\tau_w/\overline{\tau_w} > 1.1$ and $\delta t_{cr}^+ = 200$. (c) PDF of normalized wall shear stress fluctuations for $Re_\tau = 85$ and 180. Black solid lines represent the threshold criteria for the low- and high-drag events i.e. $\tau_w/\overline{\tau_w} < 0.9$ and $\tau_w/\overline{\tau_w} > 1.1$, respectively.

magnitude threshold criteria and time duration criteria are employed on the wall shear stress signals. For the threshold criteria, less than $0.9\tau_w$ for the low-drag events and greater than $1.1\tau_w$ for the high-drag events have been typically employed previously by Kushwaha et al. [2017]. Whalley et al. [2019] used the same threshold criteria for the low-drag events, but for the high-drag events they employed less stringent criteria of greater than $1.05\tau_w$, in order to obtain more data points to carry out the statistical analysis. In the present study, the same values for the threshold criteria as used by Kushwaha et al. [2017] are employed to detect the conditional events, however the effect of varying the threshold criteria will also be discussed. For the time-duration criteria, Kushwaha et al. [2017] and Whalley et al. [2017, 2019] employed a mixed scaling ($t^* = tu_\tau/h$) to detect conditional events in channel flows. They typically used $t^* = 3$ as the time-duration criterion while discussing the sensitivity of the value of the time-duration criterion on the conditional quantities. Unlike these previous studies, in the present investigation, an inner scaling is used for the time-duration criterion for the conditional events: $\delta t^+ = 200$ is used as the minimum time-duration to detect conditional events. The reasons, and implication of, choosing this scaling will be discussed in detail in the next section. The effect of varying the length of the time-duration criterion on the conditional quantities will be discussed in § 6.5. To further understand the definition of these conditional events, examples of instantaneous wall shear stress signals meeting the above-mentioned criteria for the low-drag and the high-drag events are plotted in figure 6.4. This figure shows the instantaneous normalized wall shear stress during low-drag (figure 6.4a) and high-drag (figure 6.4b) events. In figure 6.4, the acquisition time of the wall shear stress is shifted such that $t^+ = 0$ indicates the beginning of a low- or a high-drag event. Each event is shown to act longer than the minimum time duration (for "low-drag" ≈ 230 units and for "high-drag" ≈ 320 units).

6.4 Fraction of time spent in low- and high-drag events

In this study, an attempt is made to study the effect of three different scalings i.e. inner scaling, mixed scaling and outer scaling for the time-duration criteria to detect a

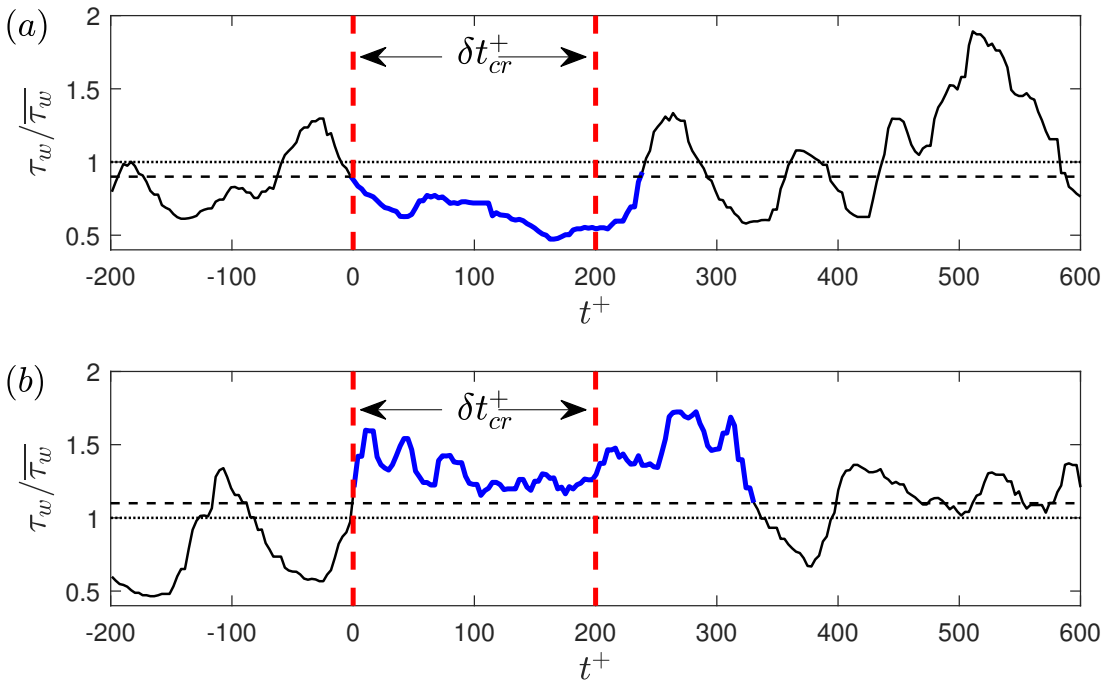

Figure 6.4: Time history of normalized wall shear stress at $Re_\tau = 180$ during (a) a low-drag and (b) a high-drag event. Blue solid lines highlight the low-drag and the high-drag events in (a) and (b). Black dotted lines show mean value of normalized wall shear stress $\tau_w/\overline{\tau_w} = 1$. Black dashed lines show $\tau_w/\overline{\tau_w} = 0.9$ and $\tau_w/\overline{\tau_w} = 1.1$ in (a) and (b), respectively. Red dashed line indicates the time-duration criteria of $\delta t^+_{cr} = 200$. In (a) and (b), t^+ is shifted such that $t^+ = 0$ indicates the beginning of a conditional event.

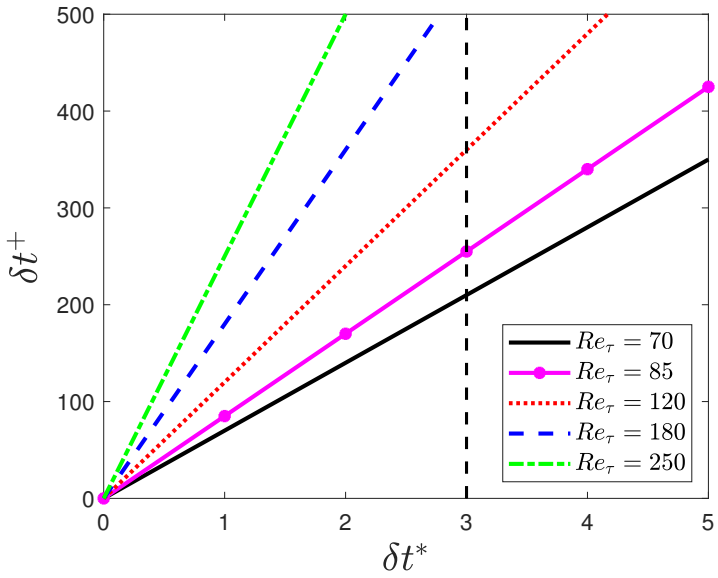

Figure 6.5: Relation between δt^* and δt^+ for various Reynolds numbers. Vertical dashed line highlights $\delta t^* = 3$ value used in previous studies by Whalley et al. [2019] and Kushwaha et al. [2017].

conditional event. Here, outer scaling is simply $\delta t \frac{U_b}{h}$, where δt is the time duration in seconds. Inner scaling ($\delta t^+ = \delta t \frac{u_\tau^2}{\nu}$) and the mixed scaling ($\delta t^* = \delta t \frac{u_\tau}{h}$) are related by the following:

$$\delta t^+ = Re_\tau \delta t^*. \tag{6.1}$$

Figure 6.5 shows the relationship between mixed and inner scalings of the time duration. From figure 6.5 and equation 6.1, it can be observed that with increasing Reynolds numbers, the δt^+ value increases for the same δt^* value. Whalley et al. [2019] studied the fraction of time spent in low- and high-drag events with changing Reynolds numbers where the time-duration criteria was kept constant in mixed scaling. They observed that with increasing Reynolds number between $70 \leq Re_\tau \leq 100$, the fraction of time spent in low-drag events decreases by approximately 500% while increasing the Re_τ from 70 to 100. Effect of other scalings have not been considered previously and is therefore studied here.

The fraction of time spent in the conditional events is investigated for $Re_\tau = 70$, 85, 120, 180 and 250 using all three scalings. For $Re_\tau = 70$, $tu_\tau/h = 3$ corresponds

to about $\delta t u_\tau^2/\nu = 200$ and $\delta t U_b/h = 42$. Based on this information, three values are chosen for each scaling to study the effect of Reynolds number on the fraction of time spent in the conditional events. For the mixed scaling, $\delta t u_\tau/h = 1$, 2 and 3, for outer scaling, $\delta t U_b/h = 15$, 30 and 45, and for the inner scaling, $\delta t u_\tau^2/\nu = 100$, 200 and 300 are used. For the low-drag events the threshold criteria is kept constant as $\tau_w/\overline{\tau_w} < 0.9$ and for the high-drag events the threshold criteria is kept constant as $\tau_w/\overline{\tau_w} > 1.1$. Figure 6.6 shows the fraction of time spent in low- and high-drag for different Reynolds numbers and the time-duration criteria. It can be observed that the fraction of time spent in low-drag or high-drag decreases with increasing Reynolds numbers when mixed or outer scaling is used for the time duration criteria. This is similar to the result obtained using the mixed scaling for the time-duration criteria by Whalley et al. [2019]. However, the fraction of time spent in the conditional events remains almost independent of the Reynolds number for $70 \leq Re_\tau \leq 250$, when the time-duration criteria is kept constant in inner units. Based on this observation, inner scaling is chosen for the time-duration criteria in the rest of this chapter. Figure 6.6(e, f) also shows that increasing the value of the time-duration criteria ($100 \leq \delta t u_\tau^2/\nu \leq 300$) decreases the fraction of time spent in these conditional events. The fraction of time spent in the intervals of low-drag is found to be greater than the intervals of high-drag for the same values of the time-duration criteria for $100 \leq \delta t u_\tau^2/\nu \leq 300$, and where the threshold criteria is kept same in terms of the magnitude ($\tau_w/\overline{\tau_w} < 0.9$ for the low-drag events and $\tau_w/\overline{\tau_w} > 1.1$ for the high-drag events). A similar observation was also made previously by Whalley et al. [2019] while using mixed scaling for the time-duration criteria.

Figure 6.6 showed that the fraction of time spent in the conditional events decreases with increasing the value of the time-duration criterion. Figure 6.7 shows the distribution of the occurrence of low- and high-drag events as a function of δt^+ for $Re_\tau = 180$. The threshold criteria to detect a low- and high-drag events are $\tau_w/\overline{\tau_w} < 0.9$ and $\tau_w/\overline{\tau_w} > 1.1$, respectively. The probability of occurrence of both low- and high-drag events decreases almost exponentially (as the y-axis is in log scale) with increasing δt^+. For $\delta t^+ \gtrsim 400$, $P(\delta t^+)$ seems to be not well-resolved because of the lower occurrence

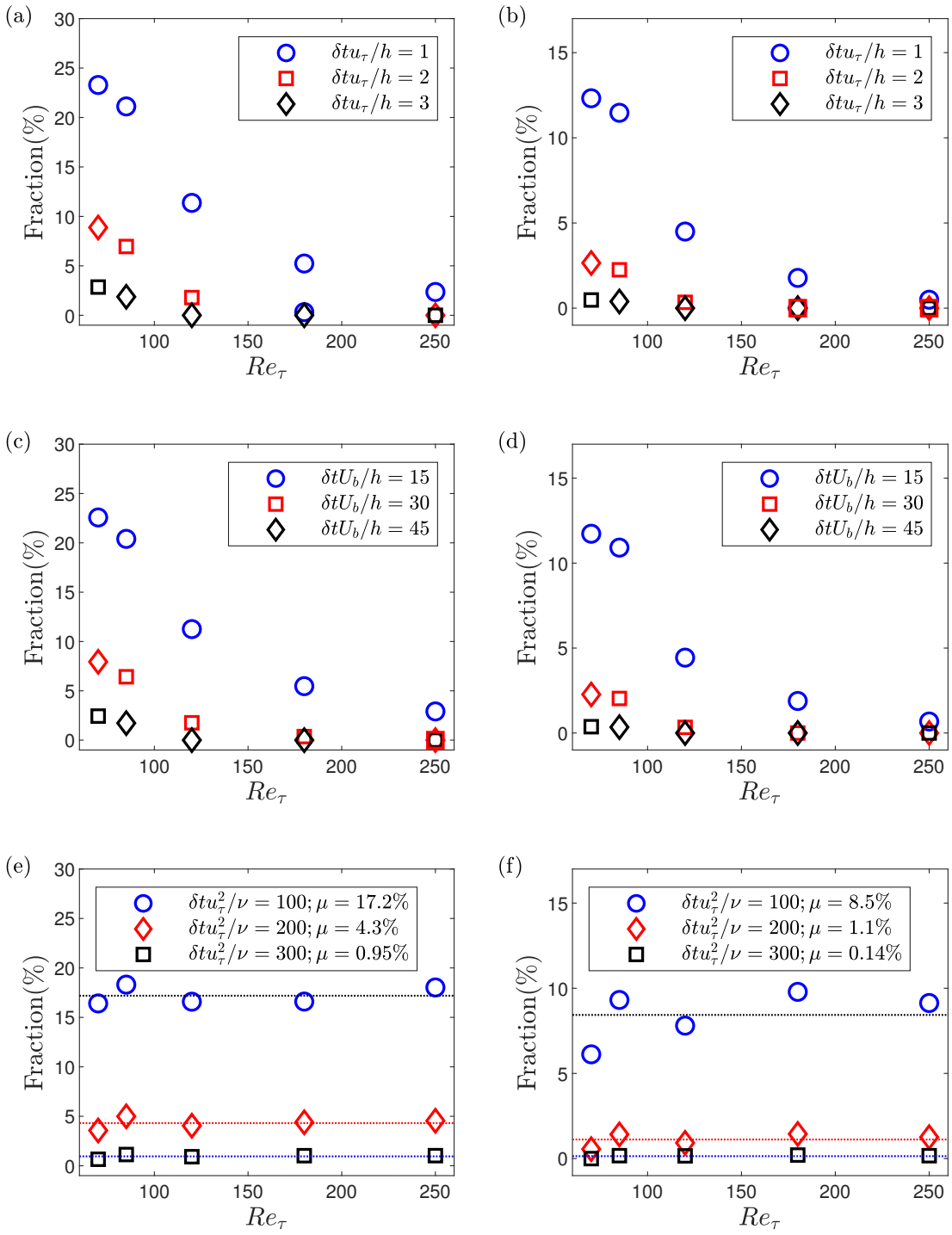

Figure 6.6: Reynolds number variation of fraction of time spent in low-drag events with using (a) mixed scaling, (c) outer scaling and (e) inner scaling for the time-duration criteria. Reynolds number variation of fraction of time spent in high-drag events with using (b) mixed scaling, (d) outer scaling and (f) inner scaling for the time-duration criteria. The threshold criteria to detect a low- and high-drag event are $\tau_w/\overline{\tau_w} < 0.9$ and $\tau_w/\overline{\tau_w} > 1.1$, respectively. Note that y-axis is not the same between low- and high-drag data. Error bars obtained by dividing the sample size into two halves and calculating the respective fraction are found to be within the size of the symbols, and are therefore removed to avoid cluttering of data.

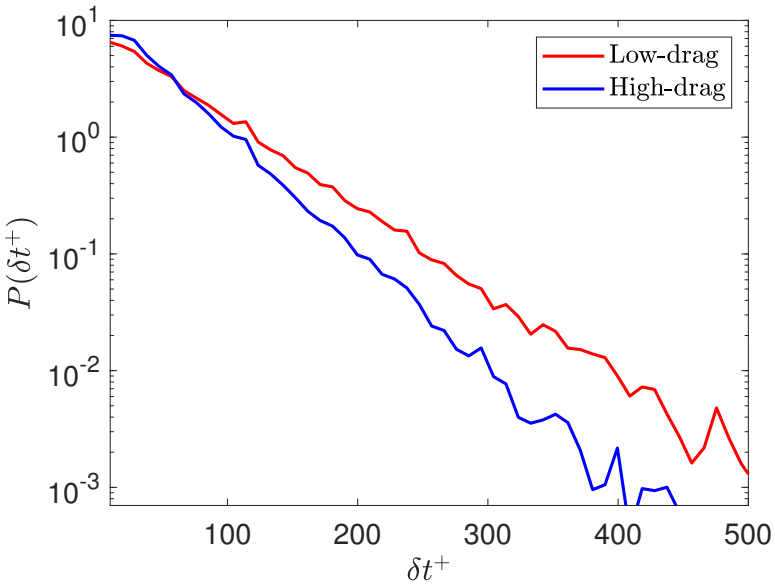

Figure 6.7: PDF of occurrence of low- and high-drag events as a function of δt^+ for $Re_\tau = 180$ where the threshold criteria for low- and high-drag events are $\tau_w/\overline{\tau_w} < 0.9$ and $\tau_w/\overline{\tau_w} > 1.1$, respectively.

of low- and high-drag events for higher δt^+, thus leading to lower number of events to carry out the statistical analysis. The distribution of high-drag events is observed to be different to the distribution of low-drag events. There is a higher probability of occurrence of high-drag events for lower δt^+ as compared to the low-drag events and vice versa. The crossover δt^+, where the behaviour of the low- and high-drag events becomes opposite, is about 60. The decay of the probability of the low- and high-drag events is then fitted with an exponential relationship for $100 \leq \delta t^+ \leq 300$, given by $P(\delta t^+) = Ae^{-\lambda \delta t^+}$. Here, λ indicates the rate of decay. The decay rate is calculated for all the Reynolds numbers. Table 6.2 shows the rate of decay obtained for low- and high-drag events at various Reynolds numbers. The rate of decay is found to almost independent of the Reynolds numbers for both low- and high-drag events, and the λ values are higher for the low-drag than the high-drag for the $100 \leq \delta t^+ \leq 300$. A slight discrepancy is observed for $Re_\tau = 70$, which can be attributed to the presence of transitional effects at this Reynolds number, as discussed in chapter 5. These results are also aligned with the results shown in 6.6(e) and 6.6(f) that the fraction of the conditional events are almost independent of the Reynolds number and the fraction of time spent in low-drag events is higher than for the high-drag events. This is the first

Table 6.2: Rate of decay (λ) of the PDF of occurrence of conditional events for $100 \leq \delta t^+ \leq 300$ at various Reynolds numbers. Numbers in brackets correspond to the R^2 value. The threshold criteria for low- and high-drag events are $\tau/\overline{\tau_w} < 0.9$ and $\tau/\overline{\tau_w} > 1.1$, respectively.

Re_τ	Low-drag	High-drag
70	0.0192 (0.89)	0.0258 (0.90)
85	0.0181 (0.95)	0.0252 (0.97)
120	0.0185 (0.98)	0.0245 (0.97)
180	0.0185 (0.96)	0.0251 (0.97)
250	0.0183 (0.99)	0.0245 (0.99)

evidence that the "low-drag" hibernating turbulent events exist significantly above the Reynolds numbers close to transition [Whalley et al., 2019] and well into the regime where the flow is considered to be fully-turbulent, i.e. $Re_\tau \geq 180$ [Kim et al., 1987].

6.5 Wall shear stress statistics during conditional events

To study the statistics of the conditional wall shear stress, the instantaneous wall shear stress during the low-drag or high-drag events is ensemble-averaged. Figure 6.8 shows the instantaneous and ensemble averaged wall shear stress fluctuations during low- and high-drag events for $Re_\tau = 180$. The ensemble averaging is executed in two ways: by shifting all the instantaneous low- and high-drag events such that $t^+ = 0$ indicates the beginning of a conditional event (shown in figure 6.8a and figure 6.8c), and by shifting all the instantaneous low- and high-drag events such that $t^+ = 0$ indicates the end of a conditional event (shown in figure 6.8b and figure 6.8d). This has been done to study the time evolution of the ensemble-averaged wall shear stress with respect to the start and the end of a conditional event. It can be seen that during the low-drag events, the ensemble averaged wall shear stress drops approximately 35% below the time-averaged value. During the high-drag events, the ensemble averaged wall shear stress rises approximately 45% above the time-averaged value. This figure also highlights that although the time-duration criteria for the conditional events is $\delta t^+_{cr} = 200$, these events can last up to $\delta t^+ \geq 400$.

The effect of the time-duration criterion on the conditional wall shear stress is investigated for $Re_\tau = 180$. For the time-duration criterion, δt^+_{cr} is varied between 100 and 300. The threshold criteria are kept constant as $\tau_w/\overline{\tau_w} < 0.9$ and $\tau_w/\overline{\tau_w} > 1.1$ for the low- and high-drag events, respectively. Figure 6.9 shows the ensemble-averaged wall shear stress for the low- and high-drag events at $Re_\tau = 180$ for various time-duration criteria. The plateau of the ensemble-averaged wall shear stress during the low- and high-drag events is observed to be insensitive to the time-duration criteria when varying δt^+ from 100 to 300, except for a minor effect for $\delta t^+_{cr} = 100$. The duration of these conditional events itself becomes smaller when lowering the δt^+_{cr} from 300 to 100. The ensemble-averaged results become less smooth with increasing time-duration criteria, especially for the high-drag events. This is attributed to the lower number of conditional events with increasing time-duration criteria as can also be seen from figure 6.6. A spike in the ensemble-averaged wall shear stress can be observed near the start and end of the low-drag events and similarly, a dip can be seen near the start and end of the high-drag events. An explanation for this phenomenon will be discussed in § 6.6.2. Analogous results corresponding to the ensemble-averaged wall shear stress during the low-drag events were also obtained by Kushwaha et al. [2017] in channel flow using DNS for $Re_\tau = 100$. They employed mixed scaling ($\delta t^* = 2$ and 3) as the time-duration criteria to detect low-drag events. Similar results were obtained for the other Reynolds numbers studied here and are not shown for brevity. It can be said that the time-duration criteria, either based on mixed or inner scaling (for the range studied), does not affect the strength of the low- or high-drag events. For the rest of this chapter, the time-duration criteria for the both low- and high-drag events is fixed at $\delta t^+_{cr} = 200$ unless stated otherwise.

6.6 Wall shear stress threshold criteria for low- and high-drag events

In the previous sections, the threshold criteria to detect a low-drag or a high-drag event was kept constant at $\tau_w/\overline{\tau_w} < 0.9$ and $\tau_w/\overline{\tau_w} > 1.1$, respectively. In this section the effect of changing the threshold criteria on the conditional wall shear stress is

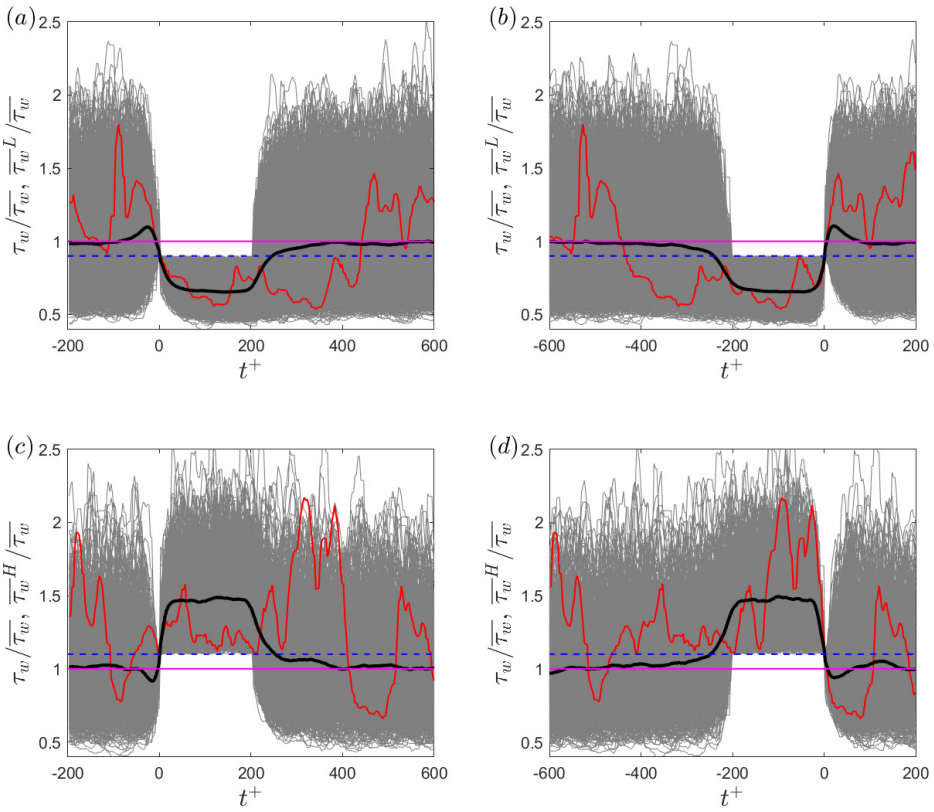

Figure 6.8: (a, b) Instantaneous normalized wall shear stress (thin grey lines) and ensemble-averaged wall shear stress (thick black line) during the low-drag events for $Re_\tau = 180$ where $t^+ = 0$ indicates (a) start of a low-drag event and (b) end of a low-drag event. Red line highlights an instantaneous low-drag event with a duration of $\delta t^+ \approx 410$. Purple line and dashed blue line represent the time-averaged value and the threshold value of $\tau_w/\overline{\tau_w} < 0.9$, respectively. (c, d) Instantaneous normalized wall shear stress (thin grey lines) and ensemble-averaged wall shear stress (thick black line) during the high-drag events for $Re_\tau = 180$ where $t^+ = 0$ indicates (a) start of a high-drag event and (b) end of a high-drag event. Red line highlights an instantaneous low-drag event with a duration of $\delta t^+ \approx 400$. Purple line and dashed blue line represent the time-averaged value and the threshold value of $\tau_w/\overline{\tau_w} > 1.1$, respectively.

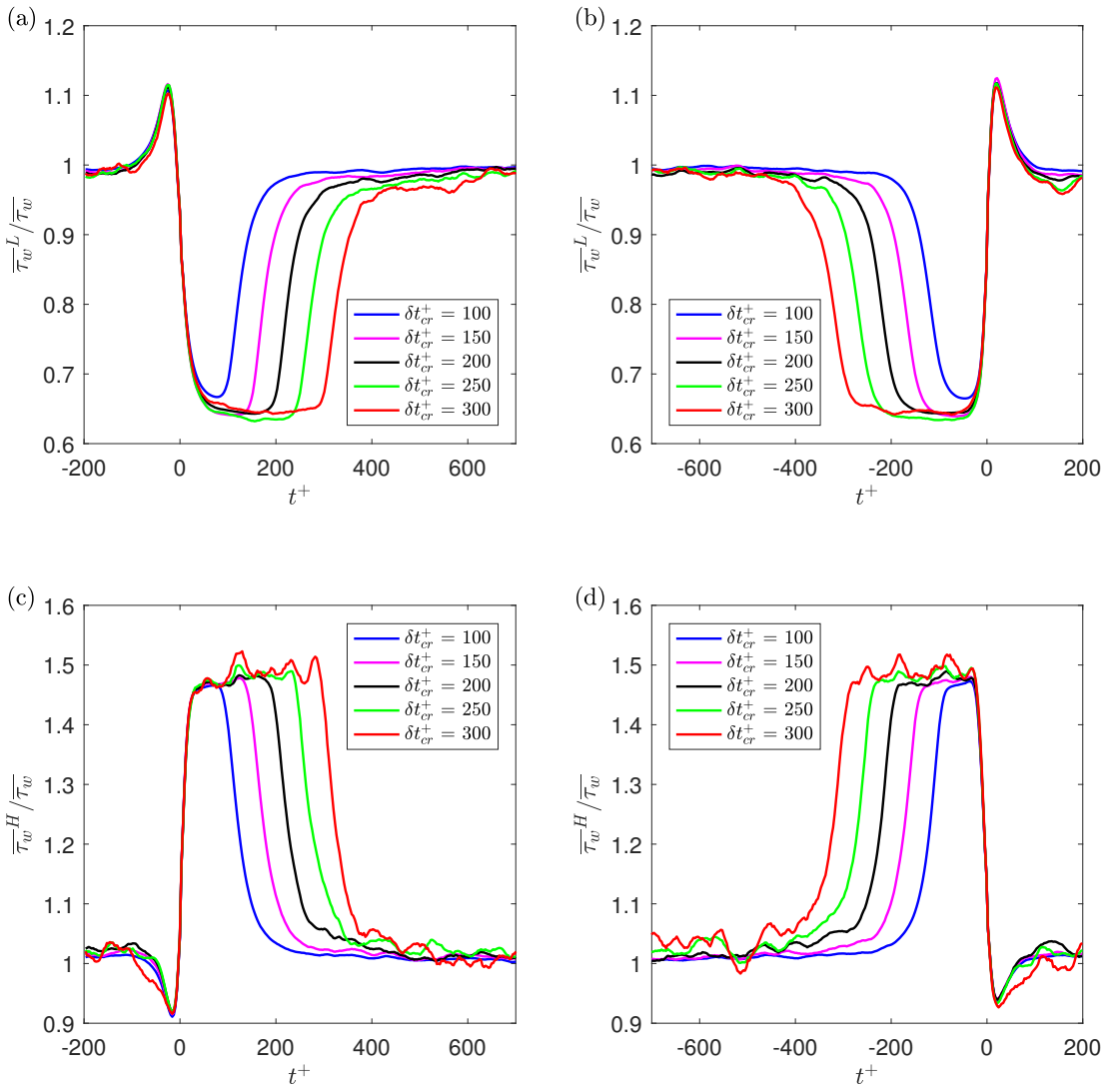

Figure 6.9: Ensemble-averaged wall shear stress for various time-duration criteria at $Re_\tau = 180$ for (a) start and (b) end of low-drag events, and (c) start and (d) end of high-drag events. The threshold criteria to detect a low- and high-drag event are $\tau_w\ /\overline{\tau_w} < 0.9$ and $\tau_w\ /\overline{\tau_w} > 1.1$, respectively.

investigated. The time-duration criterion is kept constant at $\delta t_{cr}^{+} = 200$. The results are shown only for $Re_\tau = 180$ as very similar results were obtained for the other Reynolds numbers studied.

6.6.1 Wall shear stress statistics

The threshold criteria used for low-drag events are $\tau_w/\overline{\tau_w} < 0.7$, $\tau_w/\overline{\tau_w} < 0.8$, $\tau_w/\overline{\tau_w} < 0.9$ and $\tau_w/\overline{\tau_w} < 1$, and for the high-drag events, $\tau_w/\overline{\tau_w} > 1$, $\tau_w/\overline{\tau_w} > 1.1$ and $\tau_w/\overline{\tau_w} > 1.2$. The most stringent limits for the strength in the threshold criteria are chosen based on the availability of a sufficient number of conditional events to obtain well-resolved ensemble-averaged wall shear stress results. Figure 6.10 shows the ensemble-averaged wall shear stress for the conditional events for both methods of ensemble averaging, i.e. $t^{+} = 0$ indicates either the start or end of a conditional event. As the threshold criteria is made more stringent, for the low-drag events (shown in figure 6.10a and figure 6.10b), the lower plateau of the ensemble-averaged wall shear stress decreases and for the high-drag events (shown in figure 6.10c and figure 6.10d), the upper plateau of the ensemble-averaged wall shear stress increases. Similar results were observed for low-drag events only by Kushwaha et al. [2017] at $Re_\tau = 100$.

Interestingly, as can be seen from figure 6.10, the spike in the ensemble-averaged wall shear stress for the low-drag events and dip in the ensemble-averaged wall shear stress for the high-drag events seems to be less significant with increasingly strict threshold criteria. For example, for the threshold criteria of the $\tau_w/\overline{\tau_w} < 0.7$, there seems to be almost no spike in the ensemble-averaged wall shear stress for both during the start and end of the low-drag event. Kushwaha et al. [2017] mentions that they have no physical explanation for the existence of the spike or dip in the ensemble-averaged wall shear stress data. In the following section, an explanation for this phenomenon is provided.

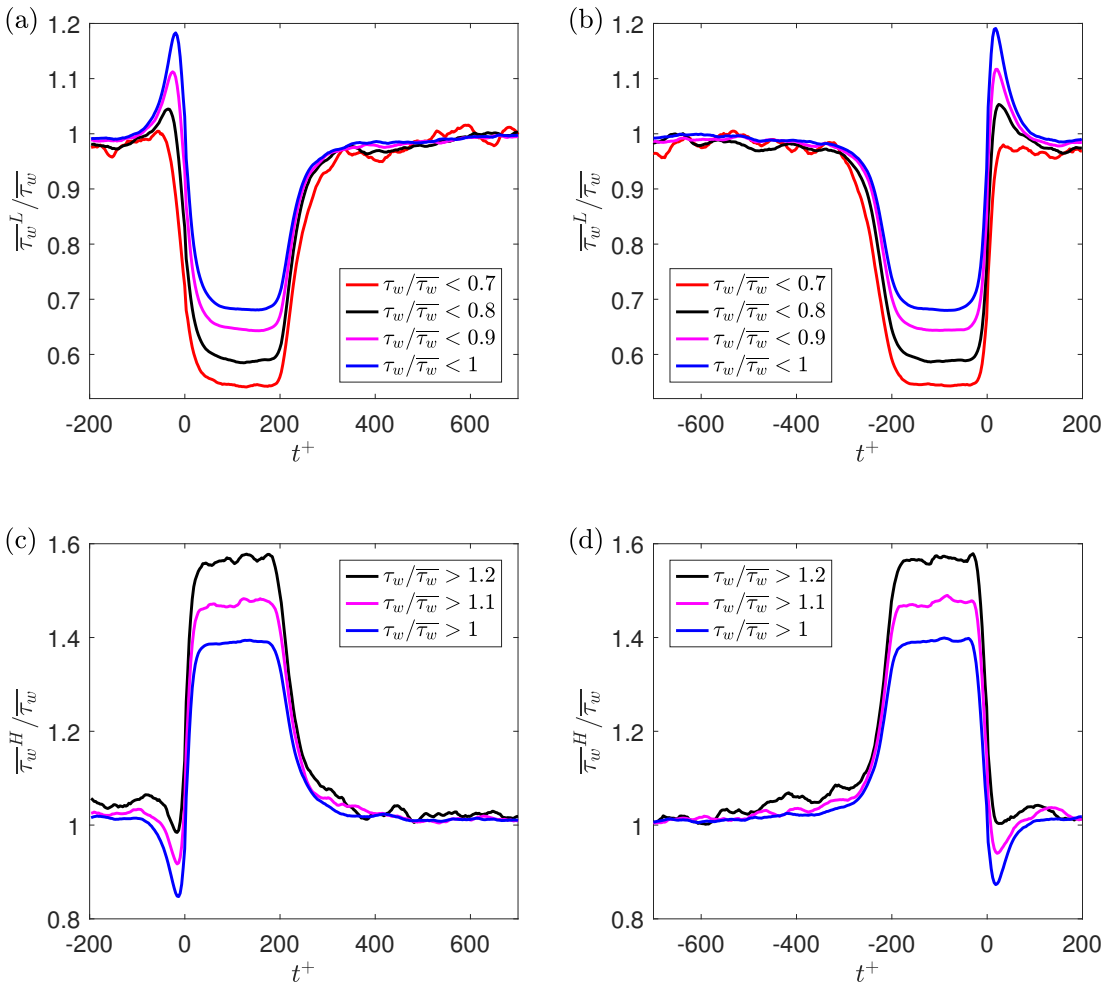

Figure 6.10: Ensemble-averaged wall shear stress for various threshold criteria at $Re_\tau = 180$ for (a) start and (b) end of low-drag events, and (c) start and (d) end of high-drag events. The time-duration criteria to detect a low-drag or a high-drag event is kept constant at $\delta t^+_{cr} = 200$.

6.6.2 Identifying reason for spike or dip before and after low-drag or high-drag events

To identify the reason for the spike or dip in the ensemble-averaged data during the conditional events, two artificially generated time series have been produced where one signal is Gaussian and the other signal has the same first four moments as the wall shear stress moments for $Re_\tau = 180$ obtained in the present experiment. The Gaussian signal has an rms value the same as the wall shear stress for $Re_\tau = 180$. This has been conducted to understand if the reason for the spike or the dip is unique to the wall shear stress signals or is merely a statistical artifact of the condition. An equal number of samples ($N = 2{\times}10^8$) are generated for both of the artificially generated signals using the inbuilt MATLAB function: "pearsrnd". Figure 6.11 shows the PDFs of the fluctuations of the three time series signals: Gaussian signal, artificial signal with the same first four moments as the wall shear stress moments for $Re_\tau = 180$, and the measured wall shear stress signal for $Re_\tau = 180$. As expected, because of the forcing of the first four statistical moments, a good agreement between the measured and the artificially generated PDFs for $Re_\tau = 180$ is observed.

A comparison of the ensemble averaged data during the conditional events is made between the two artificially generated signals. The time duration is kept the same as $\delta t^+_{cr} = 200$ to detect the low- and high-drag events. The threshold criteria are varied to study their effect on the ensemble averaged values. For the low-drag events, the threshold criteria are $\tau_w/\overline{\tau_w} < 0.925$, $\tau_w/\overline{\tau_w} < 0.95$, $\tau_w/\overline{\tau_w} < 0.975$ and $\tau_w/\overline{\tau_w} < 1$, and for the high-drag events, the threshold criteria are $\tau_w/\overline{\tau_w} > 1$, $\tau_w/\overline{\tau_w} > 1.025$, $\tau_w/\overline{\tau_w} > 1.05$ and $\tau_w/\overline{\tau_w} > 1.075$. Figure 6.12 shows the ensemble averaged wall shear stress during low- and high-drag events obtained from the two artificially generated signals. There is a spike (and dip) in the ensemble-averaged wall shear stress near the start of the low-drag (and high-drag) events for both artificially-generated signals. The existence of spikes or dips in the ensemble-averaged data from the artificially-generated signals, even in the limit of a Gaussian signal, suggest that these are artifacts of the conditional sampling and ensemble averaging and are not unique to the wall shear stress

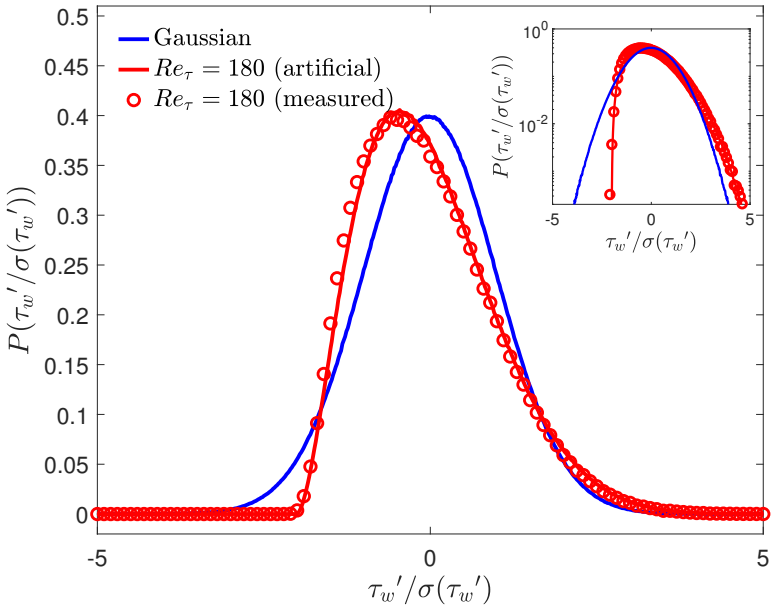

Figure 6.11: PDF of measured wall shear stress in the present channel flow facility for $Re_\tau = 180$ and artificially generated wall shear stress where blue and red lines represent the PDFs of Gaussian signal and signal with same first four moments as one measured for $Re_\tau = 180$, respectively. Inset shows the same data as the main plot but the y-axis is shown in log-scale.

signals. It is also seen that the spikes (and dips) in the ensemble-averaged data from the low-drag events (and high-drag events) becomes less significant when making the threshold criteria more stringent. This further reinforces the idea that these spikes and dips in the ensemble averaged data are the consequence of the conditional sampling of any time-series signal. Thus, these spikes or dips cannot be used to identify the onset/footprint of low- or high-drag events.

6.7 Velocity characteristics during conditional events

As mentioned in § 6.2, simultaneous measurements of velocity using LDV above the hot-film are made for various wall-normal locations (shown in table 6.1) at every Reynolds numbers studied. In this section, the criteria for conditional events are kept constant at $\delta t_{cr}^+ = 200$ and $\tau_w/\overline{\tau_w} < 0.9$ for the low-drag events, and $\delta t_{cr}^+ = 200$ and $\tau_w/\overline{\tau_w} > 1.1$ for the high-drag events, unless stated otherwise. The simultaneous measurement of streamwise velocity with the wall shear stress has been conducted for $Re_\tau = 70$, 85, 120, 180 and 250, however wall-normal velocities were measured only for $Re_\tau = 70$ and

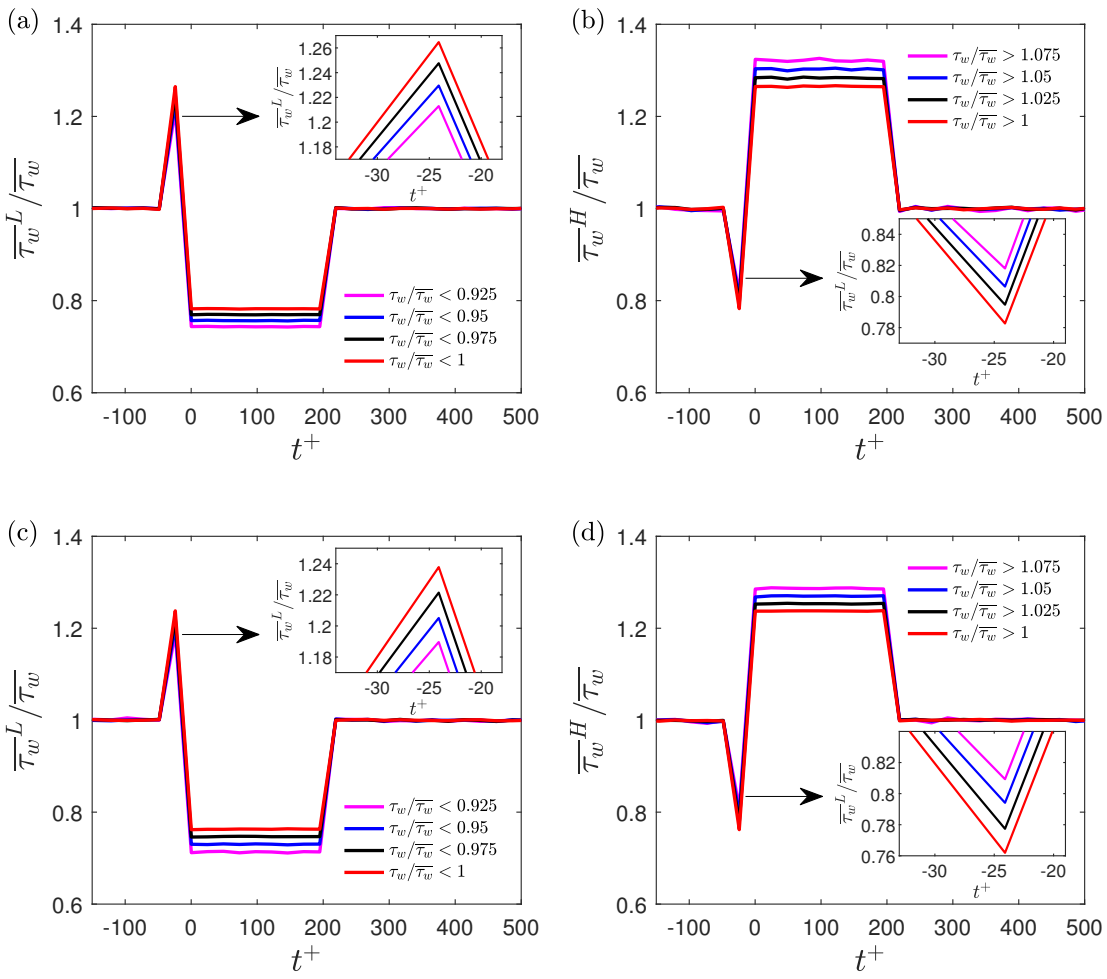

Figure 6.12: Ensemble-averaged wall shear stress during (a) low-drag events and (b) high-drag events for the artificially generated wall shear stress signal with same first four moments as one measured for $Re_\tau = 180$. Ensemble-averaged wall shear stress during (c) low-drag events and (d) high-drag events for a Gaussian signal. The time-duration criteria to detect a low-drag or a high-drag event is kept constant at $\delta t^+_{cr} = 200$. Inset plots show the same data as the main plot but only near the spike or dip in the ensemble averaged data.

85, due to the limited access of the laser beams for LDV measurements closer to the bottom wall of the channel (discussed previously in § 3.4.3).

6.7.1 Streamwise velocity

Before studying the profiles of streamwise velocity during the intermittent events, the unconditional (time-averaged) profile is shown. Figure 6.13 shows the unconditional profiles of the streamwise velocity and the streamwise turbulence intensity for Re_τ = 70, 85, 120, 180 and 250. Here, the normalization of the velocity and wall-normal locations are carried using the time-averaged wall shear stress ($\overline{u_\tau}$). DNS results obtained by Kushwaha et al. [2017] for $Re_\tau = 70$ and 85, and by Kim et al. [1987] for $Re_\tau = 180$ are shown for comparison. For $Re_\tau = 70$ and 85, the profiles of streamwise velocity and turbulence intensity obtained in the present experiment are in good agreement with the DNS profiles [Kushwaha et al., 2017]. The unconditional velocity profile obtained for $Re_\tau = 180$ is also in good agreement with the DNS profile [Kim et al., 1987], however there is some discrepancy in the turbulence intensity near the centerline of the channel. This can be attributed to the presence of ±5 - 8% error in the turbulent intensities measured using LDV and the minimum noise level of the LDV probe. It can also be seen that the velocity profiles for Re_τ of 180 and 250 approximately collapses on the log-law profile ($U^+ = 2.5 \ln y^+ + 5.5$) for y^+ greater than 30.

To carry out the conditional sampling of the velocity data, it is made sure that there are enough number of conditional events (few hundreds) to obtain well-converged results. Time evolution of the instantaneous and ensemble-averaged streamwise velocities for $Re_\tau = 70$ (at $y^+ = 28$) and 180 (at $y^+ = 30$) during the conditional events are shown in figure 6.14. During the low-drag events there is a decrease in the instantaneous and ensemble-averaged streamwise velocities, and during the high-drag events the instantaneous and ensemble-averaged streamwise velocity increases. Similar behaviour of the conditionally-sampled streamwise velocities were observed by Kushwaha et al. [2017] and Whalley et al. [2019] for Re_τ between 70 and 100, where they employed mixed scaling for the time-duration criteria to detect a conditional event. Figure 6.15 shows

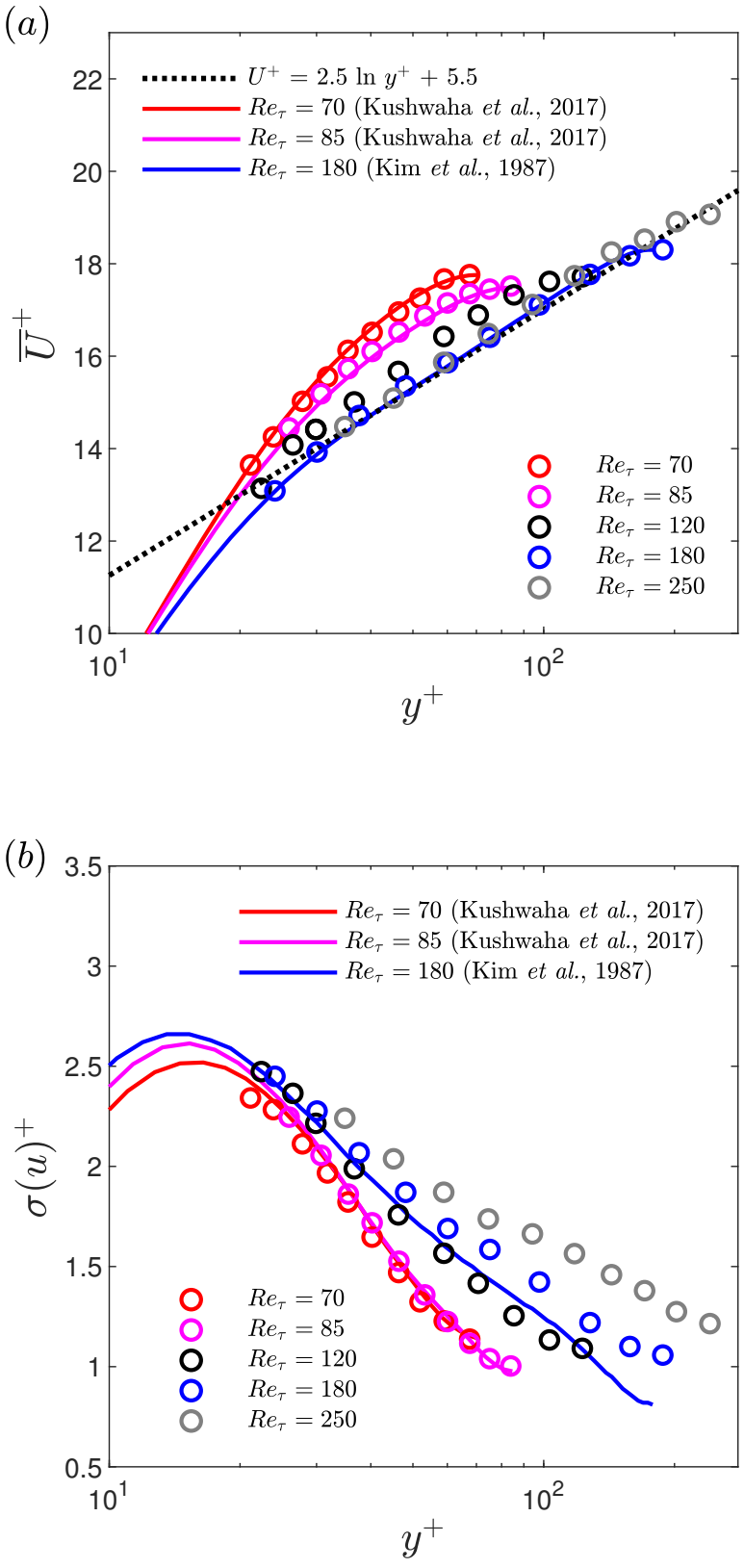

Figure 6.13: (a) Unconditional (time-averaged) streamwise velocity profiles. (b) Unconditional streamwise intensity profiles.

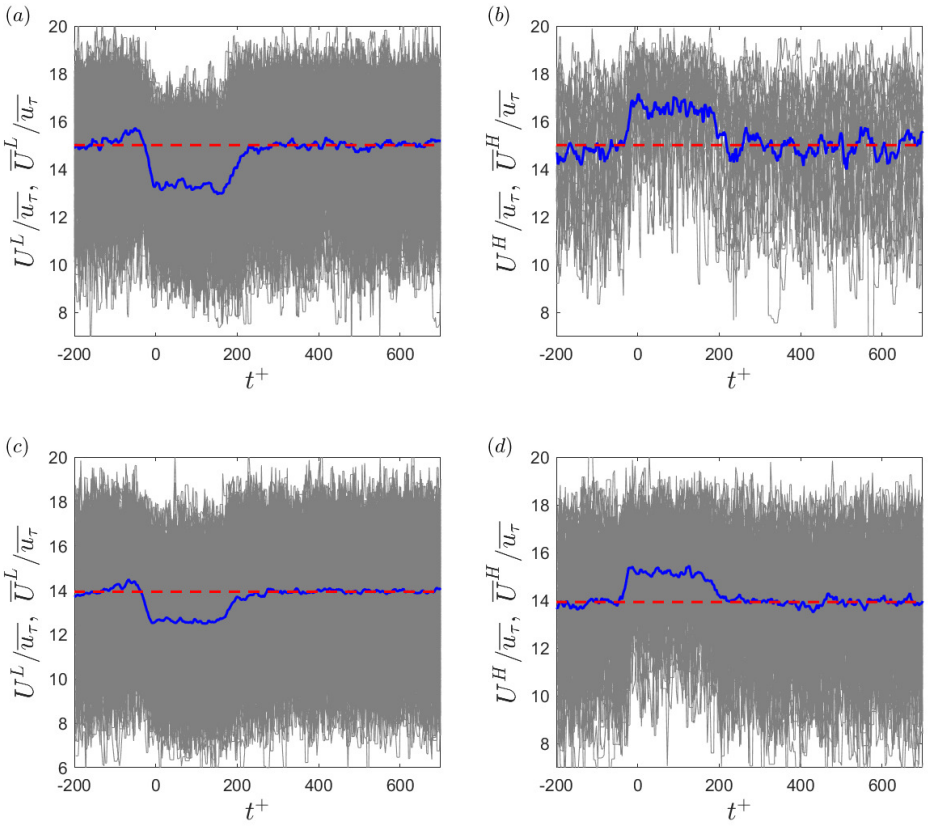

Figure 6.14: Instantaneous (thin grey lines) and ensemble-averaged (thick blue lines) streamwise velocity for $Re_\tau = 70$ (a, b) at $y^+ = 28$ and $Re_\tau = 180$ (c, d) at $y^+ = 30$, where (a, c) show the data during the low-drag events and (b, d) show data during the high-drag events. Red dashed lines indicate the time-averaged streamwise velocities for the corresponding wall-normal locations. Here, $t^+ = 0$ indicates the beginning of a low-drag or a high-drag event. The criteria to detect a low-drag event is $\delta t^+_{cr} = 200$ and $\tau_w/\overline{\tau_w} < 0.9$, and a high-drag event is $\delta t^+_{cr} = 200$ and $\tau_w/\overline{\tau_w} > 1.1$.

the ensemble averaged streamwise velocities for various wall-normal locations at Re_τ = 70, 120, 180 and 250 during the low- and high-drag events. Here, the ensemble-averaged streamwise velocities are normalized by the time-averaged friction velocities for the corresponding Reynolds numbers. The wall-normal locations are shown in both inner (yu_τ/ν) and outer (y/h) units. For the low-drag events, the drop in the ensemble averaged velocities is seen to be more significant near the wall, with the effect being disappearing near the centerline (for all the Reynolds numbers). For the high-drag events, an analogous behavior to low-drag events can be observed. Based on figure 6.15, it can be said that the streamwise velocity characteristics during the low- and high-drag events, which were previously observed for $70 \leq Re_\tau \leq 100$ by Whalley et al. [2019], also exists for higher Reynolds number at least up to $Re_\tau = 250$.

To study the velocity statistics during the conditional events, a conditional sampling of the velocity data has been carried out. This is conducted in such a way that only the upper (for high-drag) or lower plateau (for low-drag) of the instantaneous wall shear stress are considered for the conditional sampling. This is done to avoid any transient behaviours (start and end of conditional events) affecting the result. Therefore, only wall shear stress data between $30 < t^+ < t^+_{end} - 30$ are used for conditional sampling, where t^+_{end} indicates the end of a low-drag or a high-drag event. The conditionally averaged data and the corresponding wall-normal locations are normalized using two different values of mean wall shear stress: long time-averaged wall shear stress ($\overline{u_\tau}$) and conditionally averaged wall shear stress ($\overline{u_\tau}^L$ and $\overline{u_\tau}^H$ for low- and high-drag events, respectively). The effect of using two different normalizations on the conditionally averaged streamwise velocity is discussed in Xi and Graham [2012]. Conditionally averaged wall shear stress has been used earlier by Whalley et al. [2017, 2019] and Kushwaha et al. [2017] for the normalization of the conditionally averaged streamwise velocity during the low- and high-drag events in channel flows. Whalley et al. [2019] also showed the effect of normalization using the time-averaged wall shear stress on the streamwise turbulence intensity during the conditional events.

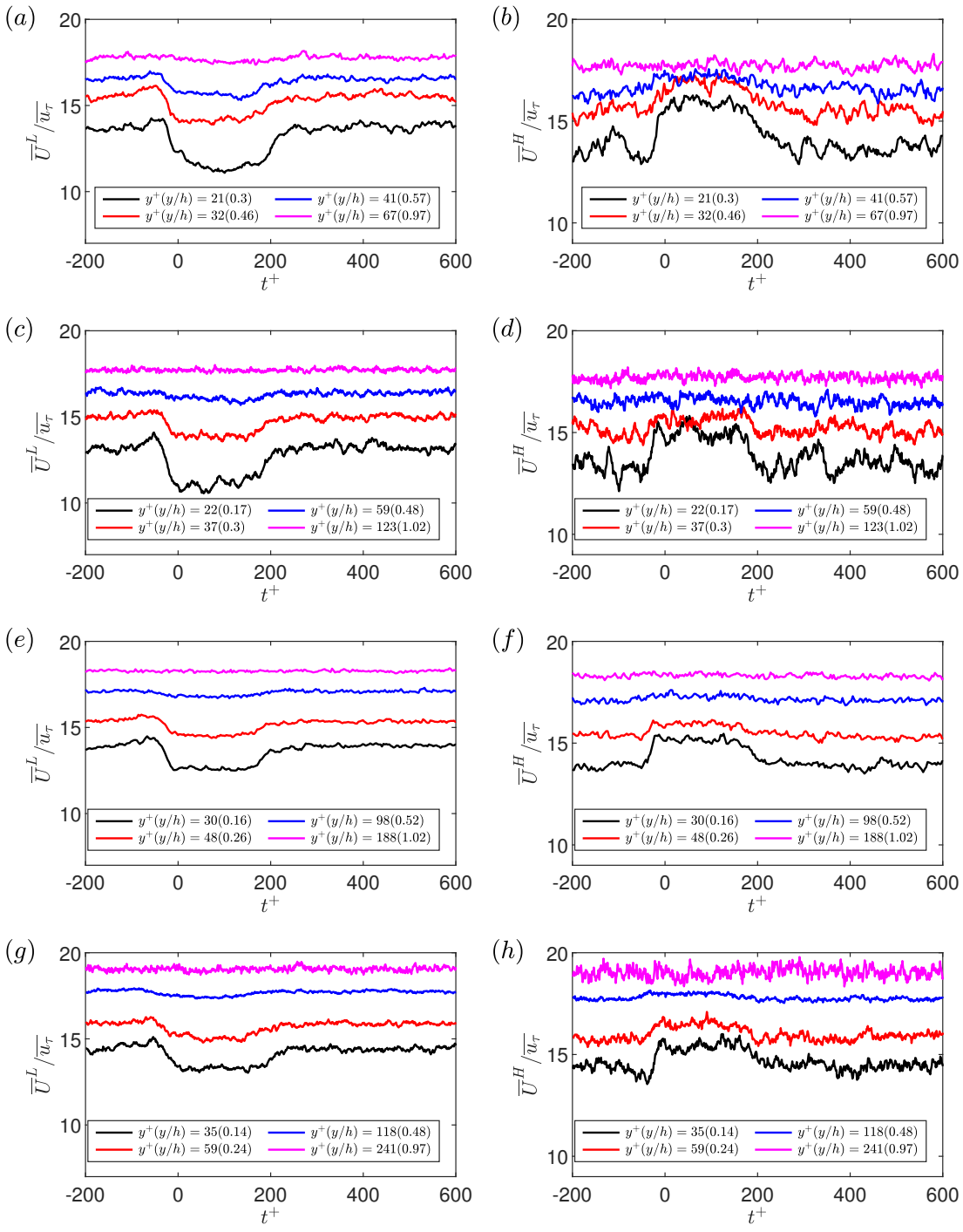

Figure 6.15: Ensemble-averaged streamwise velocity scaled with time-averaged friction velocity for $Re_\tau = 70$ (a, b), $Re_\tau = 120$ (c, d), $Re_\tau = 180$ (e, f) and $Re_\tau = 250$ (g, h), where (a, c, e, g) show the data during the low-drag events and (b, d, f, h) show data during the high-drag events. Here, $t^+ = 0$ indicates the beginning of a low-drag or a high-drag event. The criteria to detect a low-drag event is $\delta t^+_{cr} = 200$ and $\tau_w/\overline{\tau_w} < 0.9$, and a high-drag event is $\delta t^+_{cr} = 200$ and $\tau_w/\overline{\tau_w} > 1.1$.

Figure 6.16 shows the conditional streamwise velocity profiles for low- and high-drag events when the normalizations are based on time-averaged friction velocity, $\overline{u_\tau}$. The profiles are shown in two different plots based on the Reynolds numbers: $Re_\tau = 70$ and 85 for figure 6.16(a, c), and $Re_\tau = 120$, 180 and 250 for figure 6.16(b, d). This has been done to emphasize Reynolds number effects on the conditional velocity profiles. It is seen that during the low-drag events the conditional profiles ($\overline{U}^{+L}$) remain below the unconditional profile for lower y^+, and approach the unconditional mean values near the centreline, concordant with figure 6.15. For the high-drag events as shown in figure 6.16(c, d), the conditional profiles ($\overline{U}^{+H}$), remain above the unconditional profile for lower y^+, and again approach the unconditional mean values near the centreline. One more observation that can be made is that the slope of the velocity profiles during the low-drag events is higher than the slope of the time-averaged velocity profile for $y^+ \lesssim 40$. Similarly, the slope of the velocity profiles during the high-drag events is lower than the slope of the time-averaged velocity profile for $y^+ \lesssim 40$.

To further investigate the slope of the conditional velocity profiles, the so-called indicator function is calculated, which is generally used to study the logarithmic dependence of the mean velocity profile [White et al., 2012]. For the unconditional velocity data, the indicator function is given by: $\overline{\zeta} = y^+ d\overline{U}^+/dy^+$. For the conditional velocity data, the indicator functions are given by $\overline{\zeta}^L = y^{+L} d\overline{U}^{+L}/dy^{+L}$ and $\overline{\zeta}^H = y^{+H} d\overline{U}^{+H}/dy^{+H}$ for the low- and high-drag events, respectively. The profiles of indicator function are shown in figure 6.17. It can be seen that that for $Re_\tau = 70$ and 85, the $\overline{\zeta}$ profiles does not exhibit a logarithmic dependence. For $Re_\tau = 120$, 180 and 250, the $\overline{\zeta}$ profiles approximately collapse on the value of $\kappa = 2.5$ for $y^+ \geq 30$, thus suggesting a logarithmic dependence.

It is observed from figure 6.17(a, b) that the $\overline{\zeta}^L$ profiles at all Reynolds numbers are closer to the Virk's MDR ($\kappa = 11.7$) for $y^+ \leq 30$. For $Re_\tau = 120$, 180 and 250, the $\overline{\zeta}^L$ profiles remain above the unconditional profiles for $y^+ \geq 30$, thus showing that the slope of the low-drag velocity profiles is slightly higher than the unconditional profiles

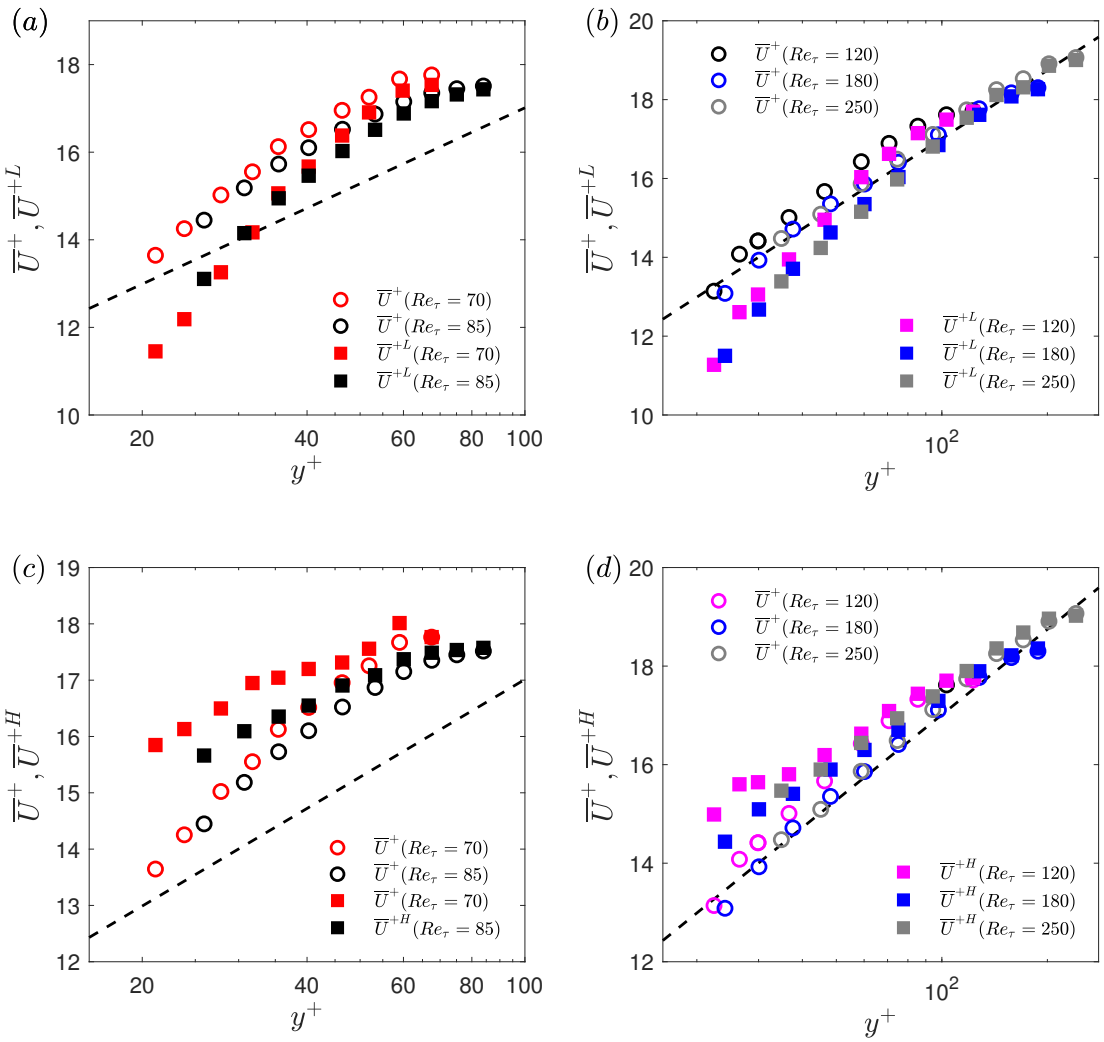

Figure 6.16: Unconditional (open circles) and conditionally averaged (closed squares) streamwise velocity profiles for (a) $Re_\tau = 70$ and 85, and for (b) $Re_\tau = 120$, 180 and 250 during low-drag events. Unconditional (open circles) and conditionally averaged (closed squares) streamwise velocity profiles for (c) $Re_\tau = 70$ and 85, and for (d) $Re_\tau = 120$, 180 and 250 during high-drag events. Here, the wall-normal locations, and the time-averaged and conditionally averaged streamwise velocity data are normalized using time-averaged wall shear stress. Black dashed line represents the Prandtl-von Kármán log-law: $U^+ = 2.5 \ln y^+ + 5.5$. The criteria to detect a low-drag event is $\delta t^+_{cr} = 200$ and $\tau_w/\overline{\tau_w} < 0.9$, and a high-drag event is $\delta t^+_{cr} = 200$ and $\tau_w/\overline{\tau_w} > 1.1$.

in the log-law region. From figure 6.17(c, d), it can be seen that the $\overline{\zeta}^H$ profiles at Re_τ = 70 and 85, are lower than the $\overline{\zeta}$ profiles (except close to the centerline), with the effect being more significant for $y^+ \leq 30$. For $Re_\tau = 120$, 180 and 250, the slope of the $\overline{\zeta}^H$ profiles is slightly lower than the $\overline{\zeta}$ profiles for all the wall-normal locations.

The streamwise velocity profiles, normalized by the conditionally averaged friction velocity ($\overline{u_\tau}^L$ for low-drag and $\overline{u_\tau}^H$ for high-drag) are shown in figures 6.18 (a) and 6.18 (b). It can be seen from figure 6.18 (a) that for $y^+ \approx 20$ - 35, the conditionally averaged velocity profiles are higher and closer to the Virk's MDR asymptote than their time-averaged values (for all the Reynolds numbers studied). Previously, Kushwaha et al. [2017] and Whalley et al. [2019] showed that at $70 \leq Re_\tau \leq 100$, the low-drag velocity profiles get closer to the Virk's MDR for similar wall-normal locations ($y^+ \approx 20$ - 35). Therefore, the present result confirms the validity of this phenomenon for Reynolds numbers in the fully-turbulent regime. For higher wall-normal locations the conditional velocity profiles start to deviate from the Virk's MDR profile, and for $y^+ \gtrsim 100$, the conditional velocity profiles have a slightly higher slope as compared to the Prandtl-von Kármán log-law, as seen for Re_τ = 180 and 250. For the high-drag events, the conditional velocity profiles are lower than the unconditional profiles for all the Reynolds numbers.

6.7.2 Similarity between turbulent drag reduction and low-drag events in Newtonian turbulence

To quantify the "drag reduction" during the low-drag events a percentage decrease in the wall shear stress, during these low-drag events, is calculated. To enable comparison with the drag-reduction literature, only the results for Re_τ = 180 and 250 are considered. It is found that the percentage drag reduction is about 36% for Re_τ = 180 and 250 when calculated using equation 6.2.

$$\%DR = \frac{\overline{\tau_w} - \overline{\tau_w}^L}{\overline{\tau_w}} \approx 36\%(Re_\tau = 180 \text{ and } 250). \tag{6.2}$$

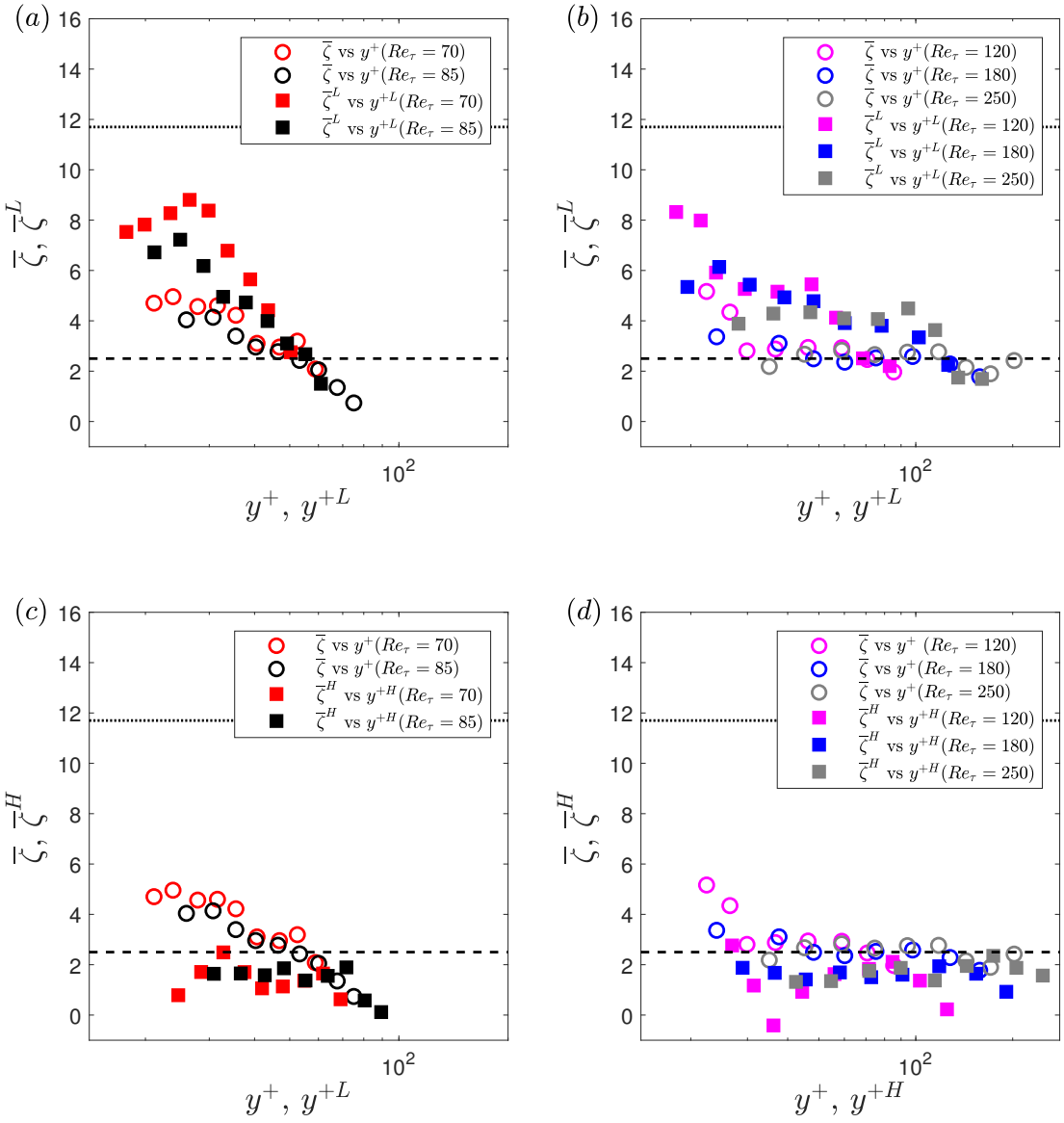

Figure 6.17: Unconditional (open circles) and conditionally averaged (closed squares) indicator functions for (a) $Re_\tau = 70$ and 85, and for (b) $Re_\tau = 120$, 180 and 250 during low-drag events. Unconditional (open circles) and conditionally averaged (closed squares) indicator functions for (c) $Re_\tau = 70$ and 85, and for (d) $Re_\tau = 120$, 180 and 250 during high-drag events. The criteria to detect a low-drag event is $\delta t^+_{cr} = 200$ and $\tau_w/\overline{\tau_w} < 0.9$, and a high-drag event is $\delta t^+_{cr} = 200$ and $\tau_w/\overline{\tau_w} > 1.1$. Dashed lines represent 2.5 and dotted lines represent 11.7.

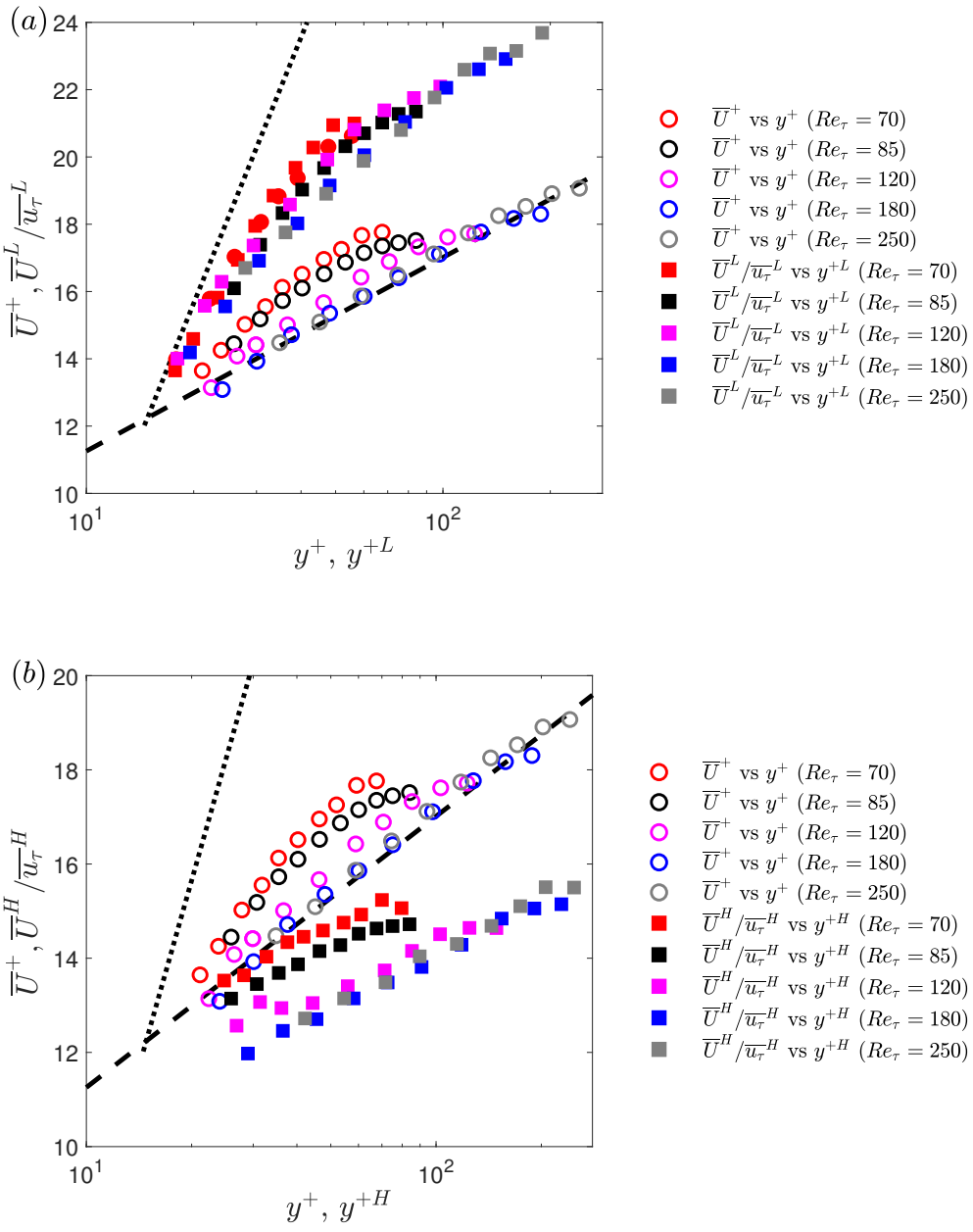

Figure 6.18: Unconditional (open circles) and conditionally averaged (closed squares) streamwise velocity profiles for $Re_\tau = 70$, 120, 180 and 250 during (a) low-drag and (b) high-drag events. Here, the conditionally averaged streamwise velocity data is normalized using conditionally averaged wall shear stress. Black dashed line represents the Prandtl-von Kármán log-law: $U^+ = 2.5 \ln y^+ + 5.5$ and the black dotted line represents the lower end of the 95% confidence interval of the Virk's MDR asymptote [Graham, 2014].

This level of drag reduction is similar to some of the other techniques employed previously to reduce drag in channel flows. For example, when using polymer additives at low concentration, the low-drag reduction (LDR) is observed [Warholic et al., 1999]. A comparison is made with the experimental data obtained by Warholic et al. [1999] for $Re_h \approx 20000$ for the case where a drag reduction of about 33% was observed. Drag reduction due to superhydrophobic surfaces was investigated by Min and Kim [2004]. They conducted DNS in a channel flow for $Re_\tau = 180$ (for DR = 0) and by using streamwise slip, they obtained a maximum drag reduction of 29%. Choi et al. [1994] implemented DNS in a channel flow at $Re_\tau = 180$ (for DR = 0) to numerically study the effect of blowing and suction on the skin-friction drag. They employed out-of-phase boundary conditions for the spanwise and wall-normal velocities to simulate the blowing and suction effects on the channel. They obtained a drag reduction of about 26% by applying spanwise control.

In figure 6.19 a comparison is made between the streamwise velocity profiles obtained using these three techniques for turbulent drag reduction and the conditional streamwise velocity profile obtained in the present experiment for $y^+ \geq 20$ at $Re_\tau = 180$ and 250. A good agreement can be seen between the conditionally averaged profile for $Re_\tau = 180$ and 250 and the profile obtained by Warholic et al. [1999] for $DR = 33\%$ using polymer additives. The agreement between the profiles obtained by Min and Kim [2004] and Choi et al. [1994], and the present experiment are also in relatively good agreement with the obvious difference arising due to the lower levels drag reduction reported in these cases. One major difference in the result obtained by Min and Kim [2004] is that the velocity profile shifts upwards even closer to the wall which is the consequence of the slip boundary condition. Therefore, it suggests that for the fully-turbulent flows ($Re_\tau = 180$ and 250), the conditional streamwise velocity for $y^+ \geq 20$ during the low-drag events mimics the flow as observed during the LDR phenomenon due to polymer addition or the drag reduction due to spanwise oscillation. For the case of superhydrophobicity, this similarity between the velocity profiles can be observed approximately in the log-law region. Thus, if a method could be found to encourage

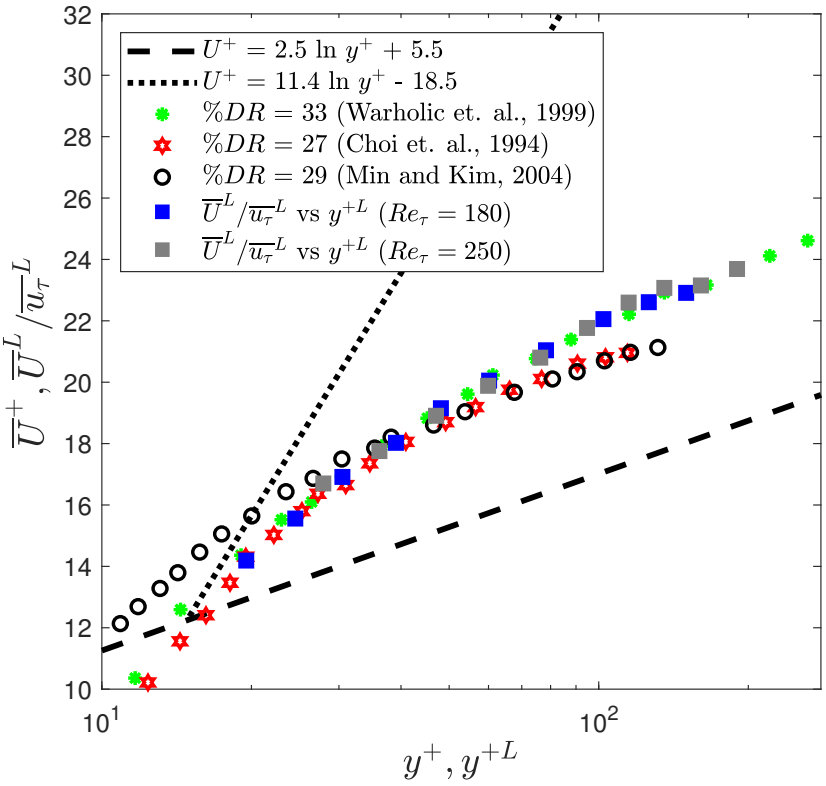

Figure 6.19: Conditional streamwise velocity profiles for $Re_\tau = 180$ and 250 during the low-drag event. Streamwise velocity profiles, where different drag reduction mechanisms are employed previously: Warholic et al. [1999] used polymeric additive, Min and Kim [2004] used hydrophobic surface in the form of slip-boundary condition for the streamwise direction and Choi et al. [1994] applied out-of-phase boundary condition to the spanwise velocity at the surface.

the turbulent state to enter the "low-drag" state more often, a significant time-averaged drag reduction would be achievable.

6.7.3 Reynolds shear stress

DNS study by Park and Graham [2015] and Xi and Graham [2012], using MFU at $Re_\tau = 85$, showed that the Reynolds shear stress drops to a very low value during the low-drag events (discussed in § 2.5.2). There is still no information about the RSS characteristics, during the conditional events, from either physical experiments or from DNS in extended domains. In this study, two-component (streamwise and wall-normal) velocity measurements have been made for $Re_\tau = 70$ and 85 to study the behaviour of the Reynolds shear stress during the conditional events. To carry out the conditional sampling, each wall-normal location is sampled for 2 hours while simultaneously measuring the wall shear stress using HFA (discussed previously in § 6.2).

The unconditional Reynolds shear stress (RSS) profiles, obtained for these two Reynolds numbers, are shown in figure 6.20. A good agreement can be observed with the unconditional profiles obtained using DNS [Kushwaha et al., 2017]. A mean momentum balance analysis is carried out to study the contribution of the Reynolds shear stress and viscous stress to the total stress in the present channel flow for $Re_\tau = 70$ and 85. The mean momentum balance, in the integrated form, is given by [Pope, 2000]:

$$u_\tau^2\Big(1 - \frac{y}{\delta}\Big) = \nu\frac{dU}{dy} - \overline{uv}. \tag{6.3}$$

This mean momentum equation shows the variation of the total stress in the wall-normal direction of the channel. The total stress can be calculated by adding the RSS and viscous stress, as shown in equation 6.3. The mean momentum balance has been previously conducted by Elsnab et al. [2011] for channel flow. An attempt is made to compare the total stress calculated from present experimental data and the theoretical total stress. The total stress is normalized by the $\overline{u_\tau}^2$, and is given by:

$$\chi = \frac{\nu\frac{d\overline{U}}{dy} - \overline{uv}}{\overline{u_\tau}^2} \tag{6.4}$$

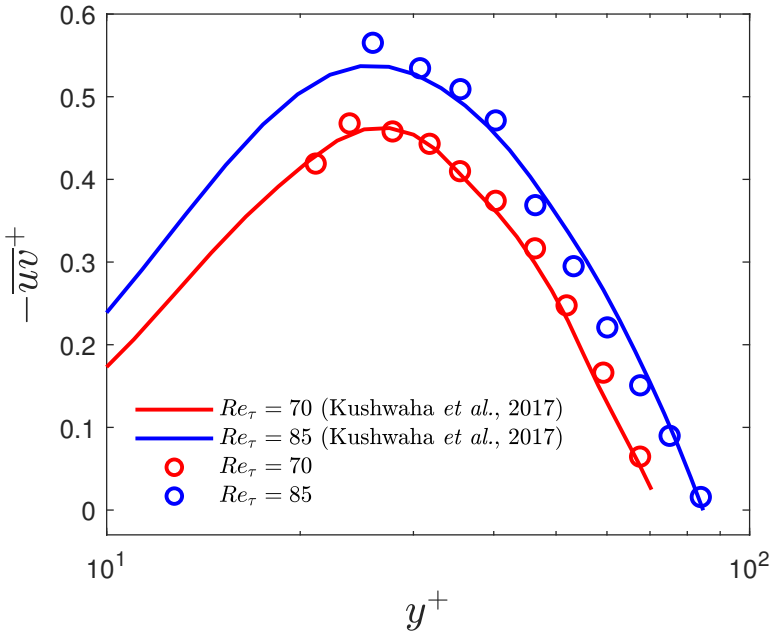

Figure 6.20: Unconditional RSS profiles for $Re_\tau = 70$ and 85, where solid lines represent DNS data [Kushwaha et al., 2017] and symbols represent data obtained in the present experiment.

Figure 6.21 shows the normalized total stress (χ) profile for $Re_\tau = 70$ and 85. The central difference method is employed for the gradient calculation except for the first and last wall-normal locations, for which forward and backward difference methods are employed, through necessity. A good agreement can be seen between the theoretical and the experimental total shear stress profile. Fairly minor deviations can be seen for some data points which is attributed to the error associated with the calculation of streamwise velocity gradients, especially for the first and last wall-normal locations.

A quadrant analysis is conducted to calculate the contribution to the Reynolds shear stress from various turbulent events [Wallace, 2016]. In quadrant analysis, the Reynolds shear stress is divided into four quadrants based on the signs of the streamwise and wall-normal velocity fluctuations: Q1 ($+u$, $+v$), Q2 ($-u$, $+v$), Q3 ($-u$, $-v$), and Q4 ($+u$, $-v$). The Q2 and Q4 events are generally related to the ejection and sweep events, respectively [Wallace, 2016]. The fundamentals of quadrant analysis has already been discussed in § 2.4.1. Figure 6.22 shows the joint distribution of the unconditional streamwise and wall-normal velocity fluctuations for $y^+ = 24$ at $Re_\tau = 70$, while also

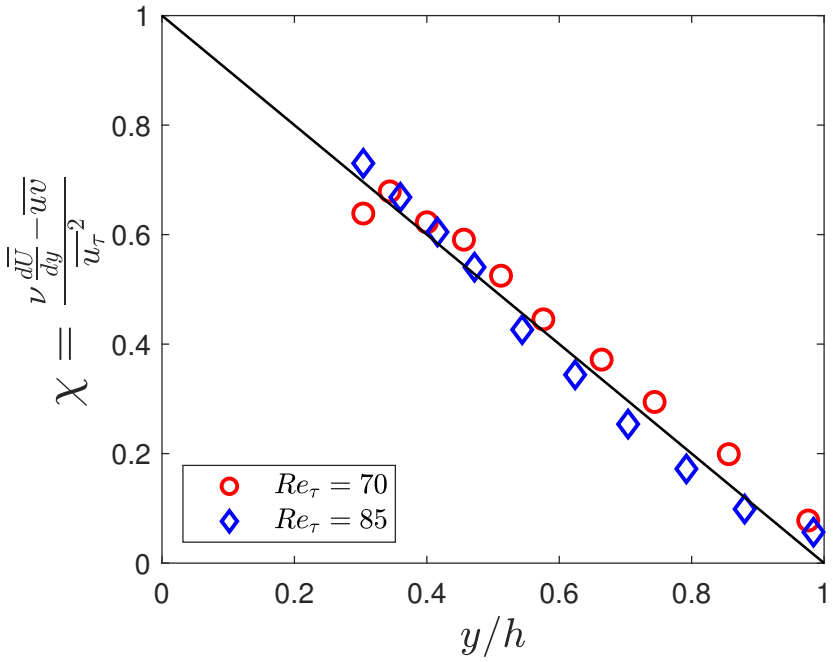

Figure 6.21: Unconditional normalized total stress (χ) profile for $Re_\tau = 70$ and 85. Solid black line indicates the theoretical total stress profile.

highlighting the four quadrants. The shape of the jpdf is roughly elliptical with its major axis tilted in the direction of Q2 and Q4 motions. Similar shape of the joint distribution of the velocity fluctuations were obtained by Wallace [2016] for $y^+ = 45$ at $Re_\tau = 194$, and has been previously shown in figure 2.10.

Figure 6.23 shows the profiles of contribution from the various quadrants in the Reynolds shear stress for $Re_\tau = 70$ and 85. It can be seen that the major contributors to the Reynolds shear stress are the Q2 and Q4 motions, which explains the reason for the tilted shape of the jpdf shown in figure 6.22. These two quadrants are considered to be responsible for the turbulence production (discussed previously in § 2.4.1). It is also observed that the Q2 motions or the "ejection" type motions are the most dominant motions for the measured wall-normal locations for $Re_\tau = 70$ and 85. This is consistent with the previous result by Kim et al. [1987] (for $Re_\tau = 180$, using DNS), where they showed that Q2 motion is the largest contributor to the Reynolds shear stress for similar wall-normal locations.

In order to calculate the conditional RSS, the streamwise velocity fluctuations and

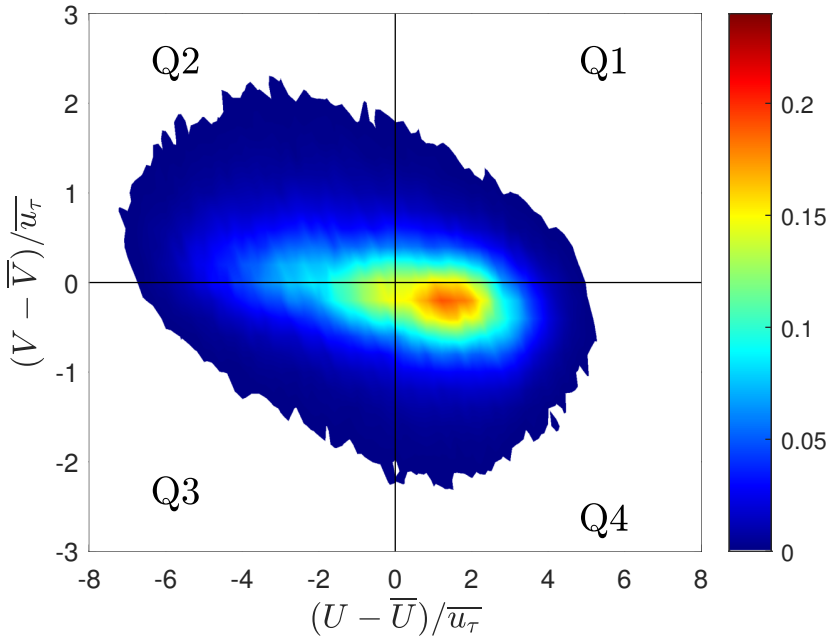

Figure 6.22: Unconditional jpdf of streamwise and wall-normal velocity fluctuations for $y^+ = 24$ at $Re_\tau = 70$. The velocity fluctuations are normalized by the time-averaged friction velocity, $\overline{u_\tau}$. Vertical and horizontal black solid lines are used to distinguish the four quadrants based on the sign of the velocity fluctuations.

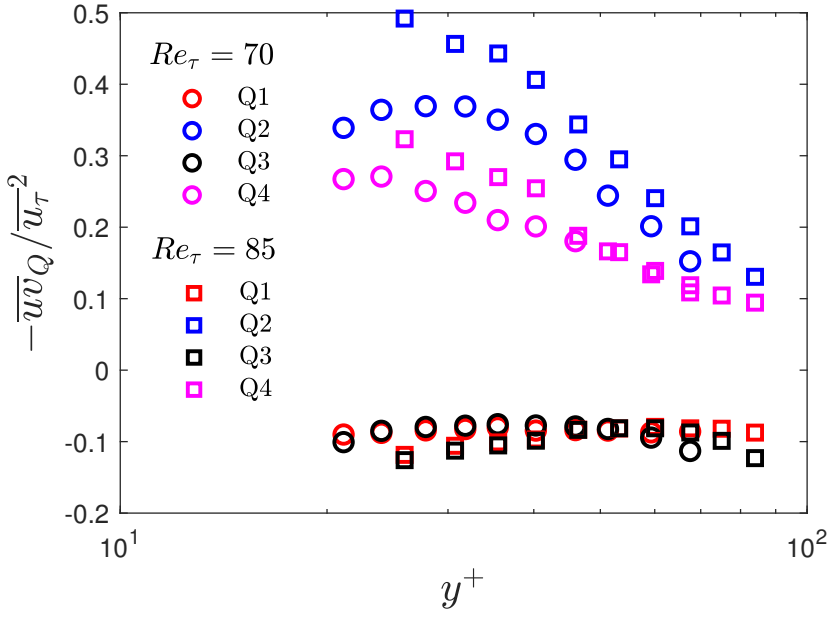

Figure 6.23: Contribution to $-\overline{uv}$ from different quadrants for $Re_\tau = 70$ and 85. The contributions from the four quadrants add to the net Reynolds shear stress (shown in figure 6.20)

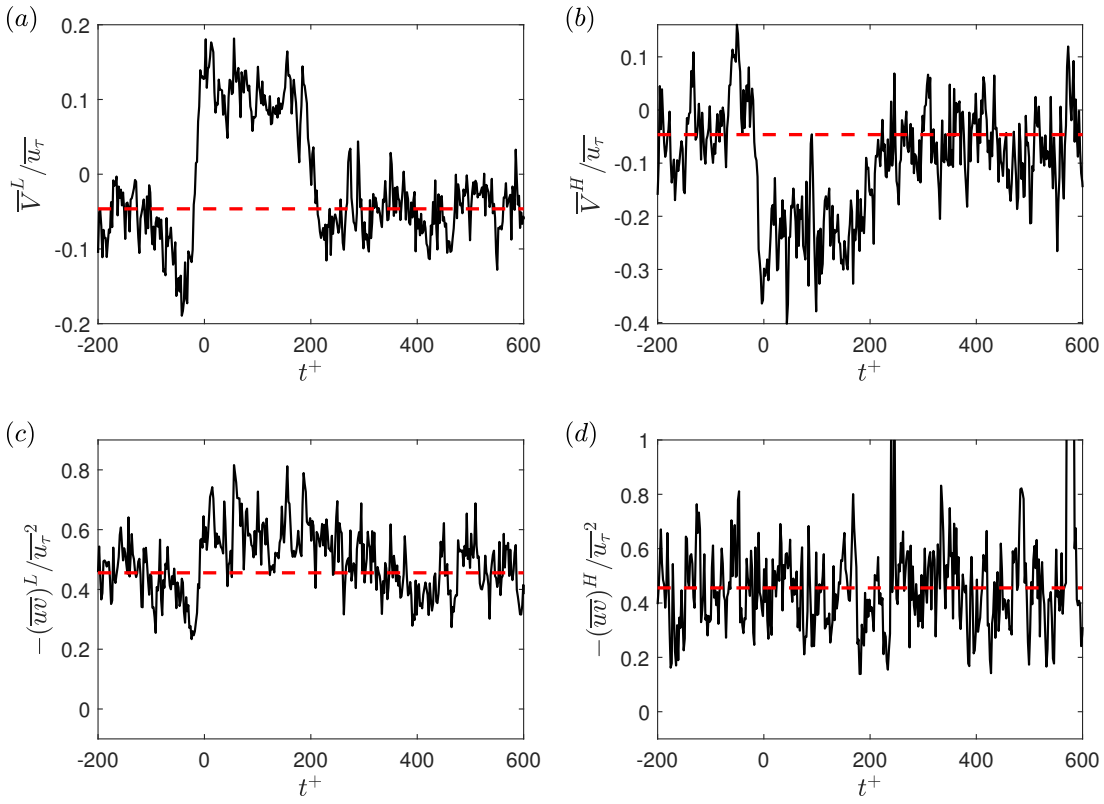

Figure 6.24: Ensemble-averaged wall-normal velocity scaled with time-averaged friction velocity for $Re_\tau = 70$ at $y^+ = 28$ during (a) low-drag events and (b) high-drag events. Ensemble-averaged Reynolds shear stress scaled with time-averaged friction velocity for $Re_\tau = 70$ at $y^+ = 28$ during (c) low-drag events and (d) high-drag events. Here, $t^+ = 0$ indicates the beginning of a low-drag or a high-drag event. The criteria to detect a low-drag event is $\delta t^+_{cr} = 200$ and $\tau_w/\overline{\tau_w} < 0.95$, and a high-drag event is $\delta t^+_{cr} = 200$ and $\tau_w/\overline{\tau_w} > 1.05$. Red dashed lines indicate the time-averaged values for the corresponding wall-normal locations.

the wall-normal velocity fluctuations during the conditional events are calculated by subtracting their time-averaged values from the instantaneous conditional values. Figure 6.24 shows the ensemble averaged wall-normal velocities ($\overline{V}^L$ and $\overline{V}^H$) and ensemble averaged Reynolds shear stress ($-\overline{uv}^L$ and $-\overline{uv}^H$). All the quantities are normalized by the time-averaged friction velocity ($\overline{u_\tau}$). The threshold criteria to detect a low- and high-drag events are $\tau_w/\overline{\tau_w} < 0.95$ and $\tau_w/\overline{\tau_w} > 1.05$. Less stringent criteria are chosen to show the ensemble-averaged profiles more clearly in figure 6.24 (a sensitivity check to the conditional values with respect to the threshold criteria will be made later in this section). The time duration criteria is kept the same at $\delta t^+_{cr} = 200$ for both types of events. The ensemble averaged streamwise velocities have already been shown in figure 6.15 (a, b) for $Re_\tau = 70$ at various wall-normal locations. It is seen that the con-

ditionally averaged wall-normal velocity is higher than the time-averaged wall-normal velocity during the low-drag events and this behaviour flips during the high-drag events where the conditionally averaged wall-normal velocity is lower than the time-averaged wall-normal velocity. Based on the conditionally-averaged streamwise and wall-normal velocities, it can be said that the low-drag corresponds to Q2 events and the high-drag corresponds to Q4 events for $y^+ = 28$ at $Re_\tau = 70$, at least in the ensemble-averaged sense. The ensemble averaged Reynolds shear stress is observed to be marginally higher than the corresponding time-averaged value during the low-drag events, whereas during the high-drag events the ensemble averaged RSS remains unchanged. This behaviour will be further investigated in the following discussions.

The conditionally-averaged RSS profiles, normalized using $\overline{u_\tau}^2$, are shown in figure 6.25. For the low-drag case, as seen in figure 6.25 (a), the conditionally averaged profiles have higher values than the unconditional profiles for all y^+ although the effect is higher for y^+ between 20 and 40. For the high-drag case, as seen in figure 6.25 (b), the conditionally-averaged RSS profiles almost collapse onto the unconditional profiles for all the wall-normal locations measured. This result suggests that the Reynolds shear stress is more affected by the low-drag events compared to the high-drag events. A sensitivity check has been executed to study the effect of changing the criteria for conditional events on the conditional RSS profiles for $Re_\tau = 70$. Figure 6.26 (a) shows the effect of changing threshold criteria ($\tau_w/\overline{\tau_w} < 1$, 0.9 and 0.8) for the time duration criteria of $\delta t^+_{cr} = 200$, and the effect of changing the time duration to $\delta t^+_{cr} = 100$ for the threshold criteria of $\tau_w/\overline{\tau_w} < 0.9$ during the low-drag events. Figure 6.26 (b) shows the effect of changing threshold criteria ($\tau_w/\overline{\tau_w} > 1$, 1.1 and 1.15) for the time duration criteria of $\delta t^+_{cr} = 200$, and the effect of changing the time duration to $\delta t^+_{cr} = 100$ for the threshold criteria of $\tau_w/\overline{\tau_w} > 1.1$ during the high-drag events. The profiles are smoother for the case of less stringent criteria to detect a conditional event. This is mainly because of the higher number of conditional events using the less stringent criteria included in the statistical analysis. No significant dependence of the RSS profiles is observed for the different values of criteria studied here.

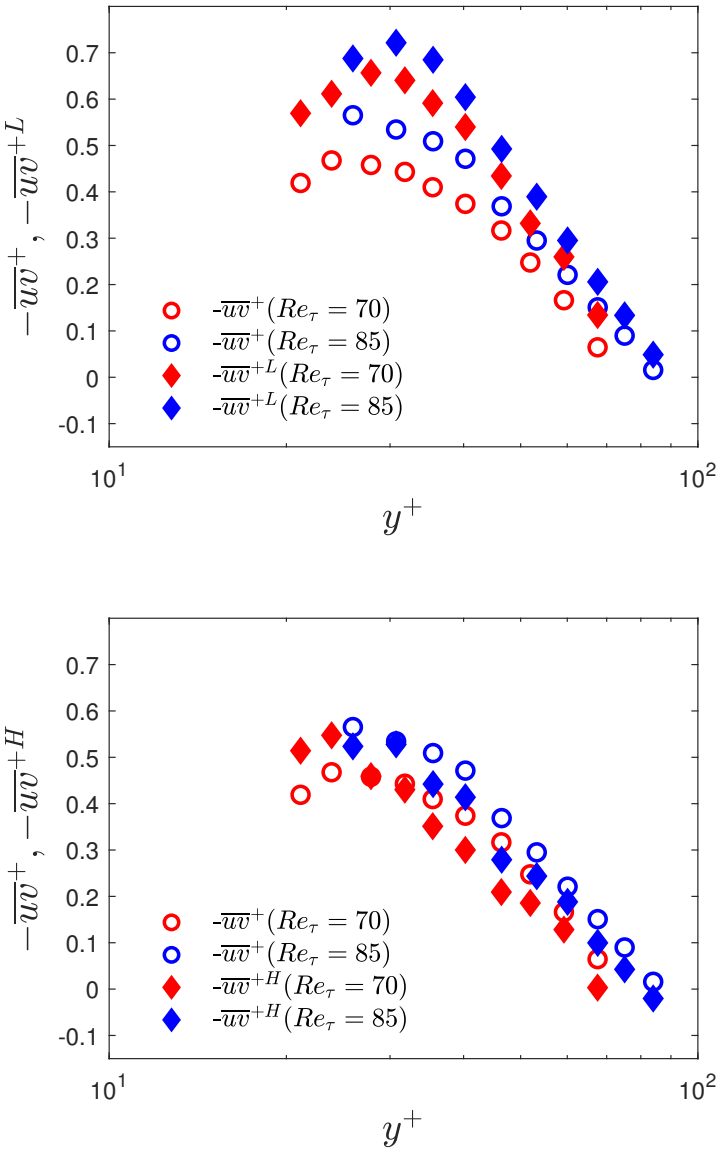

Figure 6.25: (a) Unconditional (open circles) and conditionally averaged (closed squares) RSS profiles for $Re_\tau = 70$ and 85 during low-drag events. (b) Unconditional (open circles) and conditionally averaged (closed squares) RSS profiles for $Re_\tau = 70$ and 85 during high-drag events.

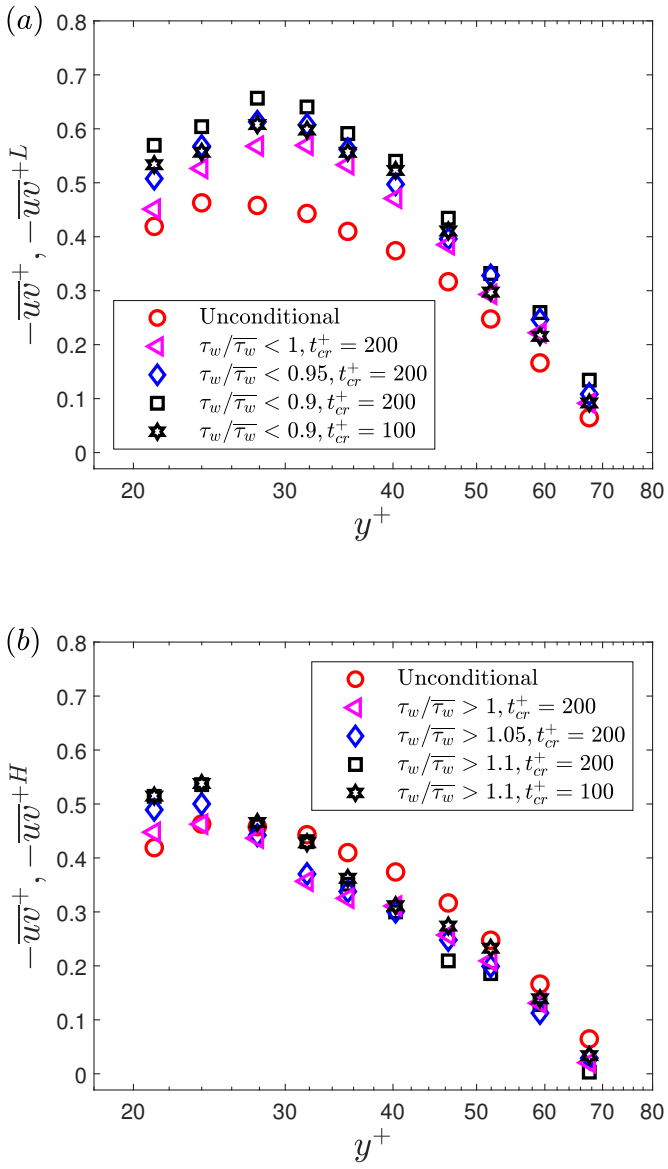

Figure 6.26: (a) Unconditional and conditionally averaged RSS profiles for $Re_\tau = 70$ during the high-drag events for various threshold criteria at two time-duration criteria. (b) Unconditional and conditionally averaged RSS profiles for $Re_\tau = 70$ during the high-drag events for various time-duration criteria. Unconditional and conditionally averaged data are normalized using the time-averaged wall shear stress.

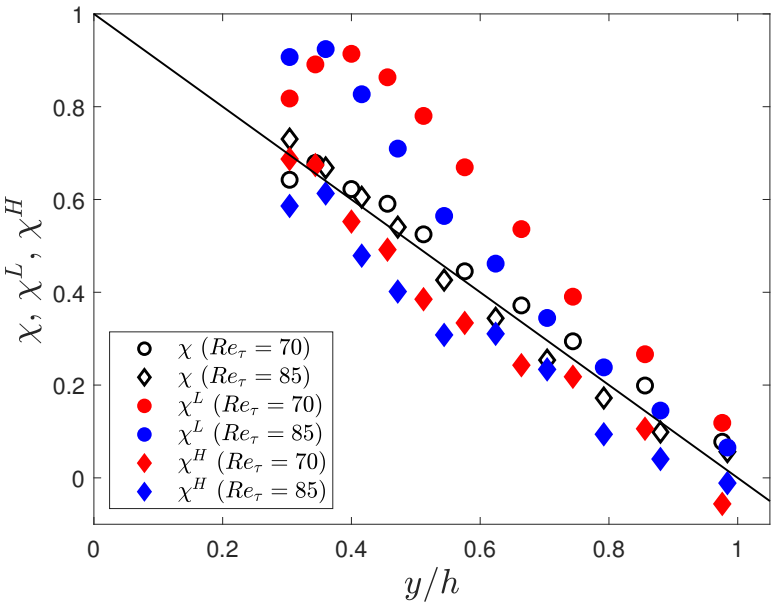

Figure 6.27: Normalized total stress profile for $Re_\tau = 70$ and 85 for the unconditional (χ) and conditional (χ^L, χ^H) data. Solid black line indicates the theoretical (time-averaged) total stress profile.

A mean momentum balance is conducted for the conditional velocity data to study the total stress profile during the conditional events. It is noted that the momentum balance is generally defined for the time-averaged data, but an attempt is made here to study the behaviour of the total stress during the conditional events. The total stress during the conditional events is calculated in a similar way as conducted for the unconditional case (using equation 6.3) but by using conditional parameters. The conditional normalized total stress is given by:

$$\chi^L = \frac{(\nu \frac{d\overline{U}^L}{dy} - \overline{uv}^L)}{\overline{u_\tau}^2} \tag{6.5}$$

for the low-drag events, and

$$\chi^H = \frac{(\nu \frac{d\overline{U}^H}{dy} - \overline{uv}^H)}{\overline{u_\tau}^2} \tag{6.6}$$

for the high-drag events. Figure 6.27 shows the profile of the total stress during the conditional events. It can be seen that during the low-drag events the total stress is higher than the unconditional total stress with the effect being more significant for $y/h \approx 0.4$. This result is consistent with the previous results where it is shown that

the slope of the velocity profile is higher for the low-drag events compared to the slope of the unconditional velocity profiles for $y^+ \approx 20$ - 40 and the Reynolds shear stress is higher for the low-drag case compared to the unconditional case for similar wall-normal locations. The total stress during the high-drag events is similar to the unconditional total stress but slightly lower, which can again be verified based on the slope of the corresponding velocity profiles and Reynolds shear stress profiles.

To understand the RSS behaviour during the low- and high-drag events, a quadrant analysis is carried out. Figure 6.28 shows the joint distribution of streamwise and wall-normal velocity fluctuations for unconditional and conditional data for $Re_\tau = 70$ at $y^+ = 24$ and 46. Here, the normalization of both unconditional and conditional velocity fluctuations is based on the time-averaged friction velocity ($\overline{u_\tau}$). For unconditional velocity fluctuations, the time-averaged velocities are subtracted from the instantaneous velocities and for the conditional velocity fluctuations, the time-averaged velocities are subtracted from the instantaneous conditional velocities during the low- or high-drag events. From figure 6.28 (b, c) it can be seen that during the low-drag events the jpdf shifts towards the Q2 quadrant, whereas during the high-drag events the jpdf shifts towards the Q4 quadrant for $y^+ = 24$. This observation is consistent with the previous results where it is shown that during the low-drag events the ensemble-averaged streamwise decreases and wall-normal velocities increases for $y^+ \approx 20$ - 40. Whereas the opposite is true for high-drag events.

Figure 6.29 shows the profile of the contributions to Reynolds shear stress from each quadrant during the low-drag and the high-drag events for $Re_\tau = 70$ and 85. Unconditional data for the corresponding Reynolds numbers and wall-normal locations are also provided for comparison. It can be seen that for both $Re_\tau = 70$ and 85, during the low-drag events the Q2 events contribute significantly more than the other quadrants. Another interesting observation is that the Q4 events contribute almost nothing during these low-drag events. This further reinforces the hypothesis that the low-drag events are composed of low-streamwise speed and upwash motions at least for $y^+ \geq 20$. The

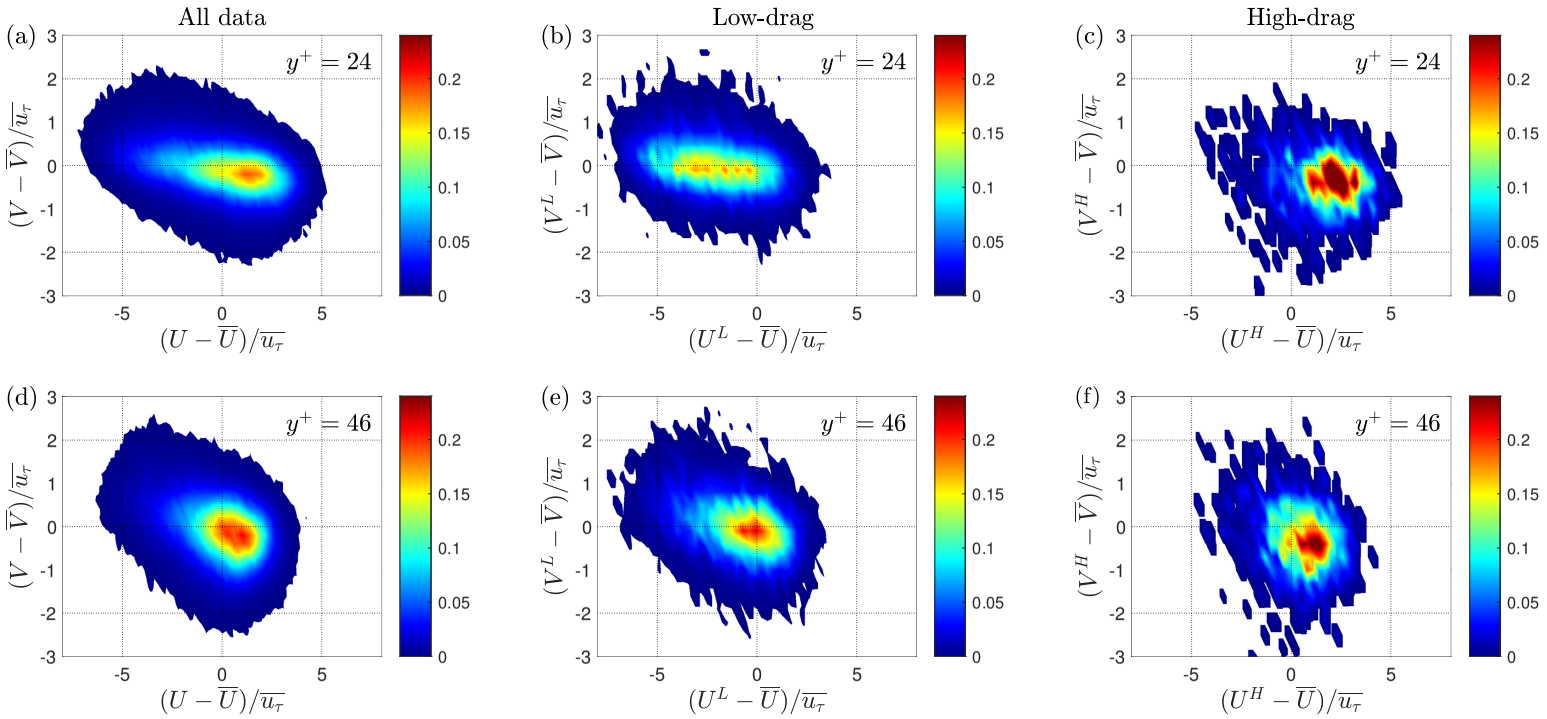

Figure 6.28: Unconditional jpdfs (a, d), low-drag jpdfs (b, e) and high-drag jpdfs (c, f) of streamwise and wall-normal velocity fluctuations for $y^+ = 24$ (a, b, c) and $y^+ = 46$ (d, e, f) at $Re_\tau = 70$. Unconditional and conditional velocity fluctuations are normalized using the time-averaged wall shear stress.

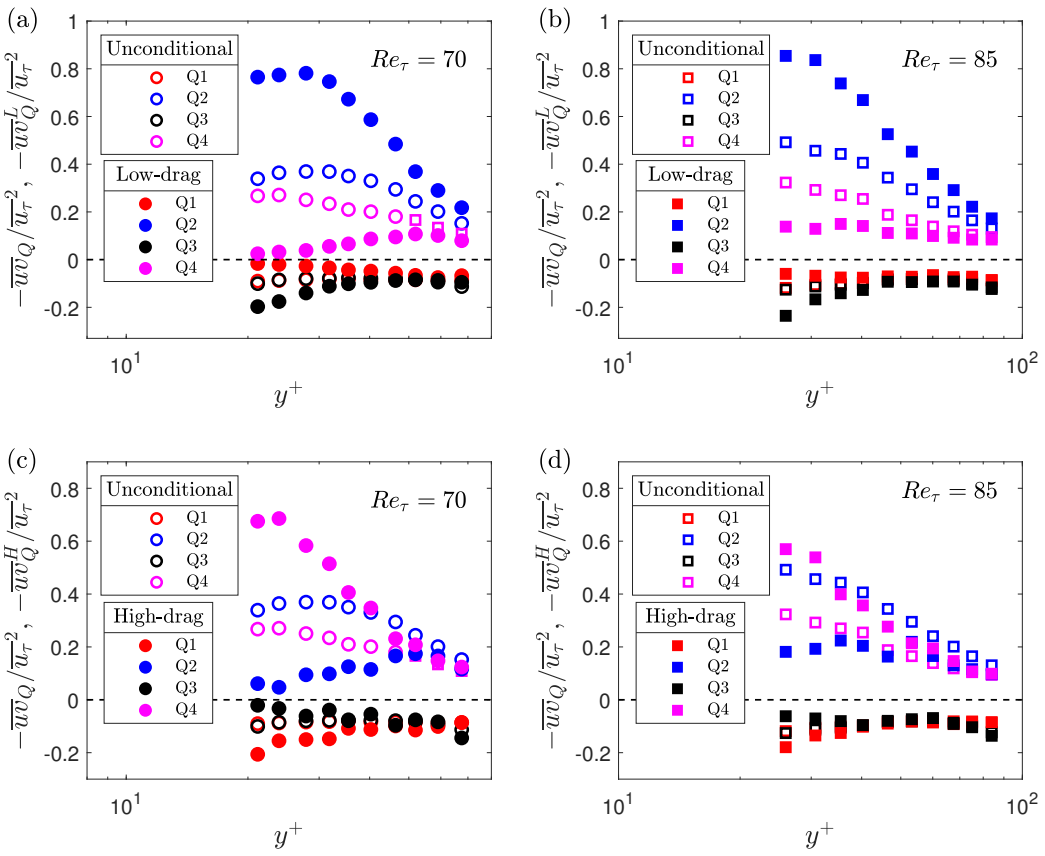

Figure 6.29: (a) Contribution to $-\overline{uv}$ from different quadrants for $Re_\tau = 70$ for the unconditional case and during the low-drag events. (b) Contribution to $-\overline{uv}$ from different quadrants for $Re_\tau = 85$ for the unconditional case and during the low-drag events. (c) Contribution to $-\overline{uv}$ from different quadrants for $Re_\tau = 70$ for the unconditional case and during the high-drag events. (d) Contribution to $-\overline{uv}$ from different quadrants for $Re_\tau = 85$ for the unconditional case and during the high-drag events. The criteria to detect a low-drag event is $\delta t_{cr}^+ = 200$ and $\tau_w/\overline{\tau_w} < 0.9$ and a high-drag event is $\delta t_{cr}^+ = 200$ and $\tau_w/\overline{\tau_w} < 0.9$. Dashed lines represent constant value of zero.

ejection and bursting processes are well studied in the past in regards to the low-speed streaks moving away from the wall and bursting in the buffer layer region [for more details, see: Dennis, 2015, Jiménez, 2018]. Adrian et al. [2000] provided a hairpin vortex model in an effort to unify the various previous findings related to the coherent structures observed in the turbulent boundary layer. It was stated that the hairpin vortex originates from the wall inducing a region of low speed between two legs of the vortex which then lifts up by ejection process. The present work suggests that the low wall shear stress events are representative of low-speed regions which are generally observed between the legs of the hairpin vortices in wall-bounded turbulent flows [Adrian et al., 2000, Adrian, 2007]. Although it should be noted that the present work employs a different criteria to detect these low-drag events ($\tau_w/\overline{\tau_w} < 0.9$ and $\delta t^+ > 200$) and therefore these conditional events form only a subset of the low-speed streaks/events observed in the past [Adrian, 2007].

The present result is also consistent with the recent numerical findings by Kushwaha et al. [2017] and Park et al. [2018]. Kushwaha et al. [2017] showed that the low-wall shear stress events are associated with counter-rotating streamwise vortex pairs transferring momentum away from the wall. Park et al. [2018] showed that the low-drag event is the precursor to the strong bursting event where the low-speed fluid moves away from the wall (ejection process) which ultimately undergo a bursting process.

Results for the high-drag events are shown in figure 6.29 (c) and figure 6.29 (d) for $Re_\tau = 70$ and 85, respectively. It can be observed that during the high-drag events, the Q4 events are the significant contributor to the Reynolds shear stress. This is again expected based on the ensemble-averaged data, i.e. high-drag events are composed of high-speed and downwash motions for $y^+ \geq 20$.

6.8 Summary

An investigation into the intermittencies associated with the low- and high-drag events in turbulent channel flow has been carried out. Simultaneous measurements of stream-

wise velocity and wall shear stress have been conducted to detect and characterize the low- and high-drag intermittencies for Re_τ between 70 and 250. The fraction of time spent in the intervals of low- and high-drag is found to be roughly independent of the Reynolds number for $70 \leq Re_\tau \leq 250$ when the criteria for minimum time-duration is kept constant in inner units. It is found that the even for artificially constructed signals (up to the limit of Gaussian signal), there is a presence of spikes and dips in the ensemble-averaged data if the same criteria is applied as used to detect a low- or high-drag event in the wall shear stress signals. This suggests that these spikes (or dips) are the consequence of the conditional averaging of any time series data. Streamwise velocity profiles, conditionally sampled during the low-drag events, get closer to the Virk's MDR profile for $y^+ \approx 20$ - 35 at all studied Reynolds numbers. For $120 \leq Re_\tau \leq 250$, in the log-law region, the conditional velocity profile is higher than the unconditional velocity profile with the slope of the profile higher during the low-drag events. Similarly, the conditional velocity profile is lower than the unconditional velocity profile with the slope of the profile slightly lower during the high-drag events. A comparison of the conditional streamwise velocity profiles at $Re_\tau = 180$ and 250 with other drag reduction techniques is made. A good agreement between the profiles in the log-law region is observed. For $Re_\tau = 70$ and 85, in addition to the streamwise velocity, wall-normal velocity is also measured to investigate the behaviour of RSS during the low- and high-drag events. There is found to be an increase in the conditionally averaged RSS during the low-drag events, whereas, for the high-drag events, the conditional RSS profile is observed to be fairly similar to the unconditional profile.

Chapter 7

Conclusions and Recommendations

In this chapter, the new findings from this research will be summarized. The chapter is organized into four main sections. In section 7.1, the major findings related to the non-linear regression technique to minimize recalibrations in thermal anemometry are discussed. In section 7.2 the major findings related to the intermittencies in transitional channel flow are provided. In section 7.3, the main findings related to the intermittencies in turbulent channel flow are discussed. Finally, the recommendations for future investigations are made.

7.1 Minimizing recalibration in thermal anemometry

A novel non-linear regression technique to minimize recalibration in thermal anemometry is proposed and investigated (results are presented in chapter 4). This technique works well in predicting the calibration coefficients for velocity and wall shear stress data obtained using thermal anemometry measurements. The robustness of this technique has been confirmed through the use of two commonly used calibration equations and using data acquired from both hot-wire and glue-on hot-film probes. Sensitivity of the non-linear regression to the number of included moments indicates that the first three moments provide a reasonable approximation, but that use of the first four moments provides better agreement. One strength of the technique is that it can account

for non-thermal calibration drifts, thereby potentially reducing the need for continuous *in-situ* calibration throughout a long measurement. When the moments of wall shear stress are obtained from a numerical database, it is demonstrated that the non-linear regression technique reported here can provide a reasonable estimate of the wall shear stress signal. This technique is also shown to work well in the estimation of wall shear stress from the hot-film voltage signal if the moments of the wall shear stress at a nearby Reynolds number are available from a previous measurement. Lastly, this technique can potentially be used to recover the time series history of wall shear stress when direct calibration methods are not readily available, such as in many external flows.

7.2 Intermittencies in transitional channel flows

An experimental investigation of transitional channel flow has been conducted using HFA and flow visualization (results are presented in chapter 5). Single-point measurements of wall shear stress indicate that the time history is free of any significant perturbations in the flow for $Re_\tau \lesssim 42.9$, suggesting that the flow is in the laminar state in the present facility. There is an appearance of high amplitude fluctuations beyond $Re_\tau = 42.9$, whose frequency seems to be increasing with increasing Reynolds numbers until the flow is seen to consist only of "turbulent" events by $Re_\tau = 67.2$. Skewness and flatness of wall shear stress fluctuations jump at the onset of transition and reach a very high magnitude, which is an indication of laminar-turbulent intermittency for these Reynolds numbers. After $Re_\tau \approx 48$, these two moments start to slowly decrease with increasing Reynolds number until there is no significant Reynolds number effects for $Re_\tau \simeq 73$ -79. Simultaneous measurements of wall shear stress at three different locations indicate the presence of large-scale turbulent structures near the onset of transition. The average angles of these large-scale structures near the onset of transition are estimated using two-point correlations and the values obtained are about 17^o for $Re_\tau = 46.8$ and between 32^o and 37^o for $Re_\tau = 48.7$ and 53.9. Flow visualizations show that the flow remains almost laminar with few fluctuations for $Re_\tau = 42.9$ and with increasing Reynolds number the flow becomes intermittent with rapidly switching between the laminar and turbulent regions. This intermittency starts to disappear after

$Re_\tau \approx 55$ and by $Re_\tau = 67.5$, it disappears almost entirely, and the flow is observed to be devoid of any laminar intervals and consists only of turbulent fluctuations.

7.3 Intermittencies in turbulent channel flows

Simultaneous measurements of wall shear stress and velocity are conducted using HFA and LDV respectively for Re_τ in the range 70 - 250 (results are presented in chapter 6). It is found that the fraction of time spent in the intervals of low- or high-drag remains almost independent of Reynolds number for Re_τ = 70 - 250 when the minimum time duration criteria is kept constant in inner scaling. The spike in the ensemble-averaged wall shear stress before and after the low-drag events (and similarly the dip in the ensemble-averaged wall shear stress before and after the high-drag events) is found to be a statistical artifact of conditional sampling and ensemble averaging of any time-series signal. The conditionally-averaged streamwise velocity profile when normalized with the conditionally-averaged wall shear stress get closer to Virk's MDR asymptote for $y^+ \approx$ 20 - 35 at all the studied Reynolds numbers. For fully-turbulent flow, Re_τ = 180 and 250, the conditional streamwise velocity profiles, when normalized with the conditional wall shear stress, look very similar to the velocity profiles obtained in the case of low-drag reduction (drag reduction of about 30%) using other drag reduction techniques (polymer additives, superhydrophobicity, and blowing and suction). For Re_τ = 70 and 85, the conditionally-averaged RSS profile during the low-drag events is observed to have higher values than the unconditional profile for all wall-normal locations measured, with the effect being most significant for $y^+ \approx$ 20 - 40. Whereas for the high-drag events the conditionally averaged RSS profile is similar to (but slightly lower than) the unconditional profile up to the channel centreline.

7.4 Recommendations

Many advancements in the understanding of the transitional and turbulent channel flows are made in the present thesis. However, still, there are still open questions in this field which require further research. Based on this, some recommendations for

future investigations are proposed.

7.4.1 Further investigation of intermittencies in turbulent channel flows

In the present thesis, the characteristics of low- and high-drag events are studied for Re_τ up to 250. The results show the existence of these intermittent events in fully-turbulent flow regime. It is still needed to investigate these events for higher Reynolds numbers in order to better understand their Reynolds number dependence. One potential issue while measuring at higher Reynolds numbers is the spatial resolution of the hot-film sensors. For $Re_\tau = 250$, these hot-film sensors have a spanwise width of $l^+ = 18$ and it can be expected that for higher Reynolds numbers the spatial resolution can be a major issue as $l^+ = 22$ is generally considered to be minimum spanwise width to resolve all scales of turbulent motion [Ligrani and Bradshaw, 1987]. This will lead to the filtering of the small-scale information present in the flow. With the recent developments in MEMS technology [Gad-el Hak, 2005] and nano-scale probes [Samie et al., 2018], novel wall shear stress probes need to be designed and manufactured which can provide well-resolved data for higher Reynolds numbers.

Reynolds shear stress (RSS) characteristics are studied only for $y/h \gtrsim 0.3$ because of the challenge in measuring RSS closer to the wall using LDV. This issue is described in § 3.4.3. At $y/h \approx 0.3$, the low-drag events are observed to consist of strong a Q2 event and this behaviour becomes less significant with increasing wall-normal location. It is necessary to study the RSS characteristics closer to the bottom wall in order to have a complete understanding of the RSS profile during these intermittent events. Other than LDV, simultaneous PIV measurements can be also made to study the Reynolds shear stress during the condition events. PIV can provide information regarding the entire flow field instantaneously. Simultaneous hot-film and PIV measurements have been carried out previously by Whalley et al. [2019] in the same channel flow facility. One challenge while measuring using PIV is the storage capacity of the PIV camera as long time measurements ($\sim$ few hours) are required to detect these intermittent events.

One potential way to solve this issue is to implement a trigger to the PIV based on the threshold for the instantaneous wall shear stress signals. This will allow the PIV to take the wall shear stress synchronized snapshots of the flow field only during the times when the threshold criteria is met. This can enable the PIV to be able to capture the images for a longer time duration compared to the case when no threshold based trigger is applied.

7.4.2 Low- and high-drag intermittencies in other wall-bounded flows

The study of intermittencies which leads to the so-called low- and high-drag events has been conducted for channel flows. It is important to investigate these intermittencies in other wall-bounded flows for example pipe flows and boundary-layer flows. This will further verify the universality of these intermittent events in wall-bounded turbulent flows. For pipe flows, carrying out wall shear stress measurements using the current hot-film probes is a challenge due to the curved shape of the wall, as the current mounting procedure works only for the flat wall. Therefore, a novel way to mount these glue-on probes needs to be investigated. For the boundary-layer flows, these glue-on probes can be mounted on the wall in a similar fashion as carried out here for channel flow. In channel flow, the calibration of the hot-film can be carried out against the pressure-drop (see, § 3.5.5). For the boundary layer flows, this approach cannot be taken as the mean wall shear stress cannot be directly related to the mean pressure-drop. One potential way to calibrate the hot-film is by measuring the mean wall shear stress using LDV in the viscous sublayer and obtain the first three/four well-converged statistical moments. The non-linear regression technique can then be utilized to generate the calibration curve using these moments. This approach is also previously discussed in § 4.5.4.

7.4.3 Flow in larger domains to study transition process

It is now well-known that the transition process in channel flow is significantly affected by its domain size [Chantry et al., 2017, Xiao and Song, 2019]. With the advancements in the numerical techniques and computational power, larger domain sizes to study transition are being employed. This has resulted in the discovery of some new phenomena, for example, existence of solitary stripes near the onset of transition [Xiao and Song, 2019] for a computational domain size of as large as $L_x \times L_z = 320h \times 320h$. These solitary stripes are found for large domain sizes where the head-tail interactions are minimum (this phenomenon is discussed in detail in § 2.2.1). It is important to validate these recent numerical findings with experimental investigations of similar domain sizes. This will provide more insights into the subcritical nature of transition in channel flows. There will be practical challenges to design and build channel flow facilities of such high domain sizes. For example, to have a channel of aspect ratio of 320 will require the channel to very wide (320 times the channel half-height). One way to achieve this is by making the channel very wide, but this might be a issue as it will require very large physical laboratory space. To put it into perspective, the present channel flow facility has an aspect ratio of about 11.9 and a width of 298 mm. If we make this channel of aspect ratio of 320 for the same channel height, the width of the channel will have to be about 8 meters. Another way can be employed which is to make the channel of very small height in order to obtain the similar desired aspect ratio. Again, the channel might have too small height to carry out any meaningful investigation. Therefore, a combination of both of these approaches can be taken to design and build channel flow facilities of larger aspect ratios.

7.4.4 Large-scale coherent structures during transition

Simultaneous hot-film measurements have been carried out to probe the wall footprint of large-scale turbulent structures during transition process. In the present work, the minimum distance between two hot-films is $5h$. Although, the current experimental set-up provided some information about the large-scale structures, locating the hot-films close together might provide better resolution of these structures. Therefore, it

is recommended that the use of multiple hot-films at closer spatial proximity should be carried out. This will allow for more well-resolved wall-footprint of the large-scale turbulent structures during the transition process in channel flow. Based on the current mounting procedure for the hot-film probes, it is not possible to keep the hot-films very close to each other. One possible option is to design and manufacture a plug on which an array of hot-films can be mounted. This can allow for multiple hot-film measurements which are in closer proximity than conducted in the present thesis. In case of non-thermal drifts in one of the hot-films, a non-linear regression method which is developed in the present study can be utilized to recover the wall shear stress signal from the drifted hot-film. An array of hot-films has been used in various previous studies, for example, Desgeorges et al. [2002] and Haselbach and Nitsche [1996].

References

H. Abe, H. Kawamura, and H. Choi. Very large-scale structures and their effects on the wall shear-stress fluctuations in a turbulent channel flow up to $Re_\tau = 640$. *J. Fluids Eng.*, 126(5):835–843, 2004.

R. Adrian and C. Yao. Power spectra of fluid velocities measured by laser Doppler velocimetry. *Exp. Fluids*, 5(1):17–28, 1986.

R. J. Adrian. Hairpin vortex organization in wall turbulence. *Physics of Fluids*, 19(4): 041301, 2007.

R. J. Adrian and J. Westerweel. *Particle image velocimetry*. Number 30. Cambridge university press, 2011.

R. J. Adrian, C. D. Meinhart, and C. D. Tomkins. Vortex organization in the outer region of the turbulent boundary layer. *Journal of fluid Mechanics*, 422:1–54, 2000.

H. Aida, T. Tsukahara, and Y. Kawaguchi. DNS of turbulent spot developing into turbulent stripe in plane Poiseuille flow. *In Proceedings of ASME 2010 3rd Joint US–European Fluids Engineering Summer Meeting*, page 2125–2130, 2010.

H. Aida, T. Tsukahara, and Y. Kawaguchi. Development of a turbulent spot into a stripe pattern in plane Poiseuille flow. *arXiv:1410.0098 [physics.flu-dyn]*, 2014.

F. Alavyoon, D. S. Henningson, and P. H. Alfredsson. Turbulent spots in plane Poiseuille flow–flow visualization. *Phys. Fluids*, 29(4):1328–1331, 1986.

H.-E. Albrecht, N. Damaschke, M. Borys, and C. Tropea. *Laser Doppler and phase Doppler measurement techniques*. Springer Science & Business Media, 2013.

P. H. Alfredsson, A. V. Johansson, J. H. Haritonidis, and H. Eckelmann. The fluctuating wall-shear stress and the velocity field in the viscous sublayer. *Phys. Fluids*, 31(5): 1026–1033, 1988a.

P. H. Alfredsson, A. V. Johansson, J. H. Haritonidis, and H. Eckelmann. The fluctuating wall-shear stress and the velocity field in the viscous sublayer. *Phys. Fluids*, 31(5): 1026–1033, 1988b.

E. v. Bacher and C. Smith. A combined visualization-anemometry study of the turbulent drag reducing mechanisms of triangular micro-groove surface modifications. In *Shear Flow Control Conference*, page 548, 1985.

A. Baron and M. Quadrio. Turbulent drag reduction by spanwise wall oscillations. *Applied Scientific Research*, 55(4):311–326, 1995.

J. S. Bendat and A. G. Piersol. *Random data: analysis and measurement procedures*, volume 729. John Wiley & Sons, 2011.

L. Benedict, H. Nobach, and C. Tropea. Estimation of turbulent velocity spectra from laser Doppler data. *Meas. Sci. Technol.*, 11(8):1089, 2000.

S. F. Benjamin and C. A. Roberts. Measuring flow velocity at elevated temperature with a hot wire anemometer calibrated in cold flow. *Int. J. Heat Mass Transf.*, 45 (4):703–706, 2002.

H. Benschop and W.-P. Breugem. Drag reduction by herringbone riblet texture in direct numerical simulations of turbulent channel flow. *J. Turbul.*, 18(8):717–759, 2017.

N. S. Berman. Drag reduction by polymers. *Ann. Rev. Fluid Mech.*, 10(1):47–64, 1978.

S. R. Bistafa. On the development of the Navier-Stokes equation by Navier. *Revista Brasileira de Ensino de Física*, 40(2), 2018.

D. Bonn, Y. Amarouchene, C. Wagner, S. Douady, and O. Cadot. Turbulent drag reduction by polymers. *J. Condens. Matter Phys*, 17(14):S1195, 2005.

J. Boussinesq. An equation for the phenomena of heat convection and an estimate of the cooling power of fluids. *Journal de Mathematiques*, 1:285–332, 1905.

P. Bradshaw. Turbulent secondary flows. *Ann. Rev. Fluid Mech.*, 19(1):53–74, 1987.

H. Bruun. Hot-film anemometry in liquid flows. *Meas. Sci. Technol.*, 7(10):1301, 1996.

H. H. Bruun. *Hot-Wire Anemometry: Principles and Signal Analysis*. Oxford University Press, New York, 1st edition, 1995.

P. Buchhave, W. K. George Jr, and J. L. Lumley. The measurement of turbulence with the laser-Doppler anemometer. *Ann. Rev. Fluid Mech.*, 11(1):443–503, 1979.

E. D. Burger, W. R. Munk, H. A. Wahl, et al. Flow increase in the trans Alaska pipeline through use of a polymeric drag-reducing additive. *J. Petrol. Technol.*, 34 (02):377–386, 1982.

B. Cantwell, D. Coles, and P. Dimotakis. Structure and entrainment in the plane of symmetry of a turbulent spot. *J. Fluid Mech.*, 87(4):641–672, 1978.

D. R. Carlson, S. E. Widnall, and M. F. Peeters. A flow-visualization study of transition in plane Poiseuille flow. *J. Fluid Mech.*, 121:487–505, 1982.

A. Cassie and S. Baxter. Wettability of porous surfaces. *Transactions of the Faraday society*, 40:546–551, 1944.

M. Chantry, L. S. Tuckerman, and D. Barkley. Universal continuous transition to turbulence in a planar shear flow. *J. Fluid Mech.*, 824, 2017.

C. Chin, J. Monty, and A. Ooi. Reynolds number effects in DNS of pipe flow and comparison with channels and boundary layers. *Int. J. Heat Fluid Fl.*, 45:33–40, 2014.

C. C. Chin, N. Hutchins, A. S. H. Ooi, and I. Marusic. Use of DNS data to investigate spatial resolution issues in measurements of wall bounded turbulence. *Meas. Sci. Technol.*, 20(11), 2009a.

C. C. Chin, N. Hutchins, A. S. H. Ooi, and I. Marusic. Use of DNS data to investigate spatial resolution issues in measurements of wall bounded turbulence. *Meas. Sci. Technol.*, 20(11), 2009b.

H. Choi, P. Moin, and J. Kim. Active turbulence control for drag reduction in wall-bounded flows. *J. Fluid Mech.*, 262:75–110, 1994.

K.-S. Choi. A new look at the near-wall turbulence structure. In *Advances in turbulence*, pages 373–382. Springer, 1987.

K.-S. Choi. Near-wall structure of a turbulent boundary layer with riblets. *J. Fluid Mech.*, 208:417–458, 1989.

J. M. Cimbala and W. J. Park. A direct hot-wire calibration technique to account for ambient temperature drift in incompressible flow. *Exp. Fluids*, 8(5):299–300, 1990. ISSN 0723-4864.

D. Collis and M. Williams. Two-dimensional convection from heated wires at low Reynolds numbers. *J. Fluid Mech.*, 6(3):357–384, 1959.

D. C. Collis. The dust problem in hot-wire anemometry. *Aeronaut. Quart.*, 4(1):93–102, 1954.

G. Comte-Bellot. Contribution à l'étude de la turbulence de conduite. *These Presente a la Faculte des Sciences de l'Universite de Grenoble*, 1963.

G. Comte-Bellot. Hot-wire anemometry. *Ann. Rev. Fluid Mech.*, 8(1):209–231, 1976.

E. R. Corino and R. S. Brodkey. A visual investigation of the wall region in turbulent flow. *J. Fluid Mech.*, 37(1):1–30, 1969.

H. Darcy. Note relative à quelques modifications à introduire dans le tube de pitot. In *Annales des Ponts et Chaussées*, volume 1, pages 351–359, 1858.

S. J. Davies and C. M. White. An experimental study of the flow of water in pipes of rectangular section. *Proc. R. Soc. London, Ser. A*, 119:92–107, 1928.

R. Dean. Reynolds number dependence of skin friction and other bulk flow variables in two-dimensional rectangular duct flow. *ASME. J. Fluids Eng.*, 100(2):215–223, 1978.

J. C. Del Alamo, J. Jiménez, P. Zandonade, and R. D. Moser. Scaling of the energy spectra of turbulent channels. *J. Fluid Mech.*, 500:135–144, 2004.

D. J. C. Dennis. Coherent structures in wall-bounded turbulence. *Anais da Academia Brasileira de Ciências*, 87(2):1161–1193, 2015.

J. E. Dennis, Jr. and R. B. Schnabel. *Numerical Methods for Unconstrained Optimization and Nonlinear Equations (Classics in Applied Mathematics, 16)*. Soc for Industrial & Applied Math, 1996.

O. Desgeorges, T. Lee, and F. Kafyeke. Multiple hot-film sensor array calibration and skin friction measurement. *Exp. Fluids*, 32(1):37–43, 2002.

G. Donohue, W. Tiederman, and M. Reischman. Flow visualization of the near-wall region in a drag-reducing channel flow. *J. Fluid Mech.*, 56(3):559–575, 1972.

J. Drappier, T. Divoux, Y. Amarouchene, F. Bertrand, S. Rodts, O. Cadot, J. Meunier, and D. Bonn. Turbulent drag reduction by surfactants. *EPL (Europhysics Letters)*, 74(2):362, 2006.

H. L. Dryden and A. M. Kuethe. The measurement of fluctuations of air speed by the hot-wire anemometer. *NACA-TR-320*, 1929.

Y. Dubief, C. M. White, E. S. Shaqfeh, and V. E. Terrapon. Polymer maximum drag reduction: A unique transitional state. *arXiv preprint arXiv:1106.4482*, 2011.

F. Durst, A. Melling, J. Whitelaw, and C. Wang. *Principles and Practice of Laser-Doppler Anemometry.* Academic Press, London, 1981.

F. Durst, S. Noppenberger, M. Still, and H. Venzke. Influence of humidity on hot-wire measurements. *Meas. Sci. Technol.*, 7(10):1517–1528, 1996.

F. Durst, S. Ray, B. Ünsal, and O. Bayoumi. The development lengths of laminar pipe and channel flows. *ASME. J. Fluids Eng.*, 127:1154–1160, 2005.

H. Eckelmann. Hot wire and hot film measurements in oil. *DISA Info*, 13:16–22, 1972.

H. Eckelmann. The structure of the viscous sublayer and the adjacent wall region in a turbulent channel flow. *J. Fluid Mech.*, 65(3):439–459, 1974.

B. Eckhardt, K. Marzinzik, and A. Schmiegel. Transition to turbulence in shear flows. In *A perspective look at nonlinear media*, pages 327–338. Springer, 1998.

R. V. Edwards and A. S. Jensen. Particle-sampling statistics in laser anemometers: sample-and-hold systems and saturable systems. *J. Fluid Mech.*, 133:397–411, 1983.

J. Elsnab, J. Klewicki, D. Maynes, and T. Ameel. Mean dynamics of transitional channel flow. *J. Fluid Mech.*, 678:451–481, 2011.

J. R. Elsnab, J. P. Monty, C. M. White, M. M. Koochesfahani, and J. C. Klewicki. High-fidelity measurements in channel flow with polymer wall injection. *J. Fluid Mech.*, 859:851–886, 2019.

H. Emmons. The laminar-turbulent transition in a boundary layer-part i. *Journal of the Aeronautical Sciences*, 18(7):490–498, 1951.

M. Escudier, A. Nickson, and R. Poole. Turbulent flow of viscoelastic shear-thinning liquids through a rectangular duct: Quantification of turbulence anisotropy. *J. Non-Newton. Fluid*, 160(1):2–10, 2009.

H. H. Fernholz, G. Janke, M. Schober, P. M. Wagner, and D. Warnack. New developments and applications of skin-friction measuring techniques. *Meas. Sci. Technol.*, 7:1396–1409, 1996.

R. P. Feynman, R. B. Leighton, and M. Sands. The feynman lectures on physics; vol. i. *Am. J. Phys.*, 33(9):750–752, 1965.

L. Fingerson. Thermal anemometry, current state, and future directions. *Rev. Sci. Instrum.*, 65(2):285–300, 1994.

O. Flores and J. Jiménez. Hierarchy of minimal flow units in the logarithmic layer. *Phys. Fluids*, 22(7):071704, 2010.

U. Frisch. *Turbulence: the Legacy of A. N. Kolmogorov*. Cambridge university press, 1995.

M. Gad-el Hak. *MEMS: Introduction and Fundamentals*. CRC press, 2005.

R. García-Mayoral and J. Jiménez. Drag reduction by riblets. *Philos. Trans. R. Soc. A: Mathematical, Physical and Engineering Sciences*, 369(1940):1412–1427, 2011.

M.-W. Ge, L. Fang, and Y.-Q. Liu. Drag reduction of wall bounded incompressible turbulent flow based on active dimples/pimples. *J. Hydrodyn.*, 29(2):261–271, 2017.

W. K. George. Is there a universal log law for turbulent wall-bounded flows? *Philos. Trans. R. Soc. A: Mathematical, Physical and Engineering Sciences A: Mathematical, Physical and Engineering Sciences*, 365(1852):789–806, 2007.

S. Gogte, P. Vorobieff, R. Truesdell, A. Mammoli, F. van Swol, P. Shah, and C. J. Brinker. Effective slip on textured superhydrophobic surfaces. *Phys. Fluids*, 17(5): 051701, 2005.

G. Gomit, R. De Kat, and B. Ganapathisubramani. Structure of high and low shear-stress events in a turbulent boundary layer. *Phys. Rev. Fluids*, 3(1):014609, 2018.

J. W. Gose, K. Golovin, M. Boban, J. M. Mabry, A. Tuteja, M. Perlin, and S. L. Ceccio. Characterization of superhydrophobic surfaces for drag reduction in turbulent flow. *J. Fluid Mech.*, 845:560–580, 2018.

M. D. Graham. Drag reduction and the dynamics of turbulence in simple and complex fluids. *Phys. Fluids*, 26(10):625–656, 2014.

A. Günther, D. Papavassiliou, M. Warholic, and T. Hanratty. Turbulent flow in a channel at a low Reynolds number. *Exp. Fluids*, 25(5-6):503–511, 1998.

J. M. Hamilton, J. Kim, and F. Waleffe. Regeneration mechanisms of near-wall turbulence structures. *J. Fluid Mech.*, 287:317–348, 1995.

F. Haselbach and W. Nitsche. Calibration of single-surface hot films and in-line hot-film arrays in laminar or turbulent flows. *Meas. Sci. Technol.*, 7(10):1428, 1996.

M. Henkel, H. Hinrichsen, S. Lübeck, and M. Pleimling. *Non-equilibrium phase transitions*, volume 1. Springer, 2008.

H. Hinrichsen. Non-equilibrium critical phenomena and phase transitions into absorbing states. *Adv. Phys.*, 49(7):815–958, 2000.

S. Hoyas and J. Jiménez. Scaling of the velocity fluctuations in turbulent channels up to Re_τ= 2003. *Phys. Fluids*, 18(1):011702, 2006.

Z. Hu, C. L. Morfey, and N. D. Sandham. Wall pressure and shear stress spectra from direct simulations of channel flow. *AIAA Journal*, 44(7):1541 – 1549, 2006.

L. Huang, B. Fan, and G. Dong. Turbulent drag reduction via a transverse wave traveling along streamwise direction induced by Lorentz force. *Phys. Fluids*, 22(1): 015103, 2010.

M. Hultmark and A. J. Smits. Temperature corrections for constant temperature and constant current hot-wire anemometers. *Meas. Sci. Technol.*, 21(10):105404, Aug 2010.

N. Hutchins, T. B. Nickels, I. Marusic, and M. Chong. Hot-wire spatial resolution issues in wall-bounded turbulence. *J. Fluid Mech.*, 635:103–136, 2009.

N. Hutchins, J. Monty, B. Ganapathisubramani, H. Ng, and I. Marusic. Three-dimensional conditional structure of a high-Reynolds-number turbulent boundary layer. *J. Fluid Mech.*, 673:255–285, 2011.

T. Itano and S. Toh. The dynamics of bursting process in wall turbulence. *J. Phys. Soc. Jpn*, 70(3):703–716, 2001.

J. Jeong, F. Hussain, W. Schoppa, and J. Kim. Coherent structures near the wall in a turbulent channel flow. *J. Fluid Mech.*, 332:185–214, 1997.

N. K. Jha, A. Bhatt, and R. N. Govardhan. Effect of bubble distribution on wall drag in turbulent channel flow. *Exp. Fluids*, 60(8):127, 2019.

J. Jiménez. The largest scales of turbulent wall flows. *CTR Annual Research Briefs*, 137:54, 1998.

J. Jiménez. Coherent structures in wall-bounded turbulence. *Journal of Fluid Mechanics*, 842, 2018.

J. Jiménez and P. Moin. The minimal flow unit in near-wall turbulence. *J. Fluid Mech.*, 225:213–240, 1991.

J. Jiménez and A. Pinelli. The autonomous cycle of near-wall turbulence. *J. Fluid Mech.*, 389:335–359, 1999.

J. Jiménez, G. Kawahara, M. P. Simens, M. Nagata, and M. Shiba. Characterization of near-wall turbulence in terms of equilibrium and "bursting" solutions. *Phys. Fluids*, 17(1):015105, 2005.

A. V. Johansson and P. H. Alfredsson. Effects of imperfect spatial resolution on measurements of wall-bounded turbulentbx shear flows. *J. Fluid Mech.*, 137:409–421, 1983.

J. Jovanović, F. Durst, and T. Johansson. Statistical analysis of the dynamic equations for higher-order moments in turbulent wall bounded flows. *Phys. Fluids A: Fluid Dynamics*, 5(11):2886–2900, 1993.

W.-J. Jung, N. Mangiavacchi, and R. Akhavan. Suppression of turbulence in wall-bounded flows by high-frequency spanwise oscillations. *Phys. Fluids A: Fluid Dynamics*, 4(8):1605–1607, 1992.

T. W. Kao and C. Park. Experimental investigations of the stability of channel flows. Part 1. Flow of a single liquid in a rectangular channel. *J. Fluid Mech.*, 43(1):145–164, 1970.

L. Keirsbulck, L. Labraga, and M. G. el Hak. Statistical properties of wall shear stress fluctuations in turbulent channel flows. *Int. J. Heat Fluid Flow*, 37:1 – 8, 2012.

B. C. Khoo, Y. T. Chew, and C. J. Teo. Near-wall hot-wire measurements. *Exp. Fluids*, (5):494–505, 2001.

H. Kim, S. Kline, and W. Reynolds. The production of turbulence near a smooth wall in a turbulent boundary layer. *J. Fluid Mech.*, 50(1):133–160, 1971.

J. Kim. Physics and control of wall turbulence for drag reduction. *Philos. Trans. R. Soc. A: Mathematical, Physical and Engineering Sciences*, 369(1940):1396–1411, 2011.

J. Kim, P. Moin, and R. Moser. Turbulence statistics in fully developed channel flow at low Reynolds number. *J. Fluid Mech.*, 177:133–166, 1987.

K. Kim, C.-F. Li, R. Sureshkumar, S. Balachandar, and R. J. Adrian. Effects of polymer stresses on eddy structures in drag-reduced turbulent channel flow. *J. Fluid Mech.*, 584:281–299, 2007.

G. E. King et al. Hydraulic fracturing 101: what every representative, environmentalist, regulator, reporter, investor, university researcher, neighbor and engineer should know about estimating frac risk and improving frac performance in unconventional gas and oil wells. In *SPE Hydraul. Fract. Pechnol. Conf.* Society of Petroleum Engineers, 2012.

L. V. King. Xii. On the convection of heat from small cylinders in a stream of fluid: Determination of the convection constants of small platinum wires with applications to hot-wire anemometry. *Philos. Trans. R. Soc. Lond. series A, containing papers of a mathematical or physical character*, 214(509-522):373–432, 1914.

S. Kline and F. McClintock. Describing uncertainties in single-sample experiments. *Mechanical Engineering*, 75:3–8, 1953.

S. J. Kline, W. C. Reynolds, F. Schraub, and P. Runstadler. The structure of turbulent boundary layers. *J. Fluid Mech.*, 30(4):741–773, 1967.

H.-P. Kreplin and H. Eckelmann. Propagation of perturbations in the viscous sublayer and adjacent wall region. *J. Fluid Mech.*, 95(2):305–322, 1979.

P.-Å. Krogstad, J. Kaspersen, and S. Rimestad. Convection velocities in a turbulent boundary layer. *Phys. Fluids*, 10(4):949–957, 1998.

A. Kushwaha, J. S. Park, and M. D. Graham. Temporal and spatial intermittencies within channel flow turbulence near transition. *Phys. Rev. Fluids*, 2:024603, Feb 2017.

F. Laadhari, L. Skandaji, and R. Morel. Turbulence reduction in a boundary layer by a local spanwise oscillating surface. *Phys. Fluids*, 6(10):3218–3220, 1994.

J. Laufer. Investigation of turbulent flow in a two-dimensional channel. *NACA Rep. 1053*, 1951.

J. Laufer. New trends in experimental turbulence research. *Ann. Rev. Fluid Mech.*, 7 (1):307–326, 1975.

E. Lauga, M. Brenner, and H. Stone. Microfluidics: the no-slip boundary condition. *Springer handbook of experimental fluid mechanics*, pages 1219–1240, 2007.

S.-J. Lee and Y.-G. Jang. Control of flow around a NACA 0012 airfoil with a micro-riblet film. *J. Fluids Struct.*, 20(5):659–672, 2005.

G. Lemoult, J.-L. Aider, and J. E. Wesfreid. Turbulent spots in a channel: large-scale flow and self-sustainability. *J. Fluid Mech.*, 731:R1, 2013.

G. Lemoult, L. Shi, K. Avila, S. V. Jalikop, M. Avila, and B. Hof. Directed percolation phase transition to sustained turbulence in Couette flow. *Nat. Phys.*, 12:254–258, 2016.

F. Li and S. E. Widnall. Wave patterns in plane Poiseuille flow created by concentrated disturbances. *J. Fluid Mech.*, 208:639–656, 1989.

K. Lien, J. Monty, M. Chong, and A. Ooi. The entrance length for fully developed turbulent channel flow. *15th Australasian Fluid Mechanics Conference (Sydney, Australia)*, 2004.

P. Ligrani and P. Bradshaw. Spatial resolution and measurement of turbulence in the viscous sublayer using subminiature hot-wire probes. *Exp. Fluids*, 5:407–417, 1987.

S. Ling and P. Hubbard. The hot-anemometers: a new device for fluid mechanics research. *J. Aero. Sci.*, 23(890-1), 1956.

Z. Liu, R. Adrian, and T. Hanratty. Large-scale modes of turbulent channel flow: transport and structure. *J. Fluid Mech.*, 448:53–80, 2001.

C. G. Lomas. *Fundamentals of hot wire anemometry.* Cambridge University Press, 2011.

P. Manneville. Transition to turbulence in wall-bounded flows: Where do we stand? *Mech. Eng. Rev.*, pages 15–00684, 2016.

I. Marusic, R. Mathis, and N. Hutchins. Predictive model for wall-bounded turbulent flow. *Science*, 329(5988):193–196, 2010. ISSN 0036-8075.

W. McComb. The physics of fluid turbulence oxford university press, 1990.

A. Melling and J. Whitelaw. Turbulent flow in a rectangular duct. *J. Fluid Mech.*, 78 (2):289–315, 1976.

T. Min and J. Kim. Effects of hydrophobic surface on skin-friction drag. *Phys. Fluids*, 16(7):L55–L58, 2004.

J. Monty, N. Hutchins, H. Ng, I. Marusic, and M. Chong. A comparison of turbulent pipe, channel and boundary layer flows. *J. Fluid Mech.*, 632:431–442, 2009.

J. P. Monty. *Developments in smooth wall turbulent duct flows.* PhD thesis, University of Melbourne, Department of Mechanical and Manufacturing Engineering, 2005.

L. F. Moody. Friction factors for pipe flow. *Trans. Asme*, 66:671–684, 1944.

R. D. Moser, J. Kim, and N. N. Mansour. Direct numerical simulation of turbulent channel flow up to $Re_\tau = 590$. *Phys. Fluids*, 11(4):943–945, 1999.

M. Nagata. Three-dimensional finite-amplitude solutions in plane Couette flow: bifurcation from infinity. *J. Fluid Mech.*, 217:519–527, 1990.

M. Nagata and K. Deguchi. Mirror-symmetric exact coherent states in plane Poiseuille flow. *J. Fluid Mech.*, 735, 2013.

H. M. Nagib and K. A. Chauhan. Variations of von kármán coefficient in canonical flows. *Phys. Fluids*, 20(10):101518, 2008.

Y. P. Nekrasov and P. Savostenko. Pressure dependence of hot-wire anemometer readings. *Meas. Tech.*, 34(5):462–465, 1991.

H. Ng, J. Monty, N. Hutchins, M. Chong, and I. Marusic. Comparison of turbulent channel and pipe flows with varying Reynolds number. *Exp. Fluids*, 51(5):1261–1281, 2011.

M. Niederschulte, R. Adrian, and T. Hanratty. Measurements of turbulent flow in a channel at low Reynolds numbers. *Exp. Fluids*, 9(4):222–230, 1990.

J. Nikuradse. Gesetzmäßigkeiten der turbulenten strömung in glatten rohren (nachtrag). *Forschung im Ingenieurwesen*, 4(1):44–44, 1933.

M. Nishioka, S. I. A, and Y. Ichikawa. An experimental investigation of the stability of plane Poiseuille flow. *J. Fluid Mech.*, 72(4):731–751, 1975.

R. Orlu and P. Schlatter. On the fluctuating wall-shear stress in zero pressure-gradient turbulent boundary layer flows. *Phys. Fluids*, 23(2)(021704), 2011.

S. A. Orszag. Accurate solution of the Orr–Sommerfeld stability equation. *J. Fluid Mech.*, 50(4):689–703, 1971.

B. E. Owolabi, D. J. C. Dennis, and R. J. Poole. Turbulent drag reduction by polymer additives in parallel-shear flows. *J. Fluid Mech.*, 827, 2017.

J. Pang and K.-S. Choi. Turbulent drag reduction by Lorentz force oscillation. *Phys. Fluids*, 16(5):L35–L38, 2004.

H. Park, G. Sun, et al. Superhydrophobic turbulent drag reduction as a function of surface grating parameters. *J. Fluid Mech.*, 747:722–734, 2014.

J. S. Park and M. D. Graham. Exact coherent states and connections to turbulent dynamics in minimal channel flow. *J. Fluid Mech.*, 782:430–454, 2015.

J. S. Park, A. Shekar, and M. D. Graham. Bursting and critical layer frequencies in minimal turbulent dynamics and connections to exact coherent states. *Phys. Rev. Fluids*, 3:014611, Jan 2018.

V. C. Patel and M. R. Head. Some observations on skin friction and velocity profiles in fully developed pipe and channel flows. *J. Fluid Mech.*, 38(1):181–201, 1969.

A. S. Pereira, R. L. Thompson, and G. Mompean. Common features between the Newtonian laminar–turbulent transition and the viscoelastic drag-reducing turbulence. *J. Fluid Mech.*, 877:405–428, 2019.

A. E. Perry. Hot-wire anemometry. Technical report, 1982.

H. d. Pitot. Description d'une machine pour mesurer la vitesse des eaux courantes et le sillage des vaisseaux. *Mémoires de L'Académie*, 1732.

Y. Pomeau. Front motion, metastability and subcritical bifurcations in hydrodynamics. *Physica D: Nonlinear Phenomena*, 23(1):3 – 11, 1986.

Y. Pomeau. The long and winding road. *Nat. Phys.*, 12(3):198, 2016.

S. B. Pope. *Turbulent Flows*. Cambridge University Press, 2000.

L. Prandtl. Essentials of fluid dynamics: with applications to hydraulics, aeronautics, meteorology and other subjets. 1953.

A. Rastegari and R. Akhavan. The common mechanism of turbulent skin-friction drag reduction with superhydrophobic longitudinal microgrooves and riblets. *J. Fluid Mech.*, 838:68–104, 2018.

H. Reichardt. Messungen turbulenter schwankungen. *Naturwissenschaften*, 26(24): 404–408, 1938.

M. Reischman and W. Tiederman. Laser-Doppler anemometer measurements in drag-reducing channel flows. *J. Fluid Mech.*, 70(2):369–392, 1975.

O. Reynolds. Xxix. an experimental investigation of the circumstances which determine whether the motion of water shall be direct or sinuous, and of the law of resistance in parallel channels. *Philos. Trans. R. Soc. Lond.*, (174):935–982, 1883.

P. Ricco. Modification of near-wall turbulence due to spanwise wall oscillations. *J. Turbul.*, 5:20–20, 2004.

J. P. Richter et al. *The notebooks of Leonardo da Vinci*, volume 2. Courier Corporation, 1970.

J. P. Rothstein. Slip on superhydrophobic surfaces. *Ann. Rev. Fluid Mech.*, 42:89–109, 2010.

M. Samie, I. Marusic, N. Hutchins, M. Fu, Y. Fan, M. Hultmark, and A. Smits. Fully resolved measurements of turbulent boundary layer flows up to Re_τ= 20000. *J. Fluid Mech.*, 851:391–415, 2018.

N. Sandham and L. Kleiser. The late stages of transition to turbulence in channel flow. *J. Fluid Mech.*, 245:319–348, 1992.

M. Sano and K. Tamai. A universal transition to turbulence in channel flow. *Nat. Phys.*, 12:249–253, 2016.

D. Seki and M. Matsubara. Experimental investigation of relaminarizing and transitional channel flows. *Phys. Fluids*, 24:124102, 2012.

C. Smith and S. Metzler. The characteristics of low-speed streaks in the near-wall region of a turbulent boundary layer. *J. Fluid Mech.*, 129:27–54, 1983.

A. J. Smits, B. J. McKeon, and I. Marusic. High–Reynolds number wall turbulence. *Ann. Rev. Fluid Mech.*, 43, 2011.

K. R. Sreenivasan and R. A. Antonia. Properties of wall shear stress fluctuations in a turbulent duct flow. *J. Appl. Mech.*, 44(3):389 – 395, 1977.

S. P. Sutera and R. Skalak. The history of Poiseuille's law. *Annu. Rev. Fluid Mech.*, 25(1):1–20, 1993.

J. Szodruch. Viscous drag reduction on transport aircraft. In *29th Aerospace Sciences Meeting*, page 685, 1991.

K. Takeishi, G. Kawahara, H. Wakabayashi, M. Uhlmann, and A. Pinelli. Localized turbulence structures in transitional rectangular-duct flow. *J. Fluid Mech.*, 782: 368–379, 2015.

K. A. Takeuchi, M. Kuroda, H. Chaté, and M. Sano. Directed percolation criticality in turbulent liquid crystals. *Phys. Rev. Lett.*, 99(23):234503, 2007.

K. M. Talluru, V. Kulandaivelu, N. Hutchins, and I. Marusic. A calibration technique to correct sensor drift issues in hot-wire anemometry. *Meas. Sci. Technol.*, 25(10): 105304, 2014.

J. Tao, B. Eckhardt, and X. Xiong. Extended localized structures and the onset of turbulence in channel flow. *Phys. Rev. Fluids*, 3(1):011902, 2018.

T. Tatsumi and T. Yoshimura. Stability of the laminar flow in a rectangular duct. *J. Fluid Mech.*, 212:437–449, 1990.

B. A. Toms. Some observations on the flow of linear polymer solutions through straight tubes at large Reynolds numbers. *Proc. of In. Cong. On Rheology, 1948*, 135, 1948.

C. Tropea and A. L. Yarin. *Springer handbook of experimental fluid mechanics*. Springer Science & Business Media, 2007.

T. Tsukahara, Y. Seki, H. Kawamura, and D. Tochio. DNS of turbulent channel flow at very low Reynolds numbers. *Proceedings of the 4th international symposium on turbulence and shear flow phenomena, Williamsburg, USA*, page 935–40, 2005.

T. Tsukahara, Y. Kawaguchi, and H. Kawamura. An experimental study on turbulent-stripe structure in transitional channel flow. *arXiv:1406.1378 [physics.flu-dyn]*, 2014.

R. Vinuesa, P. Schlatter, and H. M. Nagib. Characterization of the secondary flow in turbulent rectangular ducts with varying aspect ratio. *Proceedings of the 9th International Symposium on Turbulence and Shear Flow Phenomena, Melbourne, Australia*, page 1–6, 2015.

P. S. Virk. Drag reduction fundamentals. *AIChE Journal*, 21(4):625–656, 1975.

F. Waleffe. Exact coherent structures in channel flow. *J. Fluid Mech.*, 435:93–102, 2001.

F. Waleffe. Homotopy of exact coherent structures in plane shear flows. *Phys. Fluids*, 15(6):1517–1534, 2003.

D. Walker and W. Tiederman. Turbulent structure in a channel flow with polymer injection at the wall. *J. Fluid Mech.*, 218:377–403, 1990.

J. M. Wallace. Quadrant analysis in turbulence research: history and evolution. *Ann. Rev. Fluid Mech.*, 48:131–158, 2016.

J. M. Wallace, H. Eckelmann, and R. S. Brodkey. The wall region in turbulent shear flow. *J. Fluid Mech.*, 54(1):39–48, 1972.

M. Walsh. Turbulent boundary layer drag reduction using riblets. In *20th aerospace sciences meeting*, page 169, 1982.

M. Walsh and A. Lindemann. Optimization and application of riblets for turbulent drag reduction. In *22nd Aerospace Sciences Meeting*, page 347, 1984.

M. Walsh and L. Weinstein. Drag and heat transfer on surfaces with small longitudinal fins. In *11th Fluid and PlasmaDynamics Conference*, page 1161, 1978.

M. Warholic, H. Massah, and T. Hanratty. Influence of drag-reducing polymers on turbulence: effects of Reynolds number, concentration and mixing. *Exp. Fluids*, 27 (5):461–472, 1999.

R. D. Whalley, J. S. Park, A. Kushwaha, D. J. C. Dennis, M. D. Graham, and R. J. Poole. Low-drag events in transitional wall-bounded turbulence. *Phys. Rev. Fluids*, 2:034602, 2017.

R. D. Whalley, D. J. C. Dennis, M. D. Graham, and R. J. Poole. An experimental investigation into spatiotemporal intermittencies in turbulent channel flow close to transition. *Exp. Fluids*, 60(6):102, 2019.

C. White, Y. Dubief, and J. Klewicki. Re-examining the logarithmic dependence of the mean velocity distribution in polymer drag reduced wall-bounded flow. *Phys. Fluids*, 24(2):021701, 2012.

C. M. White and M. G. Mungal. Mechanics and prediction of turbulent drag reduction with polymer additives. *Annu. Rev. Fluid Mech.*, 40:235–256, 2008.

W. Willmarth and S. Lu. Structure of the Reynolds stress near the wall. *J. Fluid Mech.*, 55(1):65–92, 1972.

N. Worth and T. Nickels. Some characteristics of thin shear layers in homogeneous turbulent flow. *Philos. T. R. Soc. A*, 369(1937):709–722, 2011.

S. Wu and N. Bose. An extended power law model for the calibration of hot-wire/hot-film constant temperature probes. *Int. J. Heat Mass Transf.*, 37(3):437 – 442, 1994. ISSN 0017-9310.

I. Wygnanski, M. Sokolov, and D. Friedman. On transition in a pipe. Part 2. The equilibrium puff. *J. Fluid Mech.*, 69(2):283–304, 1975.

I. Wygnanski, J. Haritonidis, and R. Kaplan. On a Tollmien-Schlichting wave packet produced by a turbulent spot. *J. Fluid Mech.*, 92(3):505–528, 1979.

I. J. Wygnanski and F. Champagne. On transition in a pipe. Part 1. The origin of puffs and slugs and the flow in a turbulent slug. *J. Fluid Mech.*, 59(2):281–335, 1973.

L. Xi and M. D. Graham. Active and hibernating turbulence in minimal channel flow of Newtonian and polymeric fluids. *Phys. Rev. Lett.*, 104(21):218301, 2010.

L. Xi and M. D. Graham. Intermittent dynamics of turbulence hibernation in Newtonian and viscoelastic minimal channel flows. *J. Fluid Mech.*, 693:433–472, 2012.

X. Xiao and B. Song. The growth mechanism of turbulent bands in channel flow at low Reynolds numbers. *arXiv:1910.12254*, 2019.

X. Xiong, J. Tao, S. Chen, and L. Brandt. Turbulent bands in plane-Poiseuille flow at moderate Reynolds numbers. *Phys. Fluids*, 27(4):041702, 2015.

Y. Yeh and H. Cummins. Localized fluid flow measurements with an He–Ne laser spectrometer. *Appl. Phys. Lett.*, 4(10):176–178, 1964.

J. L. Zakin, B. Lu, and H.-W. Bewersdorff. Surfactant drag reduction. *Rev. Chem. Eng.*, 14(4-5):253–320, 1998.

Z. Zhang. *LDA application methods: laser Doppler anemometry for fluid dynamics*. Springer Science & Business Media, 2010.

J.-P. Zhao, X.-D. Du, and X.-H. Shi. Experimental research on friction-reduction with super-hydrophobic surfaces. *Journal of Marine Science and Application*, 6(3):58–61, 2007.

M. Ziegler. The construction of a hotwire anemometer with linear scale and negligible lag. *Proc. K. Ned. Akad. Wet.*, 15(1), 1934.

Appendix A

Drag reduction in channel flow using polymer injection

A.1 Introduction

In this appendix, a preliminary study carried out to investigate the effect of polymer injection in the current channel flow is discussed. Polymer drag reduction in turbulent flows was first discovered by Toms [1948]. Since then the drag reduction phenomenon due to polymer has remained an intense area of investigation in wall-bounded flows. To understand the progress made in the field of polymer drag reduction, review articles by Berman [1978], White and Mungal [2008] and Graham [2014] can be referenced. A brief introduction and literature review to the drag reduction due to polymer additives have been discussed in section 2.4. A potential issue while studying the polymer drag reduction is the degradation of the polymer with time after initially being homogenized with the flow [Owolabi et al., 2017]. One way to solve this issue is to continuously inject the polymer solution into the flow. Here, some of the studies which have employed polymer injection technique in channel flows to study drag reduction are discussed. Donohue et al. [1972] carried out a flow visualization study of modification in the near-wall region of the channel flow due to polyethylene oxide (PEO)-FRA polymer solution. The study was conducted for 139 ppm polymer solution where the Reynolds number (based on U_b and hydraulic diameter) of the flow was varied from 6000 to 22800. Reischman and Tie-

derman [1975] carried out LDV measurements in drag-reducing channel flow using PEO and polyacrylamide (PAA) at a 100 ppm concentration and observed a drag reduction of up to 40%. Walker and Tiederman [1990] carried out a detailed LDV investigation in a drag-reducing channel flow at $Re_h = 18000$, using PAA as the polymer additive. They studied the effect of polymer injection on the Reynolds stresses and observed that the rms of streamwise velocity increases in drag-reducing flows whereas the rms of wall-normal velocity and the RSS reduces. Recently, Elsnab et al. [2019] studied the effect of polymer injection on the statistical profiles of the flow for the low-drag reduction regime (DR = 6.5% to 26%). They studied for Re_τ between 650 and 1800, and employed molecular tagging velocimetry (MTV) technique to obtain the velocity profiles.

The aim of the present study is to carry out (simultaneous) wall shear stress and velocity measurements in a drag reduced channel flow using a polymer injection technique. Studies will be made for various levels of drag reduction by varying the Reynolds number and concentration of the injected polymer solution.

A.2 Experimental method

To carry out the experimental investigation, the same channel flow facility as used in the present thesis (discussed in chapter 3) has been utilized. Polyacrylamide, a flexible polymer and a good drag reducing agent [Escudier et al., 2009, Owolabi et al., 2017], has been used for the present study. Polyacrylamides have various grades and in the present study, Separan AP273E (generally called as 'Separan') has been used. Rather than mixing directly with the working fluid in the tank, polymer solution is injected in the channel through the pressure tappings. This has been done to minimize the effect of mechanical degradation of the polymer due to the pump. To provide a high concentration of the polymer in the channel the polymer solution should be injected at either very high flow rate or at a higher concentration. A 10,000 ppm by weight Separan solution is prepared in water as a polymer solution. To homogenize the solution, the polymer-water solution is kept on slow mixing for 2 days using a magnetic stirrer

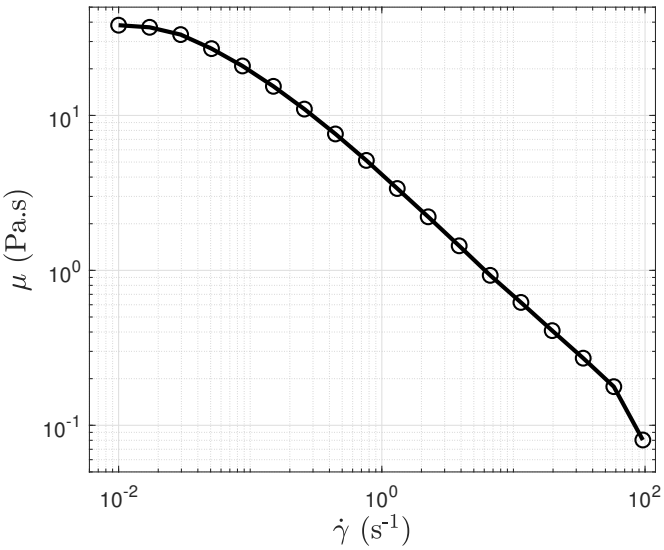

Figure A.1: Shear viscosity curve for Separan at a concentration of 10,000 ppm.

and then left still for 1 day. The solution is again mixed slowly using stirrer for a few minutes before use. To test of homogeneity of the polymer solution, 4 different samples were taken from the same batch and shear viscosity from each sample were compared. After only the observation of a good agreement between the shear viscosity curves, the sample was considered homogenized and was used for the experiment. Figure A.1 shows an example of a shear viscosity curve obtained from the polymer solution at a 10,000 ppm solution.

As the first step to study the effect of polymer injection in the channel flow, a flow visualization technique is employed to qualitatively observe the flow behaviour of the polymer solution in the channel. This has been conducted to check if the polymer solution is homogenized with the main flow. The polymer solution is mixed with a black coloured food dye prior to injection to aid the visualization. Dye visualization study is conducted for 2 different Reynolds numbers ($Re_\tau = 180$ and 490) and at three different injection speeds: 6ml/min, 24 ml/min and 48 ml/min. A syringe pump is used for the injection with the help of a 60 ml syringe. The injection is made from the pressure tappings present on the bottom plate of the channel. Table A.1 shows the various injection rates and the corresponding concentrations of the polymers in the channel. The polymer concentration is lower than the concentrations used by the previous re-

searchers (in the order of a few hundred ppm). To reach is a higher concentration is challenging in the current set-up given a very small size of the injection port.

Table A.1: Injection rates of the polymer solution and the corresponding the concentration of the polymer in the channel for the two Reynolds numbers.

Injection rate (ml/min)	Conc. for $Re_\tau = 180$ (ppm)	Conc. for $Re_\tau = 490$ (ppm)
6	0.518	0.207
24	2.073	0.828
48	4.145	1.656

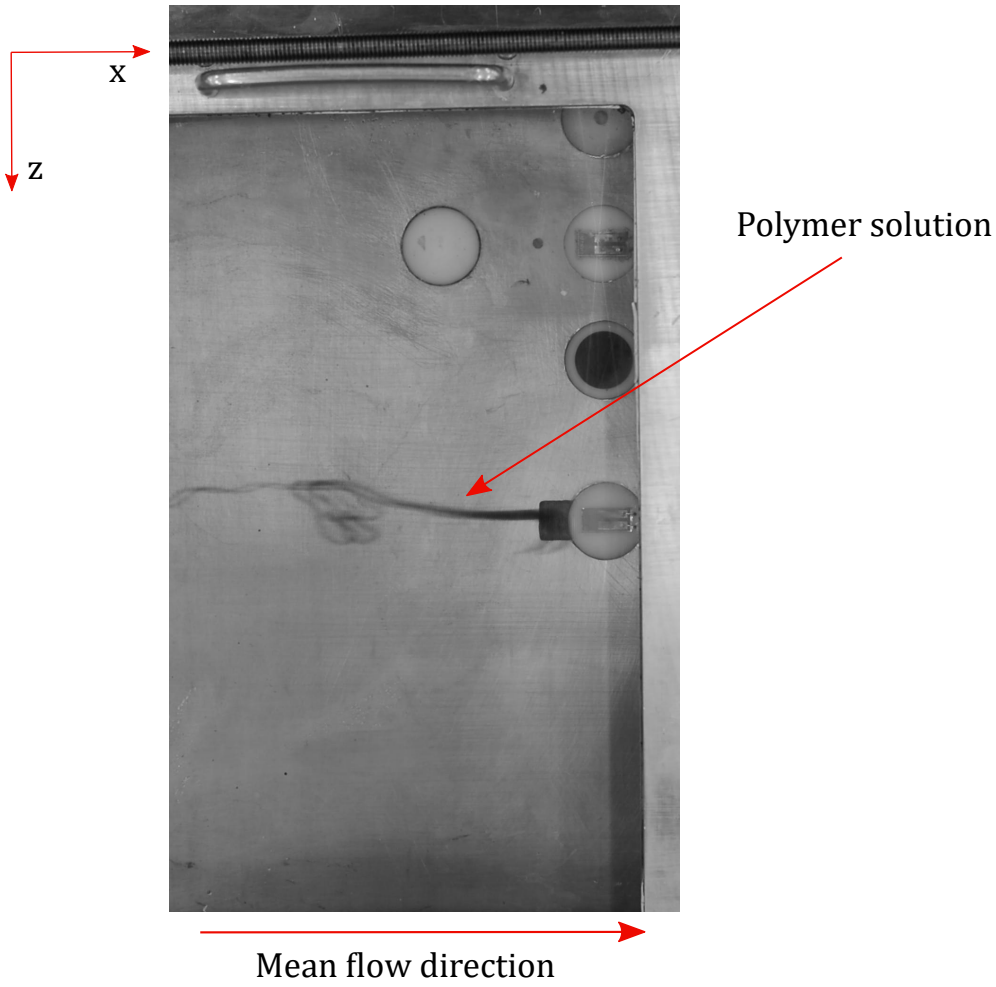

Figure A.2: Flow of the polymer solution in the test section for $Re_\tau = 180$ at the injection speed of 48 ml/min.

A.3 Flow visualization results

Same setup of the camera was employed for the flow visualization as explained in chapter 3. Videos are made for all the cases described above (two Reynolds numbers and three injection speeds). Figure A.2 shows an example of the flow visualization carried out in the present study. For $Re_\tau = 180$ at the injection speed of 48 ml/min, the polymer solution is not well homogenized with the flow by the time it reaches the test-section. Based on this result, further investigation of the effect of polymer injection in the channel was not made.

Future works involve making a bigger injection slot near the inlet of the channel. This will help in better mixing of the polymer solution with the mean flow by the time it reaches the test-section. This will allow for the higher injection rates thus increasing the polymer concentration in the flow.